IDEA League

Master of Science in Applied Geophysics

Research Thesis

Seismic Properties of Foundation Piles

Diameter determination of in-situ created foundation piles using the Seismic Tube

Aukje Veltmeijer

August 9, 2019

Delft University of Technology

Seismic Properties of Foundation Piles

Diameter determination of in-situ created foundation piles using the Seismic Tube

Master of Science Thesis

for the degree of Master of Science in Applied Geophysics

by

Aukje Veltmeijer

August 9, 2019

IDEA LEAGUE
JOINT MASTER'S IN APPLIED GEOPHYSICS

Delft University of Technology, The Netherlands
ETH Zürich, Switzerland
RWTH Aachen, Germany

Dated: *July 29, 2019*

Supervisor(s):

Dr. ir. P. Hölscher, Deltares

MSc. V. Hopman, Deltares

Dr. ir. D. S. Draganov, TU Delft

Committee Members:

Chair: Dr. ir. D. S. Draganov, TU Delft

Dr. ir. P. Hölscher, Deltares

MSc. V. Hopman, Deltares

Prof. Dr. H. Maurer, ETH Zurich

Abstract

Foundations are used for any civil structure and ensure stability and safety. A foundation method is to create piles in-situ by drilling a hole and filling it with concrete. The downside of this method is that the shape of the pile is unknown. The Seismic Tube is a device developed by Deltares to determine the radius of in-situ formed foundation piles. To test the Seismic Tube foundation piles with artificial defects such as bulging, necking and fracturing were created in a test site. Measurements are conducted and wave propagation in foundation piles is modeled. The distances traveled are small and interference of the wave arrivals takes place. These interference patterns are analysed and used for wave interpretation of the acquired data. Wave arrivals are picked in the data and used to obtain the concrete properties of the pile. Surface waves are used for MASW inversion and reflected body waves are analysed using seismic reflection theory. While MASW showed itself incapable of resolving the radius of the foundation piles, it was achieved using reflected waves. Combining all data diameter profiles are made of the foundation piles. Comparing these profiles to the with the soil conditions at the Deltares test site it can be concluded that the bulging in the piles can be related to soft soils, mostly peat, present in the subsurface. The designed necks were seen in the data, but the length of the Seismic Tube prevented detection of the deeper parts of the foundation piles. The designed bulges are either overlooked by limited number of data points, not formed or created at a too large depth. Fractures do not give a clear and characteristic responds. The data acquired with the Seismic Tube can be used to detect diameter changes in in-situ created foundation piles.

Acknowledgements

I would like to express my gratitude to my supervisors for their support and guidance at all stages in my masters thesis. These are my academic supervisor of TU Delft Deyan Draganov whose suggestions helped me get back on track with my thesis and my supervisors at Deltares Paul Hölscher and Victor Hopman where I have spend most of my time and without whom this thesis would not exist.

I would also like to thank Menno Buisman for the helpful discussions we have had. Also thanks to Martijn Smeulers for a day of measuring with the Seismic Tube and thanks to Itse Veltmeijer who spend a day of his holiday helping me performing measurements.

Finally thanks to my family and my friends from Delft, Aachen and Zürich.

Deltares/ TU Delft
August 9, 2019

Aukje Veltmeijer

Table of Contents

Abstract vii

Acknowledgements ix

Nomenclature xxv

Acronyms xxvii

1 Introduction 1

I Theory & Modeling 3

2 Foundation Piles 5

2-1 Defects in in-situ formed concrete foundation piles . . . 5

2-2 Non-Destructive Testing . . . 6

2-3 Seismic Tube . . . 7

2-4 Characteristics Investigated Piles . . . 10

3 Seismic Wave Propagation 15

3-1 Wave Theory . . . 15

3-2 Layered Medium . . . 17

3-2-1 Seismic Arrivals . . . 18

3-3 Wave types . . . 19

3-3-1 Waves in boreholes . . . 21

3-3-2 Wave Properties . . . 24

3-4 Waves in Foundation Piles . . . 26

4 Processing Techniques **29**
4-1 Seismic Processing techniques . . . 29
4-2 Multi-channel Analysis of Surface Waves . . . 31

5 Interpretation Tool **35**
5-1 Interpretation steps . . . 35

6 Modelling **39**
6-1 Forward Modelling . . . 39
6-2 Synthetic Seismograms . . . 41

II Data Examples **51**

7 Measurements **53**
7-1 Additional Measurements . . . 53
7-2 Visual Inspection . . . 56

8 Results **59**
8-1 Data Analysis . . . 59
8-1-1 Filtering . . . 61
8-1-2 Deconvolution . . . 63
8-1-3 Data Analysis Extra measurements . . . 66
Stacking . . . 67
8-2 Data Description Square Beemster Piles . . . 71
8-3 Surface Wave Inversion . . . 76

9 Discussion **81**
9-1 Data Interpretation . . . 81
9-2 Comparison with subsurface . . . 88
9-3 Data Interpretation Square Beemster Piles . . . 90

10 Conclusions **93**

11 Recommendations **95**

Bibliography **97**

A Visual Inspection Foundation Piles **101**

B Interpretation Variability **103**

C Results Deltares Data **107**
C-1 Data foundation piles Deltares test site 107
C-2 Frequency Spectrum 110
C-3 Processed Data 116

D Results Beemster Data **129**
D-1 Frequency Spectrum 130
D-2 Results Beemster processing 131
D-3 Interpreted Beemster Data 134

E Surface Wave Inversion **137**

F Profiles Foundation Piles **141**
F-1 Extracted Piles 150
F-2 Velocities 157

G CPT data **159**

List of Figures

2-1 Illustration of necking (left) and bulging (right) in foundation piles (Modified from [Chua, 2011]) . . . 6

2-2 Schematic representation of Seismic Tube (Retrieved from [Hölscher, 2019]) . . . 7

2-3 Seismic Tube, measuring tube . . . 8

2-4 Seismic Tube, recording system . . . 9

2-5 Input signal source Seismic Tube . . . 9

2-6 Frequency spectrum input signal source Seismic Tube . . . 10

2-7 Illustration of designed foundation piles for the Deltares test site. Showing the location of the PVC pipes and the designed flaws; necking, bulging and fractures. (Retrieved from from [Hopman, 2016]) . . . 12

2-8 Photo of the test site at Deltares Delft . . . 12

2-9 Photo of the piles pulled out the ground at Deltares test site. Pile number from left to right: 13, 7, 1, 8, 6, 17. . . . 13

2-10 Photo of designed neck in test pile 13 at Deltares test site . . . 13

2-11 Design test site showing the location of each pile. . . . 14

3-1 Illustration to visualize Huygens' Principle using plane waves. Each point the wave reaches act as a new source the new wave front is the envelope of all the waves generated by these point sources. The grey line, indicates the ray which is perpendicular to the wave front. (Retrieved from [Nave, 2016]) . . . 17

3-2 Different wave paths in the subsurface, refracted, reflected and direct waves (Retrieved from [Drijkoningen, 2014]) . . . 18

3-3 Illustration of different types of body and surface waves a) Compressional or P-wave b) Vertical polarized shear wave or SV-wave c) Horizontal polarized shear wave or SH-wave d) Rayleigh wave (Retrieved from [Mishra, 2018]) . . . 21

3-4 Schematic representation of particle motion of a Scholte and Stoneley wave (Retrieved from [Meegan et al., 1999]) . . . 22

3-5 a) Important sonic waveform propagation in a borehole, at time when P-wave is detected by receiver Rx. b) Schematic representation of the wavetrain recorded as a function of time. Indicated are the different wave types. (Retrieved from [Close et al., 2009]) . . . 24

3-6 First four modes of waves in a string between fixed endpoints (Retrieved from [Bormann et al., 2009]) . . . 26

3-7 Fresnel Zone (Retrieved from [Ghose, 2018]) . . . 26

3-8 Illustration of waves and layers in a foundation pile. The yellow line represents a transmitted wave, the green line a direct wave and the blue line a reflected wave. The source is indicated with a star and the first receiver with a triangle, the oil and poly ethylene layer are parts of the Seismic Tube (Note; illustration is not to scale). . . . 28

3-9 Illustration of ray paths in a foundation pile. The green line shows the direct wave, the red line shows the refracted wave path and the black lines show the ray paths of the reflected waves. The source is indicated with a black star and the receivers with red stars. layer are parts of the Seismic Tube (Note; illustration is not to scale). 28

4-1 Under-sampling causes aliased waveforms (Retrieved from [Drijkoningen, 2014]) . 29

4-2 Example of stacking (Modified from [Schlumberger, 2019]) . . . 30

4-3 Frequency filters and resulting signals in time domain (obtained from [Ghose, 2018]) 32

4-4 Example of the steps taken in a multi-channel analysis of surface waves survey (Retrieved from [ParkSeis, nd]) . . . 33

5-1 Start display when the interpretation tool is opened. . . . 36

5-2 The difference between the arrival without and with correction deflection from the pipe concrete boundary . . . 37

5-3 Display showing the interpretation tool the data with all the arrivals of the picked waves . . . 38

6-1 Snapshot at 0.02577 ms simulation time forward model of pile without defects. Note scale z and x direction are different. . . . 41

6-2 Snapshot at 0.04322 ms simulation time forward model of pile without defects. Note scale z and x direction are different. . . . 42

6-3 Snapshot at 0.05485 ms simulation time forward model of pile without defects. Note scale z and x direction are different. . . . 42

6-4 Snapshot at 0.06939 ms simulation time forward model of pile without defects. Note scale z and x direction are different. . . . 43

6-5 Snapshot at 0.09555 ms simulation time forward model of pile without defects. Note scale z and x direction are different. Wavefront hit the concrete soil boundary. 43

6-6 Snapshot at 0.11591 ms simulation time forward model of pile without defects. Note scale z and x direction are different. Reflected wave propagates towards the receivers . . . 44

6-7 Snapshot at 0.14499 ms simulation time forward model of pile without defects. Note scale z and x direction are different. Reflected wave arrives at the receivers. 44

6-8 Density and Velocity input model with a defect . . . 45

6-9 Seismogram of synthetic data, including calculated arrivals of direct, surface, refraction and reflection wave. Foundation pile modelled without defects. . . . 47

6-10 Enlarged part of seismogram of synthetic data, foundation pile modelled without defects including calculated arrival time of reflection wave. Shown are the recorded data of receiver 1 to 3 at an offset of 0.15 m, 0.30 m and 0.45 m from the source. Indicated in circles are interference patterns. 47

6-11 Seismogram of synthetic data, including calculated arrivals of direct, surface, refraction and reflection wave. Foundation pile modelled with a neck with a radius of 0.1 m and center at 0.575 m depth. 48

6-12 Enlarged part of seismogram of synthetic data, foundation pile modelled with a neck with a radius of 0.1 m and center at 0.575 m depth including calculated arrival time of reflection wave. Shown are the recorded data of receiver 1 to 4 at an offset of 0.15 m, 0.30 m, 0.45 m and 0.60 m from the source. 48

6-13 Seismogram of synthetic data, including calculated arrival of the reflection wave. Modelled with a bulge with a semi-minor axis of 0.1 m (x-direction) and a semi-major axis of 0.1 m (z-direction) and center at 0.3 m distance from the source. Reflection calculated using a concrete thickness of 0.24 m and velocity of 4000 m/s. 49

7-1 Photo of top of Pile 10 the test site at Deltares Delft. The Seismic Tube is lowered in the PVC pipe 55

7-2 Photo of top of Pile 15 the test site at Deltares Delft 55

7-3 Photo of top of Pile 12 the test site at Deltares Delft 56

7-4 Photo of the cable of the Seismic Tube with the measuring tape attached 56

7-5 Photo of a created neck on pile 17 with part of a measuring tape. 57

7-6 Photo of a bulge on pile 13 with part of a measuring tape. 57

7-7 Photo of some holes dug underneath the pile to measure the circumference. . . . 57

7-8 Photo the cleared site. Pile number from left to right: 13, 7, 1, 8, 6, 17. 57

8-1 Two shots of foundation pile nr 13 at the Deltares test site 60

8-2 Frequency spectrum for pile 13 shot 10 showing frequency distribution vs amplitude for the 8 traces. 61

8-3 Frequency spectrum for pile 13 shot 10 showing frequency distribution vs amplitude for the 8 traces in separate subplots. Black line indicates frequency spectrum after applying a low-pass filter 62

8-4 Seismograms showing the result after frequency filtering. Shot 10 of foundation pile nr 13 at the Deltares test site. 63

8-5 Seismograms showing the result before and after low-cut frequency filtering. Shot 10 of foundation pile nr 13 at the Deltares test site. 64

8-6 Deconvolution results of Pile 13 shot 10 Deltares test site 65

8-7 Deconvolution results of Pile 13 shot 10 Deltares test site 66

8-8 Data of extra measurements. First shot of pile 11 at 7.45 m depth. Showing high amplitude noise in traces 5 to 8. 67

8-9 Frequency spectrum of first shot of pile 10 at 7.45 m depth. 68

8-10 Data of the five shots of receiver 1 of pile 15 at 7.45 m depth. 68

8-11 Seismograms showing the result before and after stacking of 5 shots. Measurement depth of 7.38 m of foundation pile nr 10 at the Deltares test site. 69

8-12 Seismograms showing the result before and after stacking of 5 shots. Measurement depth of 6.93 m of foundation pile nr 12 at the Deltares test site. 69

8-13 Filtering and Deconvolution results of Pile 10 shot 11 extra measurements at Deltares test site. . . . 70
8-14 Seismograms showing the shot 34 of piles 1 to 3 at the Beemster test site. . . . 72
8-15 Frequency spectrum of pile 3 shot 34 of Beemster test site. . . . 73
8-16 Seismograms showing the result after frequency filtering. Shot 34 of foundation pile nr 3 at the Beemster test site. . . . 74
8-17 Filtering and Deconvolution results of Pile 3 shot 34 extra measurements at Beemster test site. . . . 75
8-18 Seismogram Pile 13 shot 10 with and without mute. Arrivals faster than 1200 m/s and slower than 600 m/s muted . . . 78
8-19 Frequency - Velocity spectrum pile 13 shot 10. Picked dispersion curve in black. 78
8-20 Frequency - Velocity spectrum of muted shot 10 pile 13. Picked dispersion curve in black. . . . 79
8-21 Robustness check inversion . . . 80
8-22 Inversion results surface wave inversion run 1. Shown are the p-velocity, s-velocity and density profiles of the models with the lowest misfits of the total investigated models . . . 80

9-1 Data of shot 5 pile 13, including the picked arrivals of the surface, direct, refracted and reflected wave. In lower right corner enlargement of first two traces with the interference patterns. On top the pile number, depth relative to the top of the reinforcement, concrete velocity and concrete thickness are indicated. . . . 83
9-2 Seismograms showing the result after frequency filtering with interpreted waves indicated. Shot 10 of foundation pile nr 13 at the Deltares test site. . . . 84
9-3 Profiles foundation Pile 13. Showing the radius of the pile determined using the Seismic Tube in red and designed shape in black, designed defects not to scale. The measured shape from visual inspection is shown in blue. Source location of each measurement indicated with a dot. . . . 86
9-4 Profile foundation Pile 10. First measurements in red, second measurements in blue and the designed radius in black, designed defects not to scale. Source location of each measurement indicated with a dot. . . . 87
9-5 CPT DKM102 with profiles pile 8 and 13. Dutch to English; Top: Indicative Soil description, automatically generated from CPT data valid below groundwater level. Soil layers; zand vast; solid sand, zand kleiig; clayey sand, veen; peat, organisch materiaal; organic material, klei; clay, zwak siltig tot siltig; slightly silty to silty. On the left: Diepte t.o.v. NAP; Depth relative to Amsterdam Ordnance Datum. The light green color is loamy clay. Profiles showing the radius of the pile determined using the Seismic Tube in red and nominal radius in black, designed defects excluded. The measured shape from visual inspection is shown in blue. Source location of each measurement indicated with a dot. . . . 89
9-6 Location CPT's performed at Deltares test site. . . . 90
9-7 Beemster data of shot 34 pile 1, including the picked arrivals of the surface, direct, refracted and reflected wave. In lower right corner enlargement of first three traces. 92
9-8 Beemster data of shot 34 pile 3, including the picked arrivals of the surface, direct, refracted and reflected wave. In lower right corner enlargement of first three traces. 92

A-1 Photos of diameter changes in pile 6. . . . 101
A-2 Photos of diameter changes in pile 7. . . . 101
A-3 Photos of diameter changes in pile 8. . . . 101

A-4 Photos of diameter changes in pile 13. 102
A-5 Photo of a created neck on pile 17 and slight bulging with part of a measuring tape. Orange marks indicate the measurement location of the seismic tube. . . . 102

B-1 Seismogram of shot 2 of pile 4. Source at 2.34 m depth. Reflection calculated using a concrete thickness of 0.20 m, thus when no defect would be present and velocity of 3890 m/s. 104
B-2 Seismogram of shot 2 of pile 4. Source at 2.34 m depth. Reflection calculated using a concrete thickness of 0.222 m and velocity of 3890 m/s. 104
B-3 Enlarged part of seismogram of shot 2 of pile 4. Source at 2.34 m depth. Reflection calculated using a concrete thickness of 0.20 m, thus when no defect would be present and velocity of 3890 m/s. Shown are the recorded data of receiver 1 and 2 at an offset of 0.15 m and 0.30 m from the source. 105
B-4 Enlarged part of seismogram of seismogram of shot 2 of pile 4. Source at 2.34 m depth. Reflection calculated using a concrete thickness of 0.222 m and velocity of 3890 m/s. Shown are the recorded data of receiver 1 and 2 at an offset of 0.15 m and 0.30 m from the source. 105
B-5 Enlarged part of seismogram of seismogram of shot 2 of pile 4. Source at 2.34 m depth. Reflection calculated using a concrete thickness of 0.21 m and velocity of 3890 m/s. Shown are the recorded data of receiver 1 and 2 at an offset of 0.15 m and 0.30 m from the source and lines indicating the zero of the trace and the peak part of the wiggle. 106

C-1 Seismograms of eleven shots at different heights measured at pile 13 of the Deltares test site 109
C-2 Frequency spectrum of pile 13 shot 1 of Deltares test site. 110
C-3 Frequency spectrum of pile 13 shot 2 of Deltares test site. 111
C-4 Frequency spectrum of pile 13 shot 3 of Deltares test site. 111
C-5 Frequency spectrum of pile 13 shot 4 of Deltares test site. 112
C-6 Frequency spectrum of pile 13 shot 5 of Deltares test site. 112
C-7 Frequency spectrum of pile 13 shot 6 of Deltares test site. 113
C-8 Frequency spectrum of pile 13 shot 7 of Deltares test site. 113
C-9 Frequency spectrum of pile 13 shot 8 of Deltares test site. 114
C-10 Frequency spectrum of pile 13 shot 9 of Deltares test site. 114
C-11 Frequency spectrum of pile 13 shot 10 of Deltares test site. 115
C-12 Frequency spectrum of pile 13 shot 11 of Deltares test site. 115
C-13 Filtering and Deconvolution results of Pile 13 shot 1 at Deltares test site. 117
C-14 Filtering and Deconvolution results of Pile 13 shot 2 at Deltares test site. 118
C-15 Filtering and Deconvolution results of Pile 13 shot 3 at Deltares test site. 119
C-16 Filtering and Deconvolution results of Pile 13 shot 4 at Deltares test site. 120
C-17 Filtering and Deconvolution results of Pile 13 shot 5 at Deltares test site. 121
C-18 Filtering and Deconvolution results of Pile 13 shot 6 at Deltares test site. 122
C-19 Filtering and Deconvolution results of Pile 13 shot 7 at Deltares test site. 123
C-20 Filtering and Deconvolution results of Pile 13 shot 8 at Deltares test site. 124
C-21 Filtering and Deconvolution results of Pile 13 shot 9 at Deltares test site. 125

C-22 Filtering and Deconvolution results of Pile 13 shot 10 at Deltares test site. . . . 126
C-23 Filtering and Deconvolution results of Pile 13 shot 11 at Deltares test site. . . . 127

D-1 Frequency spectrum of pile 1 shot 34 of Beemster test site. 130
D-2 Frequency spectrum of pile 2 shot 34 of Beemster test site. 131
D-3 Filtering and Deconvolution results of Pile 1 shot 34 extra measurements at Beemster test site. 132
D-4 Filtering and Deconvolution results of Pile 2 shot 34 extra measurements at Beemster test site. 133
D-5 Seismograms showing the result after frequency filtering with interpreted waves indicated. Shot 34 of foundation pile nr 3 at the Beemster test site. 134
D-6 Beemster data of shot 34 pile 2, including the picked arrivals of the surface, direct, refracted and reflected wave. In lower right corner enlargement of first three traces. 135

E-1 Inversion results surface wave inversion runs 1 to 6. Shown are the p-velocity, s-velocity and density profiles of the models with the lowest misfits of the total investigated models 140

F-1 Design test site showing the location of each pile. 142
F-2 Profile foundation piles left row. Determined thickness in red and designed shape in black. Designed defects not to scale. Source location of each measurement indicated with a dot. 143
F-2 Profile foundation piles second row from left. Determined thickness in red and designed shape in black. Designed defects not to scale. Source location of each measurement indicated with a dot. 144
F-2 Profile foundation piles third row from left. Determined thickness in red and designed shape in black. Designed defects not to scale. Source location of each measurement indicated with a dot. 145
F-2 Profile foundation piles second row from right. Determined thickness in red and designed shape in black. Designed defects not to scale. Source location of each measurement indicated with a dot. 146
F-2 Profile foundation piles first row from right. Determined thickness in red and designed shape in black. Designed defects not to scale. Source location of each measurement indicated with a dot. 147
F-3 Profile foundation Pile 10, 12 and 15 from extra measurements. First measurements in red, second in blue and nominal diameter.. Source location of each measurement indicated with a dot. 148
F-4 Close up of one side of the pile, showing the radius of the pile determine using the seismic tube in red and blue and the designed radius in black. Designed defects excluded. Location of each measurement indicated with a dot. Profile foundation Pile 10, 12 and 15 from extra measurements. First measurements in red second in blue. Source location of each measurement indicated with a dot. 149
F-5 Profiles foundation Pile 1. 151
F-6 Profiles foundation Pile 6. 152
F-7 Profiles foundation Pile 7. 153
F-8 Profiles foundation Pile 8. 154
F-9 Profiles foundation Pile 13. 155
F-10 Profiles foundation Pile 17. 156

G-1 Location CPT's performed at Deltares test site. 159

G-2 CPT DKM100 160
G-3 CPT DKM101 161
G-4 CPT DKM101 162
G-5 CPT DKM102 163
G-6 CPT DKM103 164
G-7 CPT DKM103 165
G-8 CPT DKM104 166
G-9 CPT DKM105 167

List of Tables

2-1 Characteristics of the measured foundation piles at the Deltares and Beemster test site . . . 11

3-1 Typical velocity and density values for materials used when testing concrete piles using the Seismic Tube. (Retrieved from [Drijkoningen, 2014], [Polytron Kunststoffentechnik, 2016], [Borcherdt, 1994], [Omnexus, nd] and [Dakota Ultrasonics, 2016]) . . . 27

6-1 Input Values for Velocity, Density and Attenuation Model . . . 40

6-2 Modelling parameters . . . 40

7-1 Measurement parameters extra measurements foundation piles at the Deltares test site . . . 54

8-1 Input parameters MASW inversion . . . 79

9-1 Velocities found in foundation piles at Beemster test site. . . . 91

F-1 Distance of top of reinforcement bar of each pile to flattened top concrete. . . . 141

F-2 Velocities found in foundation piles at Deltares test site. . . . 157

Nomenclature

p	acoustic pressure
v	velocity
κ	compression modulus
ρ	density
f	force density by external forces
i_v	volume density of volume injection
c	wave velocity
x, y, z	Cartesian space coordinates
t	time
A	(complex) amplitude
ω	circular frequency
$\mathbf{k}$	wave vector
$\mathbf{x}$	position vector
t	time
$\mathbf{p}$	slowness vector
$\mathbf{k} \cdot \mathbf{x} - \omega t$	phase
θ_i	angle of incidence in degrees
θ_r	angle of refraction in degrees
θ_P	angle of incident P-wave in degrees
θ_S	angle of refracted S-wave in degrees
c_P	P-wave velocity
c_S	S-wave velocity

x distance in m

z thickness of first medium in m

$\theta_c = sin^{-1}\frac{n_1}{n_2}$ critical angle in degrees

$n_x = \frac{v_v}{v_m}$ refractive index

v_v speed of light in vacuum

v_m speed of light in given material

R refection coefficient

v_p compressional or P-wave velocity

λ Lamé 's constant

μ shear modulus

K bulk modulus

v_s shear or S-wave velocity

E Young's Modulus (stiffness)

σ Poisson's Ratio

V_T Tube wave velocity

V_w fluid wave velocity

D inner diameter

e wall thickness

f frequency

Q quality factor

E energy of seismic wave

η correction constant

r radius Fresnel zone

λ wavelength

$x(t)$ recorded seismogram

$r(t)$ Earth's response

$w(t)$ seismic wavelet

$*$ convolution

Acronyms

CLS Cross-hole Sonic Logging

CPT Cone Penetration Test

DAC Deep Acoustic Check

ESAC Extended Spatial Auto-Correlation

ETH Swiss Federal Institute of Technology

FFT Fast Fourier Transform

IE Impact Echo

IR Impulse Response

MASW Multi-channel Analysis of Surface Waves

NAP Amsterdam Ordnance Datum

NDT Non-Destructive Testing

PIT Pile Integrity Test

PML Perfectly Matching Layer

PS Parallel Seismics

SASW Spectral Analysis of Surface Waves

SE Sonic Echo

SHSL Single-Hole Sonic Logging

SPAC Spatial Auto-Correlation

SSL Simple Sonic Logging

TUD Delft University of Technology

RWTH Aachen University

Chapter 1

Introduction

Foundations are used for any civil structure and ensure stability and safety. In the Netherlands foundation piles are often hammered into the ground which creates a lot of noise and vibrations. An alternative method is to create piles in-situ by drilling a hole and filling it with concrete. The downside of in-situ created piles is that a visual inspection is not possible and the shape of the pile is unknown. Defects in diameter can cause failure and correcting for these faulty piles cost the construction money and delay.

Measurement techniques used to determine whether these piles are up to standard are ambiguously and do not give any (reliable) information about the shape and diameter of the formed piles. If a pile shows a defect during testing and it is possible to determine the type and origin. Corrections could be made during construction of other foundation piles. This will eliminate the replacement of foundation piles, which results in saving time and money.

A reliable technique to determine the shape of a foundation piles does not exist yet. Geo Impuls is an program of the geo-technical engineering community in the Netherlands which aims to reduce failure in construction projects due to ground related failures. Deltares has designed the Seismic Tube to fill this gap as part of the Geo Impuls program. The Seismic Tube is based on seismic wave theory and has an acoustic source and eight receivers in a tube, as the name indicates. This tube is lowered into a hole in the middle of a foundation pile to detects defects and to prevent failure.

This thesis aims to use data acquired with the Seismic Tube to derive the diameter and show the Seismic Tube can be used to detect changes in diameter in in-situ formed foundation piles. This is done by answering the following research questions;

1. What types of defects are present in in-situ formed foundation piles?
2. What is the frequency signature of the Seismic Tube?
3. What types of wave exists within a foundation pile?
4. Is it possible to derive the thickness of a pile using surface waves and reflected waves?

5. Which defects can be detected?
6. What is the accuracy of the Seismic Tube?
7. What is the relation between subsurface and the shape of a pile?

To test the Seismic Tube and answer these questions 20 foundation piles with artificial defects were created. Field measurements were performed to collect data which were then analysed. Forward modelling gives insight of wave propagation and arrival of different wave types within a foundation pile. An interpretation tool based on wave theory is built in MATLAB® App Designed to interpret the data and derive wave parameters. Finally these results in diameters profiles of the piles which will be compared to subsurface data.

This research is done at research institute Deltares as a master thesis of the joint master Applied Geophysics of Delft University of Technology (TUD), Swiss Federal Institute of Technology (ETH) and Aachen University (RWTH).

Part I

Theory & Modeling

Chapter 2

Foundation Piles

Foundations are very important to ensure the stability and safety of civil structures. There are different foundation techniques of which piles are the most used in the Netherlands due to soft soils. In this chapter in-situ formed piles and some techniques to determine their integrity are discussed.

2-1 Defects in in-situ formed concrete foundation piles

Conventional methods for building foundation piles can cause damage to nearby structures due to vibrations. In-situ cast foundation piles are a solution for areas where no vibrations and low noise are allowed.

A difficulty with in-situ cast piles is that a visual inspection (quality control) of the pile is not possible. Piles cast without a casing form themselves to the shape of the borehole, which can lead to defects like a reduction or increase in diameter. Imperfections of in-situ formed foundations piles can arise from different sources, but often result in similar defects [Chan, 1987].

In-situ formed foundation pile are created by firstly rotating a steel casing into the ground. Reinforcement bars are put in the casing and concrete is poured in. Then the casing is pulled out with vibrating or rotating motions, whereby the tip of the screw stays behind in the ground [van t'Hek, 2019].

Defects in pile diameter are usually formed when the steel casing is removed. An decrease and increase in diameter are respectively called necking and bulging. While bulging may increase the pile ultimate load, it is still a defect [Wakil and Kassim, 2010]. Since bulging implies an non-uniform distribution of concrete along the pile, it suggest necking or other defects are present as well. Bulging occurs when the pressure between the concrete exceed the pressure in the soil and the fluid concrete will penetrate the soil. The other way around necking occurs.

Necking is the reduction of the pile diameter and reduces the loading capacity of the foundation pile. The severity of this depends on the load which has to be applied on the pile.

Necking can also occur when the shearing stresses between the steel casing and the concrete are enough to lift the concrete when the casing is taken out. Below this lifted concrete a neck is formed filled with soil or groundwater [ONeill, 1991]. In figure 2-1 a illustration of necking an bulging in piles is given.

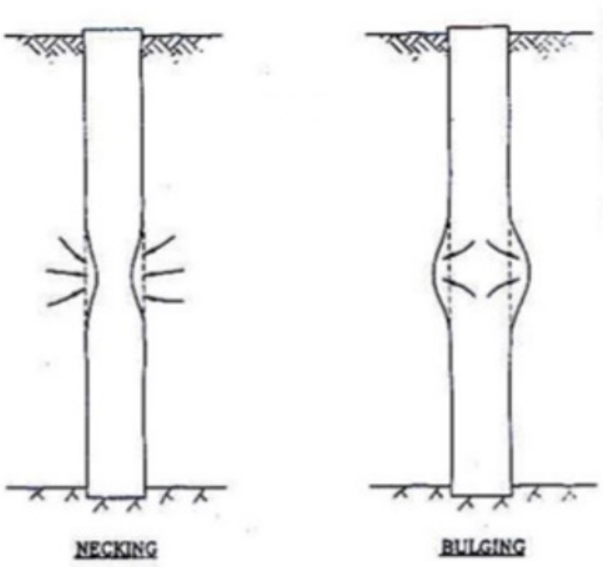

Figure 2-1: Illustration of necking (left) and bulging (right) in foundation piles (Modified from [Chua, 2011])

2-2 Non-Destructive Testing

Non-Destructive Tests Non-Destructive Testing (NDT) are used to investigate the integrity of foundation piles. It is considered to have high potential as NDT is cost effective and damage free [Liao et al., 2006]. The goal of NDT is to obtain the geometry of the piles and characterize defects, if there are any and use this to estimate the capacity of the foundation piles. Non-destructive tests can be divided in surface reflection and borehole methods [Huang and Ni, 2012].

Sonic Echo (SE), Impulse Response (IR) and Impact Echo (IE) are the most common surface reflection techniques used to determine the integrity of foundation piles. A force is applied to the pile and the receiver records the response (the reflected wave) at the head of the pile [Liao et al., 2006]. A limitation of these methods is that they can only determine the pile length if this is less than 14 meters and with a cap thickness less than 2 meters [Huang and Ni, 2012]. The advantage is that the methods are very easy and fast to use.

Borehole methods have receivers placed in a tube or borehole which needs to be made before testing causing borehole methods to be more expensive than surface methods. Examples of borehole methods are Cross-hole Sonic Logging (CLS), Simple Sonic Logging (SSL) and Parallel Seismics (PS). The advantage over surface methods is that using a borehole method pile of greater depth can be investigated [Liao et al., 2006]. CLS uses multiple boreholes

and does cross hole seismic to obtain the concrete properties of the concrete in between these boreholes. Limitations of this method are that it needs multiple boreholes and it does not look radially outwards. SSL make use of only one source and one receiver limiting the information that can be obtained.

The Seismic Tube is a borehole method designed to overcome some of the limitations of the other borehole methods. It only needs one hole in the center of foundation pile compared to multiple with CLS. The Seismic Tube looks radially outwards to determine the diameter instead of only to the concrete properties in between the boreholes needed for CLS. Compared to SSL it gives more possibilities for data processing due to its 8 receivers. SSL only has one source and one receivers limiting the information that can be obtained.

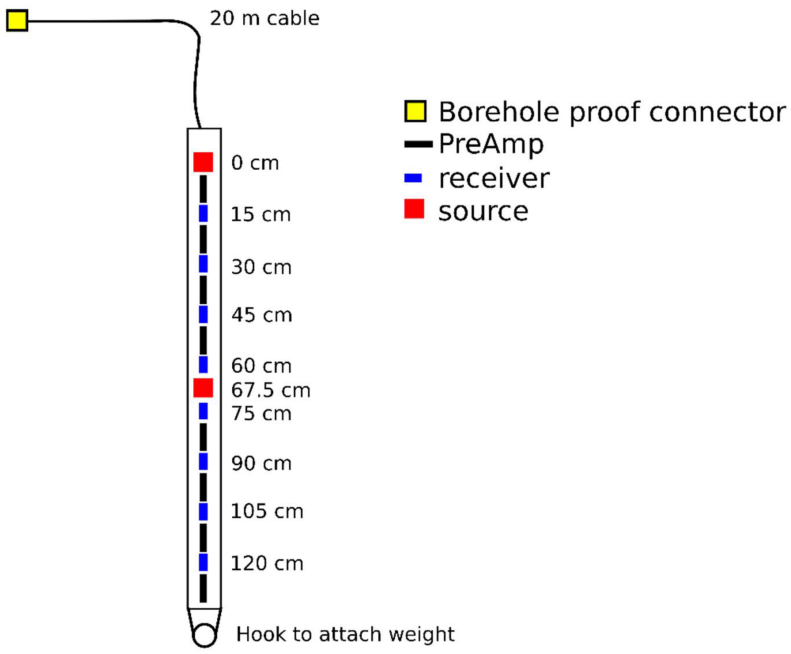

Figure 2-2: Schematic representation of Seismic Tube (Retrieved from [Hölscher, 2019])

2-3 Seismic Tube

The data recorded and processed in this thesis is recorded using the Seismic Tube. This device is developed by Deltares to investigate the thickness of in-situ formed concrete foundation piles. The tube which is lowered into the foundation pile to take measurements and the recording system together are called the "Seismic Tube". The Seismic Tube consists of two piezo-electric sources and eight hydrophones. The sources and receivers are placed within an oil filled plastic (poly ethylene) tube which hangs at a cable and has a weight of 3.8kg attached at the bottom. This weight is attached to ensure the tube will hangs straight while measuring. The whole tube from top to bottom including the weight is 2.20 m long. One

source is placed at the top and one in the center of the device, the receivers are placed 15 cm apart. In figure 2-2 a schematic representation of the Seismic Tube is given. Figure 2-3 and 2-4 shows the Seismic Tube and the recording system. The middle receiver was broken before the start of this thesis therefor only the top source is used. Besides seismic sources and receivers, many cables and eight temperature sensors are included inside the tube, these sensors aren't used in this project.

The device is lowered into a hole or pipe in the center of the foundation pile and a source will be ignited at pre-set distances. The 8 receivers simultaneously record the incoming signals. This data is recorded using software written for this Seismic Tube and stored in binary files. The processing and interpretation of the data is described in chapter 8.

Figure 2-3: Seismic Tube, measuring tube

Figure 2-4: Seismic Tube, recording system

Source signal The signal send by the piezoelectric source in the Seismic Tube is controlled by an input signal. This signal is a Ricker wavelet send by the system and is then amplified to maximum of 150V. This input signal before amplification is shown in figure 2-5. The signal is designed to have a frequency range of 60kHz to 100kHz. The frequency spectrum of the input signal and these boundaries are given in figure 2-6.

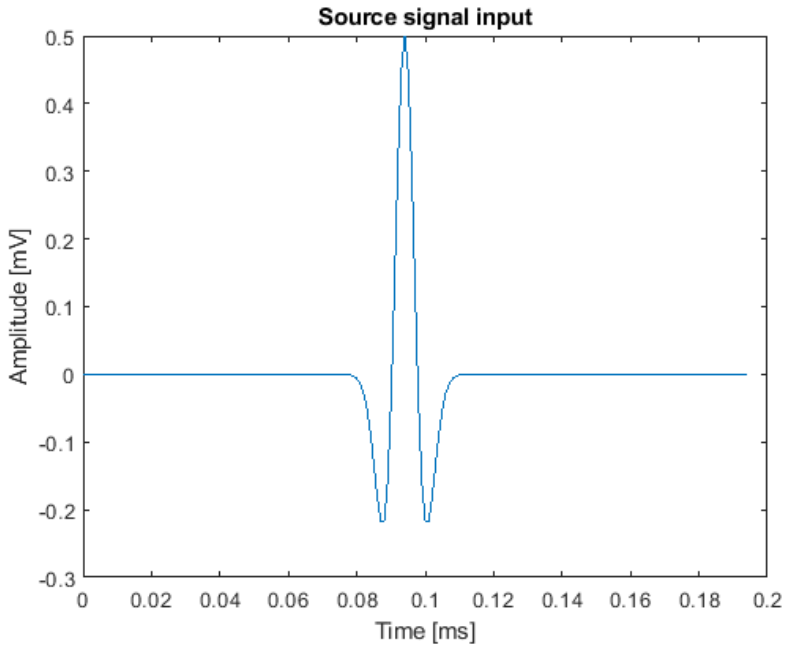

Figure 2-5: Input signal source Seismic Tube

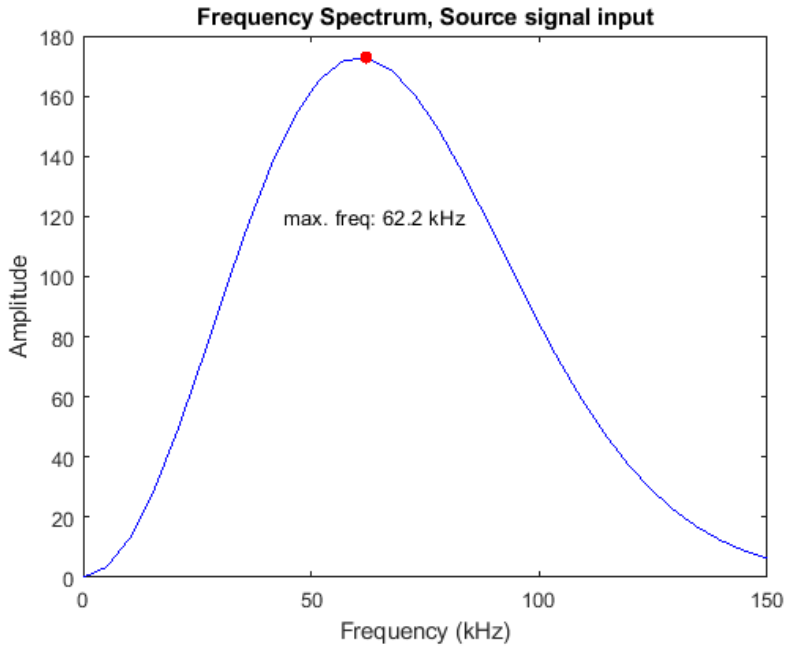

Figure 2-6: Frequency spectrum input signal source Seismic Tube

2-4 Characteristics Investigated Piles

Measurements are taken at two test sites. In-situ created piles are measured at a test site on Deltares property in Delft and prefabricated piles are measured at a test site in Midden-Beemster. Data of the Deltares and Midden-Beemster was already acquired and provided. Additional data was acquired of three piles at the Deltares test site.

The piles at the Deltares test site are created in-situ, a so called Hek-pile [van t'Hek, 2019]. Necks, bulges and fractures were added to these HEKPiles in order to investigate these piles with controlled defects. A neck was created by placing rubber tires around the reinforcement bars, which were injected with bentonite quickly after pouring the concrete into the casing. The bulges were created by adding injection channels to the reinforcement bars. Through these channels extra concrete was injected after pouring the concrete. Additionally, the reinforcement bars were cut at specific depths. After setting of the concrete the fractures were created by driving against the foundation piles [Hopman and Hölscher, 2015]. Piles 1 tot 4 were used for cross-hole seismics therefor are equipped with 3 PVC pipes of which one in the middle of the pile, instead of one PVC pipe. The characteristics of the piles are shown in table 2-1 and their design visualized in figure 2-7.

To investigate whether the artificially made defects are in place, piles number 1, 6, 7, 8, 13 and 17 were pulled out the ground and pile 11 was partially excavated. The conclusions after inspection of these piles were that the techniques to create necks and fractures worked well and it can be assumed that necking has occurred where planned. The technique to create bulging did not work as planned and therefor it cannot be assumed bulging has occurred where planned. Also the areas no defects were planned cannot be assumed defect free, as defects are observed in these areas. Thus the findings from the measurements of the Deltares

piles can deviate from the designed shape of the piles [Hopman and Hölscher, 2015]. Figure 2-8 shows the test site and figure 2-9 shows some of the piles which were pulled out the ground. Visible in this photo is the changing diameter of the piles, in figure 2-10 a neck designed in one of the piles is visualized. The piles were made, tested and pulled out the ground in 2015, as can be seen in the picture nature has been growing ever since. More photo's of the visual inspection of the piles can be found in appendix A.

The created foundation piles were used to test several measurement techniques. Techniques used, besides the Seismic Tube, are Pile Integrity Test (PIT), Deep Acoustic Check (DAC), Single-Hole Sonic Logging (SHSL), CLS, PS and temperature measurements. The subsurface is investigated by performing several Cone Penetration Test (CPT) at the test site. These are shown in appendix G.

At the Beemster test site measurements at pre-fabricated pile were performed. The first test consisted of four square standard prefabricated pile which were driven into the ground. Two piles with dimensions of 25x25 cm^2 and two piles with a dimension of 45x45 cm^2 [Hölscher, 2019].

Characteristics Test Piles		
Property	**Deltares Test site**	**Beemster Test site**
Designed Shaft Diameter	460 [mm]	25x25 and 45x45 [cm^2]
Designed Tip Diameter	560 [mm]	25x25 and 45x45 [cm^2]
Length	10 [m]	13 [m]
Diameter PVC Tube	63 [mm]	45 [mm]
Thickness PVC Tube	3 [mm]	- [mm]
Density	2400 [kg/m^3]	2400 [kg/m^3]
Poisson's ratio	0.1-0.2 [-]	0.1-0.2 [-]
Young's Modulus	27100 - 42200 [N/mm^2]	27100 - 42200 [N/mm^2]

Table 2-1: Characteristics of the measured foundation piles at the Deltares and Beemster test site

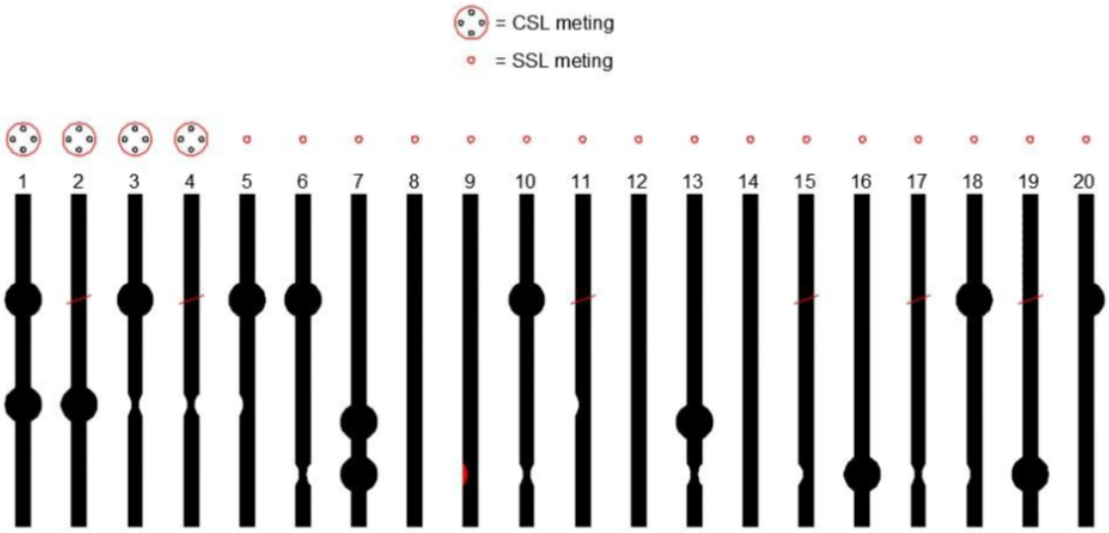

Figure 2-7: Illustration of designed foundation piles for the Deltares test site. Showing the location of the PVC pipes and the designed flaws; necking, bulging and fractures. (Retrieved from from [Hopman, 2016])

Figure 2-8: Photo of the test site at Deltares Delft

Figure 2-9: Photo of the piles pulled out the ground at Deltares test site. Pile number from left to right: 13, 7, 1, 8, 6, 17.

Figure 2-10: Photo of designed neck in test pile 13 at Deltares test site

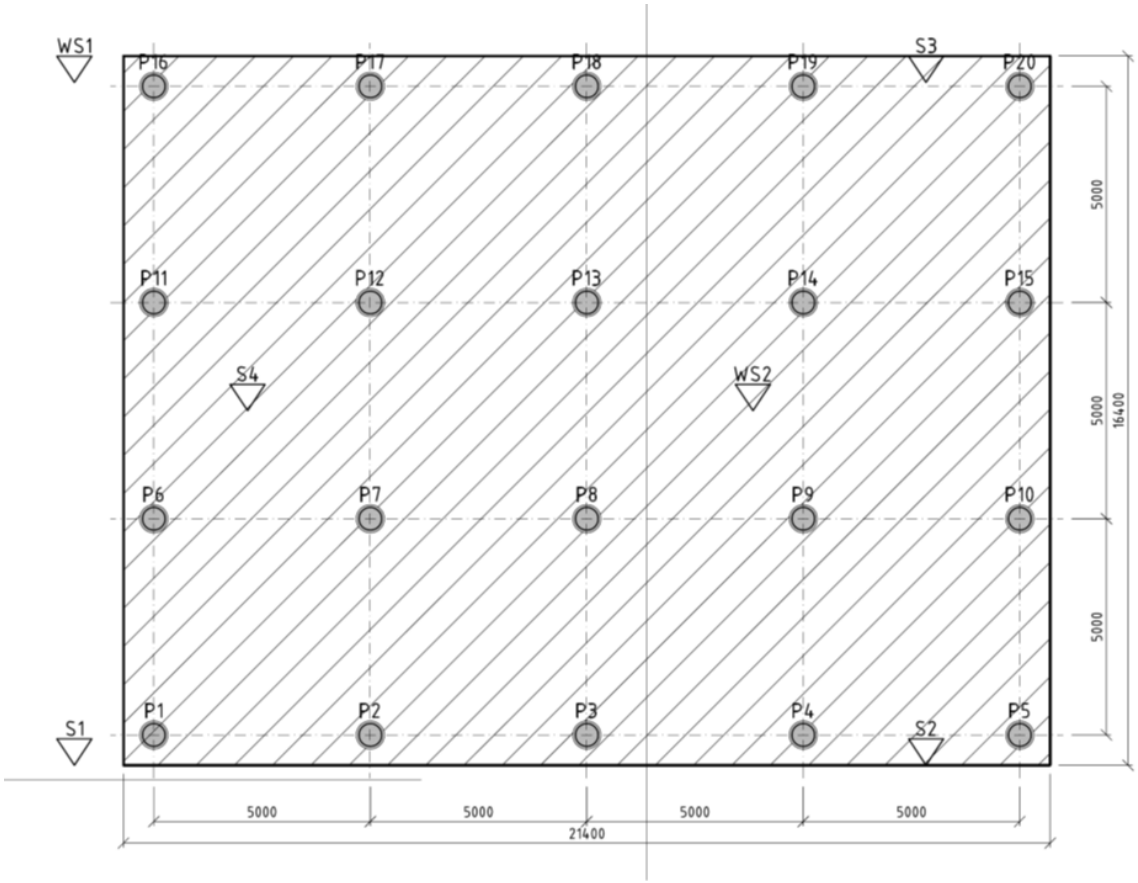

Figure 2-11: Design test site showing the location of each pile.

Chapter 3

Seismic Wave Propagation

Sound is a concept people experience everyday, it comes from many sources, like talking, and these acoustic waves are interpreted automatically in people's mind so we understand what these sounds mean and where they come from.

In seismics, acoustic waves are generated by use of a source, the source and medium the waves travel through determine the properties and propagation of these waves. This part elaborates on the wave theory, propagation through a layered medium and the wave types which can be expected measuring the concrete foundation piles.

3-1 Wave Theory

Seismic waves are elastic waves, exited by a source, for example an explosion, earthquake, airgun or hammering on foundation piles. The elastic properties of the medium determine the velocity of which the seismics waves propagate [Bormann et al., 2009]. Elasticity of the medium is described by stress (redistribution forces) and strain (modification of volume and shape) [Alsadi, 2017]. Elasticity is described by the elastic moduli, these are the Young's, Bulk and shear modulus and Poisson's ratio. These moduli describe the static deformation, but by combining dynamic behaviour the elastic wave behaviour can be derived [Society of Petroleum Engineers, 2015].

The full wave equation describes the propagation of compressional and shear waves. When both wave types are described they are referred to as elastic waves. To simplify the equation the medium is often assumed to be a perfect fluid. This excludes shear waves from the problem as only compressional waves exist in an perfect fluid. In this case the waves are referred to as acoustic or seismic waves.

The wave equation can be derived from the equation of motion and the equation of continuity. The linearized equation of motion for acoustic waves in a lossless non-flowing fluid is given by equation 3-1 and the linearized stress-strain relation by equation 3-2, where $\vec{r}$ is a short-hand notation for the Cartesian space coordinates (x, y, z) [Wapenaar and Berkhout, 1989].

$$\rho(\vec{r})\frac{\partial \vec{v}(\vec{r},t)}{\partial t} + \nabla p(\vec{r},t) = f(\vec{r},t) \tag{3-1}$$

$$\frac{1}{\kappa(\vec{r})}\frac{\partial p(\vec{r},t)}{\partial t} + \nabla \vec{v}(\vec{r},t) = \frac{\partial i_v(\vec{r},t)}{\partial t} \tag{3-2}$$

By eliminating $\vec{v}$ from equations 3-1 and 3-2 and dropping $(\vec{r},t)$ for notational convience the acoustic wave equation is obtained.

$$\rho\nabla\left(\frac{1}{\rho}\nabla p\right) - \frac{\rho}{\kappa}\frac{\partial^2 p}{\partial t^2} = -\rho\frac{\partial q}{\partial t} + \rho\nabla\left(\frac{1}{\rho}f\right) \tag{3-3}$$

For a homogeneous and source free medium equation 3-3 reduces to 3-4.

$$\nabla^2 p = \frac{\partial^2 p}{\partial x^2} + \frac{\partial^2 p}{\partial y^2} + \frac{\partial^2 p}{\partial z^2} = \left(\frac{1}{c^2}\right)\frac{\partial^2 p}{\partial t^2} \tag{3-4}$$

with,

$$c = \sqrt{\frac{\kappa}{\rho}}. \tag{3-5}$$

In a homogeneous medium, so the material properties are everywhere the same, waves propagate spherically outwards from the source, with the outer shell of the wave, the surface on which $\mathbf{k}\cdot\mathbf{x}$ in equation 3-6 is constant, is called the wavefront [Chapman, 2004]. An important law of wave propagation is the Huygens' principle which states; each point the wave front arrives at act likes a source for the wave, the new wave front is the envelope of all the waves generated by these point sources [Drijkoningen, 2014]. When the wave is far enough from the source the wavefront does not have any effective curvature anymore or is planar over a short distance, the wave has become a plane wave [Schlumberger, 2019]. The equation for a plane wave when velocity is independent of position is given in 3-6 [Chapman, 2004]. The slowness vector $\mathbf{p}$ (the reciprocal of velocity) replaces the wave vector to indicate the wave direction is independent of frequency. Acoustic or seismic waves are often simplified and treated as plane waves [Schlumberger, 2019]. With (complex) amplitude A, circular frequency ω, wave vector $\mathbf{k}$ and phase $\mathbf{k}\cdot\mathbf{x} - \omega t$.

$$p = Ae^{i(\mathbf{k}\cdot\mathbf{x}-\omega t)} = Ae^{i(\mathbf{p}\cdot\mathbf{x}-t)} \tag{3-6}$$

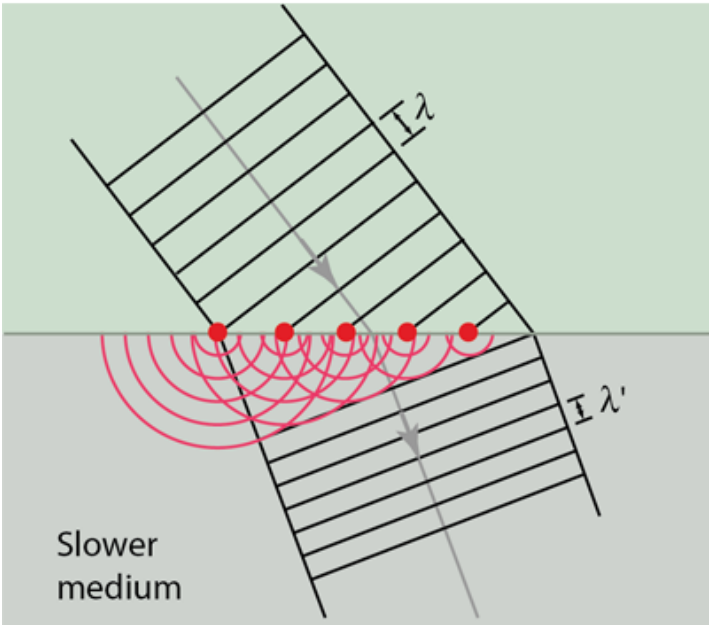

Figure 3-1: Illustration to visualize Huygens' Principle using plane waves. Each point the wave reaches act as a new source the new wave front is the envelope of all the waves generated by these point sources. The grey line, indicates the ray which is perpendicular to the wave front. (Retrieved from [Nave, 2016])

3-2 Layered Medium

When measuring the foundation piles the medium is layered, meaning different materials will be present and the waves will be reflected, refracted or transmitted at the boundary of the two materials. In figure 3-1 is illustrated how a wave propagates into the second medium.

To better understand how the waves behave in a heterogeneous medium tray tracing is used. This is a way to visualize the waves, the waves are visualized by a ray which is a line perpendicular to the wavefront and shows the direction of travel. The ray-path indicates the fastest travel path of a wave between two points. As the mathematical description of rays are much simpler than of the wavefronts, using ray tracing is especially useful for modelling and understanding where the wave travels through [Haldorsen et al., 2006]. Changes in the ray-path occur at interfaces, see figure 3-1. Snell's Law relates the angle of incidence θ_i and the angle of refraction θ_r of the waves or ray with the velocity of the two layers and is given in equation 3-7.

$$\frac{sin(\theta_i)}{c_1} = \frac{sin(\theta_r)}{c_2} \tag{3-7}$$

When an elastic medium is considered, both P-waves and S-waves exist. The properties of these waves will be further explained in 3-3. When a P-wave hits a boundary it can transmit a P- and S- wave in the second medium and reflect a P- and S-wave. The same holds for an incident S-wave [Drijkoningen, 2014]. In case an incident P-wave generates a transmitted S-wave the Snell's law will be as in equation 3-8. Where c_P and c_S are P- and S- wave velocity.

$$\frac{sin(\theta_P)}{c_P} = \frac{sin(\theta_S)}{c_S} \tag{3-8}$$

When the angle of refraction is 90 degrees the ray is refracted along the interface. This happens when the angle of incidence is at the critical angle. In seismics one of the arrivals looked at is this refracted wave. Snell's law will look as follows;

$$\frac{sin(\theta_c)}{c_1} = \frac{1}{c_2} \tag{3-9}$$

3-2-1 Seismic Arrivals

When measuring the concrete foundation piles a layered medium is expected, thus direct, refracted and reflected waves are to be recorded. A schematic representation of the wave paths is given in figure 3-2. Direct waves are the first wave to arrive (until the refracted waves take over). The velocity of the layer can easily be determined by the use of $velocity = distance/traveltime$. Another way of representing the properties of a layers is using slowness. The time difference between the P-wave arrivals divided by the distance travelled is called the slowness and is the inverse of the speed [Haldorsen et al., 2006].

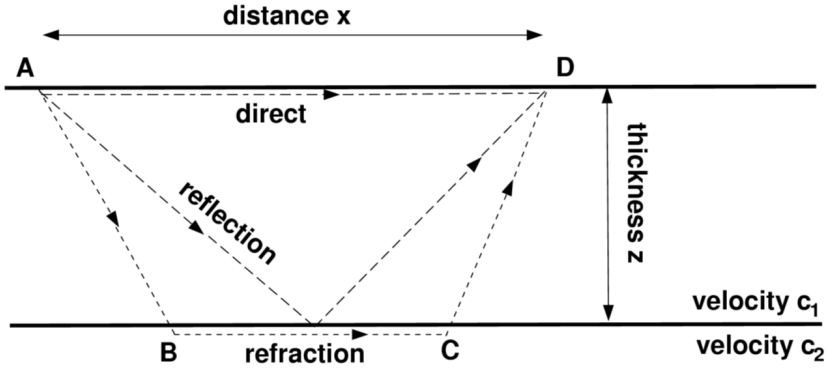

Figure 3-2: Different wave paths in the subsurface, refracted, reflected and direct waves (Retrieved from [Drijkoningen, 2014])

Refraction only depends on velocity contrast between two layers. Refraction only happens with an increasing velocity, so when the second layer has a lower velocity than the first layer no refracted wave will travel through the second layer. This is the case with the concrete and soil interface, the concrete has a much higher velocity than the soil, thus no refracted wave is expected to travel through the soil. A refracted wave from the water (in the borehole) and concrete interface is to be expected. Refracted waves travel through the second high velocity layer, this means at a distance x it will arrive before the direct wave and will be the first recorded arrival.

Using the Snell's law an equation for the travel time can be obtained. The refracted travels through the first medium, then along the interface through the second medium and back through the first medium. Figure 3-2 gives a picture of the different wave paths. Using the 'known' travel path and Snell's law the following equation for refracted waves can be obtained [Drijkoningen, 2014].

$$t = \frac{x}{c_2} + \frac{2zcos(\theta_c)}{c_1} \tag{3-10}$$

When the angle of incidence is larger than the critical angle reflection occurs, the angle of reflection is equal to the angle of incidence. From Snell's law follows that when the velocities are the same, the angles are the same. The travel time can thus easily be derived using Pythagoras' theorem and is given in equation 3-11 [Drijkoningen, 2014];

$$t = \frac{(4z^2 + x^2)^{1/2}}{c_1} \tag{3-11}$$

Whether reflections are recorded depends on the impedance, which is the product between the density and velocity of a layer. The impedance contrast determines the amount of transmitted and reflected energy. It can happen that the velocity of two layers differ a lot, but if the impedance is (almost) the same, in this case no reflections will be seen. The ratio between the impedance is the refection coefficient and given in equation 3-12, for a larger coefficient more energy is reflected [Drijkoningen, 2014].

$$R = \frac{\rho_2 c_2 - \rho_1 c_1}{\rho_2 c_2 + \rho_1 c_1} \tag{3-12}$$

3-3 Wave types

The total wavefield consist of direct and reflected body waves and surface waves [Ionov, 2018]. Body waves travel through the medium and are either compressional or shear waves. Surface waves travel along a surface or interface, these are Rayleigh, Stoneley, Scholte and Love waves.

Body waves Body waves travel through a medium in any direction, there are two types of body waves. The first is the compressional or P-wave, the particles vibrate in the direction of the wave propagation. This results in a travel path that consists of an alternation of compression and rarefaction zones. The P-wave is the fastest wave (highest velocity) and thus will be the first to arrive at the receiver. The propagation velocity of the P-waves (v_p) depends on the density and the elastic properties of the medium the wave travels through [Alsadi, 2017]. The second body wave is the shear wave or S-wave. The particles within the medium experience transverse displacement due to the strain, but the medium does not experience volume change. The shear waves are either vertical polarized, SV-waves, the particles move within the vertical plane or the waves are horizontally polarized, SH-waves, the particles move within the horizontal plane [Alsadi, 2017]. The particle motion of P- and S-waves are visualized in figure 3-3.

The compressional and shear velocity equations 3-13 and 3-14 can be found when the elastic moduli are inserted in the general wave equation 3-4 [Society of Petroleum Engineers, 2015].

$$v_p = \sqrt{\frac{\lambda + 2\mu}{\rho}} = \sqrt{\frac{K + \frac{4}{3}\mu}{\rho}} \tag{3-13}$$

where:

v_p = compressional or P-wave velocity in m/s
λ = Lamé 's constant in MPa
μ = shear modulus in MPa
K = bulk modulus in MPa
ρ = density in kg/m^3

$$v_s = \sqrt{\frac{\mu}{\rho}} = \sqrt{\frac{E}{2\rho(1+\sigma)}} \tag{3-14}$$

where:

v_s = shear or S-wave velocity in m/s
E = Young's Modulus (stiffness) in Pa or N/m^2
σ = Poisson's Ratio [-]

Surface waves Surface waves are waves that travel along a surface. The three fundamental surface waves are the Rayleigh waves which travels along the solid free surface interface, the Stoneley wave which travels along a solid solid interface and the Scholte wave which travels along a solid fluid interface [Meegan et al., 1999].

Surface waves characterize themselves from body waves, they typically have large amplitudes, low frequencies and their velocity is generally lower than the body waves [Alsadi, 2017]. Surface waves attenuates fast with depth, a rule of thumb for penetration depth is one fourth of the wavelength. The particle motion in the medium is a combination of P-waves and SV-waves. The particles have an elliptical motion in the vertical plane parallel to the direction of the propagation. A representation of the particle motion of Rayleigh waves is given in figure 3-3 and of Scholte and Stoneley waves is given in figure 3-4. The velocity of the Rayleigh waves depends on the ration between P- and S-waves, but an approximation 0.9 percent of the S-wave velocity is commonly used [Alsadi, 2017].

Found in Meegan et al. is that these three fundamental surface waves behave in a similar manner. The model equations for these three waves have the same mathematical properties. When measuring the foundation piles a solid-water interface exists therefor Scholte waves are expected to be present.

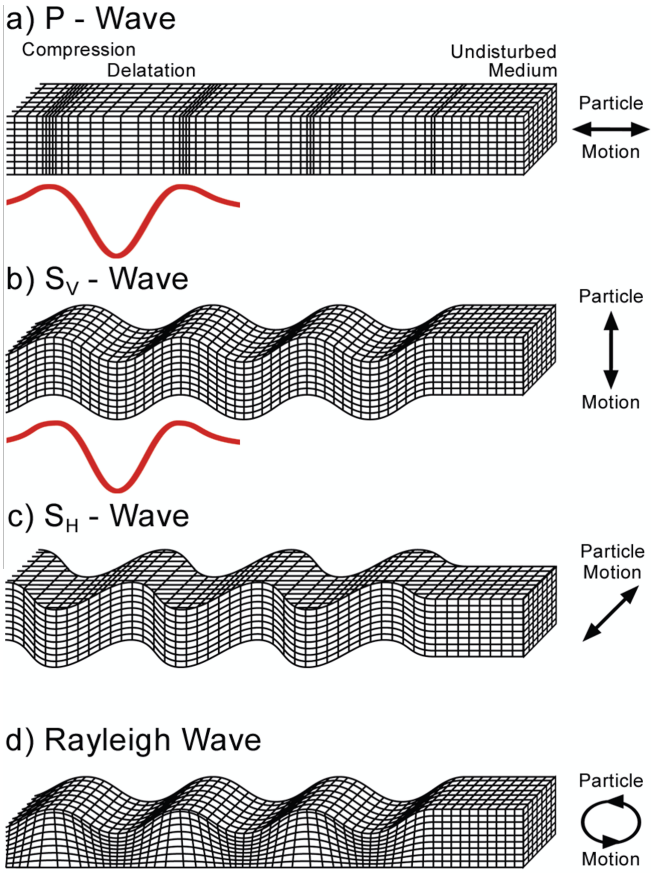

Figure 3-3: Illustration of different types of body and surface waves a) Compressional or P-wave b) Vertical polarized shear wave or SV-wave c) Horizontal polarized shear wave or SH-wave d) Rayleigh wave (Retrieved from [Mishra, 2018])

3-3-1 Waves in boreholes

In a borehole an acoustic wave is generated by the source, when the wavefront hits the borehole wall three new wavefronts are generated. A reflected wavefront with speed of the borehole fluid (v_m) and a P- and S-wave which are either refracted or transmitted by the formation [Haldorsen et al., 2006]. The critically refracted body waves form head waves which are detected by the receivers. This head is the direct compressional or P-wave which is the first arrival at the receivers, as second the direct shear or S-waves arrive, see Figure 3-5 [Close et al., 2009]. When a slow formation is present, thus when the shear wave speed is less than the mud wave speed, no shear head wave forms in the fluid because the shear wavefront never forms the right angle, the shear wave does continue into the formation [Haldorsen et al., 2006].

The P-wave arrival at further receivers is at later time as the wave has to travel further. The time difference between the P-wave arrivals divided by the distance travelled is Δt also called the slowness and is the reciprocal of the speed [Haldorsen et al., 2006].

After the body waves, the surface waves are detected by the receivers. There are various types of surface waves, but at the interface between a liquid layer and a solid half-space, Rayleigh

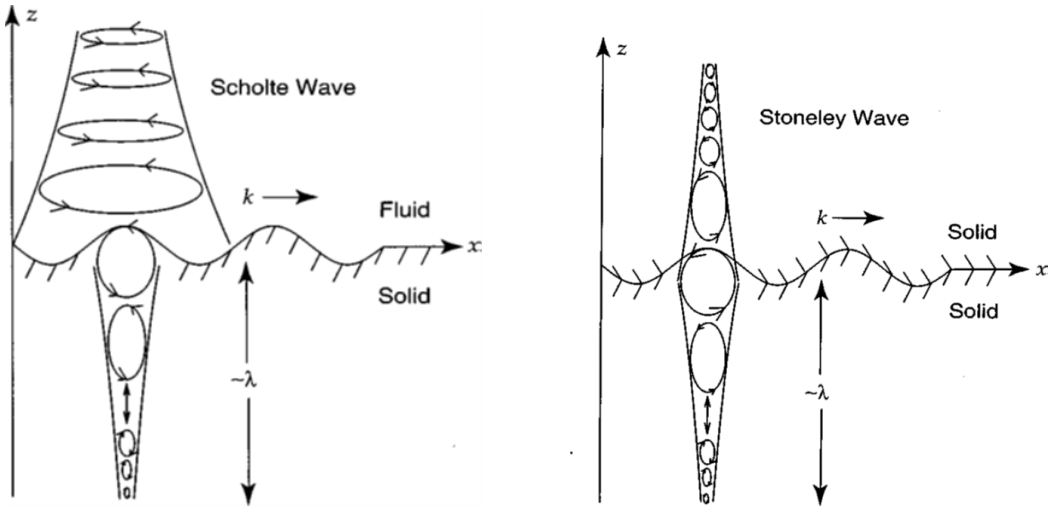

(a) Scholte wave) **(b)** Stoneley wave)

Figure 3-4: Schematic representation of particle motion of a Scholte and Stoneley wave (Retrieved from [Meegan et al., 1999])

and Scholte (Stoneley) waves are present [Khojasteh et al., 2015]. In order of arrival, these are the Rayleigh waves, Mud waves and Stoneley waves [Close et al., 2009].

Rayleigh waves are surface waves at the borehole wall, these waves are controlled by the shear velocity of the formation and these waves are often mixed with the arrival of the S-waves. Mud or borehole fluid waves are theoretically the next waves to arrive, but are often missing. The mud wave is a compressional wave through the borehole fluid, but the borehole is too small compared with the wavelength and transmitter-receiver spacing causing the mud wave to be rarely present in a borehole [Close et al., 2009].

The last arrivals are the Stoneley (Scholte) surface waves [Close et al., 2009]. The Stoneley wave is the borehole eigenmode and has a large amplitude which does not attenuate with distance as the energy is guided in the borehole [Ionov, 2018]. The amplitude of these guided waves decrease exponentially with radial distance [Henriet et al., 1983]. The Stoneley waves are dispersive waves and consists of many modes, thus the propagation velocity is split into the group velocity and phase velocity. The lowest mode of the Stoneley wave is also called Tube wave. The Tube is present in the low-frequency or long wavelength limit and propagates with a velocity lower than the speed of sound in the borehole fluid [Ionov, 2018]. In isotropic media, the velocity of the tube wave is controlled by the shear modulus of the medium and the fluid properties, namely density, bulk modulus and acoustic velocity [Henriet et al., 1983]. Tube waves reflections are generated due to changes in density, Young's modulus or shear modulus at the interfaces in the surrounding solid or abrupt changes in fluid density, borehole radius/ pipe thickness [Henriet et al., 1983].

The velocity of Tube waves can be derived from the fluid velocity, shear modulus and shear velocity of the solid. According to Henriet et al. Tube wave velocity in a burried PVC pipe can be formulated as follows.

$$V_T = V_w \left(1 + \frac{K}{M_c}\right)^{-\frac{1}{2}} \tag{3-15}$$

with,

$$M_c = E\left[2(1+\sigma) + \frac{D^2}{e(D+e)}\right]^{-1} \tag{3-16}$$

where:

V_T = Tube wave velocity in m/s
V_w = fluid wave velocity in m/s
K = fluid bulk modulus in MPa
E = Young's modulus in MPa
σ = Poisson's ratio of pipe material [-]
D = inner diameter in m
e = wall thickness in m

When the wall thickness goes to infinity the expression reduces to Lamb's formulation of a wave in a tube with infinite radius of 1898. In equation 3-17, the PVC pipe is overlooked and the Tube wave velocity can be correlated to the shear velocity of the solid [Henriet et al., 1983].

$$V_T = V_w \left(1 + \frac{K}{G}\right)^{-\frac{1}{2}} \tag{3-17}$$

with,

$$G = K\left(\frac{V_w^2}{V_T^2} - 1\right)^{-1} \tag{3-18}$$

and,

$$V_s = \left(\frac{G}{\rho}\right)^{\frac{1}{2}} \tag{3-19}$$

where:

V_T = Tube wave velocity in m/s
V_w = fluid wave velocity in m/s
V_s = shear wave velocity in m/s
K = fluid bulk modulus in MPa
ρ = wall material density in kg/m^3

Another type of tube wave is the Mach tube wave, this wave exist when the tube wave velocity is greater than the shear velocity of the solid [Ionov, 2018]. In Figure 3-5 an illustration is given of the different wave types present in a borehole from Close et al., 2019. It illustrates the wave component propagation in the borehole at the top and the recorded wavetrain at the bottom. This example assumes a homogeneous formation thus no reflections occur.

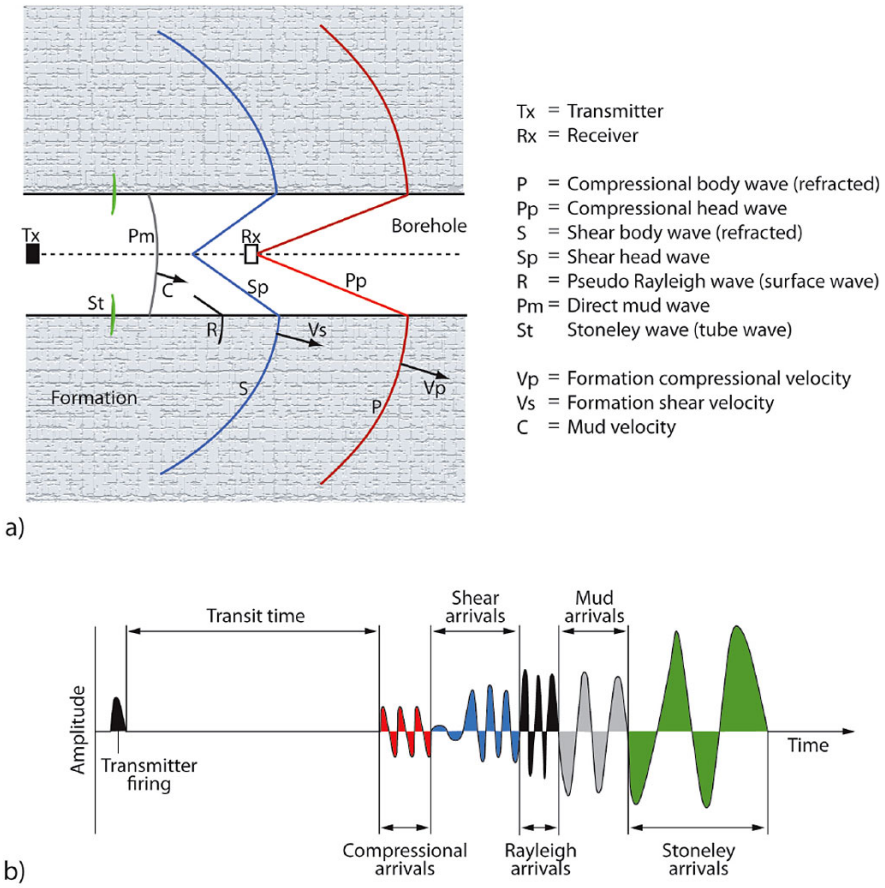

Figure 3-5: a) Important sonic waveform propagation in a borehole, at time when P-wave is detected by receiver Rx. b) Schematic representation of the wavetrain recorded as a function of time. Indicated are the different wave types. (Retrieved from [Close et al., 2009])

3-3-2 Wave Properties

Noise The signals recorded at the receivers are contaminated by noise, are attenuated and can be interfered. Noise is always present in the data, but what is considered noise is not always the same. When looking at refractions, all other signals, like reflections are considered noise and are discarded. Besides signals which are treated like noise there also is seismic noise, small amplitude signals coming from various sources, like traffic which are recorded continuously. This constant noise is called white noise [Drijkoningen, 2014].

Attenuation When the material is homogeneous the total energy will be spread over the area of the sphere, this loss of energy is proportional to $1/r^2$ and is called spherical divergence [Drijkoningen, 2014]. For surface wave, which travel along the surface the geometric spreading is in 2D, so the energy decays with $1/r$ [Rawlinson, nd]. This results in higher amplitudes for surface waves in the recordings. The loss of energy or amplitude of waves as they travel through the medium is called attenuation. Seismic waves lose energy through absorption, reflection and refraction at interface, mode conversion and spherical conversion or spreading of the wave [Schlumberger, 2019]. In the earth, higher frequencies attenuate more than lower frequencies [Ghose, 2018]. Attenuation (equation 3-20) is measured using the quality or Q-factor. This factor is the ratio between the energy of the wave and the lost energy per oscillation, see equation 3-21. The Q is the reciprocal of attenuation, meaning for low Q-factors attenuation is stronger. Q-factor increases with increasing velocity and density of the medium and ranges from 10 to 1000 in the earth. Soils or weathered rocks will have values up to one hundred, whereas for example granite will have a Q-factor in the hundreds. The quality factor is approximated frequency independent, but commonly is frequency dependent. As the frequencies increase, Q becomes frequency dependent and normally Q increases with frequency in this case Q can be corrected with a correction constant η using equation 3-22 [Morozov, 2016].

$$A(t) = A(0)exp^{\frac{-\pi f t}{Q}} \tag{3-20}$$

$$Q = 2\pi \frac{E}{\Delta E} \tag{3-21}$$

$$Q(f) = Q_0 f^{\eta} \tag{3-22}$$

Dispersion Waves are expressed in the complex frequency domain, namely in amplitude and phase spectrum. The amplitude distortion is due to an attenuation coefficient and the phase distortion is due to dispersion [Wuenschel, 1965]. Dispersion is a multi-modal phenomena which is frequency dependent. Surface waves of different wavelength travel the soil with the characteristic velocity of the soil at depth. Short wavelengths propagate slower, due to low velocity at shallower soils and long wavelength travel faster due to higher velocities at higher depths, this phenomena of applies only to surface waves and is called dispersion [Castellaro, 2016]. These separate velocities are called the phase velocities. The whole group or the envelope of the wave travels with the group velocity. The propagation mode with the lowest phase velocity is the fundamental mode and typically considered the most important [Rawlinson, nd].

Interference The investigated foundation piles are no infinite half-space, thus a finite body. This implies that the waves must be finite as well. For example waves are reflected, therefor multiple waves of different phases can arrive at the receiver locations at the same time. Depending on the time and their phase these waves can interfere with one another, either destructively or constructively, damping or amplifying the signals. Constructive interference will occur only for specific resonant frequencies, these are the so called modes. The principle

is similar to standing waves in a vibrating string fixed at both sides. In figure 3-6 the first four modes in a string are shown. The lowest frequency is the fundamental mode.

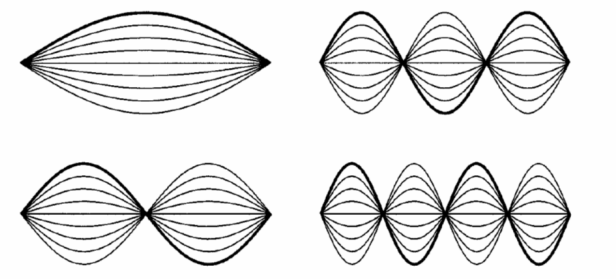

Figure 3-6: First four modes of waves in a string between fixed endpoints (Retrieved from [Bormann et al., 2009])

Resolution To resolve layers in a medium they have to be of sufficient thickness. The vertical and horizontal resolution are defined differently. The resolvable limit parallel to the propagation direction is Rayleigh's criterion of $\lambda/4$, one fourth of the dominant wavelength. The resolution perpendicular to the propagation direction is defined by first radius of the Fresnel zone. The Fresnel zone depends on frequency, velocity and two way travel time ($t = 2h/v$) and is given by equation 3-23 [Ghose, 2018].

$$r \approx \sqrt{\frac{\lambda h}{2}} = \frac{v}{2}\sqrt{\frac{t}{f}} \tag{3-23}$$

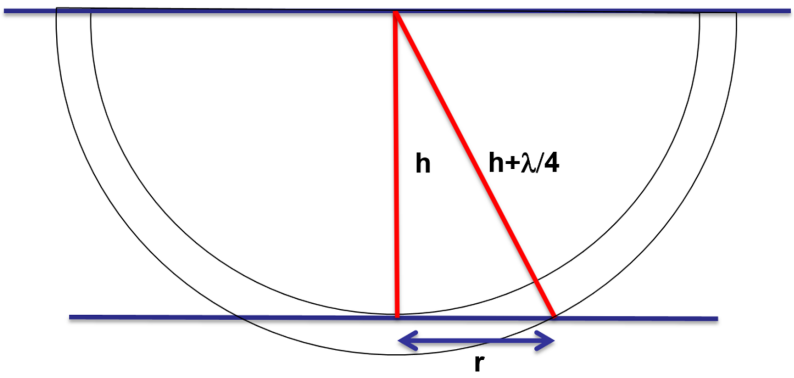

Figure 3-7: Fresnel Zone (Retrieved from [Ghose, 2018])

3-4 Waves in Foundation Piles

The set up for measuring foundation piles is comparable to borehole measurements. The measured foundation piles have a water filled PVC pipe in the middle in which the Seismic Tube is lowered. The medium the generated waves travel through consist of many (small)

layers. Figure 3-8 shows an illustration of the layers present while measuring a foundation pile and in table 3-1 their velocity and density are listed.

Reflections occur at every interface, thus many reflected waves and their multiples will be recorded. The strongest reflections recorded will be from the PVC - concrete and concrete - soil interface. Due to the concrete layer, a large change in density and velocity occurs causing a high reflection coefficient. The concrete soil interface has a negative reflection coefficient, hence the recorded reflections are of reversed polarity. Figure 3-9 show the ray paths of the reflected waves. The rays are shown until the critical angle of the PVC - concrete is reached. From this illustration can be seen that the waves are mostly refracted at the PVC - concrete, while the other interfaces do not deflect the rays much. Using the formula for the Fresnel zone an estimation of resolution of the data can be made. Assuming one concrete layer, the radius of the Fresnel zone will be $r \approx \frac{v}{2}\sqrt{\frac{(2h/v)}{f}} = \frac{4300}{2}\sqrt{\frac{(2\times 0.212/4300)}{62200}} = 0.0856$ m. The resolution parallel to the wave propagation is determined by the wavelength, this is using the center frequency of the source; $\lambda = v/f = 4300/62200 = 0.069$ m. Therefor the smallest layers (or variations in the concrete layer) theoretically detectable are $0.069/4 = 0.0173$ m or 1.73cm thick.

The direct P-wave from the source to the receiver through the oil in the Seismic Tube is expected to be the first arrival at the closest receiver, as this wave has the shortest travel path. The first arrival in the other receivers are expected to be the refracted wave. Refracted waves are expected from the PVC - concrete interface. The refracted wave will travel mostly through the concrete, at a certain distance this wave will be faster than the direct wave.

Within the tube Scholte waves are expected as a fluid - solid (water - PVC and water - Poly-Ethylene) interface is present. These Scholte waves can form a Tube waves as described in chapter 3-3-1. These waves will be recognizable by their large amplitudes. The different waves types do not have a large travel path upon arriving at the receivers. This means the different waves will arrive close to one another and interference will occur.

Typical velocity and density values

Material	P-wave Velocity [m/s]	S-wave Velocity [m/s]	Density [kg/m^3]
Soil	100-200	20-300	1000-1600
Air	343	-	1-1.3
Oil	1200-1400	-	700-960
Water	1450-1500	-	960-1000
Poly Ethylene (Plastic)	1500-1850	1000-1200	915-1060
PVC	1500-2250	1000-1200	1350-1500
Concrete	3600-4600	2000-2500	2300-2500

Table 3-1: Typical velocity and density values for materials used when testing concrete piles using the Seismic Tube. (Retrieved from [Drijkoningen, 2014], [Polytron Kunststoffentechnik, 2016], [Borcherdt, 1994], [Omnexus, nd] and [Dakota Ultrasonics, 2016])

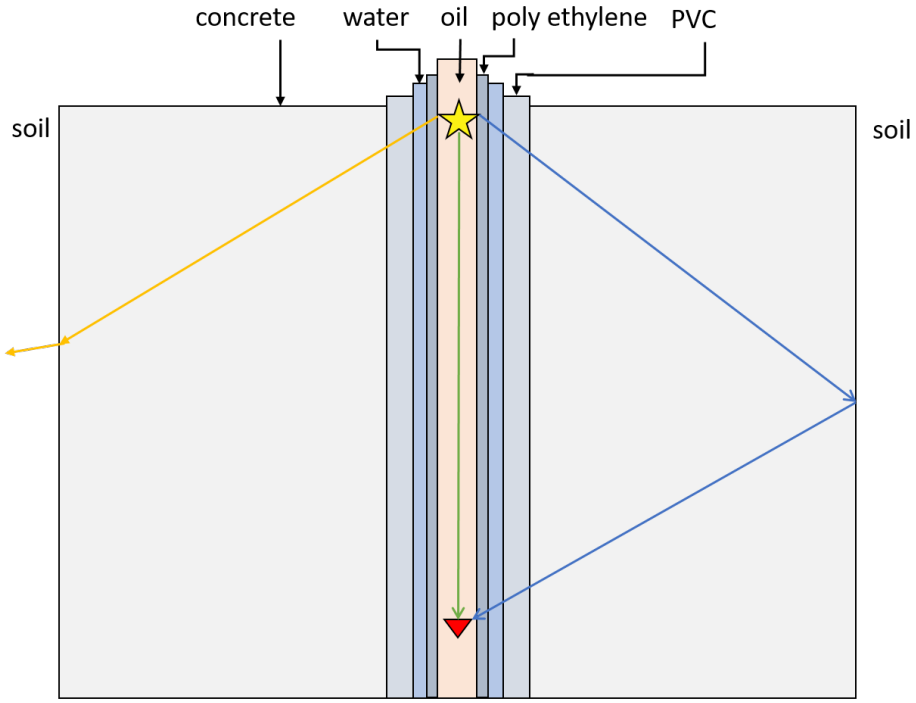

Figure 3-8: Illustration of waves and layers in a foundation pile. The yellow line represents a transmitted wave, the green line a direct wave and the blue line a reflected wave. The source is indicated with a star and the first receiver with a triangle, the oil and poly ethylene layer are parts of the Seismic Tube (Note; illustration is not to scale).

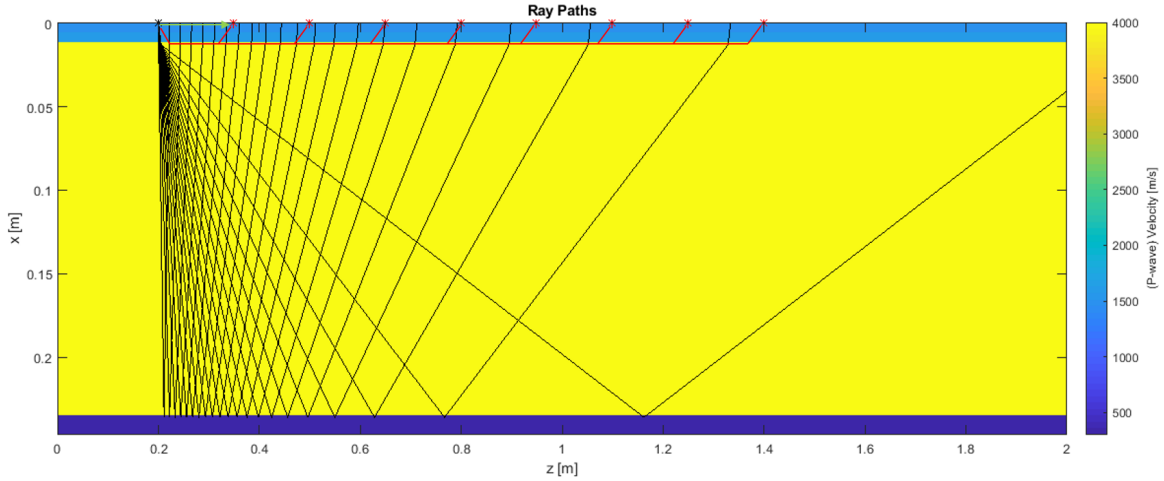

Figure 3-9: Illustration of ray paths in a foundation pile. The green line shows the direct wave, the red line shows the refracted wave path and the black lines show the ray paths of the reflected waves. The source is indicated with a black star and the receivers with red stars. layer are parts of the Seismic Tube (Note; illustration is not to scale).

Chapter 4

Processing Techniques

In this chapter processing techniques are described. These are later used to process the data acquired with the Seismic Tube. Some of these techniques are quite commonly used, such as stacking and deconvolution these are described in chapter 4-1. An approach for surface wave inversion is described in chapter 4-2.

4-1 Seismic Processing techniques

Nyquist When recording the incoming waves a proper sampling time has to be chosen to avoid aliasing. The highest frequency should be sampled at least twice per period. This Nyquist frequency is given by: $f_N = 1/(2\Delta t)$. The effects of aliasing are illustrated in figure 4-1. The frequencies above the Nyquist frequencies are aliased and can be suppressed by a high-cut filter [Drijkoningen, 2014].

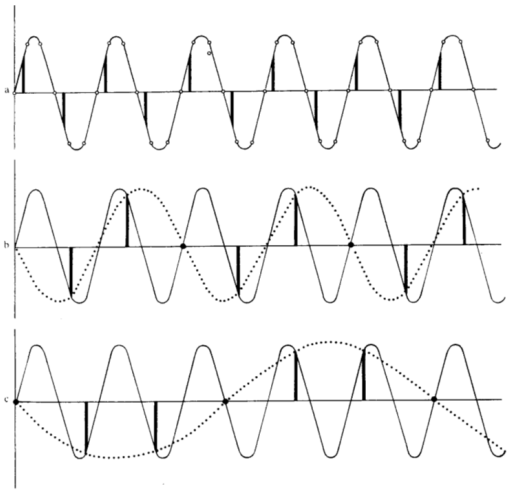

Figure 4-1: Under-sampling causes aliased waveforms (Retrieved from [Drijkoningen, 2014])

Stacking To increase the signal to noise ration (S/N ratio) stacking of data can be performed. Stacking adds traces and thus enhances the signal as is visualized in figure 4-2.

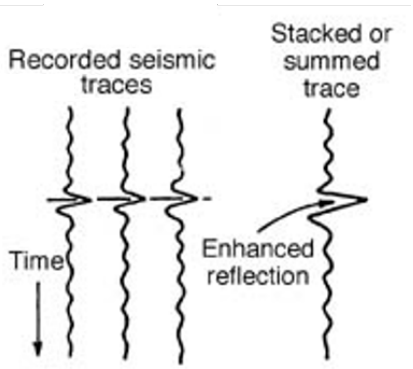

Figure 4-2: Example of stacking (Modified from [Schlumberger, 2019])

Deconvolution Recorded seismograms can be estimated as a convolution of the earths impulse response or the reflectivity with the seismic wavelet. In the convolution equation 4-1 noise is not included. The wavelet includes source signature, recording filter, surface reflections, and receiver-array response while the earth response consists of primary reflections and multiples [Yilmaz, 2001].

$$x(t) = r(t) * w(t) \tag{4-1}$$

where:

$x(t)$ = recorded seismogram
$r(t)$ = Earth's response
$w(t)$ = seismic wavelet
$*$ = convolution

Deconvolution compresses the wavelet and eliminates multiples such that the earth reflectivity is recovered [Yilmaz, 2001]. This can be done using a filter operator $f(t)$ such that convolution of $f(t)$ with known $w(t)$ produces a spike, an estimate of $\hat{r}(t)$ [Yao et al., 1999].

$$\hat{r}(t) = w(t) * f(t) \tag{4-2}$$

substitute 4-2 into 4-1

$$\hat{r}(t) = r(t) * w(t) * f(t) \tag{4-3}$$

therefor

$$\delta(t) = w(t) * f(t) \tag{4-4}$$

In real applications $w(t)$ and $f(t)$ are discrete and equation 4-4 can be written in matrix form [Yao et al., 1999].

$$\underline{\underline{W}}\ \underline{F} = \underline{Y} \tag{4-5}$$

the inverse filter is written as

$$\underline{F} = (\underline{\underline{W}}^T \underline{\underline{W}})^{-1}\ \underline{\underline{W}}^T\ \underline{Y} \tag{4-6}$$

This filter called the Wiener filter satisfies 4-5 and is determined using least squares. The operator $\underline{F}$ corresponds to a zero time delay spike delta function and is the spiking deconvolution operator [Yao et al., 1999].

Filtering Frequency filter can be applied to investigate the effect of certain frequency ranges and to filter noise from the data. The size and shape of the frequency filter has a big effect on the shape and resolution of the remaining signal in the time domain, as is illustrated in figure 4-3. To avoid ringing of the signal a filter of trapezoidal shape can be applied. The steepness of the slopes determine the size and occurrence of the side-lobes of the signal [Ghose, 2018]. The Ormbsy filter is defined by four corner frequencies, f1, f2, f3, f4. This filter rejects below f1 and above f4, is linear from f1 to f2 and from f3 to f4, and flat from f2 to f3.

4-2 Multi-channel Analysis of Surface Waves

Dispersion is a multi-modal phenomena. The propagation mode with the lowest phase velocity is the fundamental mode and typically considered the most important [Rawlinson, nd]. The higher modes gain importance if a stiff layer overlies a soft layer. The sensitivities of higher modes have a broader frequency bandwidth than the fundamental mode sensitivity, thus a multi-mode analysis can improve the resolution of S-wave velocity models and an increase of the depth [Ikeda et al., 2015].

Through analysis of dispersion properties it is possible to obtain a shear wave velocity profile. This can be done using various techniques example are; MASW and SASW using actives sources and SPAC and ESAC using passive sources. The methodology of all these techniques are very similar and the differences are in the details of processing [Castellaro, 2016]. This implies that all these techniques have the same limits, namely; which lack of a ideal white spectrum in the source dispersion curves vary and the fundamental mode might not be the strongest making interpretation difficult. Secondly, when a stiff layer is present at shallow depth the penetration depth is limited for high frequencies and the inversion of dispersion curves is only in 1D plane assuming plane parallel stratigraphy.

Multi-channel Analysis of Surface Waves (MASW) is a method which inverts the dispersion curves of surface waves to obtain a shear wave velocity profile of the subsurface. Soil can vibrate at specific frequencies, the resonance frequencies, which depends on the stiffness and thickness of the soil layers. The stiffness is an elastic constant proportional to v_s^2 (shear wave velocity) [Castellaro, 2016]. This follows from equation 3-14 when a constant Poisson's ratio is assumed, thus the ration between v_p and v_s is constant.

MASW consists of three steps visualized in figure 4-4. Firstly multi-channel data is acquired. Secondly, dispersion curves are interpreted from the data and thirdly an 1D vertical shear

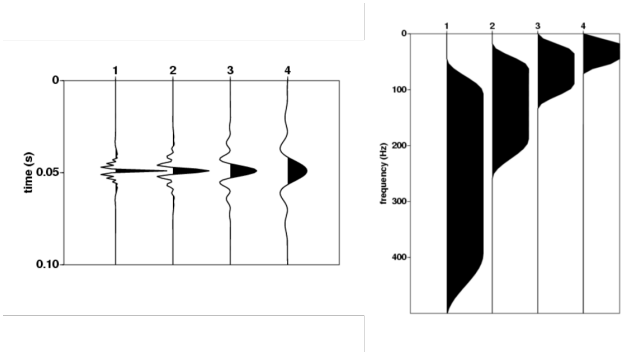

(a) Frequency filters showing the effect of frequency range

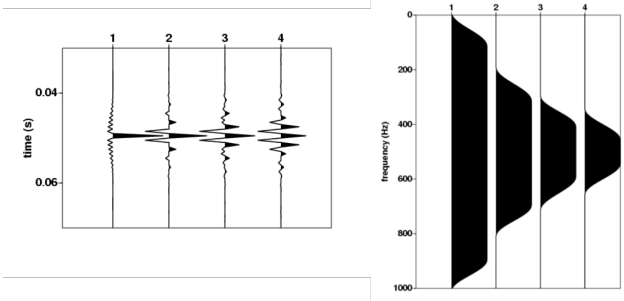

(b) Frequency filters showing the effect of frequency bandwidth

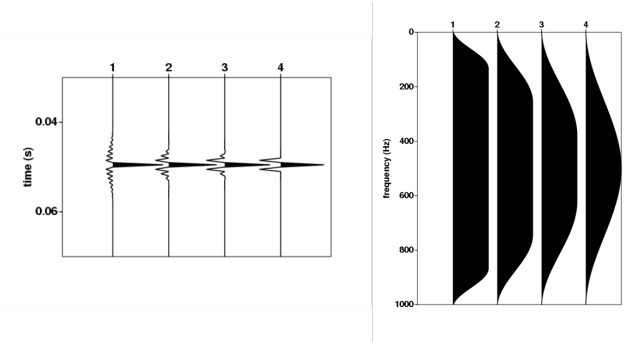

(c) Frequency filters showing the effect of the slope of the filter

Figure 4-3: Frequency filters and resulting signals in time domain (obtained from [Ghose, 2018])

velocity profile is obtained by inversion matching the measured dispersion curves with calculated/ simulated dispersion curves [Caldern-Macas and Luke, 2007].

Dispersion curves usually visualized as phase velocity versus frequency (FV-plot), the phase velocities can be calculated from the linear slope of each component of the frequency record (slant stack and Fast Fourier Transform (FFT)) [Park et al., 1999]. Surface waves have multiple modes of propagation and each mode has its own dispersion curve, therefor more maxima or possible velocities should be visible in the FV-plot at the same frequency. The inversion of the dispersion curves is mostly restricted to the fundamental mode of surface waves [Duputel et al., 2010]. In a ideal case (meaning; an ideal source i.e. with white spectrum, an ideal receiver geometry i.e. well tuned for all frequencies and an ideal soil i.e. isotropic,

normally dispersive and laterally homogeneous where attenuation exists) the fundamental mode is dominant. In reality a seismic array is tuned to specific wavelengths and does not sample the whole frequency range uniformly. Furthermore, seismic sources have no ideal white spectrum and the plane wavefront requirement is not always fulfilled. Additionally the stratigraphy of the layers has an effect on visibility of higher modes as stiff shallow layers trap high frequencies and constructively interfere with higher modes from deeper layers [Castellaro, 2016].

A dispersion curve is obtained by picking the maximum amplitudes at each velocity and frequency in the phase velocity versus frequency spectra of the data. The picked dispersion curve from the data is called an apparent or effective dispersion curve. A loss of information occurs as only one velocity per frequency is picked while multiple modes cane have different velocities at the same frequency [Castellaro, 2016].

V_s profiles are determined by iterative inversion of the picked dispersion curves and estimations of Poisson's ratio, density and thickness parameters [Park et al., 1999]. An initial model is required as input of which the initial pick of v_s has a significant effect on convergence [Park et al., 1999]. The v_s of the model is updated for each iteration until the misfit between the theoretical and picked dispersion curves is below a certain threshold.

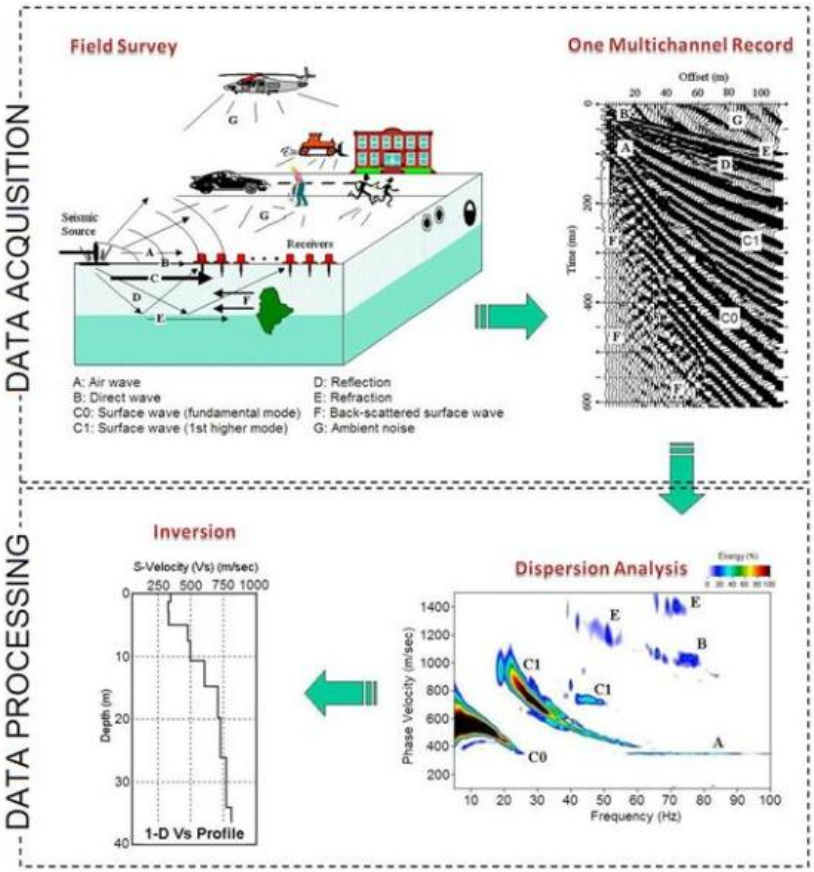

Figure 4-4: Example of the steps taken in a multi-channel analysis of surface waves survey (Retrieved from [ParkSeis, nd])

Chapter 5

Interpretation Tool

To interpret the arrivals in the Seismic Tube data an interpretation tool in MATLAB® App Designer was built. This tool calculates and plot the arrival of refraction, reflection or direct waves according to the input parameters on top of the recorded data from the Seismic Tube. Input parameters are the velocity and thickness of the layers. Using sliders for the velocity and concrete layer thickness, the arrivals are interactively changed and plotted. Such that it gives understanding of the different wave arrivals and makes interpretation easier. The recorded arrivals in the data can be classified as reflection, refraction, direct or surface wave and the thickness of the foundation pile is derived. After analysing all the recordings of a foundation pile a velocity and thickness profile of the foundation pile is derived.

5-1 Interpretation steps

This tool is written in MATLAB using the MATLAB® App Designer. The math is based on the theory explained in chapter 3. The arrivals of the refracted, reflected, surface and direct wave can be plotted and fitted to the data.

Figure 5-1 shows screen when the tool is opened. In the left top corner the seismic data can be loaded, this data is then plotted in the large figure in the middle. The button called "Amp" can be used to amplify the data, this can be turned on and off. The traces will be multiplied with a amplification factor, their trace number, to visualize and enlarge the small amplitude arrivals of the later receivers.

Using the colored buttons, an arrival can be picked. The assumption is made that the pile is symmetrical about the center of the pile. Therefor the arrivals are calculated using the radius of the tube and the concrete layer. The direct arrival will be visualized in a green line is calculated by $t = \frac{x}{v}$. The distance is from the source to the receiver, the velocity can be picked using the slider. The calculated arrival moves interactively with the velocity change. The refracted wave can be picked by clicking on the yellow button. The refracted wave is calculated by $t = \frac{(x)}{c_2} + \frac{2zcos(\theta_c)}{c_1}$. The refraction first travels through the layers of the tube. The radius and the average velocity can be adjusted. The pipe is approximated as one layer.

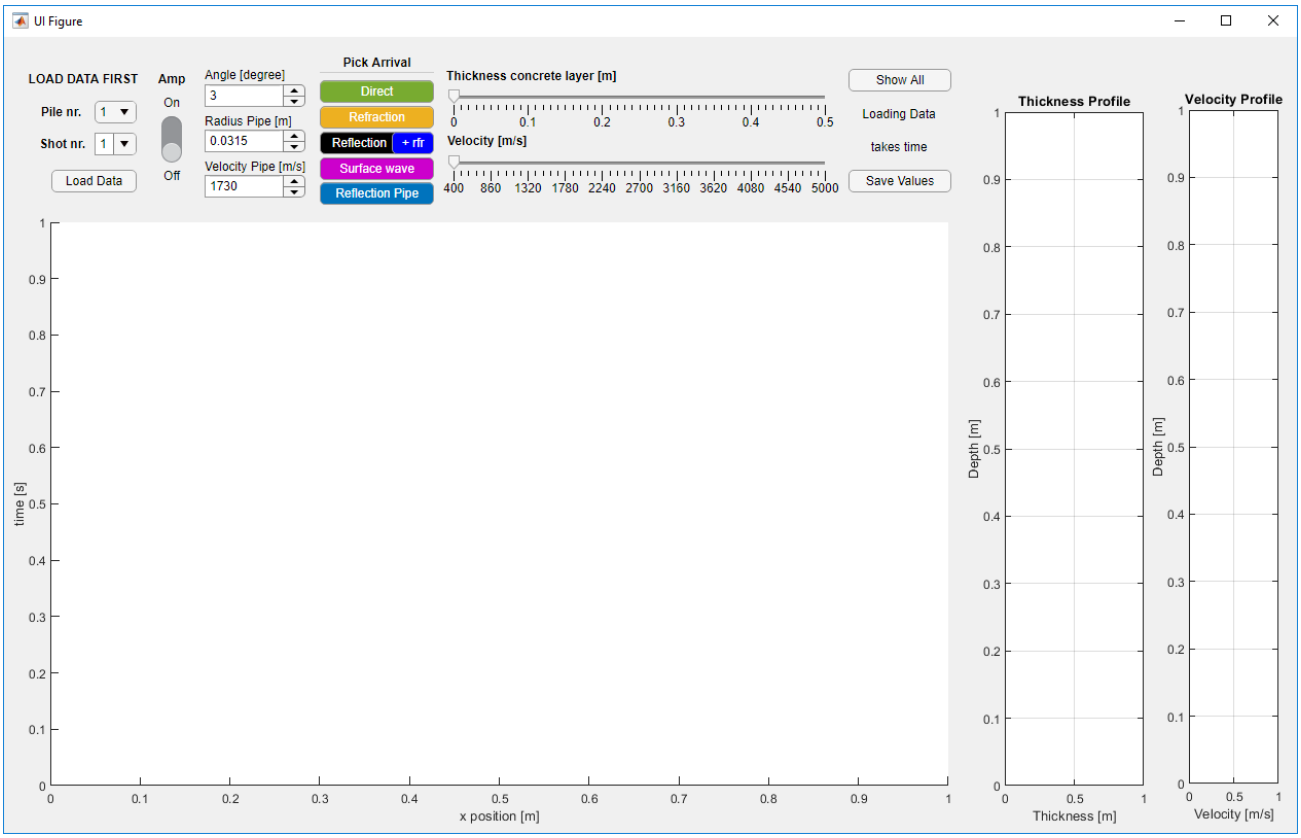

Figure 5-1: Start display when the interpretation tool is opened.

The velocities of the various layers in the pipe are close to another and to combine the layers simplifies the system. The velocity of the concrete layer can be adjusted via the velocity slider, using this velocity and the velocity of the pipe the critical angle is calculated. The refracted wave will adjust interactively as the velocity is changed. The velocity is saved and will be used for the reflected wave.

The next arrival to pick is the reflected wave. Using $t = \frac{(4z^2+x^2)^{1/2}}{c_1}$ the reflected wave is calculated and plotted. The reflected wave is deflected at the pipe concrete boundary, this is included in the tool. The arrivals are calculated using the ray tracing theory. The change in direction due to the pipe concrete boundary is calculated for all incoming angles up to the critical angle using Snell's law. In figure 5-2 the difference between the arrival without and with deflection is shown. The thickness of the concrete layer can be picked using the slider. This slider ranges from 0 to 50 cm with steps of 1 mm, an accurate estimation of the concrete thickness can be made. However the final picked value depend much on interpretation of the data. In appendix B shows that the differences in arrival time can be very small using different input values. This is done showing a seismogram with the arrivals of the reflected wave using different input for the concrete thickness.

The reflected wave can refract at the opposite pipe concrete boundary, to visualize this wave an additional button is added next to the reflection button with plus rfr. The reflected waves are calculated using ray tracing. The path of a reflected wave is calculated and then refracted. Using the angle input, the angle of incidence at the pipe concrete boundary of the reflected

wave can be chosen.

The surface wave is calculated like the direct wave. The velocity can be chosen via the slider and the arrival is plotted in a purple/pinkish color. The last wave plotted is the direct reflection from the pipe concrete boundary. Using the show all button all these arrivals are plotted onto the data see figure 5-3. The four most important arrivals, namely, the direct, surface, refracted and reflected from the concrete soil boundary are saved as a figure with the data when the button Save Values is pressed.

Upon pressing this button all the picked velocities and layer thicknesses are stored in a matrix which is saved on the computer (outside the program). The picked thickness and velocity of the concrete layer are also plotted at the depth of the shot which is analysed. Upon analysing all the the measurements of a foundation pile a profile of the radius of the pile, thickness of the concrete, velocity of the concrete and the velocity of the pipe is obtained. Some of these profiles can be seen in chapter 8. Between the show all and save button space is save for messages, such as values are saved, critical angle is reached and the visualization of the picked concrete velocity and thickness.

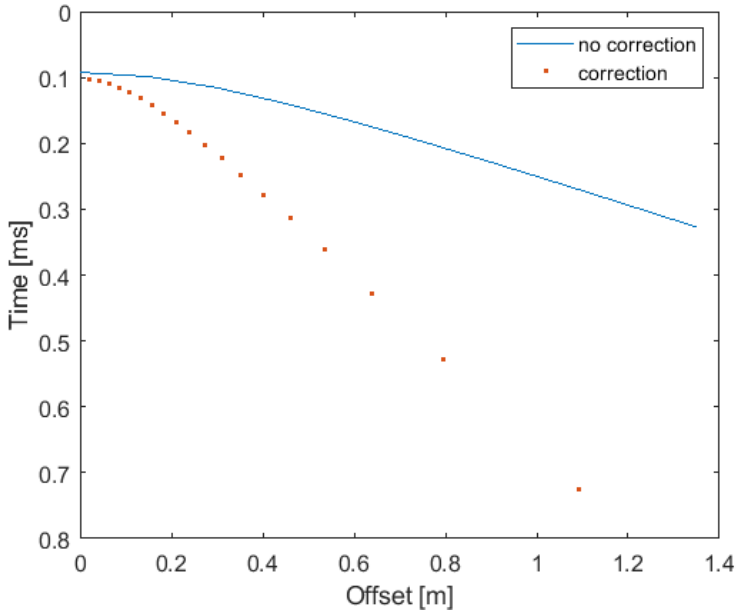

Figure 5-2: The difference between the arrival without and with correction deflection from the pipe concrete boundary

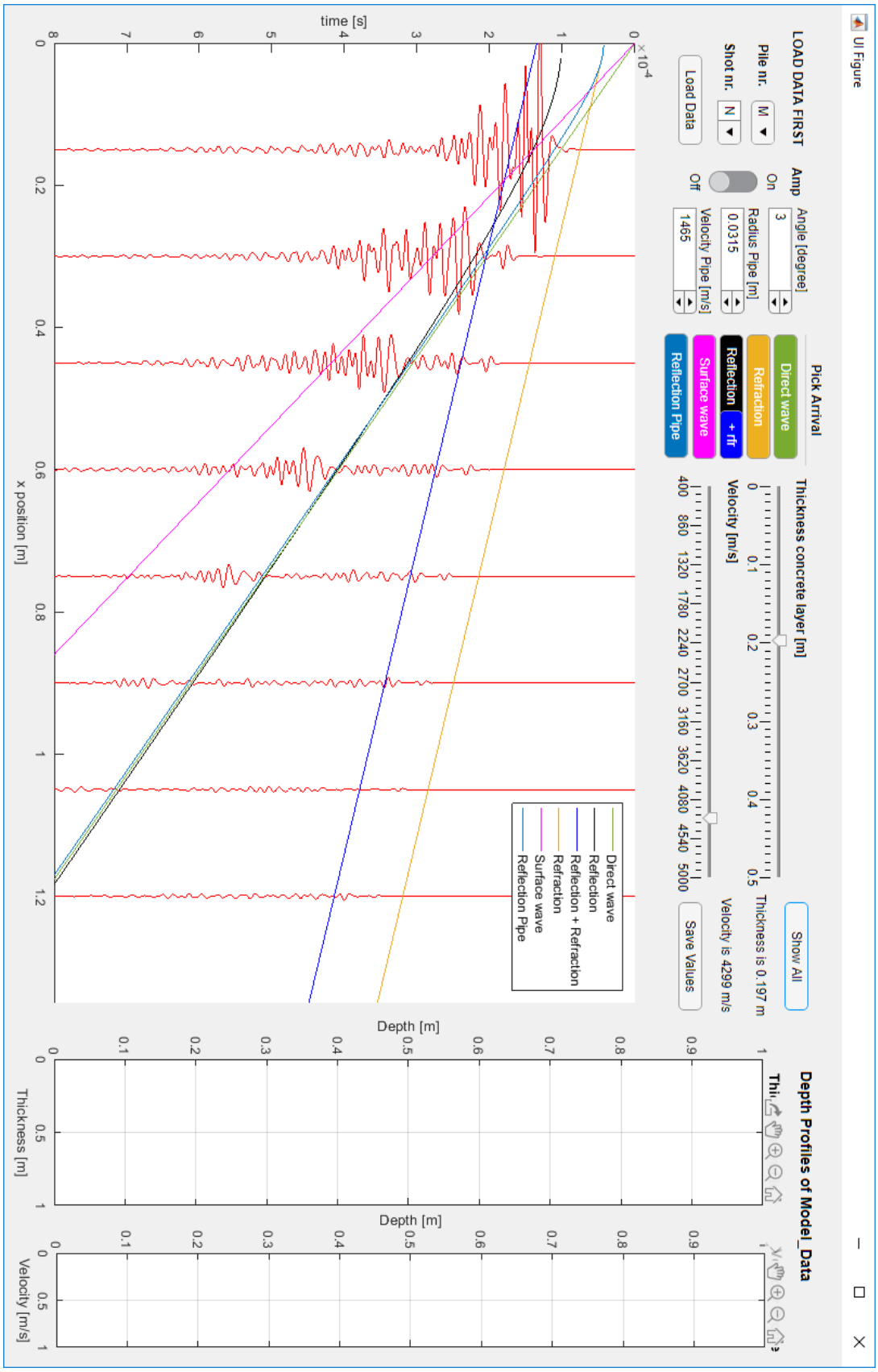

Figure 5-3: Display showing the interpretation tool the data with all the arrivals of the picked waves

Chapter 6

Modelling

Synthetic data is made by forward modelling. An acoustic forward model is build to gain insight and understanding of the wave propagation within the foundation piles. The size of the modelled piles correspond to the designed size of piles made at the Deltares test site. Just like the piles at the test site, defects are added to the modelled piles to investigate the effect. The model is tested for bulging and necking of different sizes and depths.

6-1 Forward Modelling

An acoustic forward model is build to simulate the wave propagation in the foundation piles. The source signal of figure 2-5 is injected at the source point of the Seismic Tube and the incoming waves are recorded at the receiver locations corresponding to the Seismic Tube location. To avoid spurious reflections from the boundaries of the model a perfectly matching layer or PML boundary is added.

The acoustic wave equation is solved for each grid point each time step using finite differences. The acoustic simulation has five variables each grid point. Three field variables, namely particle velocity (x - and z- direction) and pressure and two model variables, density and P-velocity. To avoid model dispersion a certain number of points per wavelength is required [Chapman et al., 2014]. The number depends on the order of discrete operators used to approximate the spatial operators and the accuracy required. The grid spacing is determined by the shortest wavelength, thus the lowest velocity in the model and the center frequency. To ensure no grid dispersion occurs and sufficient resolution is obtained, the grid spacing is defined by: $dx = \frac{v_{min}}{10 f_c}$, which means each wavelength is sampled at least 10 times. The temporal stability is obtained by the time step which is controlled by the Courant criterium. The Courant criterium is defined as $dt = \frac{dx}{v_{max}\sqrt{D}}$ for which dt is the maximum stable time step, dx the spatial step size, D is the dimension and v_{max} the maximum velocity in the model. To ensure stability, the time step is defined as $0.75 * dt$.

The finite difference uses a staggered grid to solve the first order differential wave-equations. This method is fourth order accurate in space and second order accurate in time. The model

is x-direction 0.68 m and in z-direction 2 m in size with a grid spacing of 2.4 mm x 2.4 mm and a time step of 3.1561 x 10^{-7} seconds. Three input models were used, a p-wave velocity and density model to solve the wave equation and a Q-factor model to simulate attenuation. The forward models simulated 0.8 ms of wave propagation. The recorded wavefields are used for comparison and interpretation of the field data. The model is tested for bulging and necking of different sizes and depths.

The model input is listed in tables 6-1 and 6-2.

Model Input				
Layer	**Thickness [m]**	**Velocity [m/s]**	**Density [kg/m^3]**	**Q-factor**
Oil	0.0145	1700	850	150
Plastic	0.004	1480	920	300
Water	0.008	1500	1000	10000
PVC	0.005	1620	1380	50
Concrete	0.1985	4000	2400	120
Soil	0.11	300	1600	30

Table 6-1: Input Values for Velocity, Density and Attenuation Model

Input Parameters	
Parameter	**Value**
Model length x- direction	0.68 m
Model length z- direction	2 m
Grid spacing	2.4 mm x 2.4 mm
Time step	3.1561 x 10^{-7} s
Simulation time	0.8 ms
PML-boundary length	50 grid points
PML-boundary factor	0.5
PML-boundary exponent	1.8
Central frequency Source	62.2 kHz
Correction Q-factor	0.5
Radius Defects	0.05/0.1 m
Depth Defects	0.5/0.575/0.8 m

Table 6-2: Modelling parameters

6-2 Synthetic Seismograms

Chapter 3-4 describes waves expected to be present in foundation piles. Using the simulation waves present foundation piles can be characterized. The wavefield is captured at several moments in time and visualized in figures 6-1 to 6-7. The figures show the boundaries of the different layers found in the foundation pile. The snapshots are made of a modelled foundation pile without any defects. The source position is indicated with a black star and the first three receivers in red. Note that the z and x direction have another scale, therefor the wavefronts are slightly elongated. From these figures several wave phenomena can be determined, ergo the formation of tube waves can be seen, the arrival of the first reflection and the reflections of the tube within the concrete.

In the first figure the Ricker wavelet is injected and the wave has propagated outwards. The layers of the tube have a very similar p-wave velocity see table 6-1, therefor the wave does not show much refraction at these interfaces. The velocity change of the PVC-concrete interface is large and the wave refracts at this interface as can be seen in figure 6-1. Figures 6-2 to 6-6 show that the wave travels faster in the concrete and a head wave is formed.

Many reflections occur within the tube, which leads to the formation of a Tube wave. This wave forms around 0.05 ms and a early stage can be seen in figure 6-3. The Tube wave is a guided wave, due to the reflections and interference the wave develops a large amplitude.

As the wave propagate outwards it hits the concrete soil boundary at 0.069 ms. The reflection coefficient of this interface is -0.9, thus most of the energy is reflected. This can also be seen in figures 6-5 to 6-7 as very little energy propagates further into the soil.

In the last figure the first reflection of the concrete soil boundary reaches the first receiver. Visible is that due to many reflections and interference a complicated wave patterns is created and it becomes more difficult to distinguish a separate wave types.

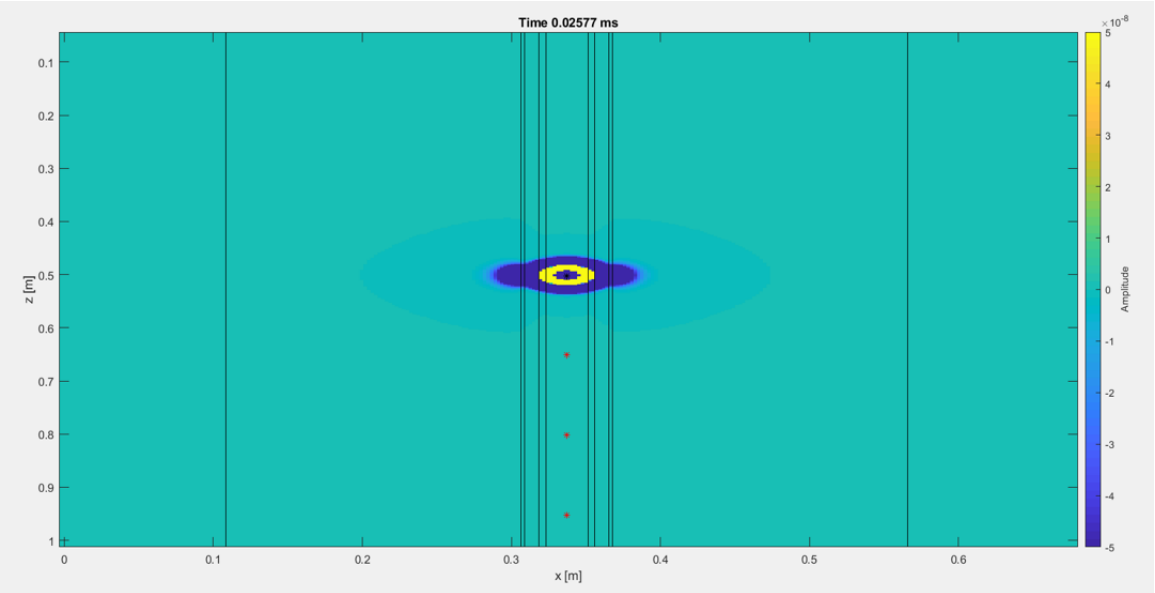

Figure 6-1: Snapshot at 0.02577 ms simulation time forward model of pile without defects. Note scale z and x direction are different.

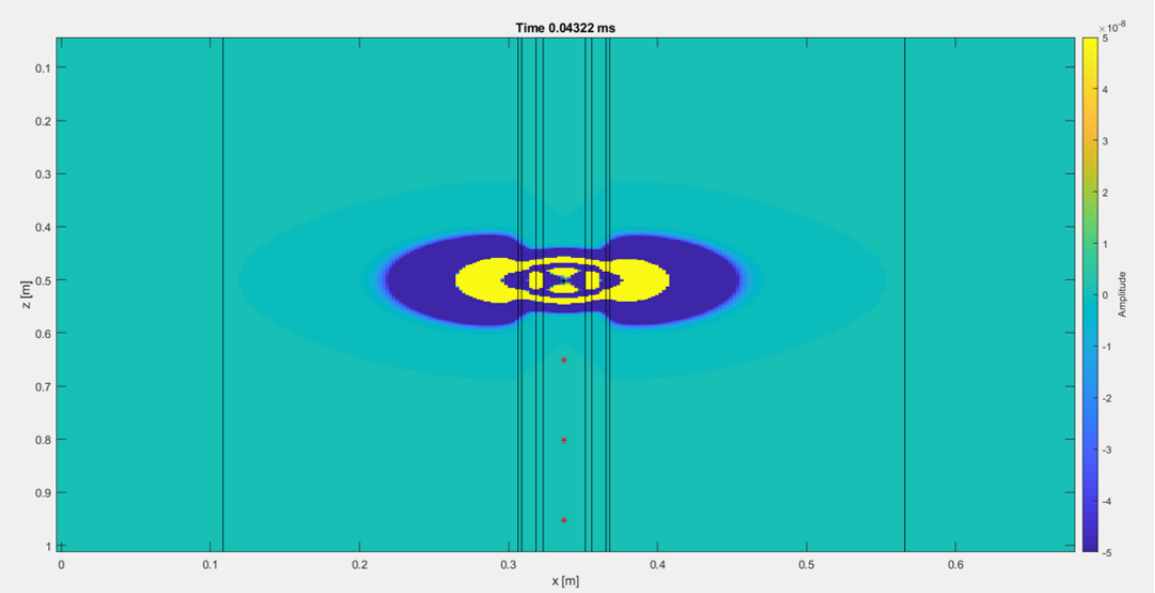

Figure 6-2: Snapshot at 0.04322 ms simulation time forward model of pile without defects. Note scale z and x direction are different.

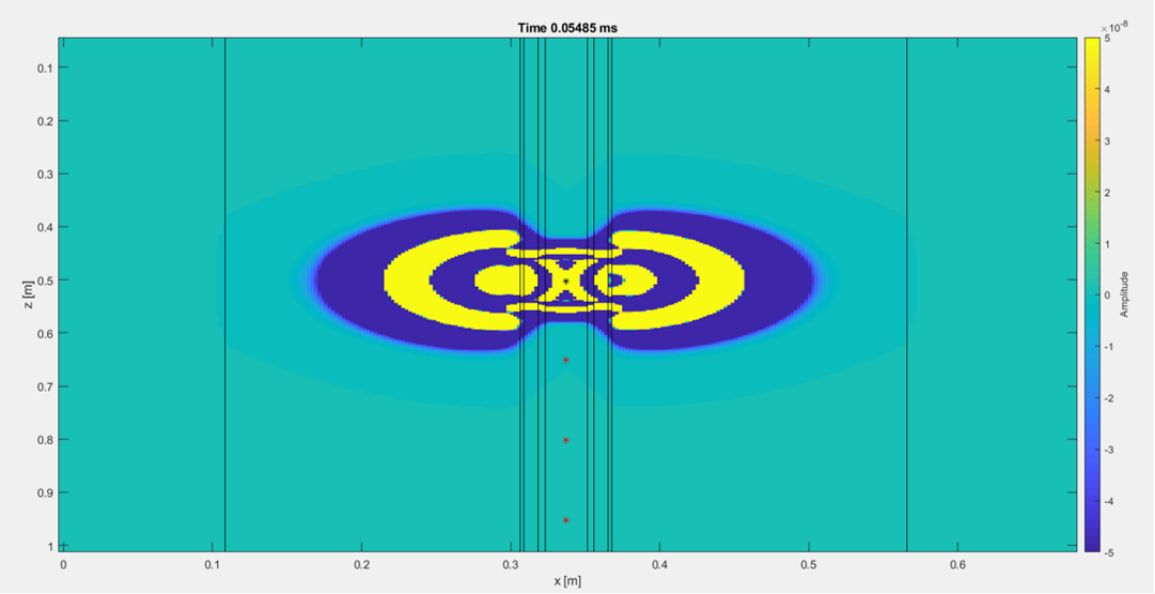

Figure 6-3: Snapshot at 0.05485 ms simulation time forward model of pile without defects. Note scale z and x direction are different.

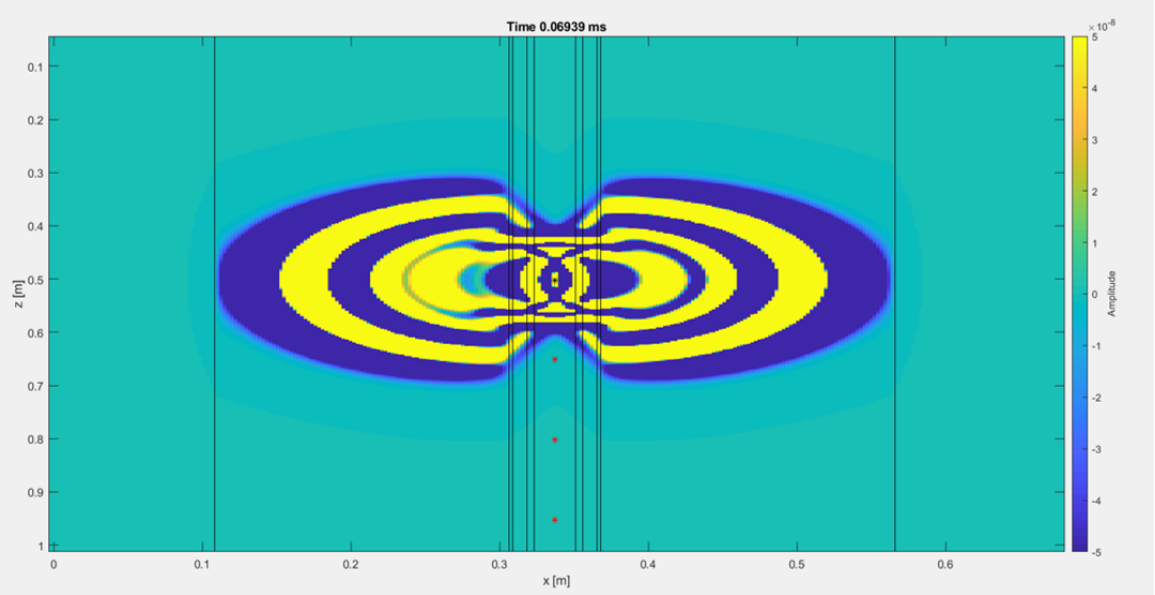

Figure 6-4: Snapshot at 0.06939 ms simulation time forward model of pile without defects. Note scale z and x direction are different.

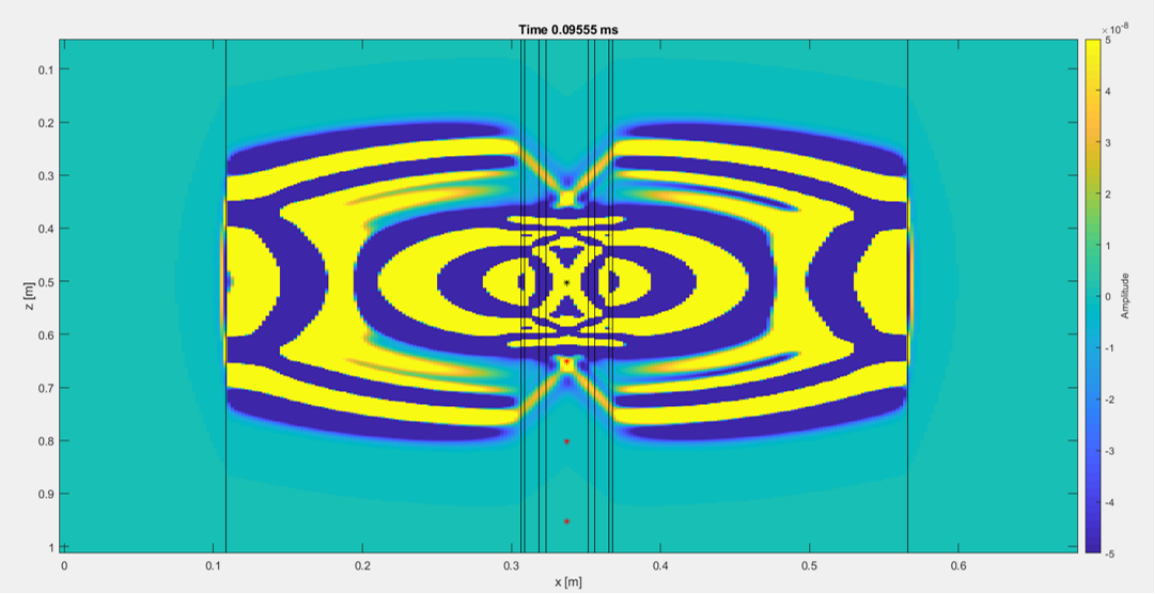

Figure 6-5: Snapshot at 0.09555 ms simulation time forward model of pile without defects. Note scale z and x direction are different. Wavefront hit the concrete soil boundary.

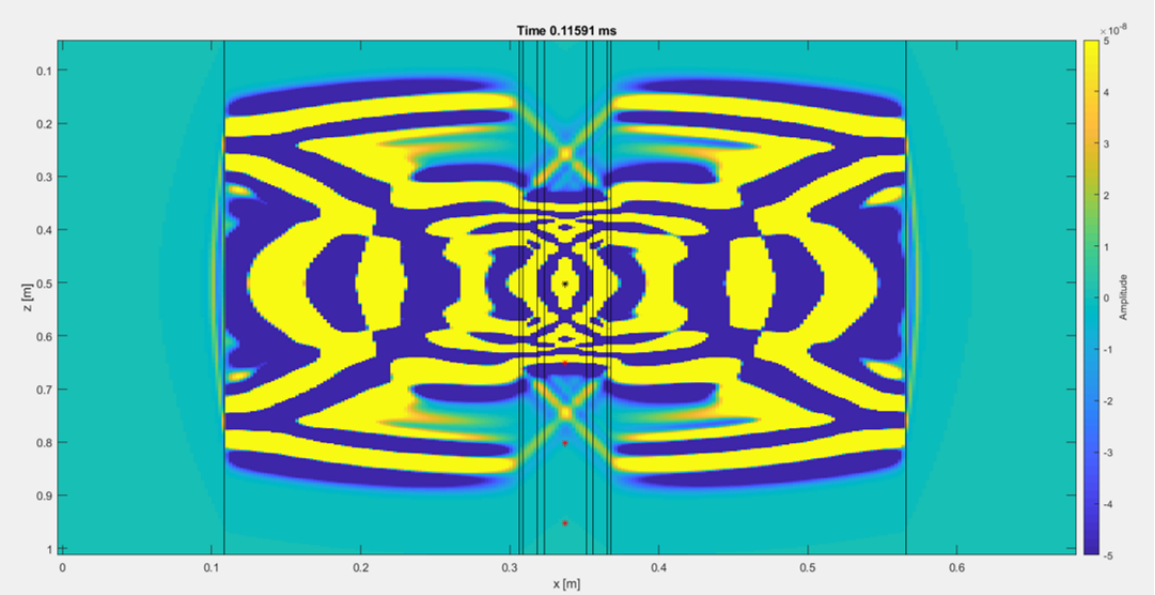

Figure 6-6: Snapshot at 0.11591 ms simulation time forward model of pile without defects. Note scale z and x direction are different. Reflected wave propagates towards the receivers

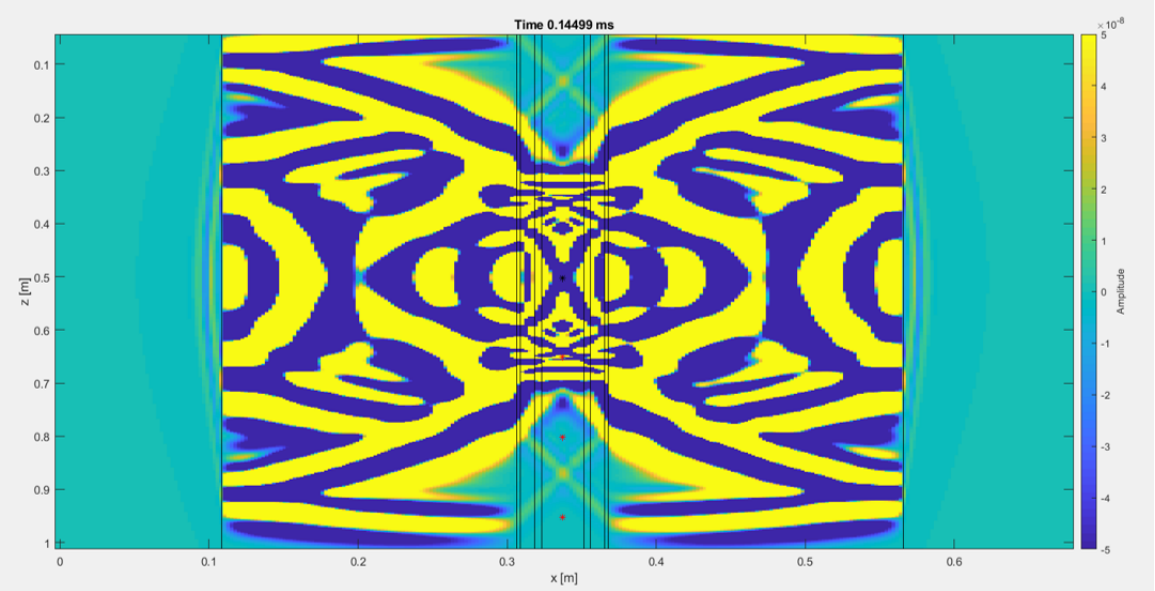

Figure 6-7: Snapshot at 0.14499 ms simulation time forward model of pile without defects. Note scale z and x direction are different. Reflected wave arrives at the receivers.

Various simulations were run with and without defects. These modelled defects were symmetrical along the pile. The defects were modelled as ellipse with a variable semi-major axis and semi-minor axis. The defects modelled are a small and large radius neck and bulge with its center at the source depth, at the midpoint source and first receiver and at the depth of second receiver. An example of the density and velocity input model with a defect are given in figure 6-8.

The modelled wavefields were recorded at receiver locations corresponding to the Seismic Tube. An example is given in figure 6-9.

Arrival times of the different waves can be calculated as the velocities and layer thicknesses are known. Using the theory of chapter 3-2-1 the reflection curves were calculated and plotted onto the data, such that a good comparison can be made. For this the interpretation tool described in chapter 5 is used.

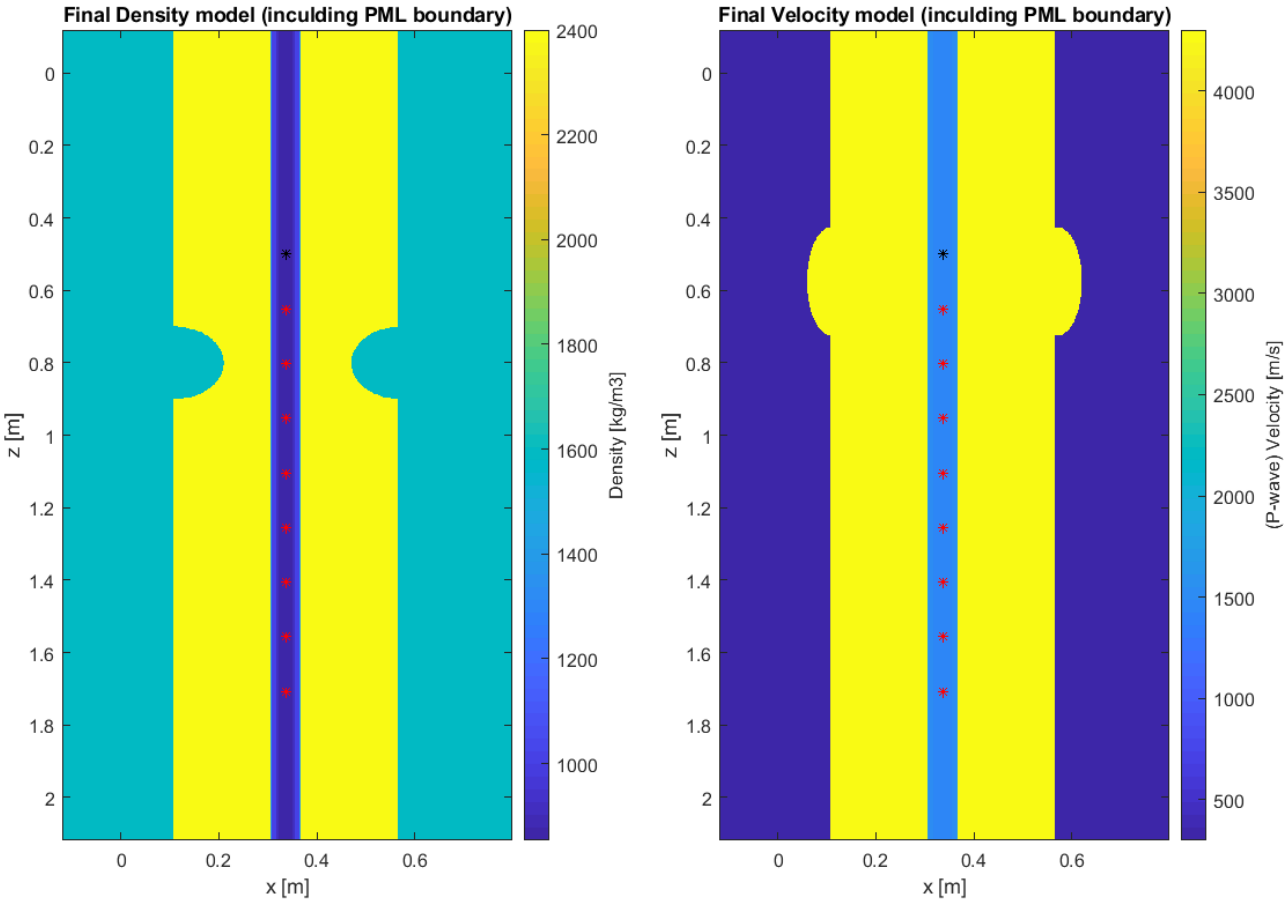

(a) Density input model with a neck with a radius of 0.1 m and center at 0.8 m depth.

(b) Velocity input model with a bulge with a thickness of 0.05 m, length of 30 cm and center at 0.575 m depth.

Figure 6-8: Density and Velocity input model with a defect

Figure 6-9 shows the recorded data of the modelled waves within a pile without any defect added. The concrete thickness is 0.1985 m and it's velocity 4000 m/s. The radius of the pipe is 0.0135 m. These values are used to calculate the arrivals according to the theory of chapter 3-2-1. The resulting arrivals are shown in figure 6-9.

The refracted wave arrivals are visualized with a yellow line, these arrivals are the first arrivals at each receiver. Note that while it seems that the refracted wave does not cross any wiggles, the arrivals have a very small amplitude and therefor not well visible. The direct P- wave is the second to arrive. The velocity of the direct wave is 1561 m/s which correspond to the average velocity of the layers of the pipe, this velocity is also used as the average velocity of the pipe. The Tube wave is a guided surface wave and characterized by the large amplitudes, the velocity of the Tube wave is determined to be 1112 m/s.

The reflected wave from the concrete soil interface is plotted with a black line into the seismogram. Due to interference these are not large spikes. The arrival of the reflection is about the same time as the arrival of the Tube wave. The reflection is a strong arrival of reversed polarity, due to a negative reflection coefficient, therefor destructive interference occur. In figure 6-10 the first three receivers are enlarged and the interference signature encircled.

Found is that these interference signatures are visible in each seismogram independent of the type of defect is or isn't added, only the arrival time changes. Thus when a neck is present these patterns exist at earlier times as can be seen in figure 6-11. The four arrivals shown have the same wave velocity as above stated. The only difference is the thickness of the concrete layer, as the pile has a reduced diameter. The defect added has a radius of 0.1 m and the center is located at 0.5 depth, at the same depth as the source location.

Analysis of synthetic data showed that interpretation is very important. As the arrivals are picked visually an human error is introduced. This "interpretation" error is within the mm-cm scale. In chapter 3-4 the limits of resolvability of the defects are discussed. Found is that the position relative to the source position is important for detection. In figure 6-13 the defect has a radius of 0.1 meter and is located at 0.8 m depth, thus 0.3 m below the source. The arrival of the refection of the concrete soil boundary, thus the interference patterns are clear. Fitting these patterns to a reflections line the thickness corresponds to 0.24 m (+/- 1 cm see appendix B). This is neither the thickness without a defect as the thickness including the defect. The defect therefor is not fully resolved, when its positioned too far from the source. But when the Seismic Tube is moved along the pile it can function as a precursor of a defect. The profiles obtained of the diameter of the foundation piles are hereof not very accurate in depth as the resolution from the Fresnel zone 17.12 cm and the ray-paths in figure 3-9 indicated.

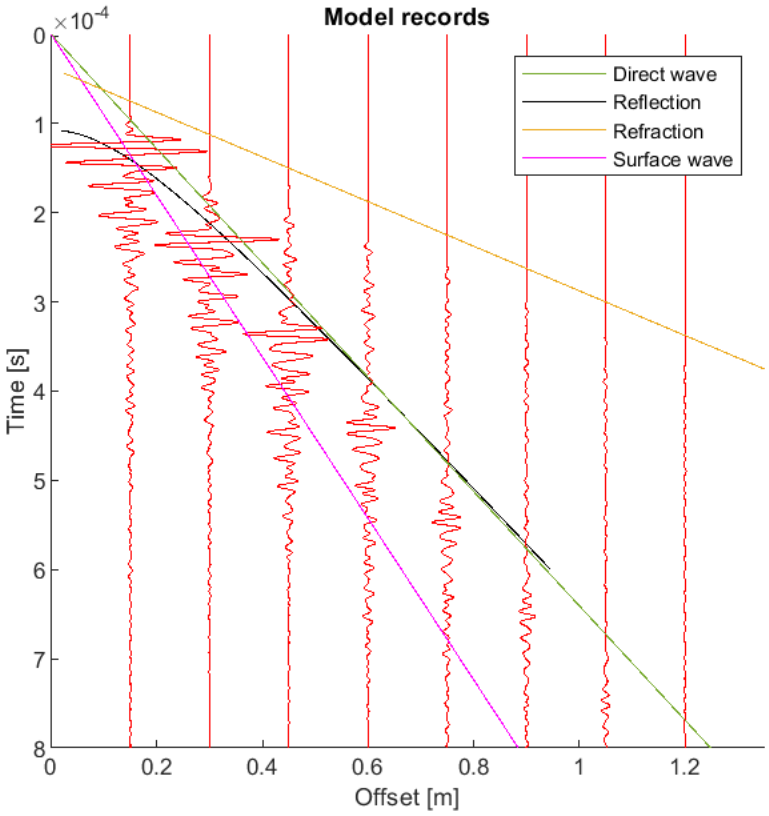

Figure 6-9: Seismogram of synthetic data, including calculated arrivals of direct, surface, refraction and reflection wave. Foundation pile modelled without defects.

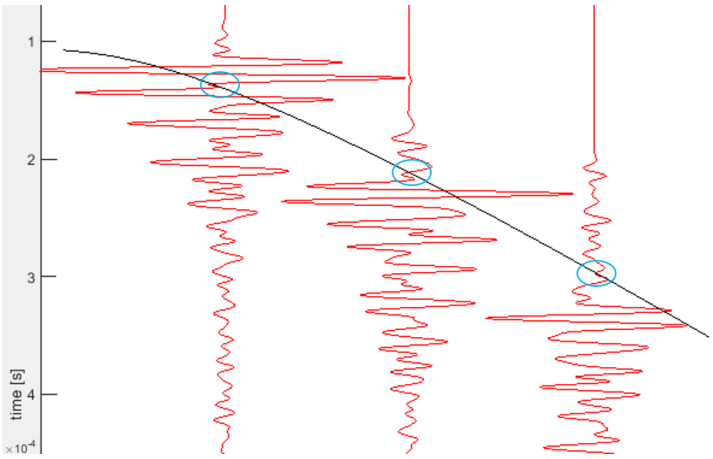

Figure 6-10: Enlarged part of seismogram of synthetic data, foundation pile modelled without defects including calculated arrival time of reflection wave. Shown are the recorded data of receiver 1 to 3 at an offset of 0.15 m, 0.30 m and 0.45 m from the source. Indicated in circles are interference patterns.

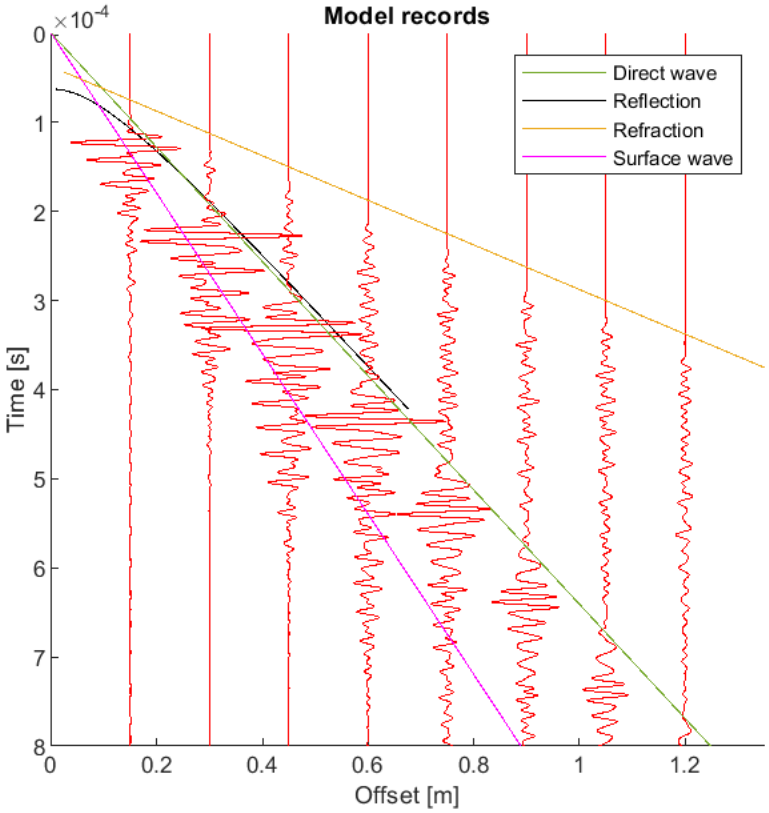

Figure 6-11: Seismogram of synthetic data, including calculated arrivals of direct, surface, refraction and reflection wave. Foundation pile modelled with a neck with a radius of 0.1 m and center at 0.575 m depth.

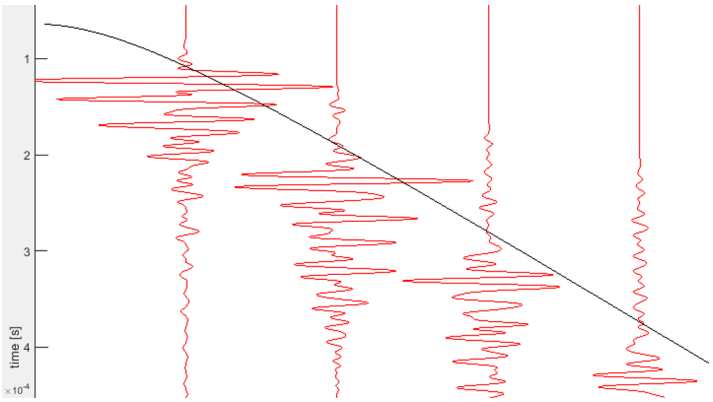

Figure 6-12: Enlarged part of seismogram of synthetic data, foundation pile modelled with a neck with a radius of 0.1 m and center at 0.575 m depth including calculated arrival time of reflection wave. Shown are the recorded data of receiver 1 to 4 at an offset of 0.15 m, 0.30 m, 0.45 m and 0.60 m from the source.

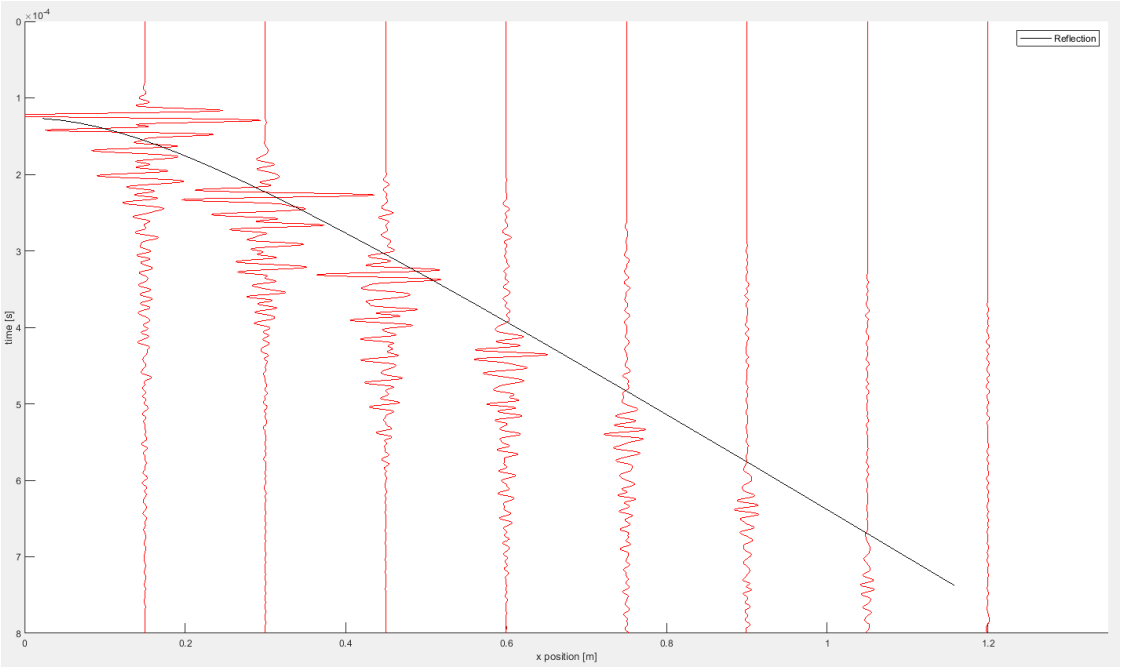

Figure 6-13: Seismogram of synthetic data, including calculated arrival of the reflection wave. Modelled with a bulge with a semi-minor axis of 0.1 m (x-direction) and a semi-major axis of 0.1 m (z-direction) and center at 0.3 m distance from the source. Reflection calculated using a concrete thickness of 0.24 m and velocity of 4000 m/s.

Part II

Data Examples

Chapter 7

Measurements

This chapter describes additional the measurements performed at the Deltares test site. Three in-situ created piles at this test site are measured more thoroughly. A description of the Seismic Tube and the characteristics of the piles measured are given in chapter 2-3 and 2-4.

7-1 Additional Measurements

Eleven to thirteen measurements per pile were performed on the piles at the Deltares test site, this corresponds to roughly one measurement per 60 cm. To obtain a better profile of the pile diameter, additional measurements were taken for three piles. These piles, piles 10, 12 and 15 were measured every 7 cm and were chosen because together they contain every designed defect. Pile 12 is designed without any defects and is used as reference, pile 10 is designed with a neck and bulge and pile 15 is designed with a fracture and a small neck at one side of the pile [Hopman, 2016]. The pile are designed with defects at 3, 6 and 8 meters depth from the top of the reinforcement bars. The designs of the piles are shown in figure 2-7.

The measurements were performed by lowering the Seismic Tube into the PVC pipe in the middle of the foundation pile until the weight attached to the bottom touched the bottom see figure 7-1. Then the tube was lifted up in steps of 7 cm to perform the measurements. The source was triggered 5 times at every measurement depth, thus 5 shots were recorded. The signal was recorded for 10 ms with a sampling time was $1x10^{-6}$ seconds. The receivers started recording 1 ms before triggering the source because of a set delay of 1 ms and the time between every shot was set to 5 ms. The source was located at 8.20 or 8.10 meters depth from the top of the reinforcement bars, when the weight touched the bottom of the PVC pipe. The depth of the Seismic Tube was determined via the measuring tape attached to the cables of the Seismic Tube, see figure 7-4. An error of about 2 to 5 cm in determination of the depth is included via this method of measuring. As can be seen in figure 7-4 the measuring tape is taped to the cables, this tape was loose at a few spots and the measuring tape could slide a bit along the cables adding an additional uncertainty of about 5 cm to the depth

determination. The measuring tape was cut off at 2.03 meters, consequently this was the most shallow measurement which was performed. Due to the length of the Seismic Tube and the measuring tape, only middle part of the foundation pile can be measured.

All the measured depth are from the top of the reinforcement bars. These reinforcement bars have a different length above the concrete pile. To level all the measurements this distance above the concrete is later subtracted from the depth measurements. The new reference level for the depth is the flat surface of the concrete made for PIT testing. This flat surface is about ground level as can be seen in figure 7-3. This flat surface is also well visible in figure 7-1 showing pile 10. This flat surface is just above ground level because the top few cm of ground around pile 10 and 15 was excavated to make measuring easier.

Measurements Test Piles	
Parameter	**Value**
Pile nr.	10, 12 and 15
Nr. of measurements	86, 89, 87
Nr. of shots per depth	5
Start depth	8.10 m, 8.20 m and 8.10 m
Sample depth (dz)	7 cm
Sample time (dt)	1 x 10^{-6} sec
Recording time	10 ms
Time between shots	5 ms
Delay	1 ms
Top reinforcement above concrete	77 cm, 59 cm and 72 cm
Source input	Ricker wavelet

Table 7-1: Measurement parameters extra measurements foundation piles at the Deltares test site

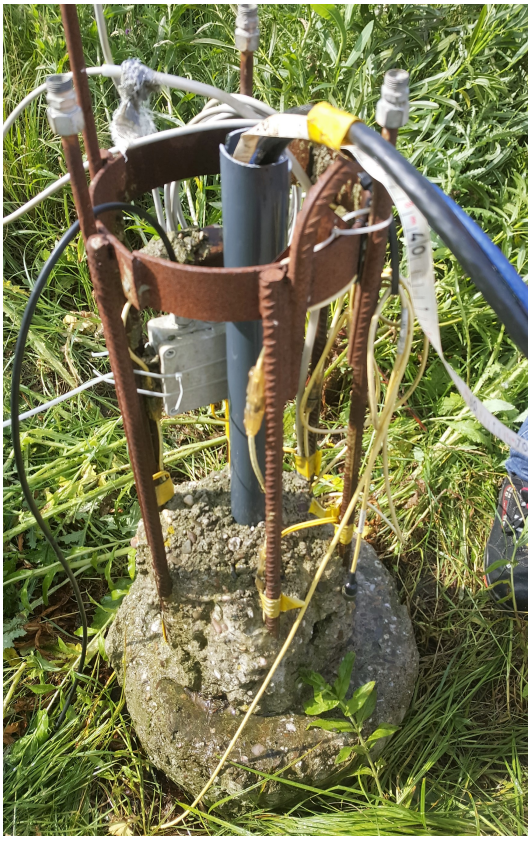

Figure 7-1: Photo of top of Pile 10 the test site at Deltares Delft. The Seismic Tube is lowered in the PVC pipe

Figure 7-2: Photo of top of Pile 15 the test site at Deltares Delft

Figure 7-3: Photo of top of Pile 12 the test site at Deltares Delft

Figure 7-4: Photo of the cable of the Seismic Tube with the measuring tape attached

7-2 Visual Inspection

Piles 1, 6, 7, 8, 13 and 17 were pulled out of the ground and laid down so that the diameters of these piles could be measured. This was done for a random number and at a random distance from the top. These diameter measurements are added with additional measurements at the location the Seismic Tube has measured for a good comparison of the diameter. The diameter was determined by measuring the circumference. This is done by excavating a bit of soil underneath the pile and measuring with an measuring tape as can be seen in figure 7-7. A error of about half a cm could have been made with measuring. Due to a root, sand or weed which could have been stuck to the bottom of the pile additionally to the human error. The circumference of the piles were determined for piles 13, 7, 1 and 8 as pile 6 and 17 are too close to one another and no holes could be dug. At some measurement points rocks, roots and weather complicated the digging and were therefor skipped. In the figures below the measurement locations are indicated with a orange marks on the concrete.

From inspecting the piles is found that the diameter can change within 10 cm as can be seen in figure 7-6 and the created necks are about 10 to 15 cm in length which can be seen in figure 7-5. Also found is that at the location of the created necks the pile additionally bulges a little. The bulges found on the piles are mostly 30 to 70 cm long. More photos of the piles can be seen in in appendix A.

Figure 7-5: Photo of a created neck on pile 17 with part of a measuring tape.

Figure 7-6: Photo of a bulge on pile 13 with part of a measuring tape.

Figure 7-7: Photo of some holes dug underneath the pile to measure the circumference.

Figure 7-8: Photo the cleared site. Pile number from left to right: 13, 7, 1, 8, 6, 17.

Chapter 8

Results

This chapter describes the data and results of processing. Discussed are results the data sets of the measured foundation piles at the Deltares test site and the Beemster test site. First the measured data is described and frequency analysis is performed. In 8-3 the inversion of surface waves using MASW is described.

8-1 Data Analysis

In this section the measured data is described and the incoming waves categorized. The data set of pile number 13 is taken as representative data set for the foundation piles at the Deltares test site. After measuring, this pile is pulled out of the ground for visual inspection. This pile was designed with a bulge and a neck, upon recovering the pile determined was that at the designed depth of the bulge at 6.25 to 6.75 meters below the top, a small neck is present, furthermore at a depth of 1.5 meters (no designed defect) and 8 meters (a designed neck) a neck and at 5.3 meters (no designed defect) a bulge are present. The presence of both a neck, bulge and no defects in the pile makes this pile a good representative pile. Two shots of this foundation pile, shot 6 at 4.76 m and shot 10 at 7.48 m depth are shown in figure 8-1. The shots in this pile are taken with a separation of 68 cm in a water filled hole in the center of the foundation pile, the top source is used of the Seismic Tube is used. The other data recorded of this pile is shown in appendix C-1.

The amplitudes of the incoming waves have decreasing much after the first two to four receivers. The last 4 traces show very little amplitude, the waves have attenuated much upon arrival at the Seismic Tube.

A common feature in these shots is the large amplitude arrival in the first trace. All shots taken in pile 13 this arrival has its peak amplitude at around 0.17 ms. Shot nr 6 is the only shot with a later arrival time of this peak, indicating a difference in the concrete pile. This large amplitude arrival is not the first arrival, it could be a reflection or surface wave arrival. Before interpretation of the different arrivals frequency analysis is performed. Another notable feature is the first arrival of each trace. This arrival is a short wavetrain instead of one pulse,

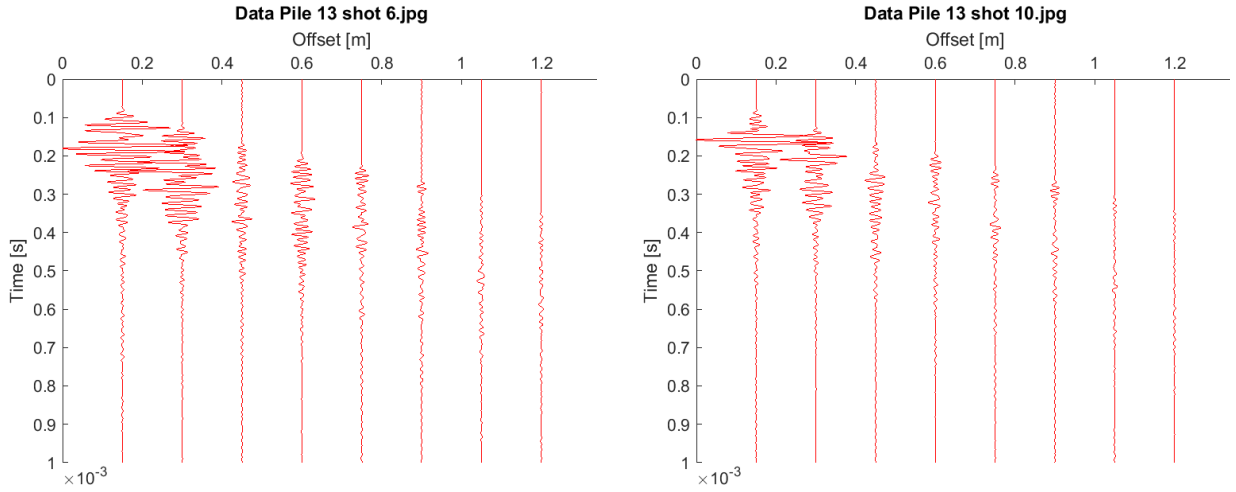

(a) Shot 6 at 4.76 m depth

(b) Shot 10 at 7.48 m depth

Figure 8-1: Two shots of foundation pile nr 13 at the Deltares test site

implying the source emits another signal than the desired Ricker wavelet. The interference patterns found in the synthetic data in chapter 6 can be seen in this data as well. In the first trace and second trace of these shots this pattern can be observed around 0.15 ms and 0.2 ms.

The data is transformed to frequency domain using FFT and visualized in figures 8-2 and 8-3 for pile 13 shot 10 which is at a depth of 7.48 m from the top of the pile. The amplitudes of the first two traces is much larger than the others, which is in line with the amplitudes found in the time domain. In figure 8-3 the frequencies of each trace are plotted separately. The frequency spectra of the other shots of pile 13 are shown in appendix C-2.

To check for aliasing Nyquist theorem is used. The Nyquist frequency is $f_N = 1/(2\Delta t) = 1/(2 * 1e^{-6}) = 500kHz$ this means the frequencies of interest are sampled correctly and the Nyquist filter does not filter the signal of interest.

The center frequency of the source is 62.2 kHz, most of the energy in the frequency domain, especially clear for traces 1 and 2 is concentrated just below this center frequency. Between 30 kHz and 40 kHz a peak in amplitude is present for most traces. A peak is in the lower frequencies often associated with surface waves, these waves have a higher wavelength and velocity. High amplitudes at higher frequencies than the center frequency can also be observed. Mostly these high frequencies peak around 75 kHz. An increase in frequency originates from different sources. A likely explanation for these higher frequencies are resonance, interference, standing waves occur in the foundation piles.

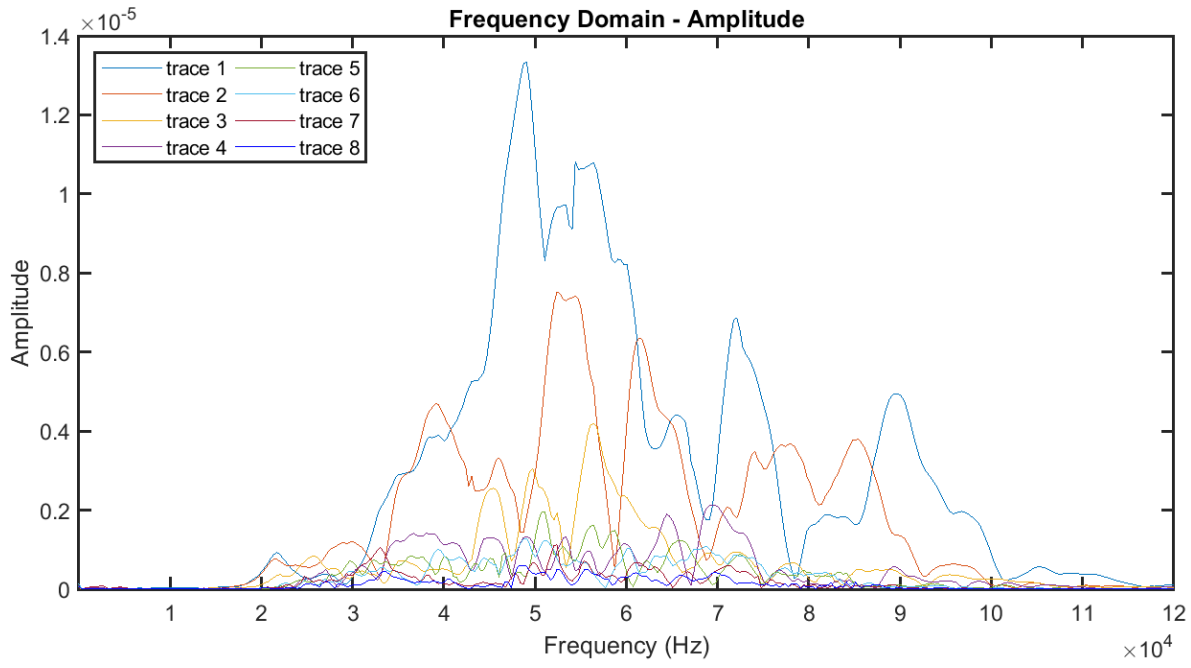

Figure 8-2: Frequency spectrum for pile 13 shot 10 showing frequency distribution vs amplitude for the 8 traces.

8-1-1 Filtering

To better investigate the effect of these frequency phenomena, frequency filters are applied. The frequency spectrum is split into three ranges of low, middle and high frequencies. A trapezoidal filter is applied with the corner frequencies for the three filters as follows; Low-pass corner frequencies: [1500 20000 40000 50000], mid-bandpass corner frequencies: [40000 50000 65000 70000] and high-pass corner frequencies: [63000 73000 100000 120000]. The frequency spectrum after the low-pass is shown in figure 8-3. After filtering the frequency spectra are converted into time domain using inverse Fourier transform. The resulting seismographs are shown in figure 8-4. The seismograms show a ringing effect due to filtering, but some notable features in the seismograms appear as well.

Figure 8-4b shows the resulting seismogram after applying a low-pass filter. A clear low frequent arrival appears in the seismogram. This low frequent arrival shows similarities with a direct or surface wave arrival. In figure 8-4c the result of the mid-frequency bandpass is shown. These frequencies have the highest amplitudes and contain the center frequency of the source signal. The biggest difference with the original seismogram can be observed in the arrivals of the first and second trace. The large amplitude arrival in the first trace is present but the later arrivals are muted and can be seen in figure 8-4d containing high frequency arrivals. The second trace shows two clear arrival. As just mentioned figure 8-4d shows the resulting seismogram after applying the high pass filter. The first arrivals of each trace contain higher frequencies as well as the later arrival of the first trace. These arrivals imply that the refracted wave is high frequent.

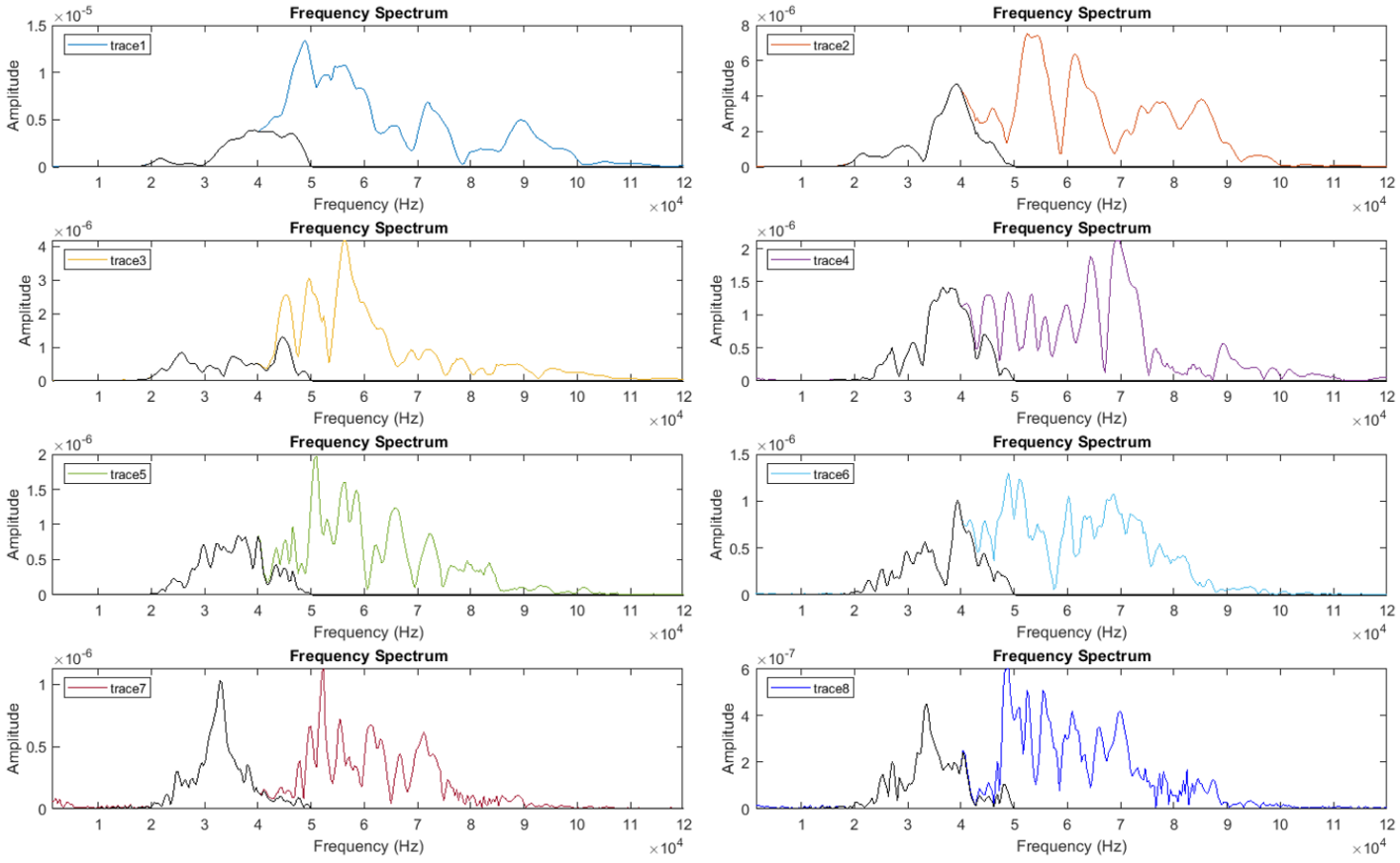

Figure 8-3: Frequency spectrum for pile 13 shot 10 showing frequency distribution vs amplitude for the 8 traces in separate subplots. Black line indicates frequency spectrum after applying a low-pass filter

The reflections of the concrete soil boundary contain information about the diameter of the foundation pile. Surface wave often contain low frequencies, by filtering these from the data the data can be improved. A low cut filter with corner frequencies [40000 50000 100000 120000] is applied to remove the low frequencies from the data. The data after filtering is shown in figure 8-5b. The data improves slightly, the interference patterns indicating the reflected wave around 0.13 ms and 0.19 ms are more pronounced in the first two traces after filtering.

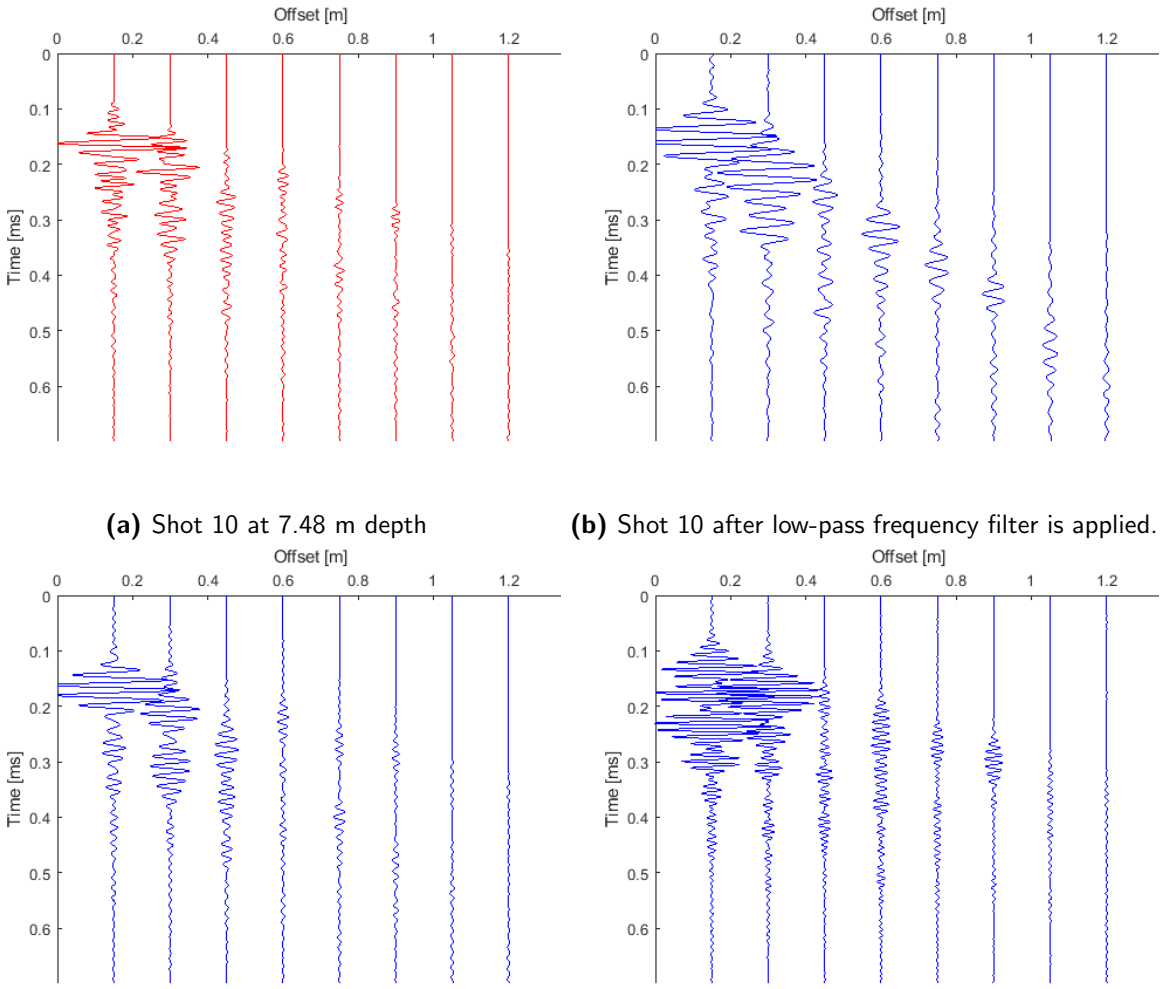

(a) Shot 10 at 7.48 m depth

(b) Shot 10 after low-pass frequency filter is applied.

(c) Shot 10 after mid-pass frequency filter is applied.

(d) Shot 10 after high-pass frequency filter is applied.

Figure 8-4: Seismograms showing the result after frequency filtering. Shot 10 of foundation pile nr 13 at the Deltares test site.

8-1-2 Deconvolution

Spiking deconvolution is performed on the data using the CREWES Matlab Toolbox Version: 860 [Margrave and Hall, 1991]. The deconvolution is based on time domain computation of the inverse of a minimum phase filter given its autocorrelation. The autocorrelation of the wavelet can be obtained from the seismogram, therefor two criterion must be set. Firstly, the number of lags need to be chosen, this is the length of inverse operator. Secondly, a stabilization factor needs to be added to the zero lag of the autocorrelation to avoid the truncated autocorrelation contains zeros. The input for the deconvolution are the recorded seismic data, the wavelet which is used for the operator design, the number of lags and the stabilization factor. Used are the Ricker wavelet as input for the operator design, 25 lag points and 4 as stabilization factor. The resulting deconvolved data is visualized in figure 8-6b. The inverse operator used for deconvolution is shown in figure 8-6c. The data is shown

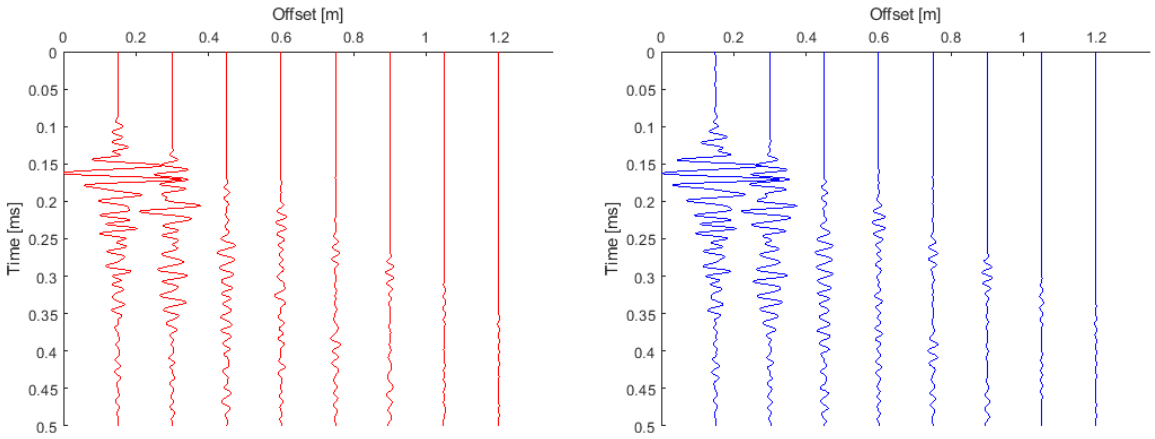

(a) Shot 10 at 7.48 m depth

(b) Shot 10 after low-cut frequency filter is applied.

Figure 8-5: Seismograms showing the result before and after low-cut frequency filtering. Shot 10 of foundation pile nr 13 at the Deltares test site.

for pile 13 shot 10.

For comparison the two seismogram are plotted in one graph. The first four traces are plotted for 0.05 ms to 0.4 ms as these are most interesting arrivals. The interference patterns characterizing the reflection from the concrete soil boundary (see chapter 6) are slightly changed after deconvolution. Besides these arrivals the deconvolution did not improve the data much, this can be seen in the other results of the other shots of pile 13 in appendix C-3.

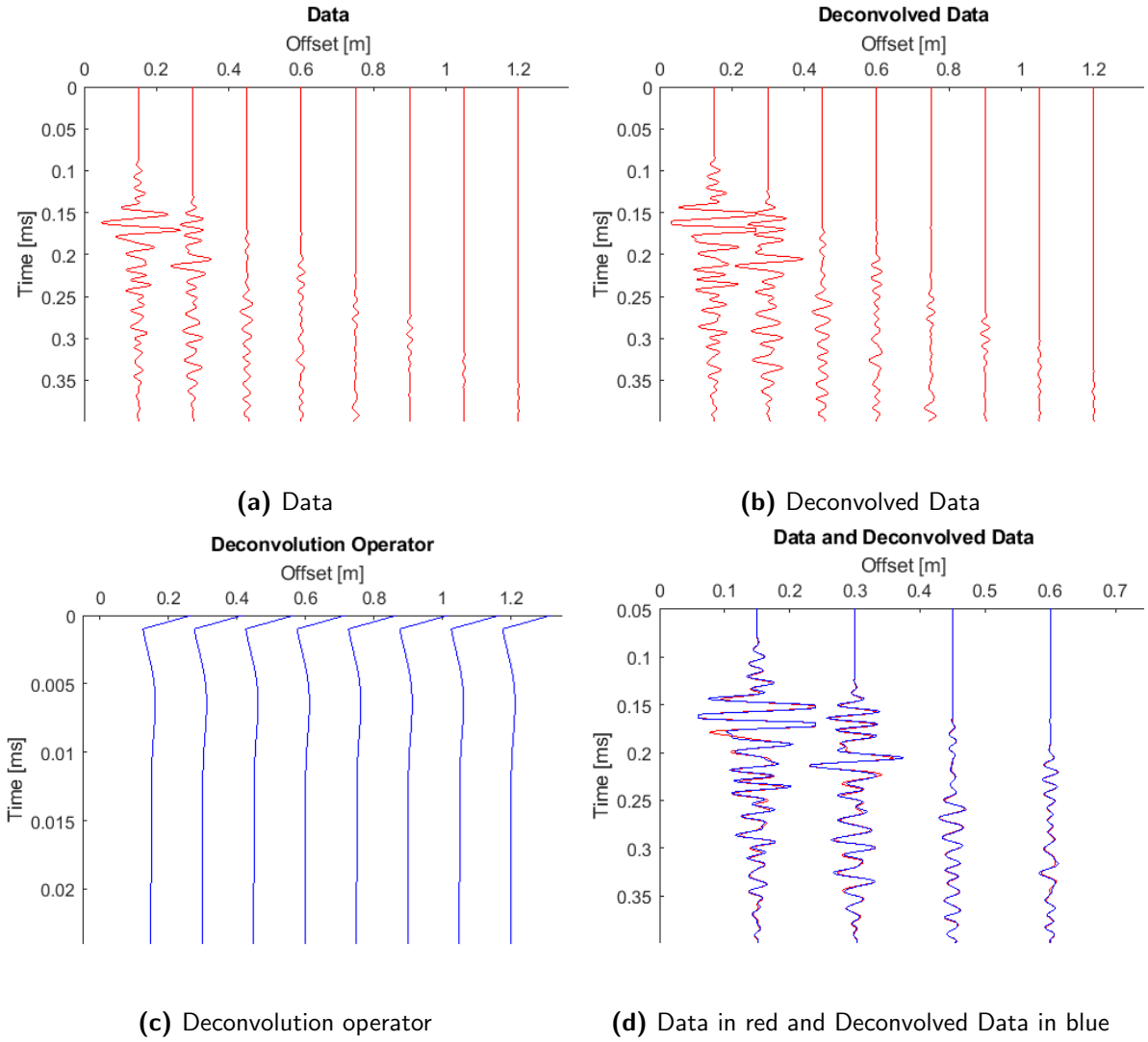

(a) Data

(b) Deconvolved Data

(c) Deconvolution operator

(d) Data in red and Deconvolved Data in blue

Figure 8-6: Deconvolution results of Pile 13 shot 10 Deltares test site

The low cut filter somewhat improved the data therefore deconvolution of this filtered data is performed. The filtered data of pile 13 shot 10 is shown in figure 8-7a next to the deconvolved data in figure 8-7b. Used for the spiking deconvolution are the Ricker wavelet as input for the operator design, 25 lag points and 4 as stabilization factor. The data before and after deconvolution are plotted in one graph for easy comparison. Deconvolution has not much improved the data. The main difference is at the interference patterns at around 0.13 ms and 0.19 ms, however these pattern were already recognizable before deconvolution.

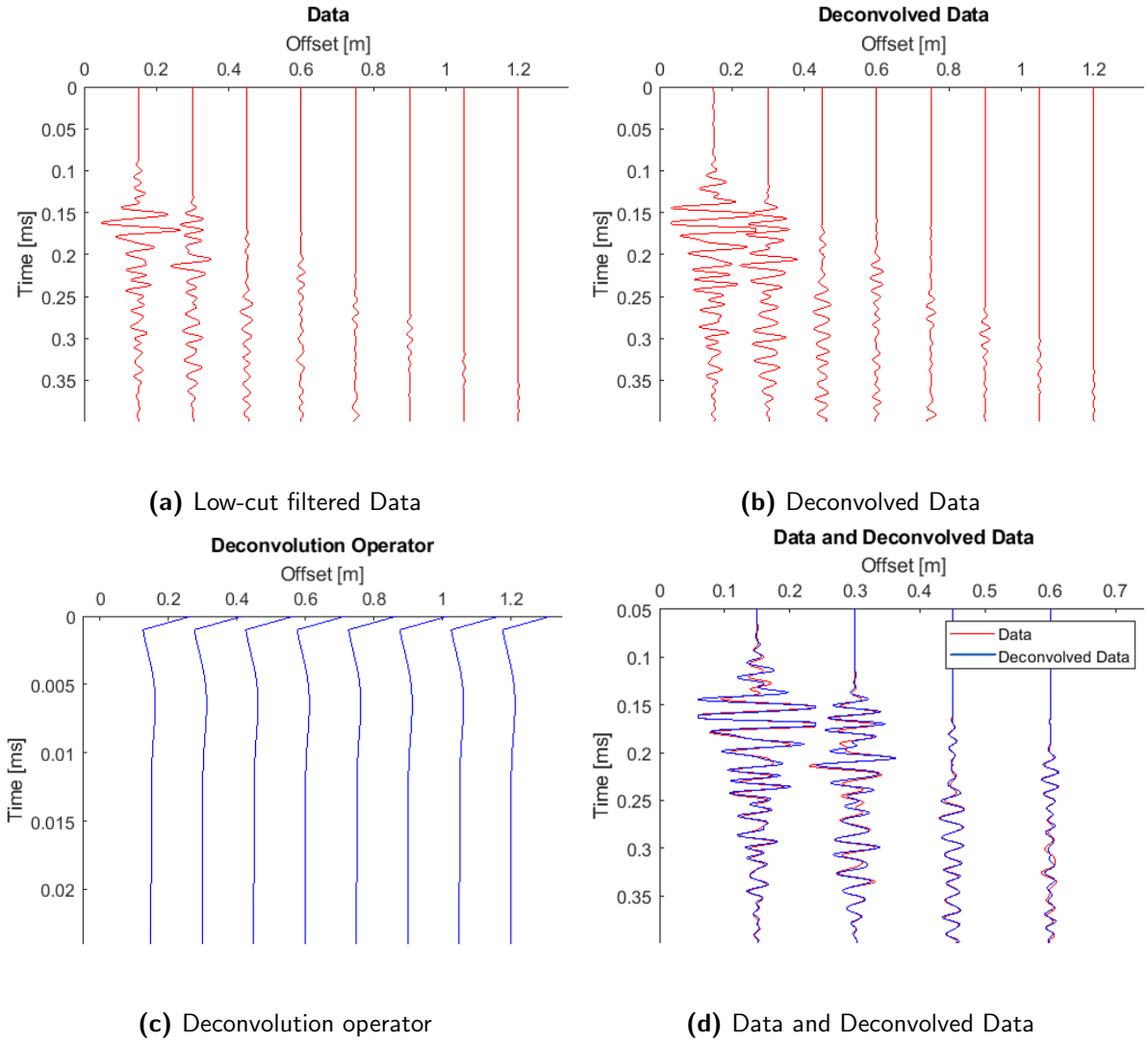

(a) Low-cut filtered Data

(b) Deconvolved Data

(c) Deconvolution operator

(d) Data and Deconvolved Data

Figure 8-7: Deconvolution results of Pile 13 shot 10 Deltares test site

8-1-3 Data Analysis Extra measurements

Additional measurements were taken for piles 10, 12 and 15. At each measurement depth, the source was triggered 5 times. The individual measurements from one depth can be compared to see whether the recorded data is constant and then be stacked to increase the signal to noise ratio of the data.

Some of the data acquired with the additional measurements show some large amplitude noise in the recordings. This large amplitude noise is only visible in the last four traces and can be seen in figure 8-8. This figure shows the data of the first shot recorded at 7.45 meter depth in pile 10. The corresponding frequency spectrum is shown in figure 8-9. The frequency spectrum of traces 5 to 8 show a large peak at 63.04 kHz, while the spectra of traces 1 to 4 show a frequency distribution more similar to the spectra of previous measurements without this large amplitude noise. This noise in the data is a continuous wave, therefor it is easy to

determine the frequency. This continuous wave has a frequency of 63 kHz which corresponds to the peak in the spectrum shown in figure 8-9. Because this frequency is about the peak frequency of the source input and in the middle of the spectrum, wanted arrivals will be removed when this frequency is filtered from the data. By stacking the data of the five shots recorded at each measurement depth, the signal to noise ratio is increased and this noise can be damped. Most of the measured data of pile 10 show this phenomena, while the measured data of pile 15 is mostly free of this high amplitude noise in the last four receivers. The cause is of this noise is not certain, it only shows at the last four receivers and not for all recordings. The Seismic Tube was adjusted before measuring, such that the individual parts were combined into one for a more robust measurement device. It is possible that this noise is a result of this procedure.

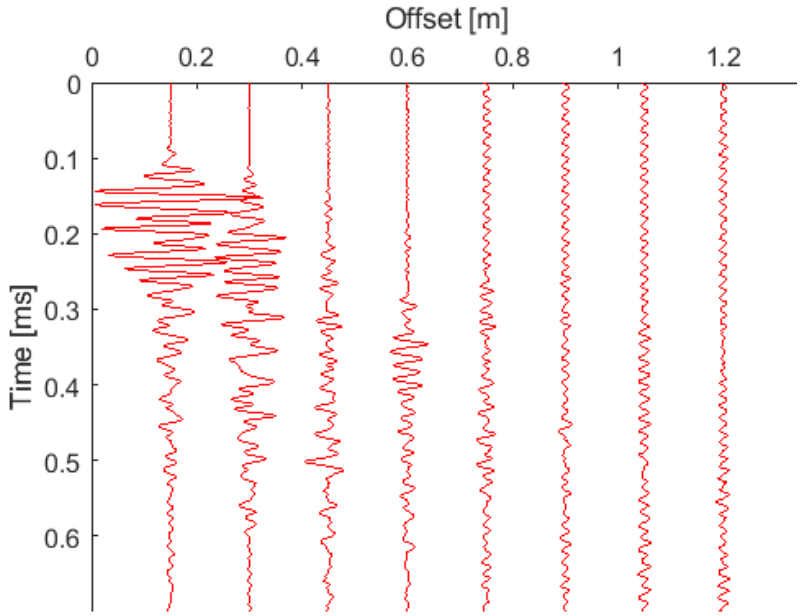

Figure 8-8: Data of extra measurements. First shot of pile 11 at 7.45 m depth. Showing high amplitude noise in traces 5 to 8.

Stacking

At each measurement depth, the source was triggered 5 times. The first trace of the five shots at 7.45 meter depth in pile 15 are plotted in figure 8-10. For visibility the trace is plotted from t is 1 to 1.9 ms and are some peaks of the arrivals clipped. This shows that the recorded signals are very constant, while the noise appear more random. When analysing this noise it is similar to the noise found in the traces 5 to 8. It is a continuous wave with a frequency of 124.5 kHz, which is twice the frequency of the source signal. This noise however has a low amplitude and does not interfere with the wanted signals. The five shots are stacked and visualized in figure 8-11. Where the arrivals are the same for each shot thus amplified, the noise is damped. Figure 8-12 shows a measurement without this additional noise and the result of stacking.

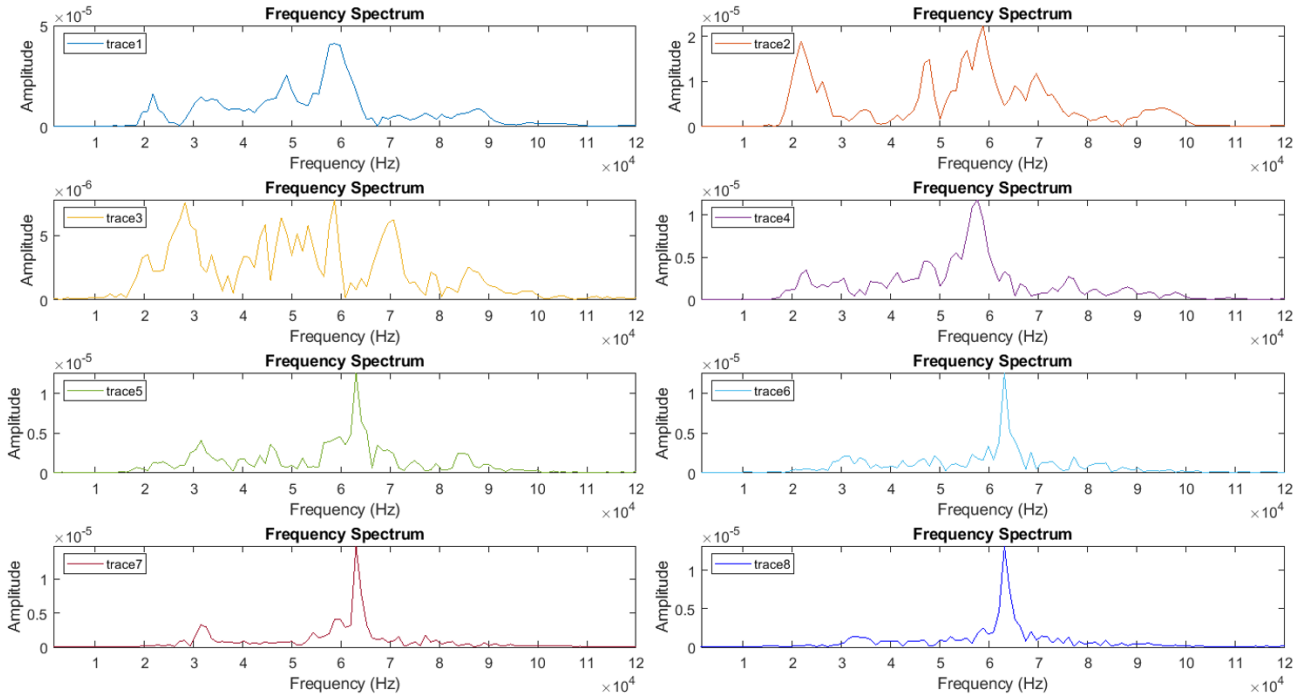

Figure 8-9: Frequency spectrum of first shot of pile 10 at 7.45 m depth.

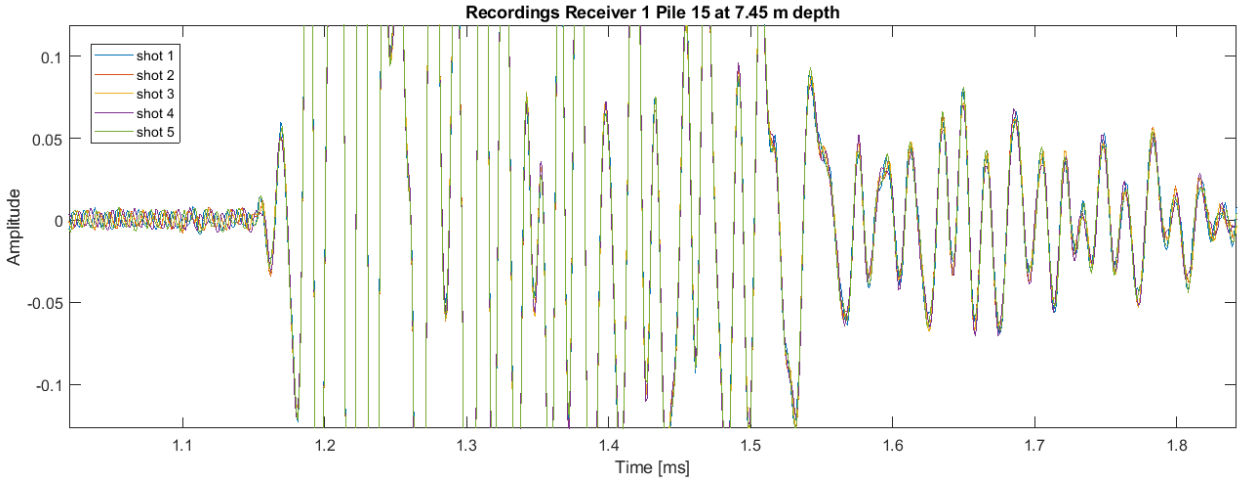

Figure 8-10: Data of the five shots of receiver 1 of pile 15 at 7.45 m depth.

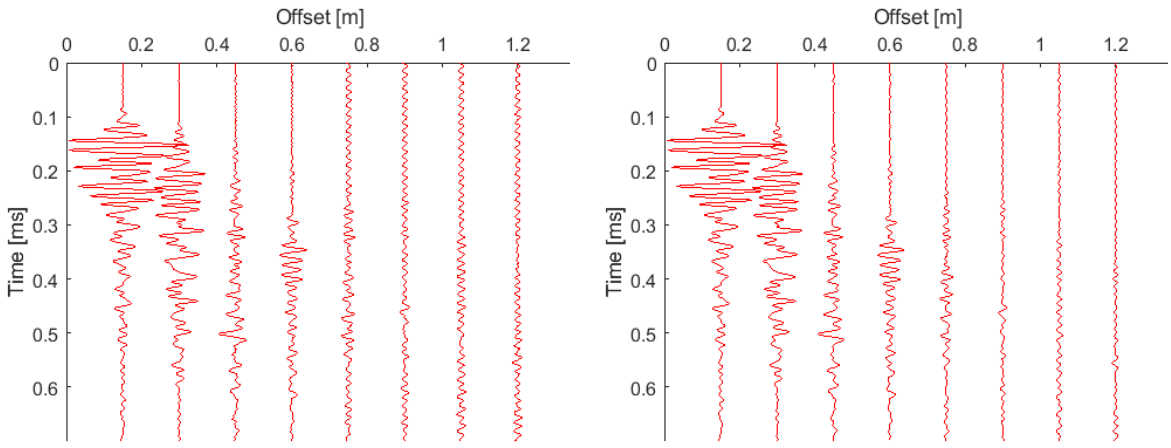

(a) Single shot **(b)** Stacked shots

Figure 8-11: Seismograms showing the result before and after stacking of 5 shots. Measurement depth of 7.38 m of foundation pile nr 10 at the Deltares test site.

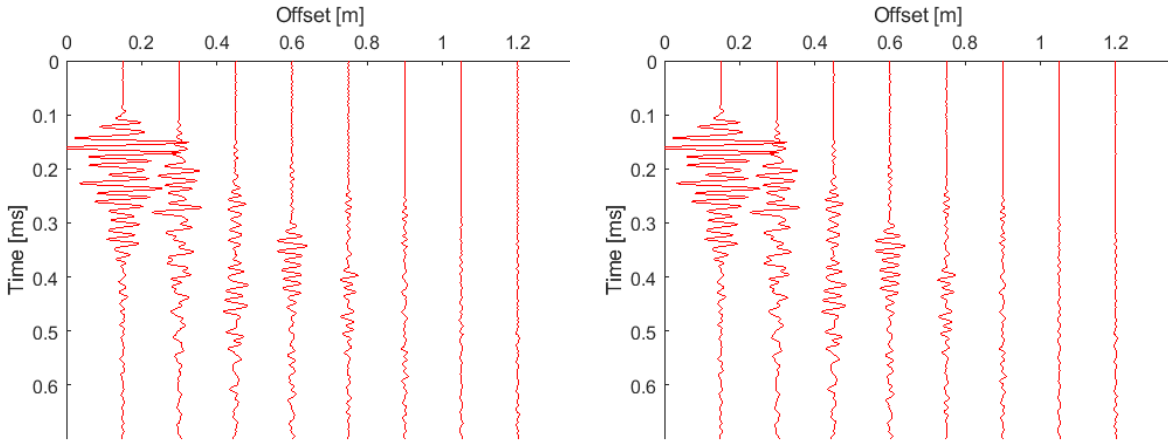

(a) Single shot **(b)** Stacked shots

Figure 8-12: Seismograms showing the result before and after stacking of 5 shots. Measurement depth of 6.93 m of foundation pile nr 12 at the Deltares test site.

Applying a low-cut filter with corner frequencies [40000 50000 100000 120000] and spiking deconvolution to this stacked data results in figures 8-13a to 8-13f. The Spiking deconvolution is applied with the Ricker wavelet as input for the operator design, 25 lag points and 3.8 as stabilization factor. The results in figure 8-13 show that filtering and deconvolution results in a marginal improvement of the data.

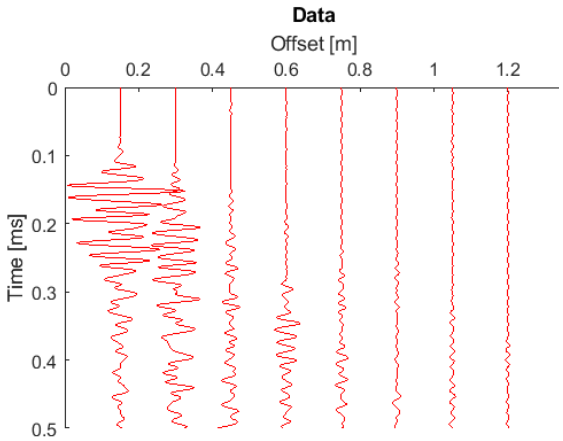

(a) Stacked Data

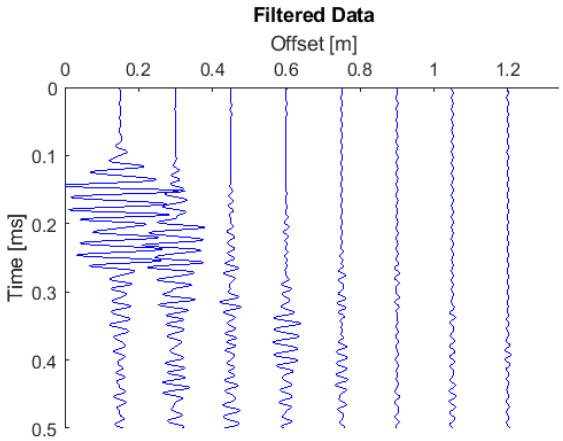

(b) Low-cut Filtered Data

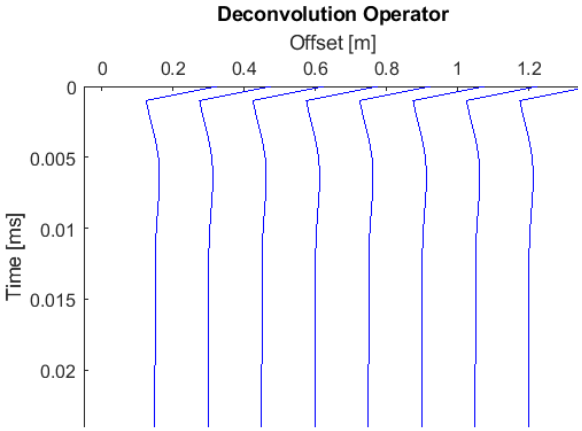

(c) Deconvolution operator

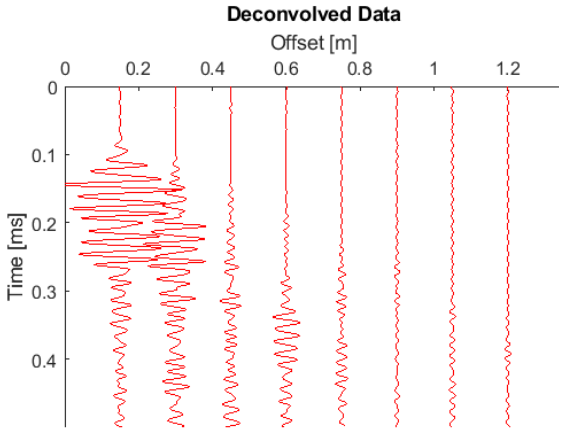

(d) Deconvolved Data

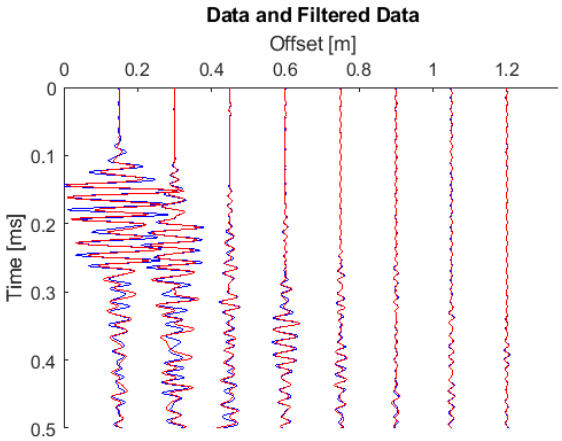

(e) Stacked Data in red and Filtered Data in blue

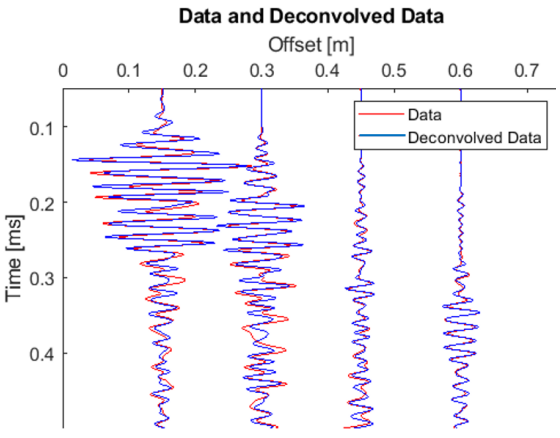

(f) Stacked Data and Deconvolved Data

Figure 8-13: Filtering and Deconvolution results of Pile 10 shot 11 extra measurements at Deltares test site.

8-2 Data Description Square Beemster Piles

In this section the measured data from the piles at the Midden-Beemster test site are described. The piles at this site are square piles which are driven into the ground. Because these piles are square the assumption that the incoming signal is the same from all direction cannot be made. Nevertheless a similar approach is used to interpret the data from these piles. Because the piles are driven piles, the piles are made in a factory and a visual inspection is possible. The piles did not have a visible defect before being driven into the ground. This can let us make the assumption each shot recorded should be the same as the piles are homogeneous. The goal from the these piles is to determine the radius from the thick and the thin pile.

Four piles were driven into the ground pile 1 and 2 of size 45x45 cm and piles 3 and 4 of 25x25 cm. During measuring the Seismic Tube was broken, thus not all piles have been measured. Pile 1 and 2 are fully measured and half of pile 3 was measured before the Seismic Tube stopped performing. This is still enough data to investigate the size of the pile.

One shot (shot 34) of each the three piles used in this report to represent the whole pile. The recorded data of piles one to three are visualized in figure 8-14. The data is similar to the data recorded at the Deltares test site, but the later receivers show stronger arrivals as the data seems less attenuated. A FFT is performed on this data and the frequency spectrum for pile 3 is shown in figure 8-15.

Comparing these frequency spectra with the spectra in figure 8-3 of the circular piles at the Deltares test site, it can be concluded these are similar. One difference is that this data shows some clear outliers. When applying the same three frequency filters as previously, thus a trapezoidal filter with the corner frequencies for the three filters as follows; Low-pass corner frequencies: [1500 20000 40000 50000], mid-bandpass corner frequencies: [40000 50000 65000 70000] and high-pass corner frequencies: [63000 73000 100000 120000]. Figure 8-16 shows the resulting seismograms, similar patterns show up as with the data of the piles at the Deltares test site.

The next processing step is a low-cut filter and deconvolution. A low-cut filter with corner frequencies [40000 50000 100000 120000] and spiking deconvolution with the Ricker wavelet as input for the operator design, 25 lag points and 1 as stabilization factor are applied. The results in figure 8-17 show that filtering and deconvolution results in a marginal improvement of the data. The results of FFT, filtering and deconvolution of piles 1 and 2 are shown in appendix D.

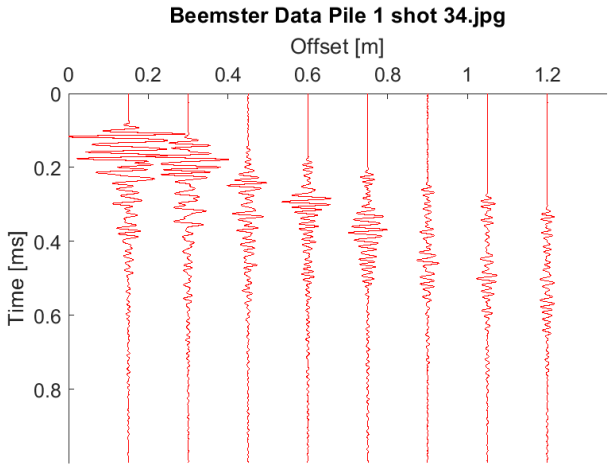

(a) Pile 1.

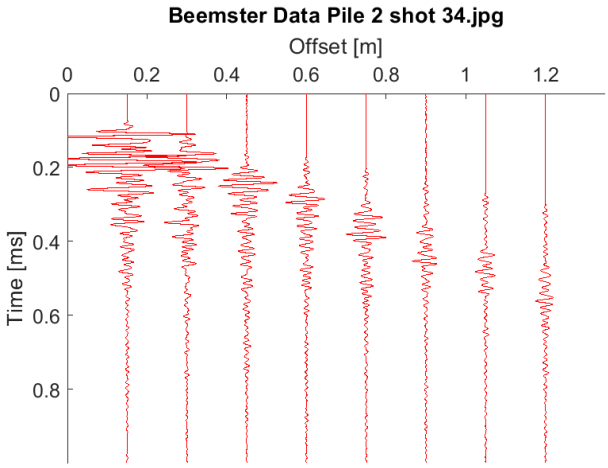

(b) Pile 2.

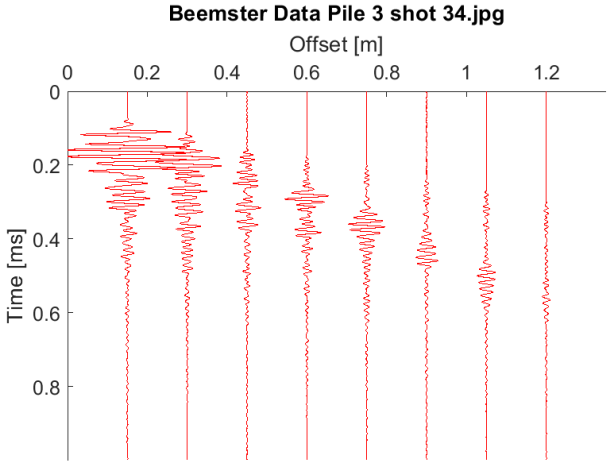

(c) Pile 3.

Figure 8-14: Seismograms showing the shot 34 of piles 1 to 3 at the Beemster test site.

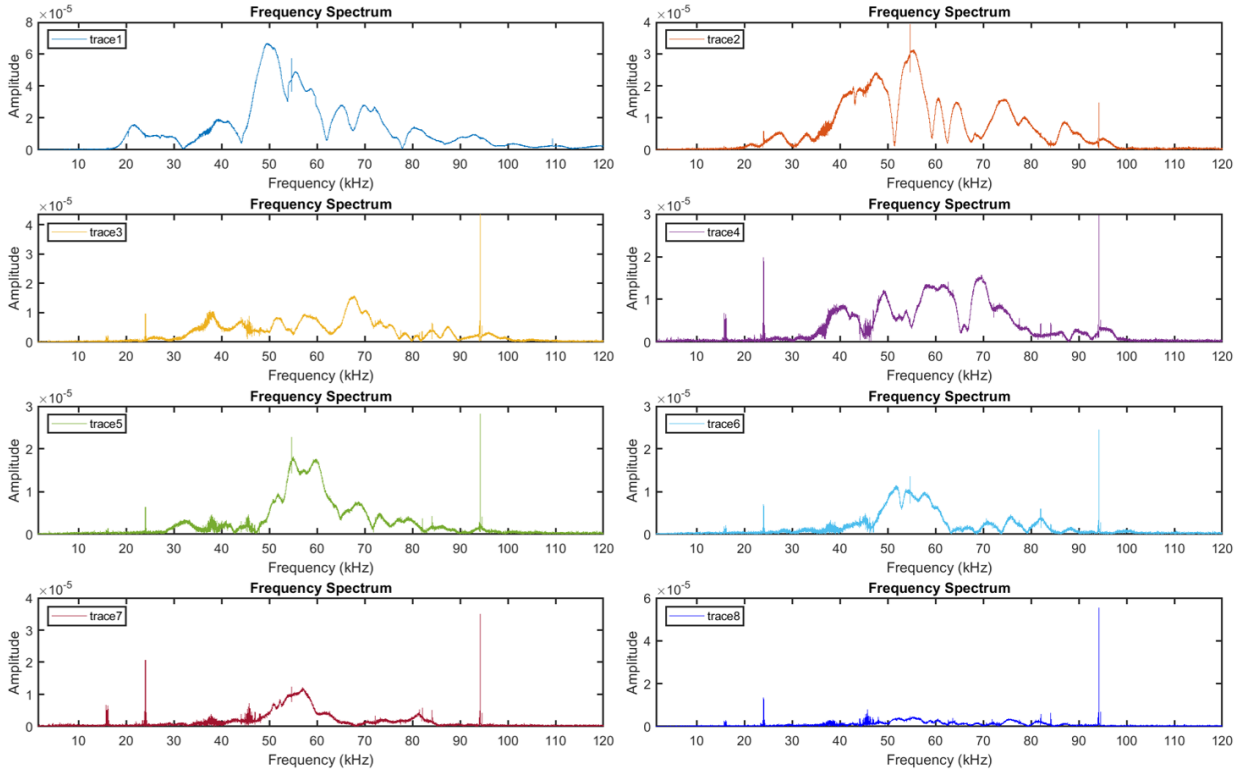

Figure 8-15: Frequency spectrum of pile 3 shot 34 of Beemster test site.

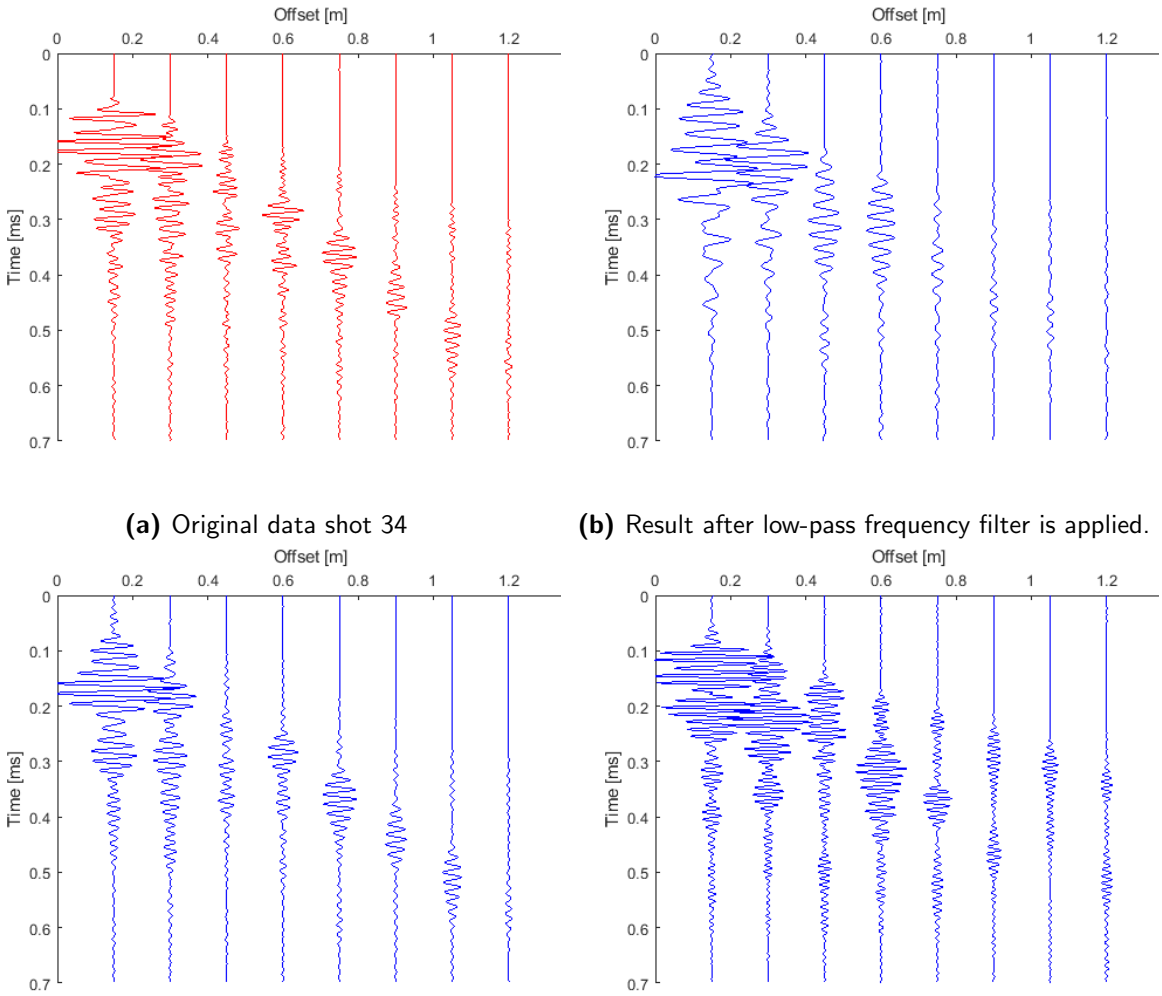

(a) Original data shot 34

(b) Result after low-pass frequency filter is applied.

(c) Result after mid-pass frequency filter is applied.

(d) Result after high-pass frequency filter is applied.

Figure 8-16: Seismograms showing the result after frequency filtering. Shot 34 of foundation pile nr 3 at the Beemster test site.

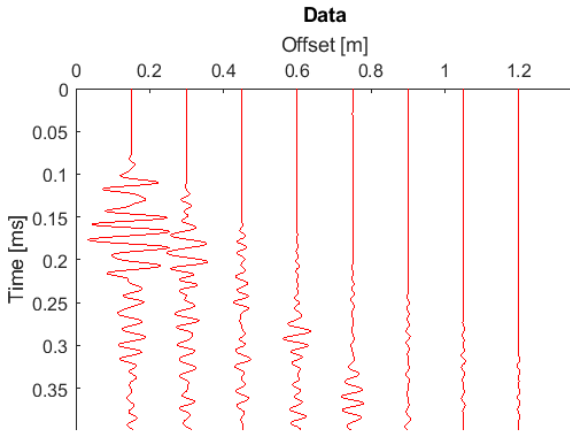

(a) Original Data

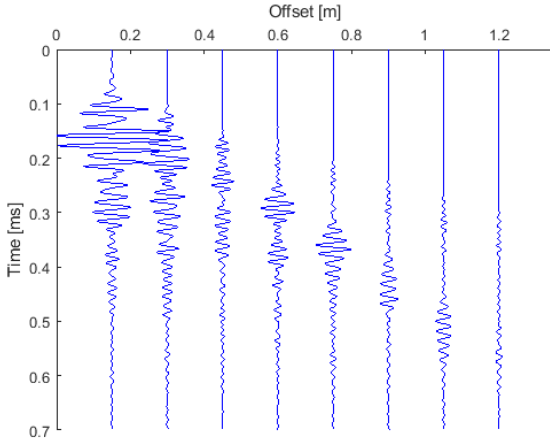

(b) Low-cut Filtered Data

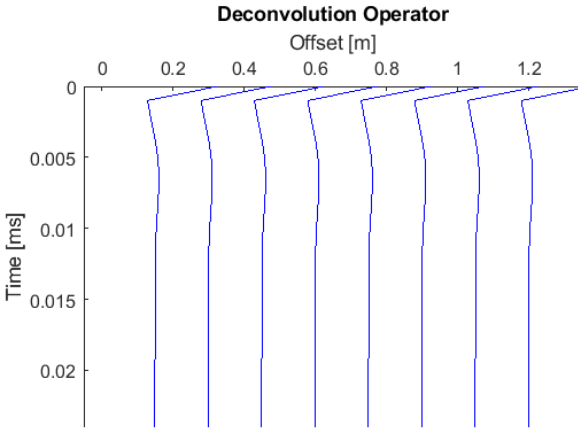

(c) Deconvolution operator

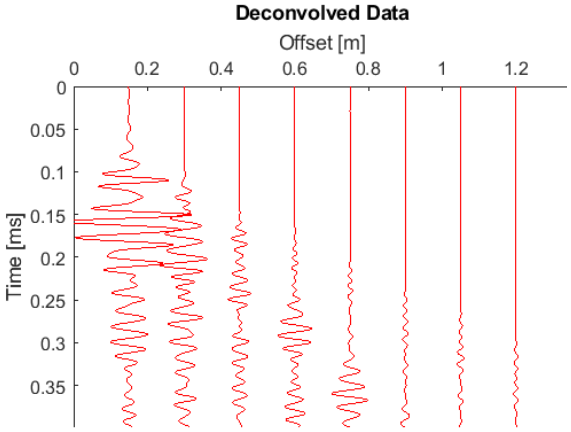

(d) Deconvolved Data

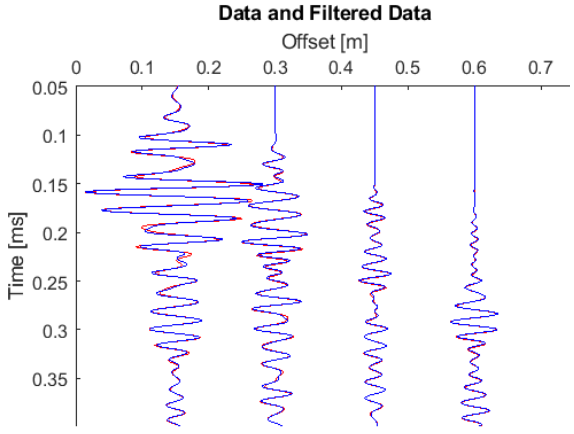

(e) Original Data in red and Filtered Data in blue

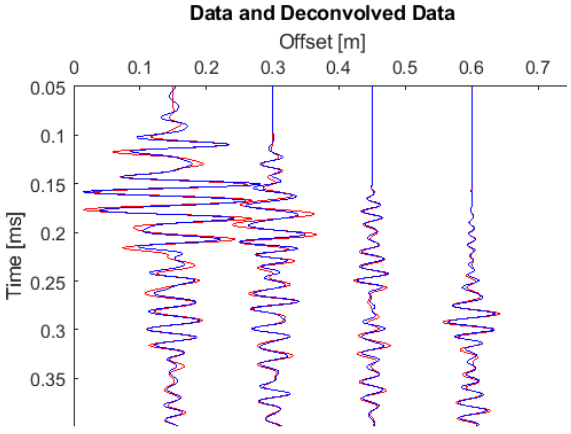

(f) Original Data in red and Deconvolved Data in blue

Figure 8-17: Filtering and Deconvolution results of Pile 3 shot 34 extra measurements at Beemster test site.

8-3 Surface Wave Inversion

The recorded surface waves are analysed using the MASW method. A MATLAB® code provided by Deltares Utrecht is used for dispersion curve picking and the inversion is done using Geophsy Dinverdc Surface Wave Inversion. This inversion program uses a neighbourhood algorithm based on the method proposed in Sambridge (1999).

The data was converted to the frequency velocity spectrum, an example of shot 10 of pile 13 is given in figure 8-19. This figure shows a wide range of frequencies and the corresponding phase velocity. Dispersion characteristics can be observed, namely between 20 kHz and 40 kHz high amplitudes are present with velocities between 2500 and 4000 m/s, indicating these are the the resonance frequencies. The high amplitudes are visible for multiple velocities, these indicate higher modes present in the data. The black line is the dispersion curve picked for the fundamental mode, this curve is used for the inversion.

Before inversion the frequencies of the dispersion curve are scaled and divided by a 100. The depths of the model thus multiplied with a 100. This is needed because the program uses meters and the layers of the foundation piles are too small if not scaled. The input model has 6 layers and consists of compressional and shear velocity, Poisson's ratio and density, the last layer is the bottom half-space. The input is given as a range of possible values and are linked to another to ensure the parameters will form layers at the same depths. The input is given in figure 8-1.

The inversion is performed according to the following steps [Sambridge, 1999];
(1) Generate an initial set of 2500 models,
(2) Calculate the misfit function for the generated models and determine the global misfit using the 50 models with the lowest misfit of all models generated so far,
(3) Generate 2500 new models by performing a uniform random walk in the Voronoi cell of each of the 50 chosen models (i.e. 2500/50 samples in each cell),
(4) Return to step 2.

The final misfit is normalized by the slowness value, hence a misfit of 10 percent corresponds to a misfit of approximately of 0.1. The robustness of the inversion is checked by running the inversion 6 times, this is necessary because the exploration paths differs as the inversion is based on a pseudo random generator. The runs are visualized in figure 8-21. The left of the figure shows the development of the misfit during the inversion, the misfit decreases and converges to a minimum as more models are evaluated. The misfit of all the runs is very high and it is likely that the runs are converging to local minima.

The result of the first run is visualized in figure 8-22. The other results are shown in Appendix E. The results from these runs are clearly different. The resulting profiles are not only different none of them represent the real situation well. The inverted p - and s - velocities, density and depths of the layers are off. Many runs are performed using the dispersion curves of other shots and piles, the resulting profiles were as different as the resulting profiles of the inversion of the shot visualized in figure 8-22.

A top and bottom mute is applied to the data to single out the surface waves and clarify the dispersion curves. All waves arriving with a velocity higher than 1200 m/s and lower than 600 m/s are muted. The seismogram mutes other arrivals than the surface wave and the resulting seismogram is shown in figure 8-18b. The frequency phase velocity spectrum of this

muted data is visualized in figure 8-20. The dispersion characteristics are more pronounced compared to the spectrum before muting in figure 8-19. The fundamental dispersion curve is picked from this data and used for inversion.

The models have converged to local minima, as a good starting model is very import this was adjusted. Various combination were tested, fixing depth, velocities and density of the known layers resulting in higher misfits and similar spreading in the resulting models or error messages of models not within the parameter space. From the results it can be concluded this method is not a feasible method for determination of the diameter of the foundation piles. MASW assumes a horizontally homogeneous medium, the piles have changing diameters, therefor MASW might not be a good method to interpret the data acquired with the Seismic Tube. Another possibility is that this inversion program is not suited for this data. The inversion gives results in meters and while the frequencies are scaled, another inversion program better suited for small scale changes and high frequencies might give improved results.

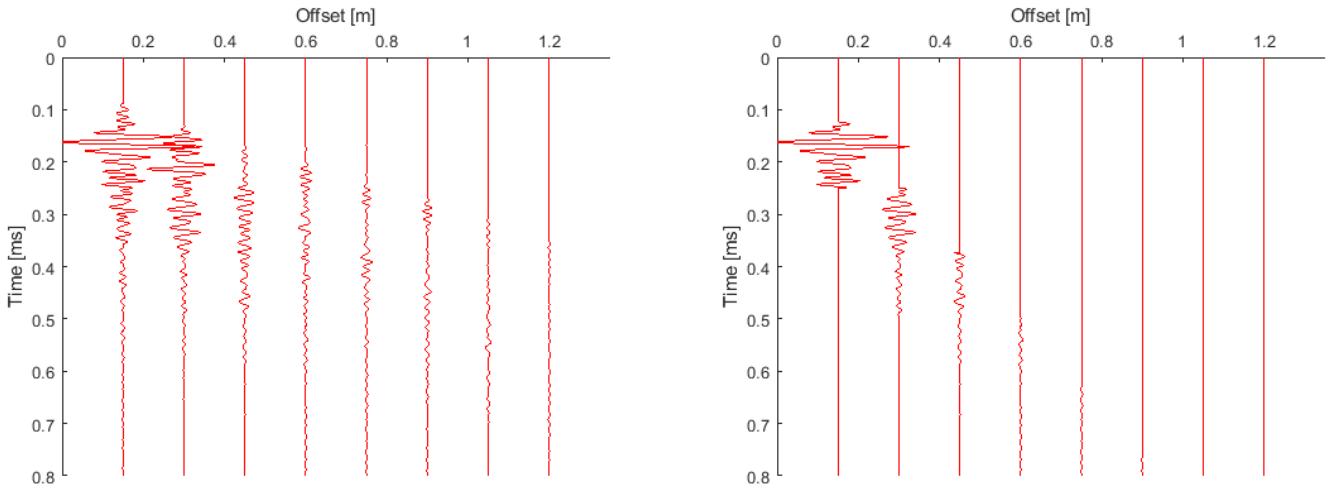

(a) No mute applied

(b) Mute applied

Figure 8-18: Seismogram Pile 13 shot 10 with and without mute. Arrivals faster than 1200 m/s and slower than 600 m/s muted

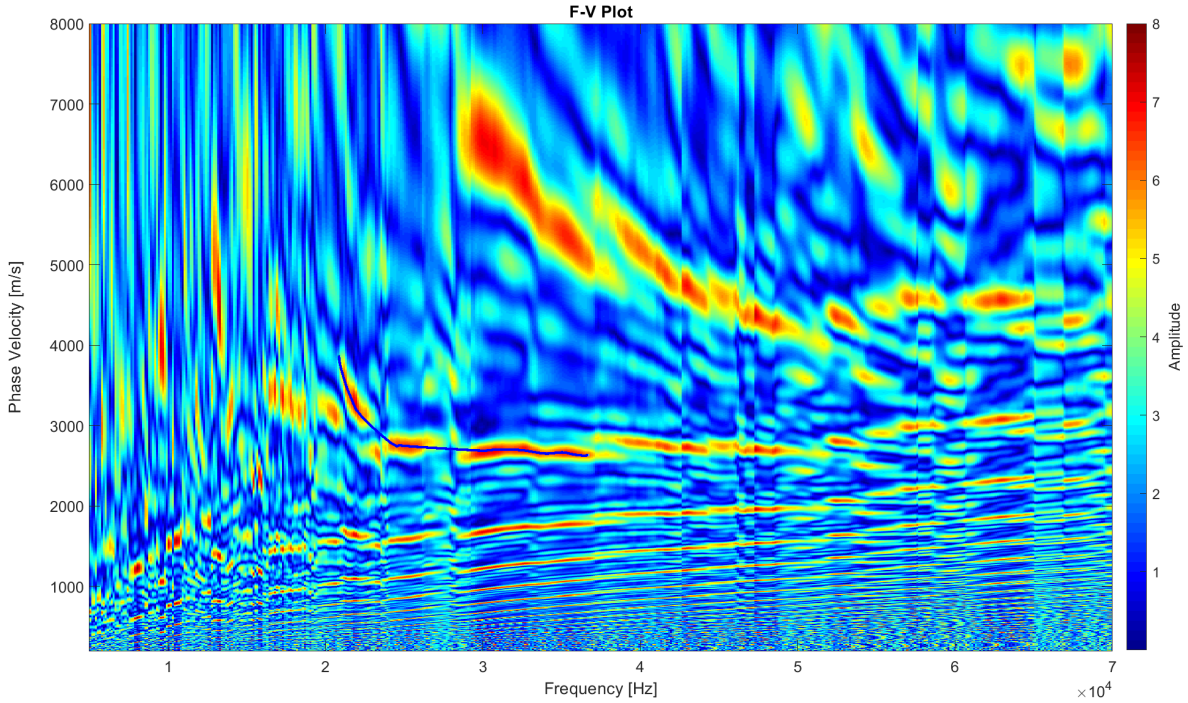

Figure 8-19: Frequency - Velocity spectrum pile 13 shot 10. Picked dispersion curve in black.

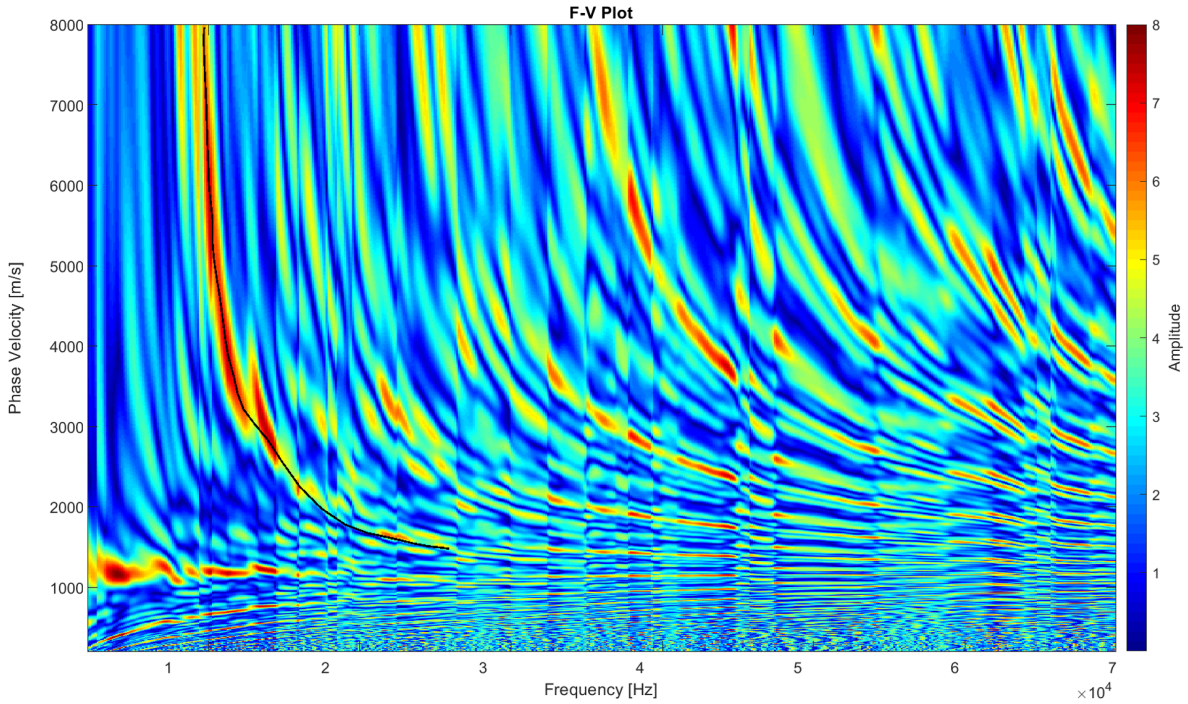

Figure 8-20: Frequency - Velocity spectrum of muted shot 10 pile 13. Picked dispersion curve in black.

Input parameters			
P-wave velocity [m/s]	**S-wave velocity [m/s]**	**Density [kg/m^3]**	**Bottom depth [m]**
1200-1500	150-300	800-900	1.45
1400-1500	150-300	900-1200	1.45 - 1.85
1450-1500	150-300	980-1000	1.85 - 2.65
1500-1800 (vp2<vp3)	150-300	1200-1400 (rho2<rho3)	2.65 - 3.15
3500-4500 (vp3<vp4)	150-1000 (vs3<vs4)	2300-2500 (rho3<rho4)	4-40
200-400	150-300	1500-1700	half-space
Poisson's ratio	all layers :	0.2 - 0.5	

Table 8-1: Input parameters MASW inversion

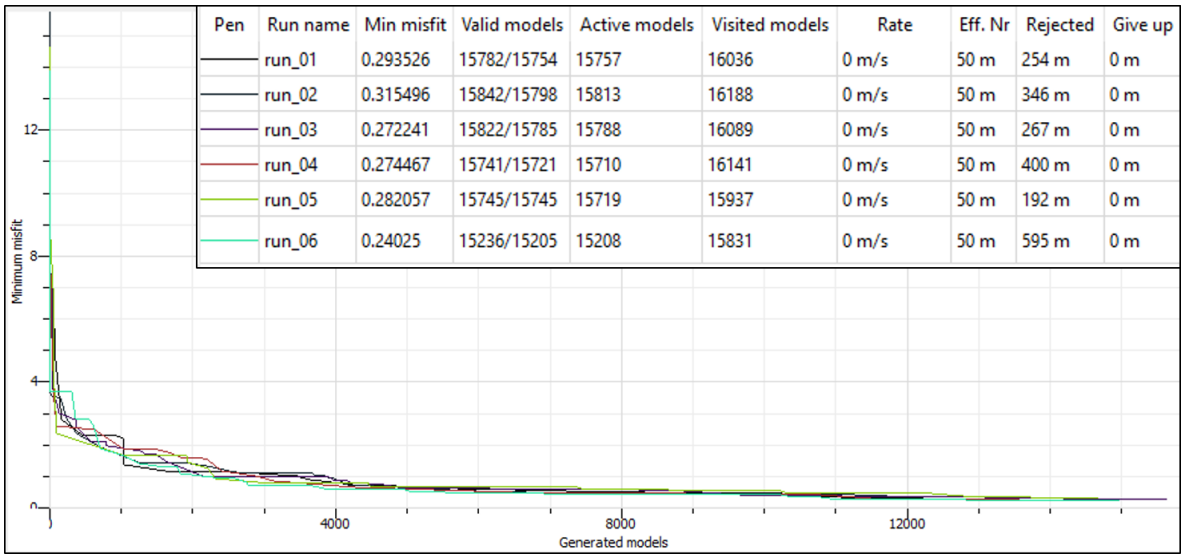

Figure 8-21: Robustness check inversion

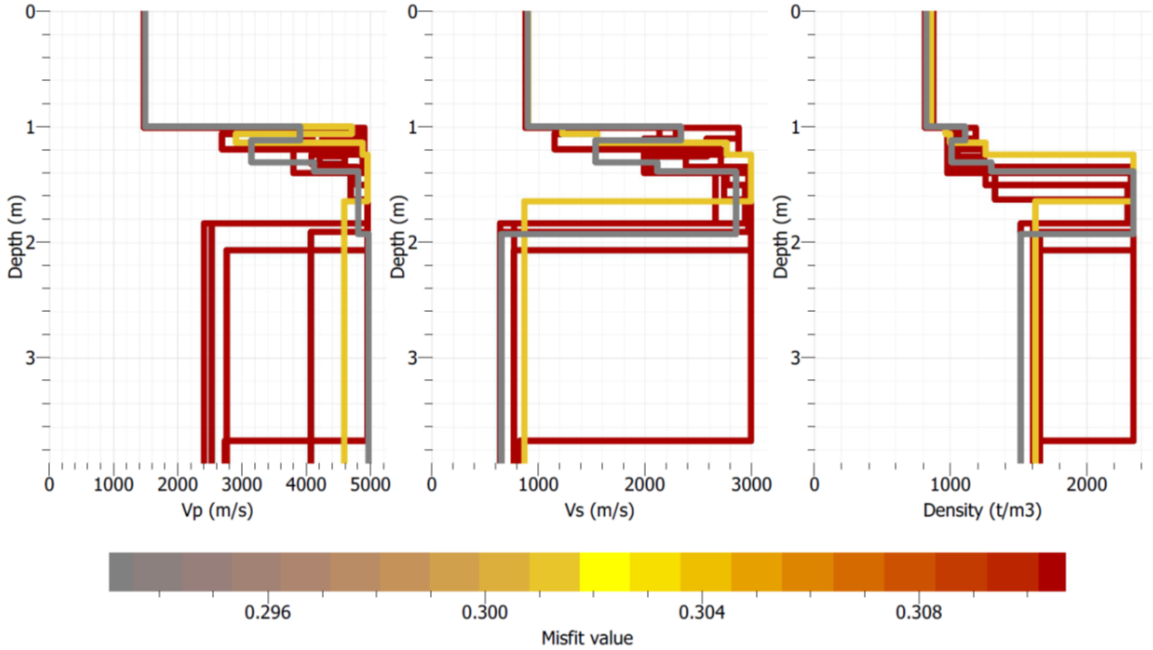

Figure 8-22: Inversion results surface wave inversion run 1. Shown are the p-velocity, s-velocity and density profiles of the models with the lowest misfits of the total investigated models

Chapter 9

Discussion

Using the results of processing and modelling the data is interpreted and profiles of the foundation piles are made with the interpretation tool. These are compared to the designs and the soil conditions of the test site.

9-1 Data Interpretation

In chapter 8 can be seen that the improvements made to the data by filtering and deconvolution are not significant or not existent. The indicators of reflected waves can already be observed in the unprocessed data. By limiting the number of processing steps needed for interpretation time thus money are saved. Considering the lack of improvement by processing and the clarity of the unprocessed data, interpretation is performed at the unprocessed data using the knowledge and information obtained from modelling, the synthetic data and frequency analysis. Interpretation is performed under the assumption that the foundation piles are symmetrical about the center of the pile and therefore the incoming signal is equal from all sides.

To interpret the arrivals in the seismograms the interpretation tool (chapter 5) is used. The direct wave travels directly to the receiver through the pipe and is determined first. Found in the modelled data is that this velocity is about the average velocity of the pipe and is used as such. The refracted wave can be used to determine the p-wave velocity of the concrete. Like with the modelled data, the refracted wave is the first arrival at every receiver in the measured data.

The found concrete velocity is then used for the reflection arrival, adjusting the thickness of the concrete the theoretical derived hyperbole can be aligned with the arrivals of the data. From the forward model arrival time of the reflected wave can be estimated. From the snapshots in chapter 6, the reflected wave is expected to arrive around 0.14 ms at the first receiver. The model showed interference takes place which can complicate interpretation of the different arrival. The distances traveled in the medium are short thus the different waves arrive at the same time and interfere. This interference is constructive because the reflection

coefficient at the concrete soil interface is negative, therefore the reflected wave are of opposite polarization as the direct, refracted and surface waves. The modelled data showed distinctive interference patterns at the arrival time of the reflected wave. These interference patterns are also found in the measured data and used to determine the thickness of the concrete layer.

Surface waves often have a low velocity and high amplitude. In the foundation piles the surface waves travel along the water - PVC or PVC - concrete interface and are Scholte or Stoneley waves. The lowest mode of the latter is the Tube wave, from the simulation using the forward model expected to be found in the seismograms. Figure 9-1 shows the surface wave arrival in pink, the velocity is much lower than other arrivals. Using the formula in chapter 3-3-1, the Tube wave velocity can be determined. The parameters used are 27100 MPa as Young's Modulus of the concrete, fluid velocity 1350 m/s, a fluid bulk modulus of 2150 MPa, Poisson's ratio is 0.4 for PVC [Crow, 2015] and an inner diameter of 0.057 m with a wall thickness of 4 mm. Inserting these values a velocity of 894.35 m/s is obtained. This velocity corresponds very well with the found surface wave velocities from the seismograms see table F-2 in Appendix F. Variations in the Tube wave are because the input parameters of the fluid and concrete can differ from pile to pile. The found surface wave arrival can thus assumed to be the Tube wave.

In figure 9-1 the data of shot 5 pile 13, including the picked arrivals of the surface, direct, refracted and reflected wave is visualized. This shot is taken at 4.08 m depth relative to the top of its reinforcement bars. These reinforcement bars have a different length above the concrete pile. To level all the piles, the measurements this distance above the concrete is subtracted from the depth measurements after interpretation. The new reference level for the depth is the flat surface of the concrete which is about the ground level. The corrected distance is 3.41 m for pile 13, the correction distance for all piles are listed in table F-1.

The velocities found are 1848 m/s for the direct wave (average velocity pipe), 878 m/s for the Tube wave and 3945 m/s for the concrete velocity (refracted wave). The first two traces of this data set show clear interference patterns, indicating the arrival of the reflected wave. The visualization of all the waves in the data shows that the reflected wave interferes with the surface wave and direct wave. By fitting this wave to the data, the concrete thickness at this depth is 0.221 m. Adding the pipe radius to this concrete thickness results in the total radius of 0.2525 m at 3.41 m depth. By interpretation all shots in a pile, a profile of it's thickness can be made. The thickness profile of foundation pile number 13 is plotted in figure 9-3a along with the designed shape of the pile. The diameter of the pile is mostly equal or greater than designed.

In the frequency analysis performed in the previous chapter, wave arrivals appeared when certain frequency bands were filtered from the data. These frequencies can be linked to wave type by comparing them to the interpreted data and interpret their properties. In figure 9-2 the interpreted data and frequency filtered data of shot 10 of pile 13 is shown. From these figures can be seen that the direct wave aligns with the low frequencies and the refracted waves with high frequencies. While the reflected and Tube wave can best be seen in the middle frequencies. This implies these waves mainly consist of these frequencies.

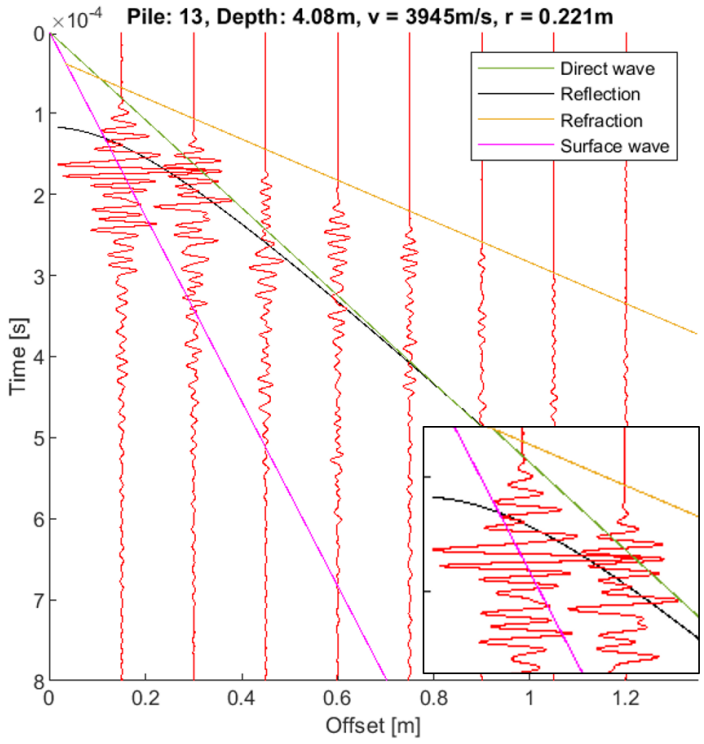

Figure 9-1: Data of shot 5 pile 13, including the picked arrivals of the surface, direct, refracted and reflected wave. In lower right corner enlargement of first two traces with the interference patterns. On top the pile number, depth relative to the top of the reinforcement, concrete velocity and concrete thickness are indicated.

After measurements were concluded six piles were extracted from the ground for visual inspection. The circumference of pile 13 was measured at 8 random places and the measurement locations of the Seismic Tube. These are plotted together with the derived profile in figure 9-3b and for better interpretation enlarged in figure 9-3c. From this figure can be seen that both profiles do not completely follow the same pattern of bulging, but most points from the Seismic Tube are close to the measured diameter.

The largest deviation between the measured radius from visual inspection and determined radius from the data of the Seismic Tube is at 4.77 meter depth. The difference between the measured radius from visual inspection and determined radius from the data of the Seismic Tube is 2.3 cm in radius. Considering the tool has a 1 to 2 cm error margin in concrete thickness determination and an error of about half a cm in measuring the diameter in the field, this largest error of 2.3 cm falls just within the error range.

Pile 13 is designed with a bulge between 5.6 and 6.1 meter and a neck at 7.3 meters. The Seismic Tube is too long to measure the neck and from visual inspection was concluded that instead of a bulge, a slight neck was formed at 5.6 meters. This slight neck can be seen in both profiles in figure 9-3c. Other observations made were a small neck at 0.8 m and a bulge at 4.60 m [Hopman, 2016]. All these observed defects are visible in the data. From visual inspection is also found that the piles can deviate in diameter within 10 cm as can be seen

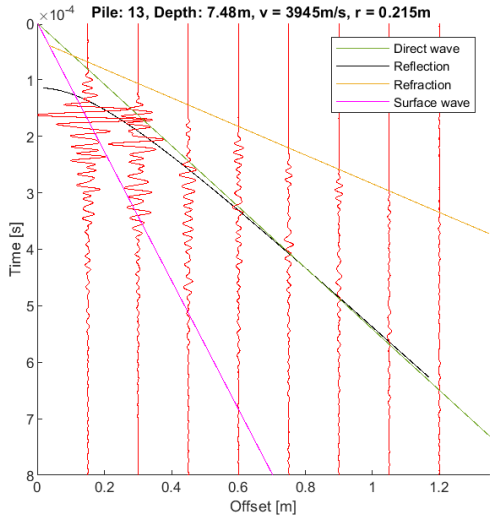

(a) Shot 10 at 7.48 m depth. Direct wave, refracted wave, surface (Tube) wave and reflected wave indicated.

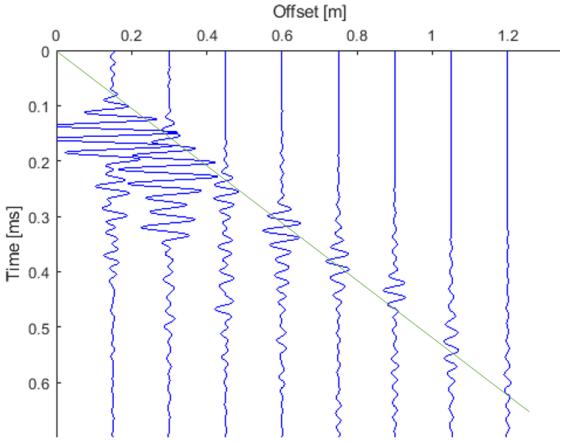

(b) Shot 10 after low-pass frequency filter is applied (low-pass corner frequencies: [1500 20000 40000 50000]). Direct wave indicated.

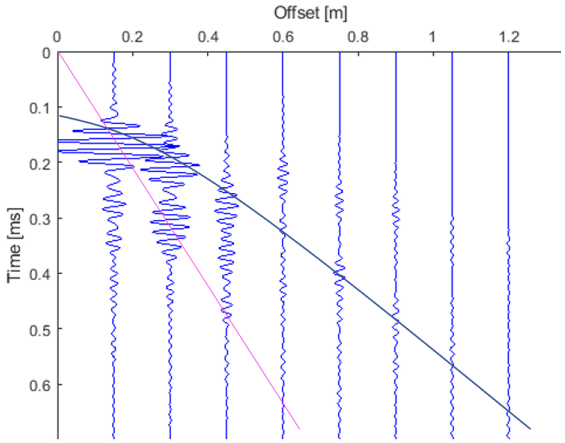

(c) Shot 10 after mid-pass frequency filter is applied (mid-bandpass corner frequencies: [40000 50000 65000 70000]). Surface (Tube) wave and reflected wave indicated in pink and black respectively.

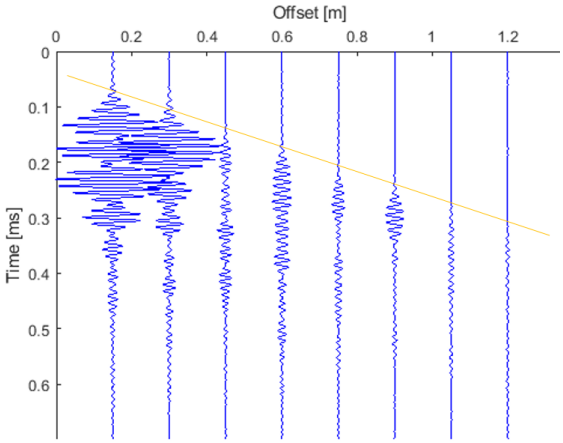

(d) Shot 10 after high-pass frequency filter is applied (high-pass corner frequencies: [63000 73000 100000 120000]). Refracted wave indicated.

Figure 9-2: Seismograms showing the result after frequency filtering with interpreted waves indicated. Shot 10 of foundation pile nr 13 at the Deltares test site.

from the photo in figure 7-6 and bulges can have a length of only 30 cm. The sampling of one measurement per 60 cm is too coarse and defect are overlooked. therefore a smaller sampling interval is needed to obtain a more accurate profile of the pile.

The profiles of piles 1, 6, 7, 8 and 17 (which are also pulled out the ground for visual inspection) can be found in appendix F-1. From all these profiles can be seen that the profiles are some

follow the same pattern of bulging, while other do not. This can either be due to a lack of measurement points or to a different determination of the radius of the pile. The difference between the two curves is for all piles within a 1 to 3 cm error range. This error margin is important to take in account, as from figure 9-3c it can be seen that a 1 to 2 cm deviation can mean the radius can be below designed. This results in a lower bearing capacity than designed and can have consequences.

Because of the limited number of measurement points per pile was decided to remeasure three piles at a smaller interval and perform multiple shots at each depth. These remeasured piles are piles number 10, 12 and 15. By remeasuring the piles, the two obtained profiles and the found velocities can be compared. Two years are in between the two measurements and the concrete has changed properties. Concrete solidifies over time and therefore the concrete velocity should increase. The concrete velocity found for pile 10 is 4298 m/s, this is an increase of 7.08 % compared to the first measurement were a velocity of 4013 m/s was found. This increase is due to further consolidation of the concrete and is in line with expectation. The other two piles show a similar increase (6.11 % and 7.67 %) in velocity as can be seen in table F-2.

In figure 9-4 the profiles of pile 10 are shown. A profile with 11 measurements and the profile measured two years later with a interval of 7 cm are plotted in one graph. A dot is shown for the source location at each measurement depth. Most of the measurement points coincide and give the same pile radius. But in these profiles can also be seen that by measuring with a large interval, defects go undetected.

Pile 10 was designed with a bulge at 2.20 m and a neck at 7.20 meter. Both the neck and the bulge are well visible in the data of the second measurements, while with the lower sampling interval these defects are overlooked. Other defects visible in the data result from interaction with the soil layers present in the subsurface.

The visual inspection in Hopman, 2016 concluded that creating bulges did not work as expected and therefore cannot be expected to be present, necking was and faults were present in all piles at designed location and therefore can be expected in the piles, if designed. In appendix F the profiles of all 20 piles are plotted with their designs for comparison. It can be determined that most of the defects are either not present or overlooked due to a limited number of measurements. The deepest defects are designed too deep for the Seismic Tube and therefore none of these are detected.

The diameter changes can be determined quite well using the data of the Seismic Tube, however the fractures designed do not give a clear and characteristic responds. This can be due to various reasons. Firstly the fractures can be closed in the soil, therefore no large contrast is present and the fracture is overlooked by the tube. Secondly the resolution of the tube is 2cm this fractures can just be averaged out in the signal, as this layer, the fracture is too thin. Thirdly the measurements can be taken at the wrong depths, as not many measurements were performed.

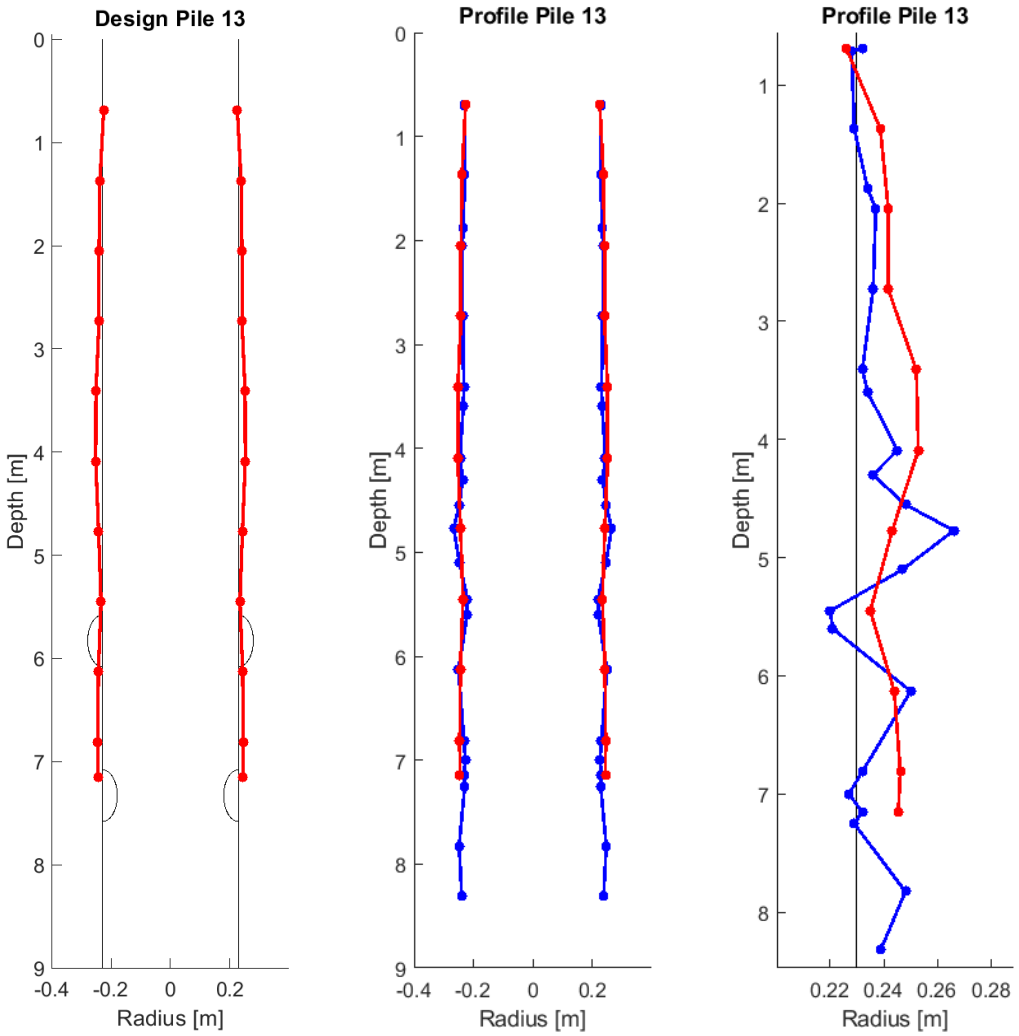

(a) Profile from Seismic Tube measurements and designed shape.

(b) Profile of Seismic Tube and visual inspection data.

(c) Close up of one side of the pile.

Figure 9-3: Profiles foundation Pile 13. Showing the radius of the pile determined using the Seismic Tube in red and designed shape in black, designed defects not to scale. The measured shape from visual inspection is shown in blue. Source location of each measurement indicated with a dot.

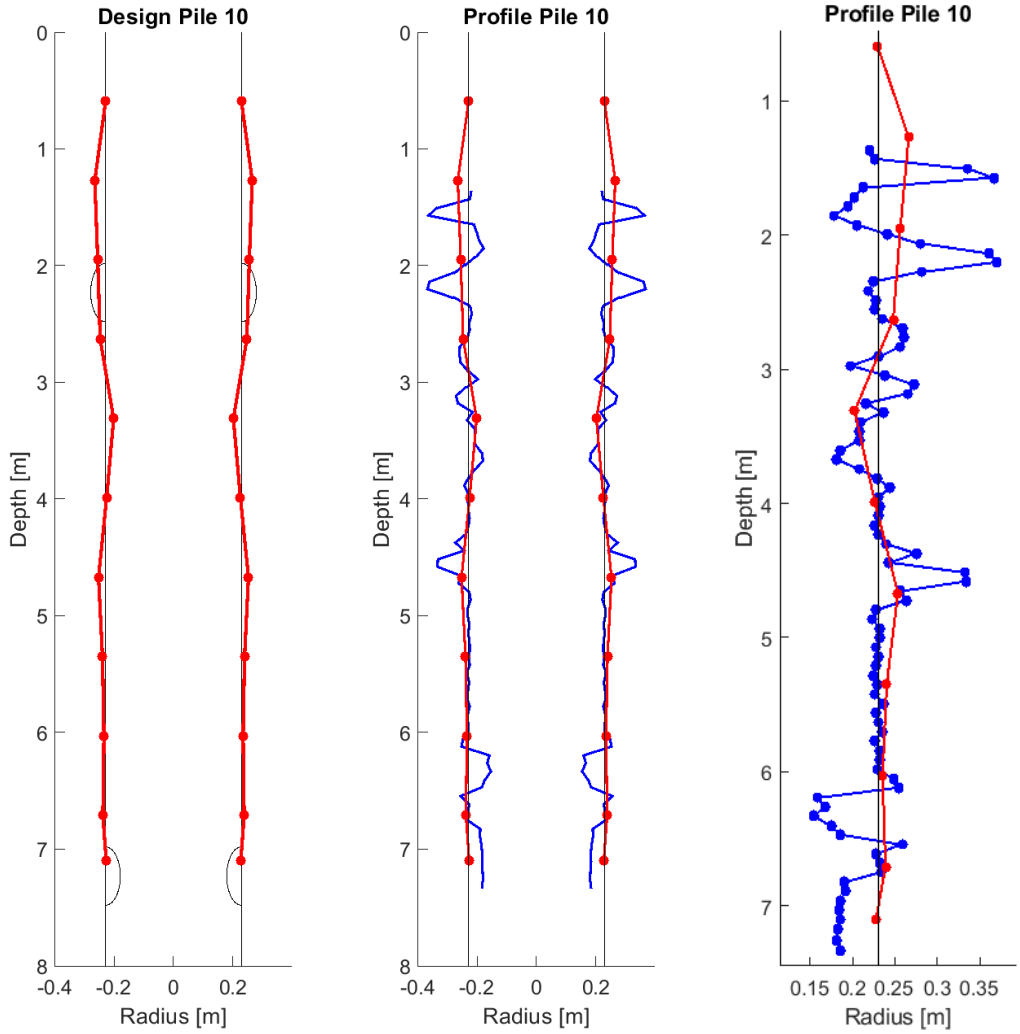

(a) Profile from Seismic Tube measurements and designed shape.

(b) Profile of the two measurements of pile 10 and nominal diameter.

(c) Close up of one side of the pile and nominal diameter.

Figure 9-4: Profile foundation Pile 10. First measurements in red, second measurements in blue and the designed radius in black, designed defects not to scale. Source location of each measurement indicated with a dot.

9-2 Comparison with subsurface

Before construction CPT's were conducted to obtain an indication of the subsurface. The ground profiles resulting from these CPT's can be compared with the profiles to relate soil to defect were possible as some defects are artificially. The CPT starts at ground level but gives the measured depth relative to meters below Amsterdam Ordnance Datum (NAP). As can be seen in the CPT data the ground level is not fully flat and the CPT starts between 2 and 2.5 m below NAP. The CPT's are takes in between the piles and give an indication of the soil layers present in the subsurface. As the ground varies it is possible layers seen in the CPT can be at another depth or not present at the location of the foundation pile.

Weaker layers such as peat tend to move for the concrete and bulges can develop while in sand bodies the piles mostly keep their shape and preferred diameter. Necking can occur when the casing is pulled at a faster speed for compensation of sand layers present or stronger water flow is present and the concrete is washed out. The CPT in this area shows that in this test field sand, peat, silty and loamy clay's are present and are shown in appendix G.

The soil profiles obtained from the CPT data can be compared with the pile profiles in appendix F. The designed defects are indicated thus a distinction can be made with designed defects and defects due to the soil conditions. Most piles show bulging between 1 and 2 meters depth, while no defect is designed. Bulging has thus occurred "naturally". In the soil profiles from the CPT can be seen that at around 4 meters below NAP a peat layer is present. This peat layer corresponds to the bulging found in the profiles of the foundation piles as the CPT starts at 2/2.5 meters.

The CPT data shows another peat layer of varying thickness between 8 and 9 meter below NAP. This peat layer causes bulging around 6 meters depth in the pile profiles in appendix F, this bulge is especially clear in profile of pile 1, 3 and 17.

Figure 9-5 below shows a part of CPT DKM102 with profiles pile 8 and 13. The CPT's are in Dutch but the terms are translated below the figure. This CPT is positioned in between these two piles as can be seen in figure 9-6. Pile 8 was designed without any defects, but three bulges can be seen from the Seismic Tube data which are validated by visual inspection. The first and third bulge at around 2 and 5.5 meters depth are present due to two peat (in CPT VEEN) layers. Pile 13 shows a similar set of bulges around the same depths. Pile 13 was designed with a bulge at 6 m, however from this data it cannot be said this bulge exists due to the peat layer and/or to the injection of extra concrete. These bulges are due to interaction with the subsurface where the concrete has pushed soft soil layers away. The second bulge is at around 4 meters depth and is different as it does not have a clear layer to explain its existence. Many other piles in appendix F, show a bulge is present around this 3 to 4 meters depth of which none is a designed defect. At this depth a loamy clay layer and a change in friction ratio (the ratio between skin friction and tip resistance) is present in the CPT data. This layer around this depth must be soft, such that these bulges were formed.

The ground profile of CPT DKM104 shows a different sequence than the other CPT's. A sand layer is present at 8 to 9 meters below NAP instead of a peat layer visible in the other CPT's. therefore no bulge is present in the profiles of piles 5 and 10 which are closest to this CPT. The profiles of piles 5 and 10 also show a neck is present at 3.5 to 4 meters depth instead of the bulge previously discussed. This neck is also present in profiles 4 and 15 next

to piles 5 and 10. This neck can be formed by compensation of sand layers present found by the CPT.

The bulging in the piles can be related to soft soil mostly peat present in the subsurface. The size of the bulging depends on the thickness (and presence) of this soft layer.

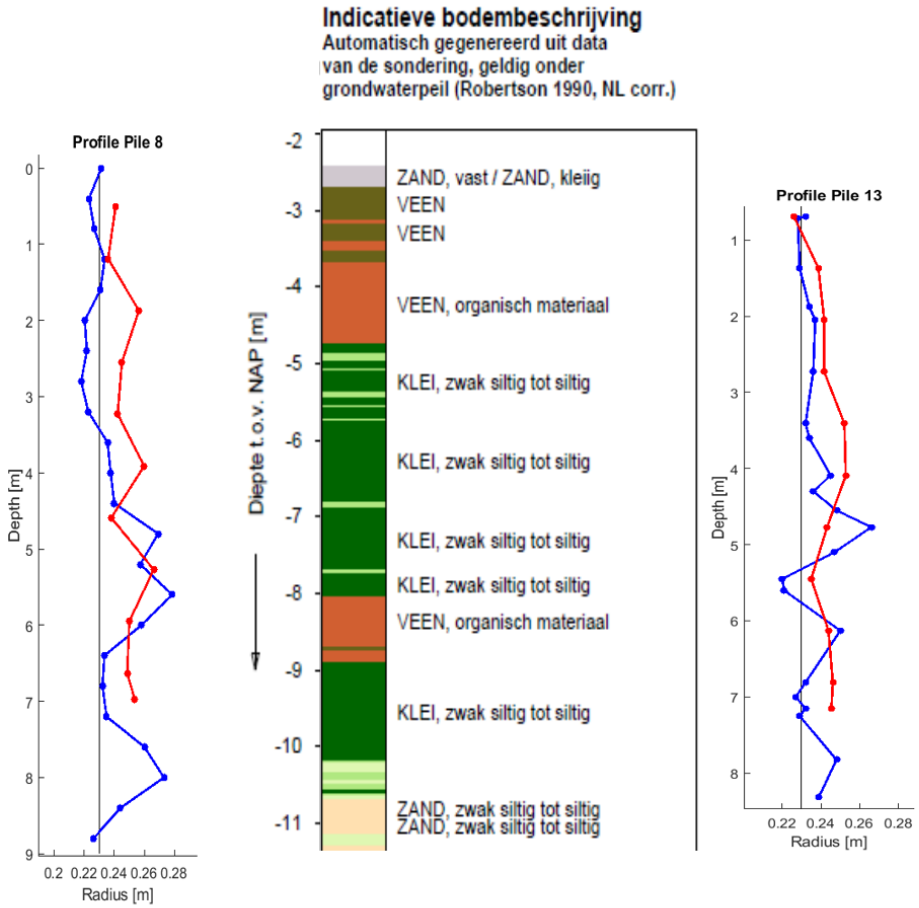

Figure 9-5: CPT DKM102 with profiles pile 8 and 13. Dutch to English; Top: Indicative Soil description, automatically generated from CPT data valid below groundwater level. Soil layers; zand vast; solid sand, zand kleiig; clayey sand, veen; peat, organisch materiaal; organic material, klei; clay, zwak siltig tot siltig; slightly silty to silty. On the left: Diepte t.o.v. NAP; Depth relative to Amsterdam Ordnance Datum. The light green color is loamy clay. Profiles showing the radius of the pile determined using the Seismic Tube in red and nominal radius in black, designed defects excluded. The measured shape from visual inspection is shown in blue. Source location of each measurement indicated with a dot.

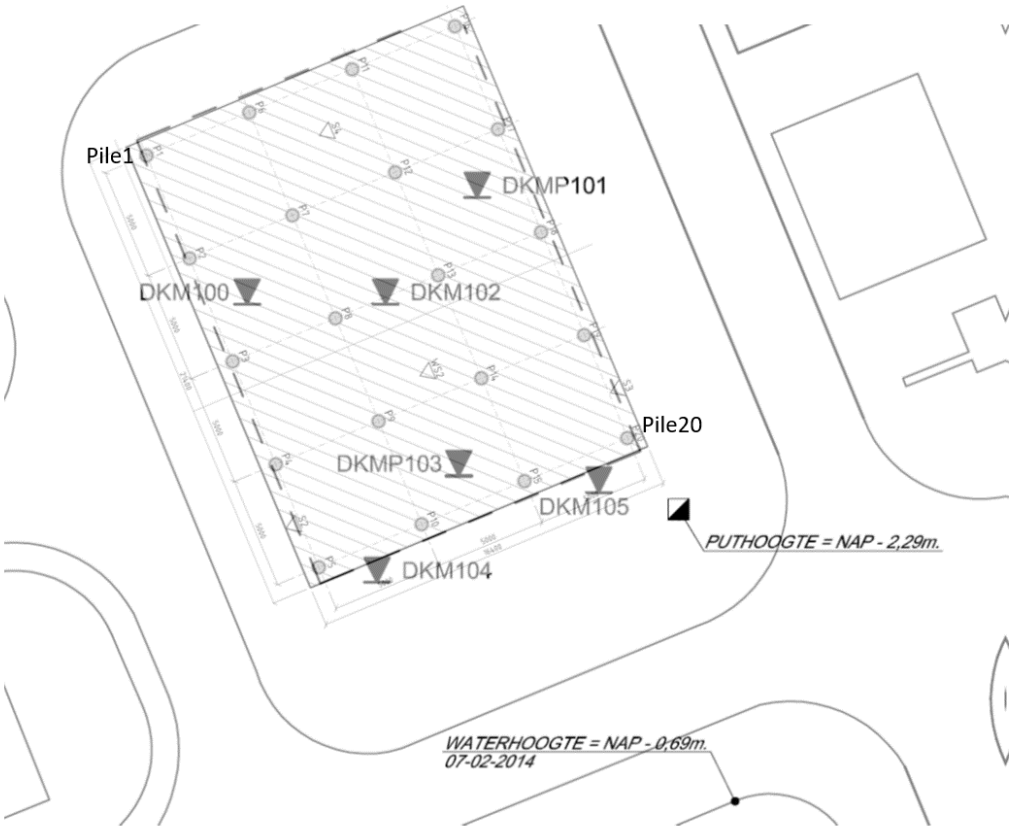

Figure 9-6: Location CPT's performed at Deltares test site.

9-3 Data Interpretation Square Beemster Piles

In chapter 8 can be seen that the improvements made to the data by filtering and deconvolution are not significant, similar as to the Deltares test piles. Hence, interpretation is performed on the unprocessed data as what has been done with the data of the Deltares test piles.

Because these piles are square the assumption that the incoming signal is the same from all direction cannot be made. Nevertheless a similar approach is used to interpret the data from these piles. Because the piles are driven piles, the piles are made in a factory and a visual inspection is possible. The piles did not have a visible defect before being driven into the ground. This can let us make the assumption each shot recorded should be the same as the piles are homogeneous and one shot is chosen to determine the thickness from the thick and the thin pile. Pile 1 and 2 have a size of 45x45 cm and pile 3 of 25x25 cm.

The interpretation tool is used to visualize and pick the different arrivals. A direct wave, surface wave and refraction wave are picked according to the same assumptions as previously described and shown in table 9-1. In the frequency analysis performed in the previous chapter, wave arrivals appeared when certain frequency bands were filtered from the data. These frequencies can be linked to wave type by comparing them to the interpreted data and interpret their properties similar to what has been done previously with the Deltares test site

piles. The results are similar and visualized in appendix D-3. The direct wave aligns with the low frequencies and the refracted waves with high frequencies. While the reflected and Tube wave can best be seen in the middle and high frequencies.

The concrete velocities found in these foundation piles are much higher of those at the Deltares test site. This can have several reason's. Firstly these piles are made in a factory and have been solidifying before being hammered into the ground. The piles were in the ground for a year before measurements took place, in total these piles have solidified for two year. Secondly as the piles are fabricated in a factory the concrete is very even and homogeneous, this can cause a higher velocity than when the concrete is poured into a hole and left for solidification.

The Tube wave velocities are much alike the Tube wave velocities previously found. The PVC pipe in these piles is has a smaller radius, recalculating a theoretical Tube wave velocity results in 944 m/s, which is about the velocities found.

The reflection arrivals however cannot straightforward be chosen. Multiple arrivals of various concrete thicknesses fit the data well. This is visualized for pile 1 and 3 in the figures below. The two picked arrivals correspond to a diameter of 25 cm and 45 cm. Pile 1 has a diameter of 45 cm and Pile 3 has a diameter of 25 cm, thus the picks in figure 9-7b and 9-8a are correct. While the pick with the smaller diameter crosses clear interference patterns, the other picked reflection arrival crosses the first large negative amplitude. This is similar for pile 2, thus without knowing the correct diameter, it is difficult to determine the correct arrival. This phenomena of multiple possible arrivals can be due to the square shape of the pile, with arrivals from the corners.

Velocities Test Piles Beemster test site			
Pile	**Velocity Pipe [m/s]**	**Surface wave velocity [m/s]**	**Concrete Velocity [m/s]**
nr. 1	1984	896	4388
nr. 2	1991	915	4388
nr. 3	2010	958	4377

Table 9-1: Velocities found in foundation piles at Beemster test site.

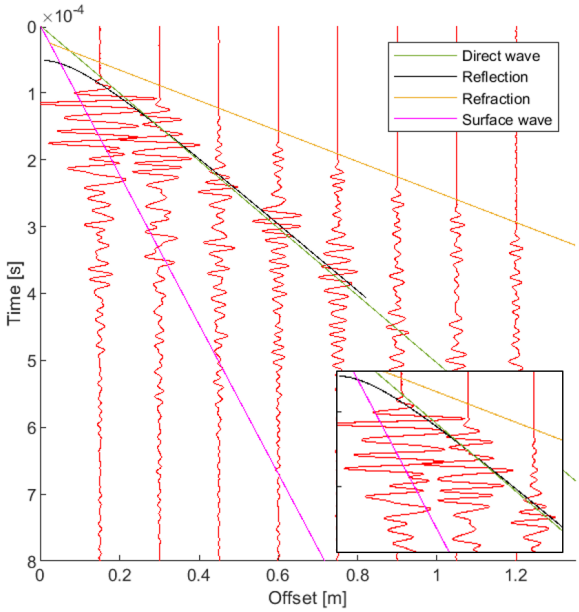

(a) The picked concrete thickness is 0.101 m corresponds to a diameter of 0.247 m.

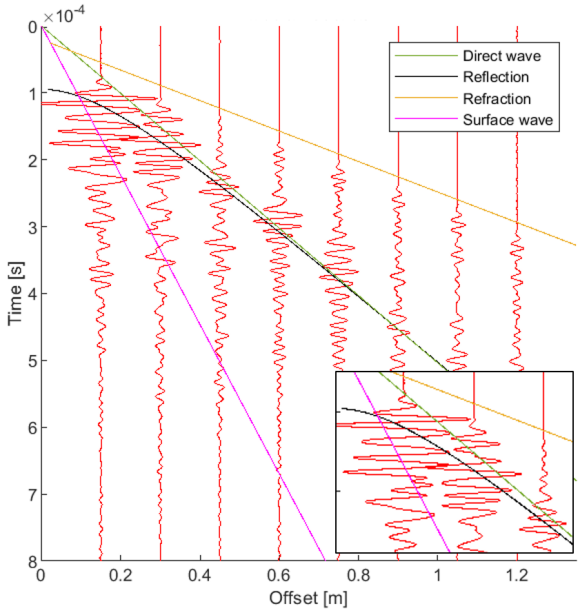

(b) The picked concrete thickness is 0.201 m corresponds to a diameter of 0.447 m.

Figure 9-7: Beemster data of shot 34 pile 1, including the picked arrivals of the surface, direct, refracted and reflected wave. In lower right corner enlargement of first three traces.

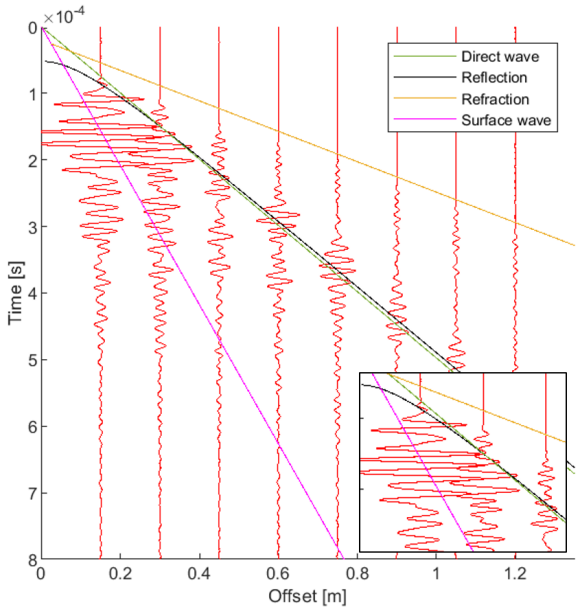

(a) The picked concrete thickness is 0.102 m corresponds to a diameter of 0.249 m.

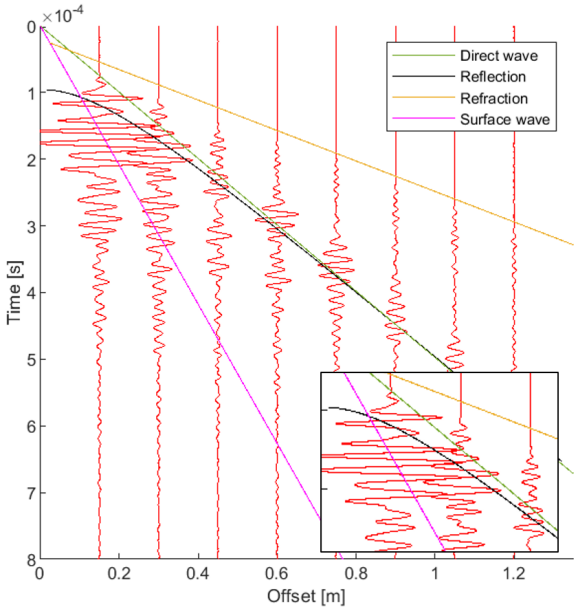

(b) The picked concrete thickness is 0.203 m corresponds to a diameter of 0.451 m.

Figure 9-8: Beemster data of shot 34 pile 3, including the picked arrivals of the surface, direct, refracted and reflected wave. In lower right corner enlargement of first three traces.

Chapter 10

Conclusions

This thesis has tested and evaluated the data of the Seismic Tube, a device developed by Deltares to determine the radius of in-situ formed foundation piles. To test the Seismic Tube 20 foundation piles with artificial defects, as bulging, necking and fracturing were created in a test site. Six of these piles were pulled out the ground for visual inspection after measurements were concluded.

Waves present in the foundation piles are the direct wave, a refracted wave from the PVC pipe - concrete interface, reflected waves from the concrete - soil boundary and a Tube wave. From surface wave inversion results it can be concluded MASW is not a feasible method for determination of the diameter of the foundation piles.

From the reflection arrival the thickness of the concrete could be determined and profiles of the foundation piles were made. This wave interferes with the Tube and direct wave, but has distinctive patterns which show the arrival of the reflected wave.

Analysing the wave arrivals has shown that interpretation is very important and showed that the picking of these arrivals results in the biggest error. The Seismic Tube itself has a center frequency of 62.2 KHz, thus a radial resolution of 1.73 cm. Important to take in account is thus that the results can vary about 2 cm in radius. The results of the Seismic Tube can be used to indicate there is a defect present opposed to determination of the real size of the defect.

From the diameter profiles of the piles can be concluded that it is important to take enough measurement points to obtain a accurate profile. Changes in diameter occur within 10 cm and are easily overlooked with a limited number of data points resulting in incorrect profiles. From comparison with the soil conditions at the Deltares test site it can be concluded that the bulging in the piles can be related to soft soils, mostly peat, present in the subsurface. The size of the bulging depends on the thickness (and presence) of this soft layer. Not all of the designed defects in the foundation piles are resolved. The designed necks were seen in the data, but the length of the Seismic Tube prevented detection of the deeper parts of the foundation piles. The designed bulges are either overlooked by limited number of data points, not formed or created at a too large depth. The diameter changes can be determined quite

well using the data of the Seismic Tube, however the fractures designed do not give a clear and characteristic responds.

The application for square piles will be more difficult as it is difficult to pick the correct arrival without any foreknowledge. The size of a pile is easy to determine as the top is at the surface, thus it can be used. However all square pile are pre-fabricated and can be visually checked before installation. The Seismic Tube is therefore not of added value for hammered piles.

It can be concluded that the data acquired by the Seismic Tube can be to determine the diameter and find defects such as necking and bulges in in-situ formed foundation piles.

Chapter 11

Recommendations

While it is possible to resolve the diameter of a foundation pile using the Seismic Tube further research should be done. First of all it would be recommended to measures the signal generated by the source. It will give insight in the signal sent and can be used to improve the acquired data.

Surface wave inversion with MASW proved incapable for concrete thickness determination. Nevertheless surface waves can provide shear parameters of the concrete and can be used to determine concrete quality. Further research into surface waves is therefor recommended.

The bottom part of the foundation piles were not measured because the length of the Seismic Tube. With placing the source at the bottom of the Tube, it is possible to measure the bottom part of the foundation pile. The has as consequence that the top 2 meters are not fully measured, but this part can either be excavated to check or measured with limited number of receivers if the design will be adjusted.

It is recommended in further research to keep a small measurement interval, as shown is that certain defects are overlooked. It would also be advisable to investigate the possibilities of other frequency ranges to improve the resolution.

Bibliography

[Alsadi, 2017] Alsadi, H. N. (2017). Seismic waves. In *Seismic Hydrocarbon Exploration*, pages 23–51. Springer.

[Borcherdt, 1994] Borcherdt, R. D. (1994). *The Loma Prieta, California, Earthquake of October 17, 1989: Strong Ground Motion*. US Government Printing Office Washington, DC.

[Bormann et al., 2009] Bormann, P., Engdahl, B., and Kind, R. (2009). Seismic Wave Propagation and Earth models. In Bormann, P., editor, *New Manual of Seismological Observatory Practice (NMSOP)*, pages 1 – 70. Deutsches GeoForschungsZentrum GFZ, Potsdam.

[Caldern-Macas and Luke, 2007] Caldern-Macas, C. and Luke, B. (2007). Improved parameterization to invert rayleigh-wave data for shallow profiles containing stiff inclusions. *GEOPHYSICS*, 72(1):U1–U10.

[Castellaro, 2016] Castellaro, S. (2016). The complementarity of h/v and dispersion curves. *GEOPHYSICS*, 81(6):T323–T338.

[Chan, 1987] Chan, H.-F. C. (1987). Non-destructive testing of concrete piles using the sonic echo and transient shock methods.

[Chapman, 2004] Chapman, C. (2004). *Fundamentals of seismic wave propagation*. Cambridge university press.

[Chapman et al., 2014] Chapman, C. H., Hobro, J. W. D., and Robertsson, J. O. A. (2014). Correcting an acoustic wavefield for elastic effects. *Geophysical Journal International*, 197(2):1196–1214.

[Chua, 2011] Chua, T. S. (2011). Supervision of piling works, aces, 2011, singapore. Retrieved from https://www.slideshare.net/TongSengChua/supervision-of-piling-works-aces-2011-singapore. Visited on 10.04.2019.

[Close et al., 2009] Close, D., Cho, D., Horn, F., and Edmundson, H. (2009). The sound of sonic: A historical perspective and introduction to acoustic logging. *CSEG Recorder*, 34(5):34–43.

[Crow, 2015] Crow (2015). Polymer properties database. Retrieved fro-murl=http://polymerdatabase.com/polymer physics/Poisson Table2.html. Visited on 20.06.2019.

[Dakota Ultrasonics, 2016] Dakota Ultrasonics (2016). Dakota ultrasonics sound solutions, references: Appenic a velocity table. Retrieved from https://dakotaultrasonics.com/reference/. Visited on 03.04.2019.

[Drijkoningen, 2014] Drijkoningen, G. (2014). Lecture notes of introduction to reflection seismology AESB2140 (B.Sc. Applied Earth Sciences). TU Delft.

[Duputel et al., 2010] Duputel, Z., Cara, M., Rivera, L., and Herquel, G. (2010). Improving the analysis and inversion of multimode rayleigh-wave dispersion by using group-delay time information observed on arrays of high-frequency sensors. *GEOPHYSICS*, 75(2):R13–R20.

[Ghose, 2018] Ghose, R. (2017-2018). Lecture notes of seismic resolution AES1590 (M.Sc. Applied Geophysics). TU Delft.

[Haldorsen et al., 2006] Haldorsen, J. B., Johnson, D. L., Plona, T., Sihna, B., Valero, H.-P., and Winkler, K. (2006). Borehole acoustic waves. *Oilfield Review*, pages 34–43.

[Henriet et al., 1983] Henriet, J., Schittekat, J., et al. (1983). Borehole seismic profiling and tube wave applications in a dam site investigation. *Geophysical Prospecting*, 31(1):72–86.

[Hölscher, 2019] Hölscher, P. (2019). Seismische controle funderingspalentestveld van 't hek vierkante palen nadere analyses. Deltares.

[Hopman, 2016] Hopman, V. (2016). Opzet testlocatie voor in de grond gevormde palen installatie meetfaciliteit defecte palen. Deltares.

[Hopman and Hölscher, 2015] Hopman, V. and Hölscher, P. (2015). Non-destructive quality check on cast in-situ piles. Deltares.

[Huang and Ni, 2012] Huang, Y.-H. and Ni, S.-H. (2012). Experimental study for the evaluation of stress wave approaches on a group pile foundation. *NDT & E International*, 47:134–143.

[Ikeda et al., 2015] Ikeda, T., Matsuoka, T., Tsuji, T., and Nakayama, T. (2015). Characteristics of the horizontal component of rayleigh waves in multimode analysis of surface waves. *GEOPHYSICS*, 80(1):EN1–EN11.

[Ionov, 2018] Ionov, A. M. (2018). Analytical expressions for the borehole seismic signatures excited by an explosive source buried in an elastic half-space. *Geophysical Prospecting*, 66(S1):161–174.

[Khojasteh et al., 2015] Khojasteh, A., Bagheri, A., Rahimian, M., and Greenhalgh, S. (2015). Dispersion of Rayleigh, Scholte, Stoneley and Love waves in a model consisting of a liquid layer overlying a two-layer transversely isotropic solid medium. *Geophysical Journal International*, 203(1):195–212.

[Liao et al., 2006] Liao, S.-T., Tong, J.-H., Chen, C.-H., and Wu, T.-T. (2006). Numerical simulation and experimental study of parallel seismic test for piles. *International Journal of Solids and Structures*, 43(7):2279 – 2298.

[Margrave and Hall, 1991] Margrave, G. F. and Hall, K. W. (1991). Crewes matlab toolbox. https://www.crewes.org/ResearchLinks/FreeSoftware/.

[Meegan et al., 1999] Meegan, G., Hamilton, M., Ilinskii, Y. A., and Zabolotskaya, E. (1999). Nonlinear stoneley and scholte waves. *The Journal of the Acoustical Society of America*, 106(4):1712–1723.

[Mishra, 2018] Mishra, S. (2018). Which seismic wave is the most dangerous? why? Retrieved from https://www.quora.com/Which-seismic-wave-is-the-most-dangerous-Why. Visited on 19.03.2019.

[Morozov, 2016] Morozov, I. (2016). Lecture notes GEOL 335.3, university of saskatchewan: Seismic attenuation. Retrieved from seisweb.usask.ca/classes/GEOL335/2016/Lectures/PDF/13-Attenuation.pdf. Visited on 15.05.2019.

[Nave, 2016] Nave, R. (2016). Huygens' principle. Retrieved from hyperphysics.phy-astr.gsu.edu/hbase/phyopt/huygen.html. Visited on 20.03.2019.

[Omnexus, nd] Omnexus (n.d.). Density of plastics: Technical properties. Retrieved from https://omnexus.specialchem.com/polymer-properties/properties/densityPS-X. Visited on 01.05.2019.

[ONeill, 1991] ONeill, M. W. (1991). Construction practices and defects in drilled shafts. *Transportation Research Record*, 1331:6–14.

[Park et al., 1999] Park, C. B., Miller, R. D., and Xia, J. (1999). Multichannel analysis of surface waves. *GEOPHYSICS*, 64(3):800–808.

[ParkSeis, nd] ParkSeis (n.d.). Multichannel analysis of surface waves (masw). Retrieved from http://www.masw.com/Advantages.html. Visited on 05.04.2019.

[Polytron Kunststoffentechnik, 2016] Polytron Kunststoffentechnik (2016). Material properties sound transmitting plastics. Retrieved from https://epda.com/wp-content/uploads/2016/07/Fred-Busen.pdf. Visited on 29.03.2019.

[Rawlinson, nd] Rawlinson, N. (n.d.). Surface waves and dispersion. Retrieved from http://rses.anu.edu.au/~nick/teachdoc/lecture5.pdf. Visited on 29.03.2019.

[Sambridge, 1999] Sambridge, M. (1999). Geophysical inversion with a neighbourhood algorithmI. Searching a parameter space. *Geophysical Journal International*, 138(2):479–494.

[Schlumberger, 2019] Schlumberger (2019). The oilfield glossary: Where the oil field meets the dictionary. Retrieved from https://www.glossary.oilfield.slb.com/. Visited on 20.03.2019.

[Society of Petroleum Engineers, 2015] Society of Petroleum Engineers (2015). Petrowiki: Compressional and shear velocities. Retrieved from https://petrowiki.org/Compressional_and_shear_velocities. Visited on 28.03.2019.

[van t'Hek, 2019] van t'Hek (2019). Hekpile. Retrieved from https://www.vanthek.com/techniques/hekpile. Visited on 11.03.2019.

[Wakil and Kassim, 2010] Wakil, A. Z. E. and Kassim, M. (2010). Bulging as a pile imperfection. *Alexandria Engineering Journal*, 49(4):387 – 391.

[Wapenaar and Berkhout, 1989] Wapenaar, C. and Berkhout, A. (1989). *Elastic wave field extrapolation redatuming of single- and multi-component seismic data*. Elsevier.

[Wuenschel, 1965] Wuenschel, P. C. (1965). Dispersive body waves; an experimental study. *Geophysics*, 30(4):539–551.

[Yao et al., 1999] Yao, Z., Margrave, G. F., and Gallant, E. V. (1999). Optimal time-delay spiking deconvolution and its application in the physical model measurement. Technical report, CREWES Research Report.

[Yilmaz, 2001] Yilmaz, Ö. (2001). *Seismic data analysis: Processing, inversion, and interpretation of seismic data*. Society of exploration geophysicists.

Appendix A

Visual Inspection Foundation Piles

This appendix shows some photo's of pile 1, 6, 7, 8, 13 and 17. These six piles were extracted from the ground for visual inspection. The photo's document defects found.

Figure A-1: Photos of diameter changes in pile 6.

Figure A-2: Photos of diameter changes in pile 7.

Figure A-3: Photos of diameter changes in pile 8.

Figure A-4: Photos of diameter changes in pile 13.

Figure A-5: Photo of a created neck on pile 17 and slight bulging with part of a measuring tape. Orange marks indicate the measurement location of the seismic tube.

Appendix B

Interpretation Variability

To illustrate the importance of interpretation a shot at 2.34 m depth of pile 4 is chosen to visualize the range of possible picks for the thickness. In figures B-1 to B-4 the data and possible interpretation of the reflected wave are shown. In figure B-1 and B-3 a concrete thickness of 0.20 m is used. The theoretical calculated arrival is now at the early end of the interference patterns characteristic for the reflection. In figure B-2 and B-4 a concrete thickness of 0.222 m is used. The arrival in these figure is at the lower end of the interference patterns characteristic for the reflection. Any value between these could be interpreted as possible thickness for the concrete layer, with the best fit when the arrival crosses the zero axis of the trace at the time when the negative wiggle of the interference pattern is present. This is visualized in figure B-5. This final pick visualized in figure B-5 has a concrete thickness of 0.21 m. The interpretation thus has a variability of plus or minus 1 cm of the picked pile radius.

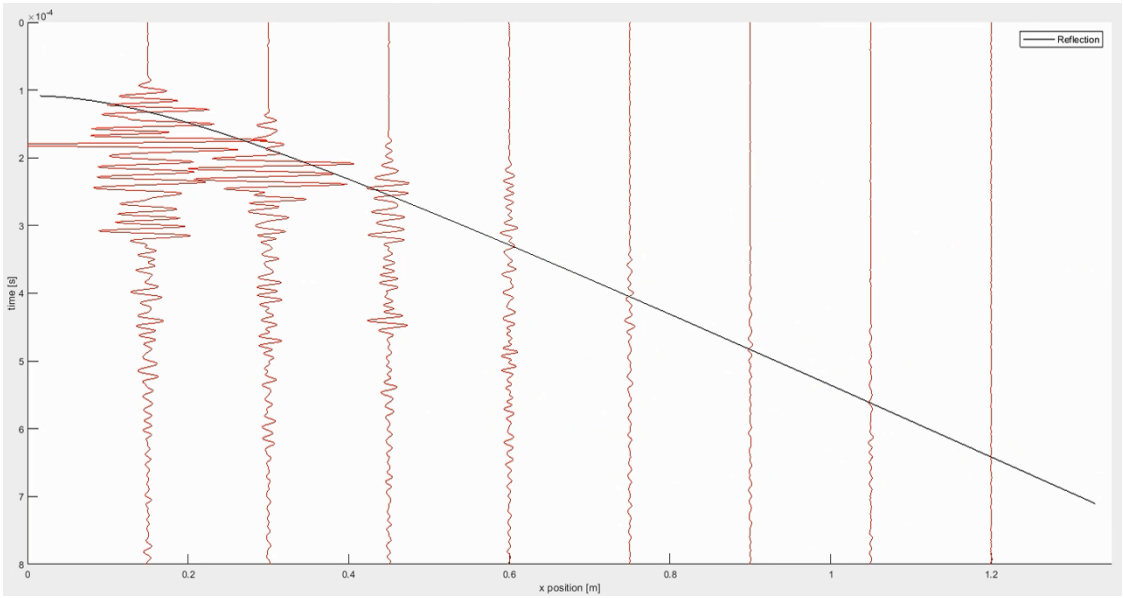

Figure B-1: Seismogram of shot 2 of pile 4. Source at 2.34 m depth. Reflection calculated using a concrete thickness of 0.20 m, thus when no defect would be present and velocity of 3890 m/s.

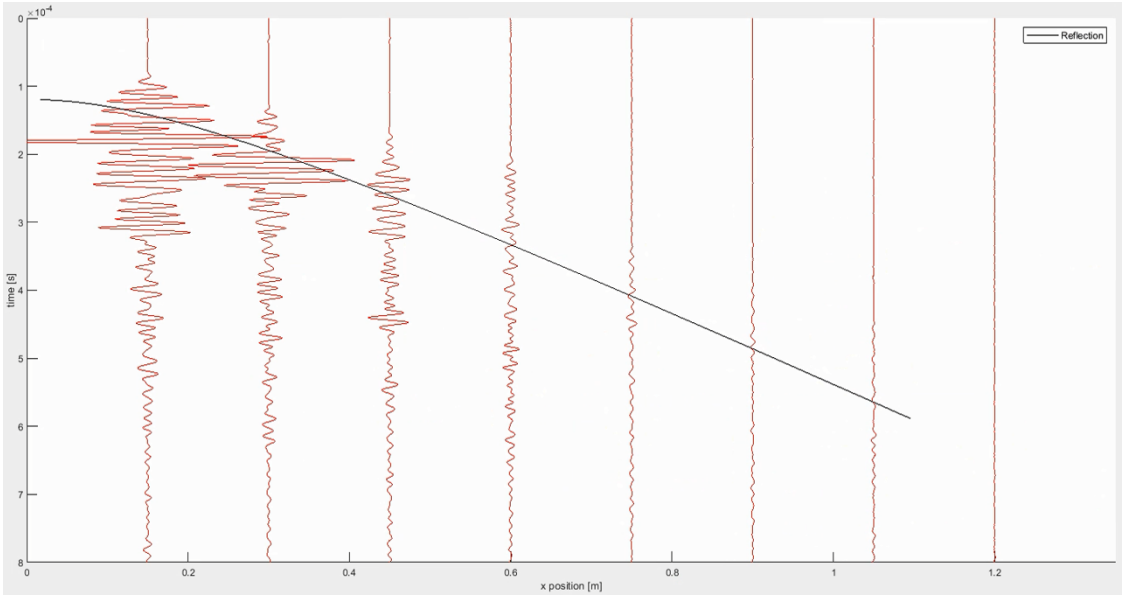

Figure B-2: Seismogram of shot 2 of pile 4. Source at 2.34 m depth. Reflection calculated using a concrete thickness of 0.222 m and velocity of 3890 m/s.

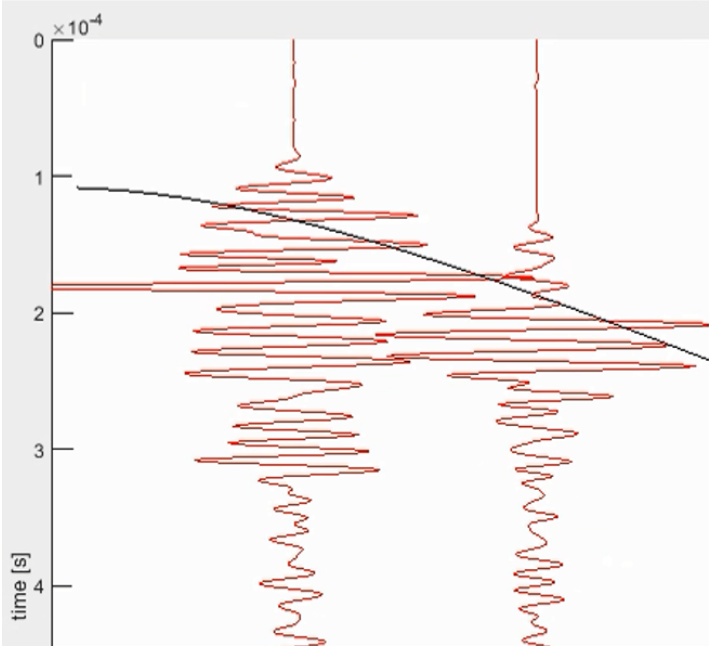

Figure B-3: Enlarged part of seismogram of shot 2 of pile 4. Source at 2.34 m depth. Reflection calculated using a concrete thickness of 0.20 m, thus when no defect would be present and velocity of 3890 m/s. Shown are the recorded data of receiver 1 and 2 at an offset of 0.15 m and 0.30 m from the source.

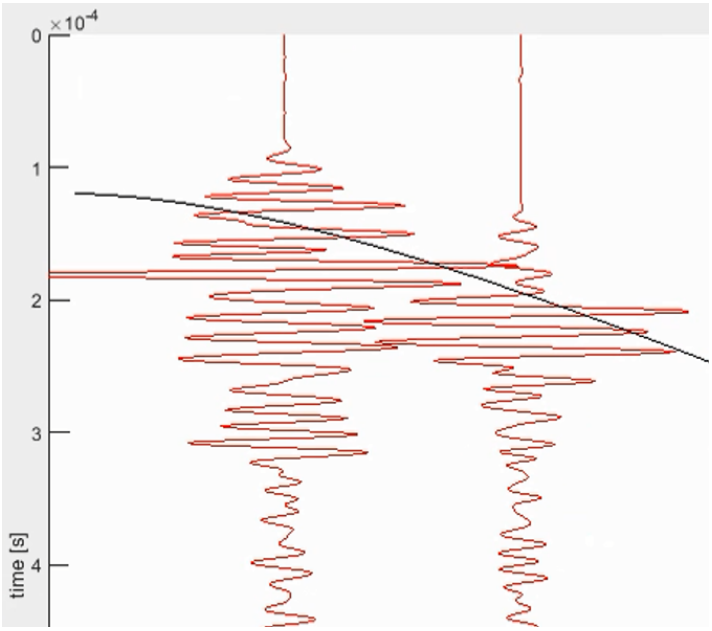

Figure B-4: Enlarged part of seismogram of seismogram of shot 2 of pile 4. Source at 2.34 m depth. Reflection calculated using a concrete thickness of 0.222 m and velocity of 3890 m/s. Shown are the recorded data of receiver 1 and 2 at an offset of 0.15 m and 0.30 m from the source.

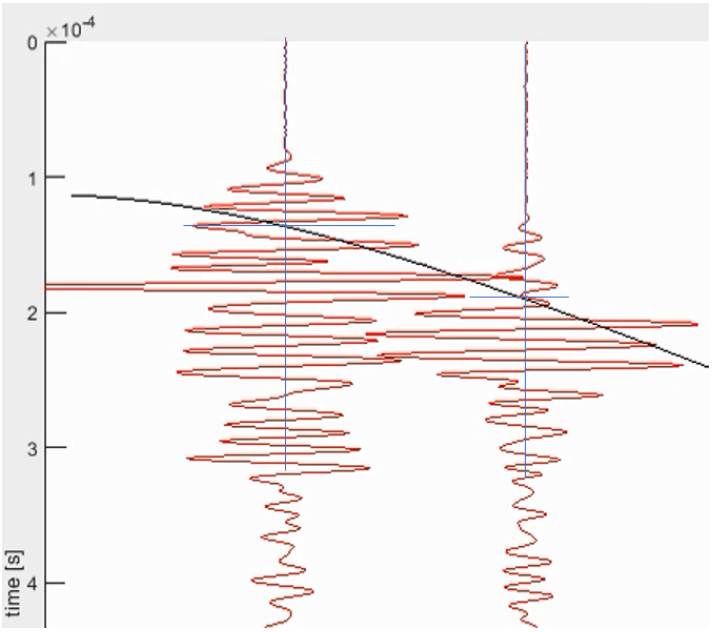

Figure B-5: Enlarged part of seismogram of seismogram of shot 2 of pile 4. Source at 2.34 m depth. Reflection calculated using a concrete thickness of 0.21 m and velocity of 3890 m/s. Shown are the recorded data of receiver 1 and 2 at an offset of 0.15 m and 0.30 m from the source and lines indicating the zero of the trace and the peak part of the wiggle.

Appendix C

Results Deltares Data

This appendix shows all the seismograms of foundation pile 13 as representative pile for all 20 piles at the Deltares test site

C-1 Data foundation piles Deltares test site

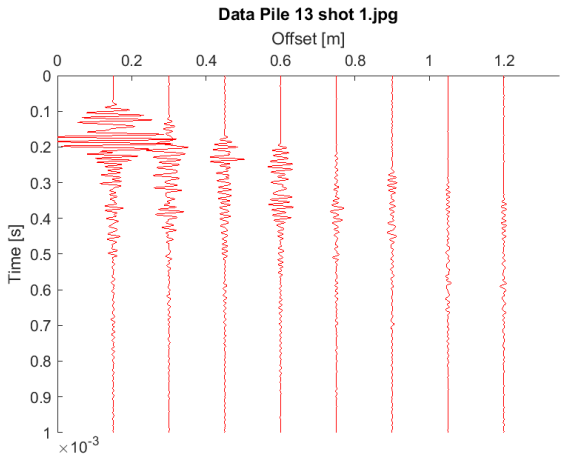

(a) Shot 1 at 1.36 m depth

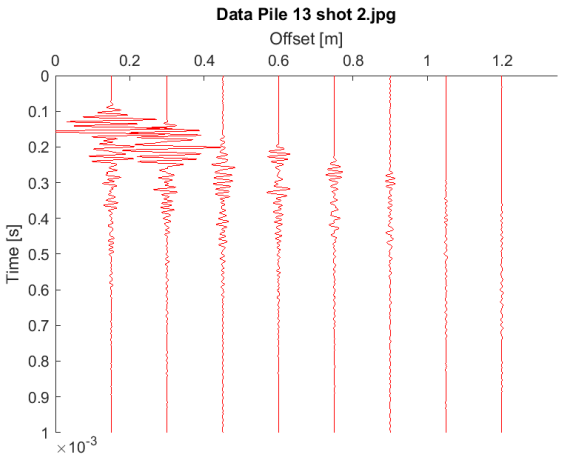

(b) Shot 2 at 2.04 m depth

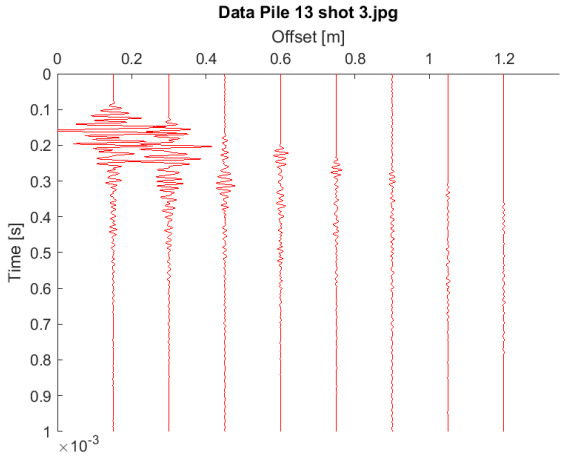

(c) Shot 3 at 2.72 m depth

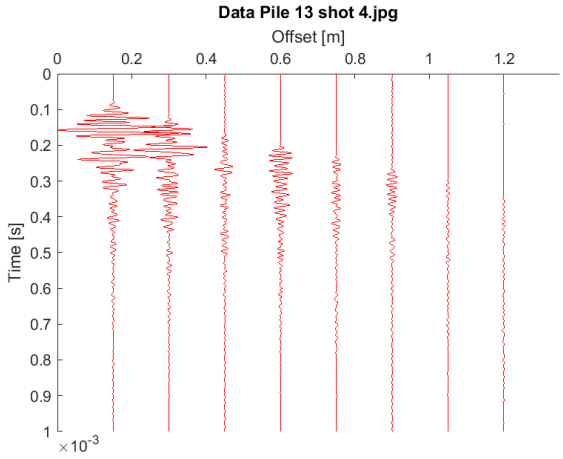

(d) Shot 4 at 3.4 m depth

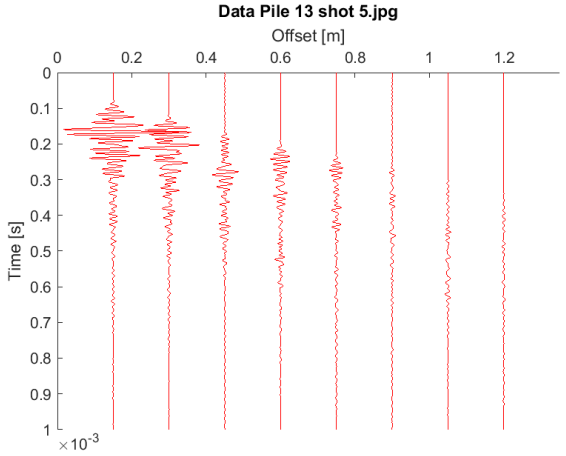

(e) Shot 5 at 4.08 m depth

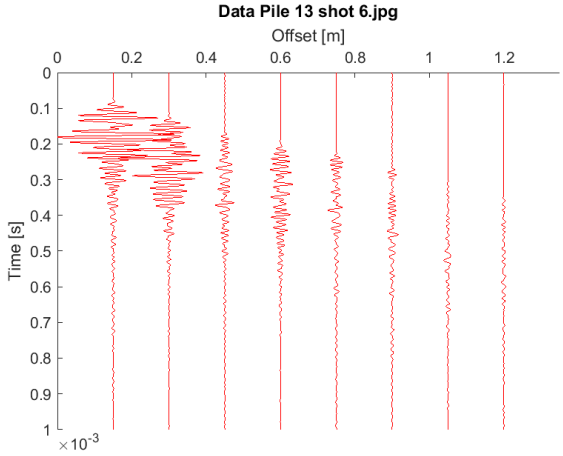

(f) Shot 6 at 4.76 m depth

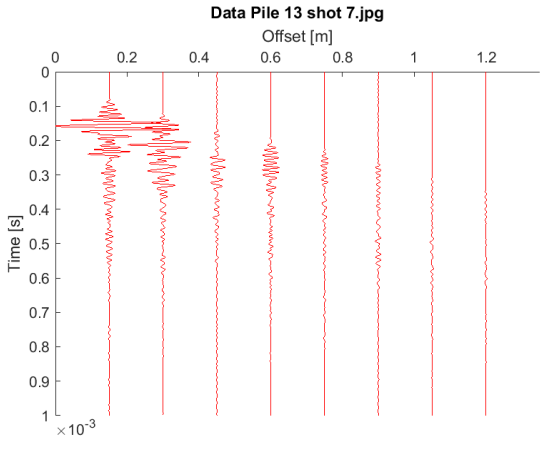

(g) Shot 7 at 5.44 m depth

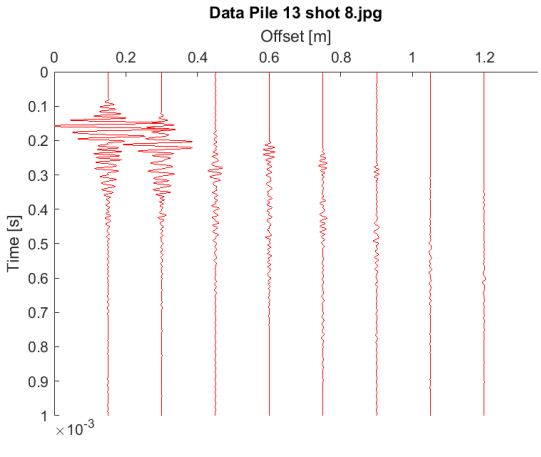

(h) Shot 8 at 6.12 m depth

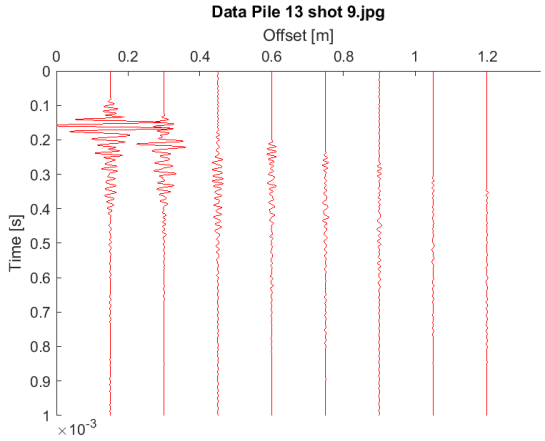

(i) Shot 9 at 6.8 m depth

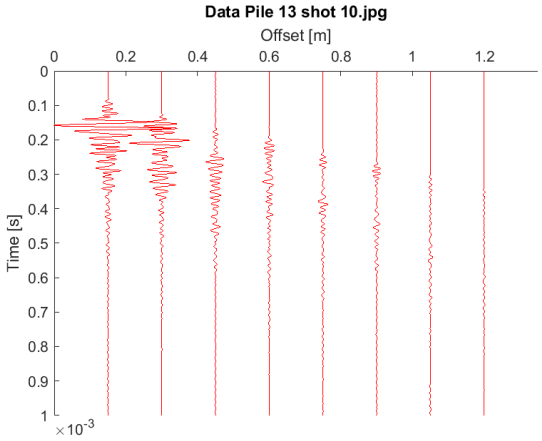

(j) Shot 10 at 7.48 m depth

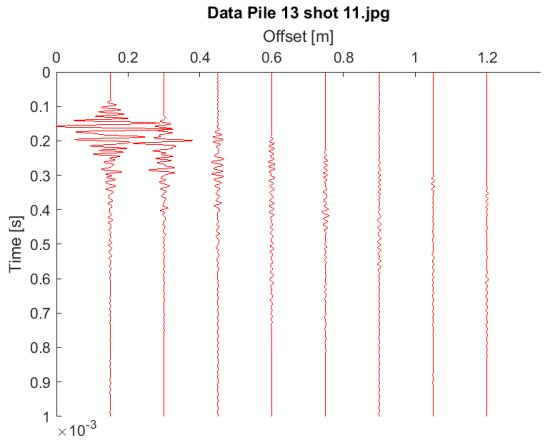

(k) Shot 11 at 7.82 m depth

Figure C-1: Seismograms of eleven shots at different heights measured at pile 13 of the Deltares test site

C-2 Frequency Spectrum

This appendix shows the frequency spectrum of all shots of pile 13 at the Deltares test site.

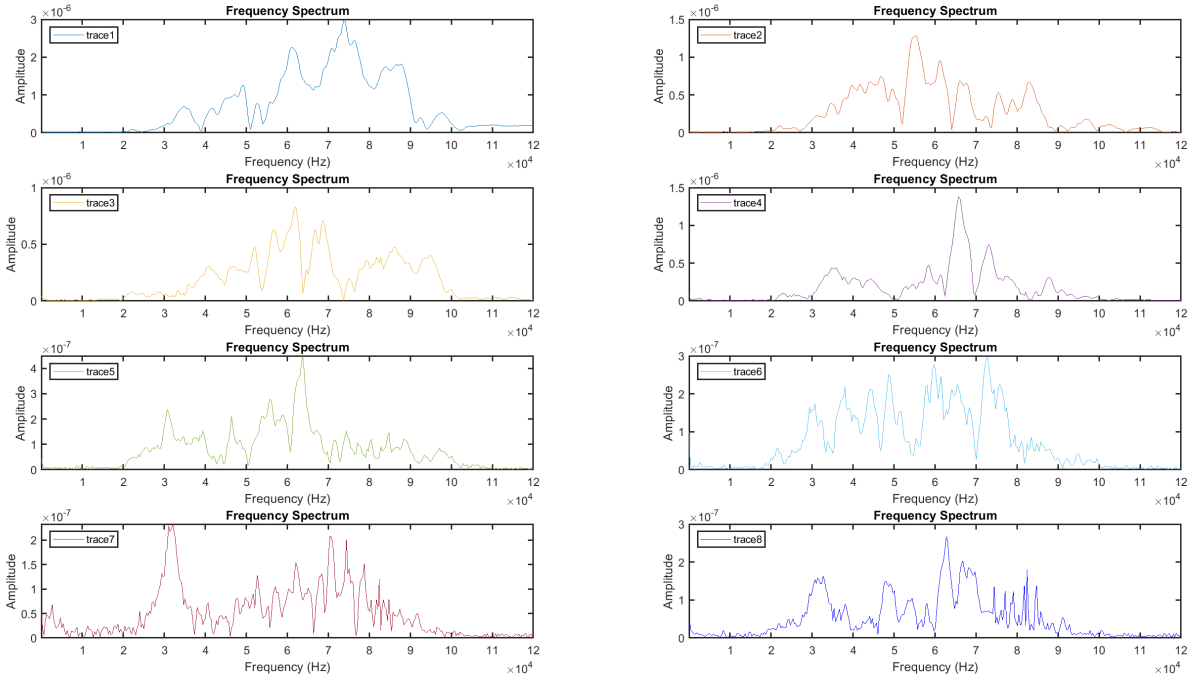

Figure C-2: Frequency spectrum of pile 13 shot 1 of Deltares test site.

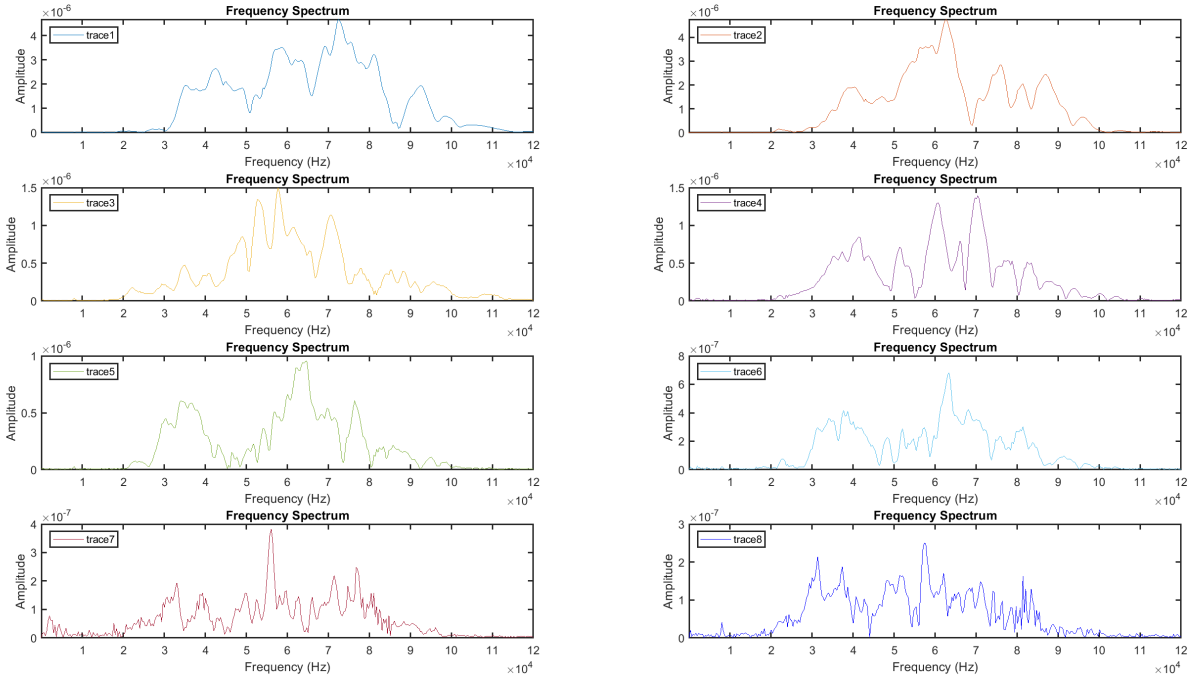

Figure C-3: Frequency spectrum of pile 13 shot 2 of Deltares test site.

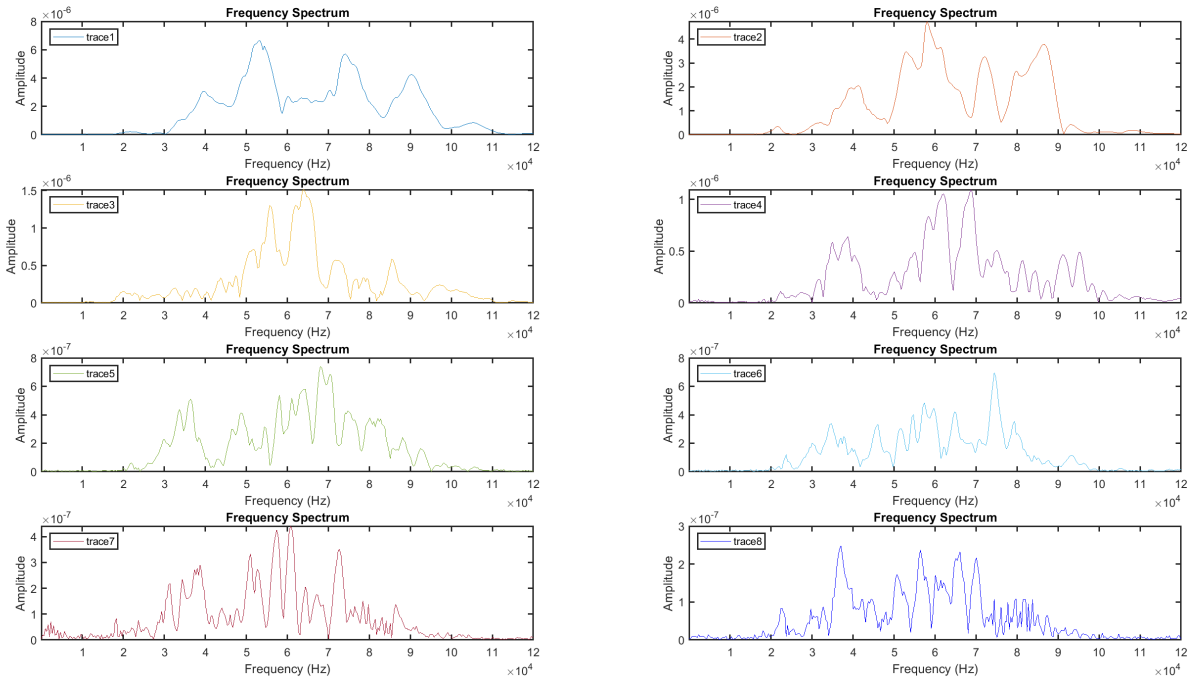

Figure C-4: Frequency spectrum of pile 13 shot 3 of Deltares test site.

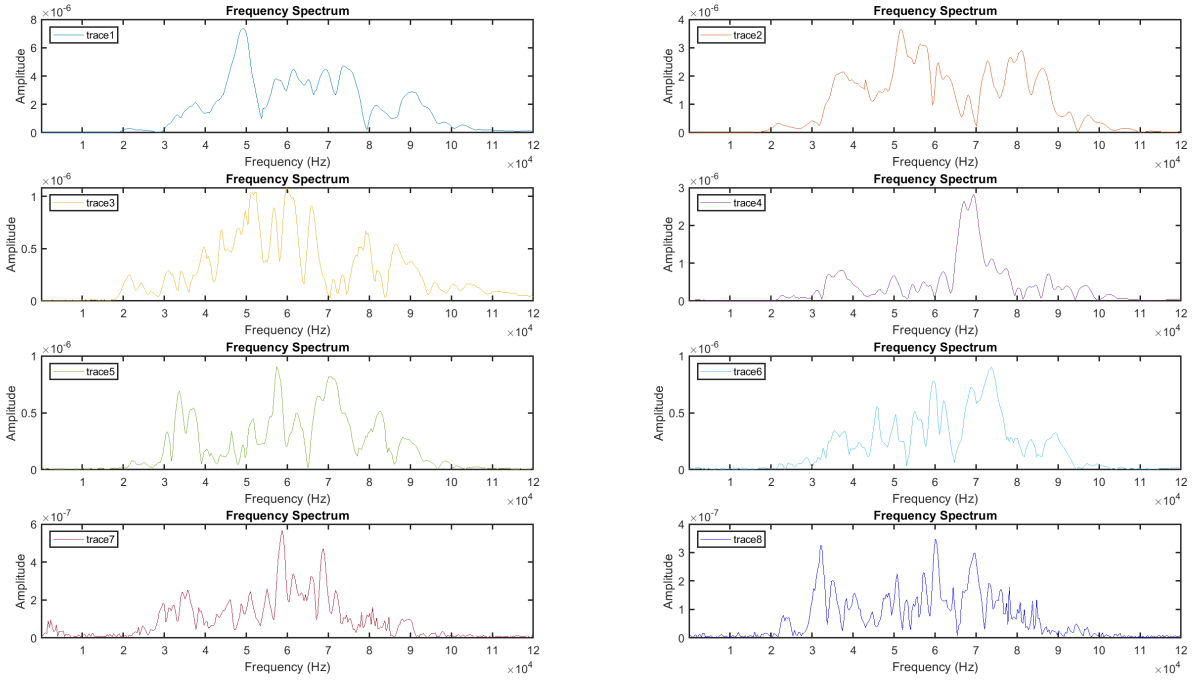

Figure C-5: Frequency spectrum of pile 13 shot 4 of Deltares test site.

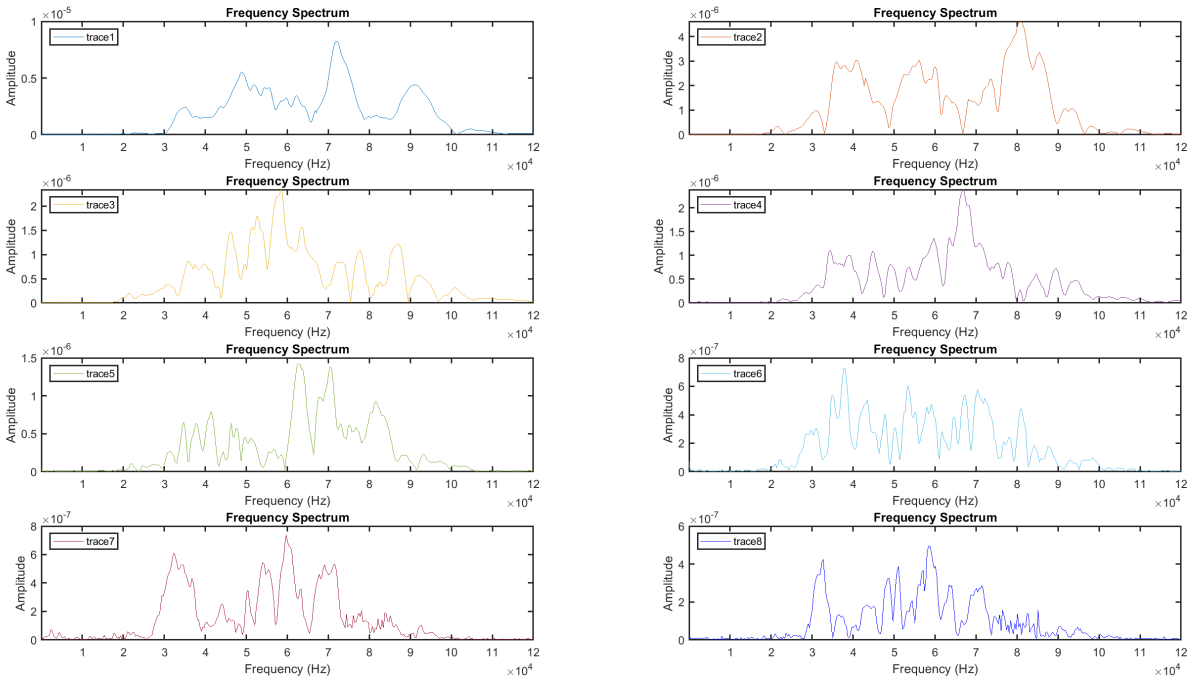

Figure C-6: Frequency spectrum of pile 13 shot 5 of Deltares test site.

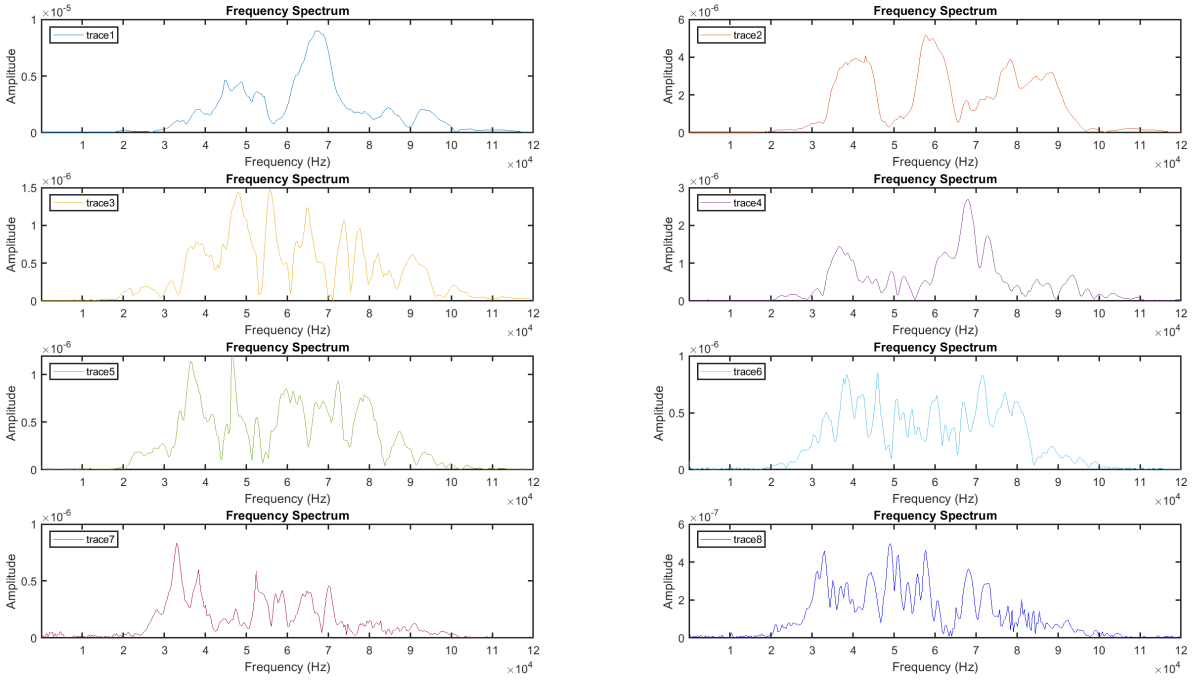

Figure C-7: Frequency spectrum of pile 13 shot 6 of Deltares test site.

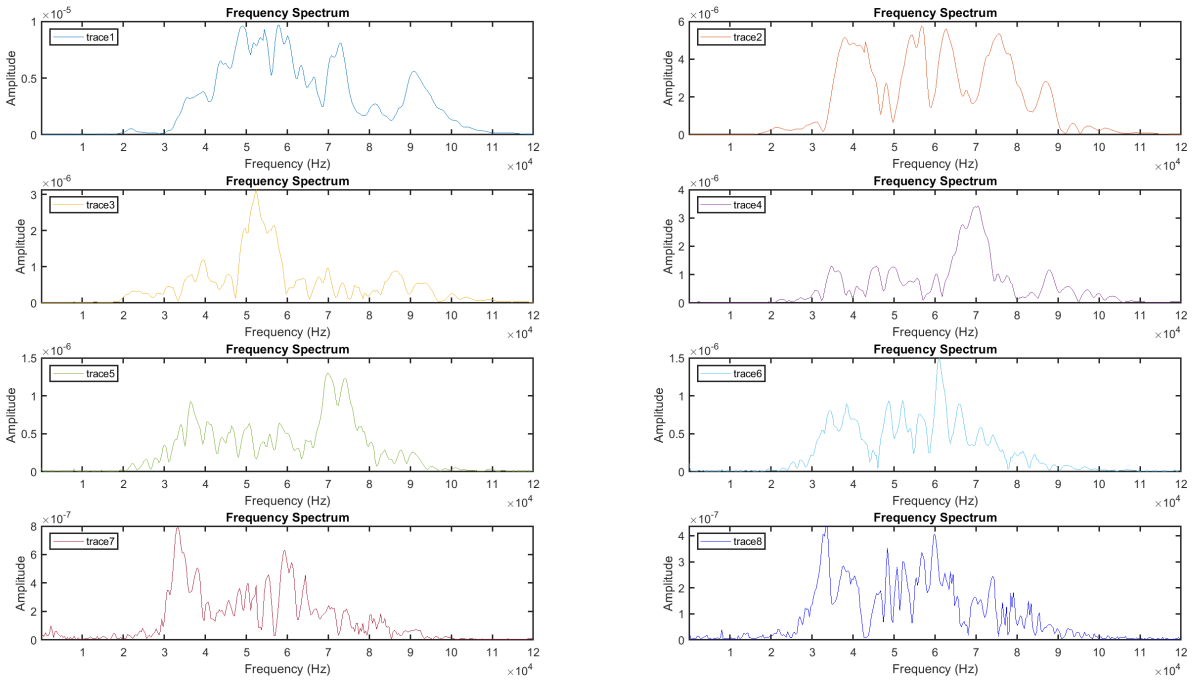

Figure C-8: Frequency spectrum of pile 13 shot 7 of Deltares test site.

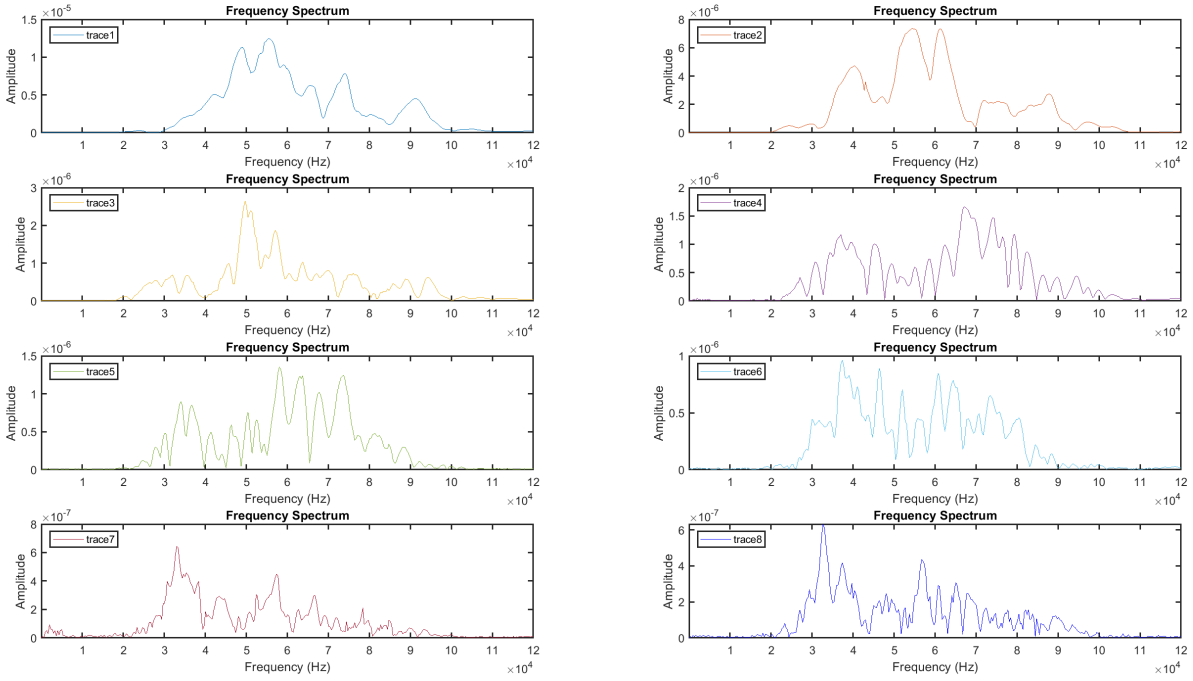

Figure C-9: Frequency spectrum of pile 13 shot 8 of Deltares test site.

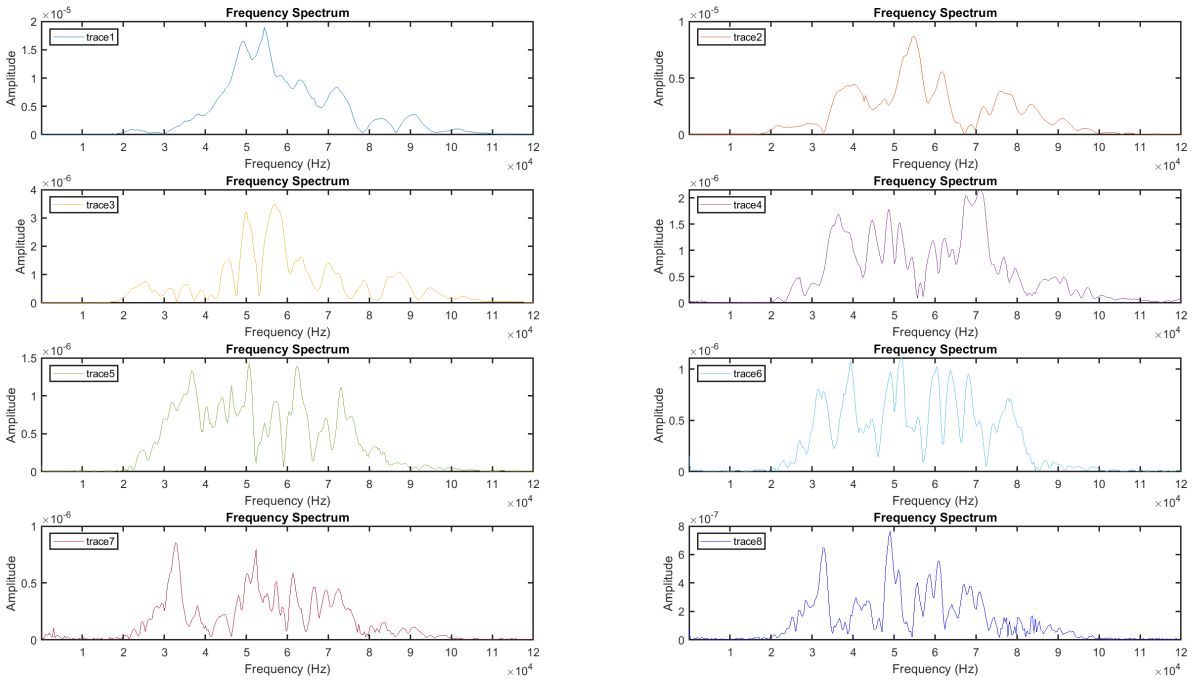

Figure C-10: Frequency spectrum of pile 13 shot 9 of Deltares test site.

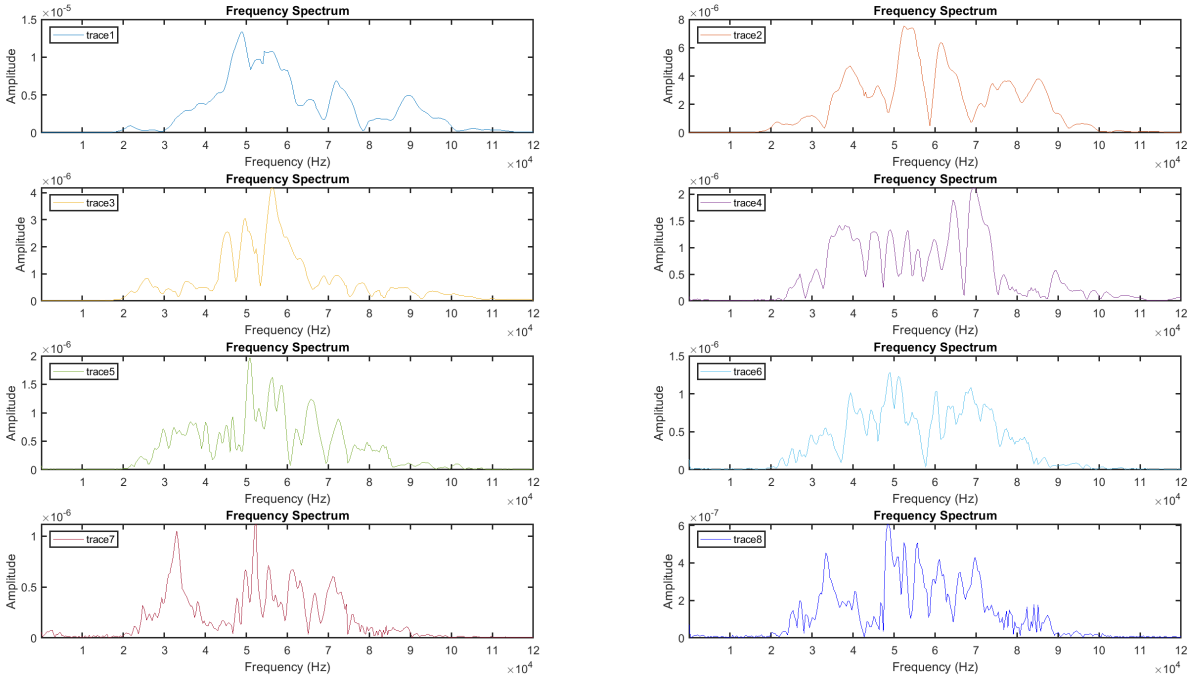

Figure C-11: Frequency spectrum of pile 13 shot 10 of Deltares test site.

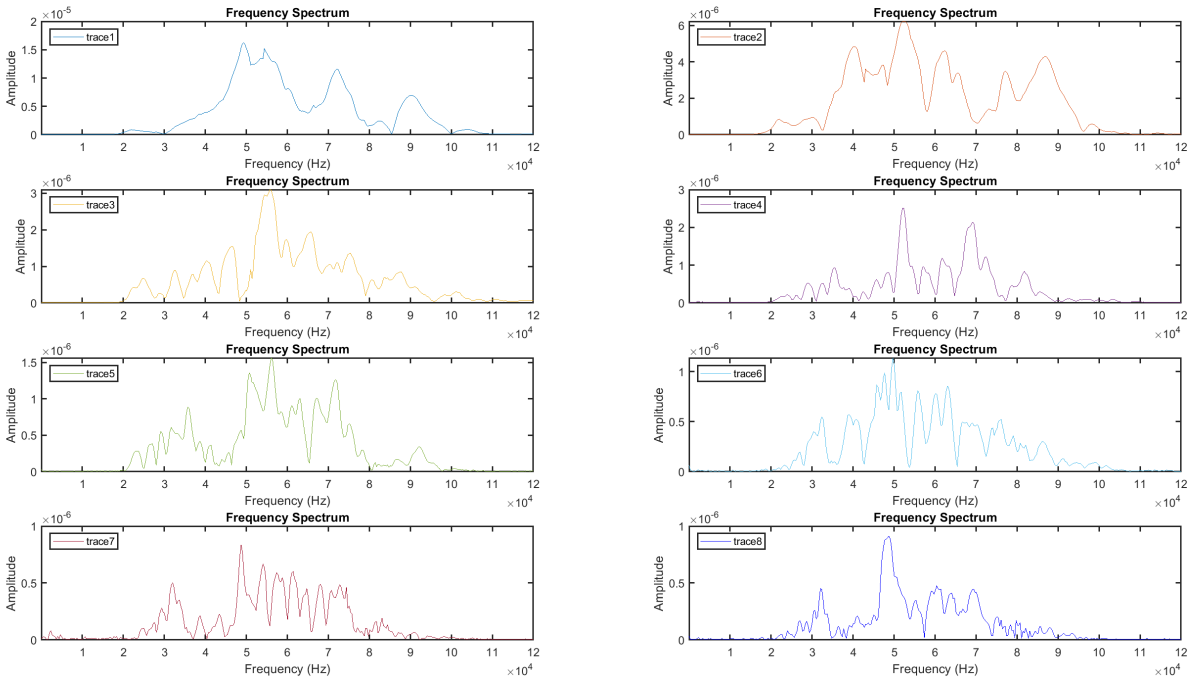

Figure C-12: Frequency spectrum of pile 13 shot 11 of Deltares test site.

C-3 Processed Data

This appendix shows the filtered and deconvolved data of all shots of pile 13 at the Deltares test site. It shows the original data next to the filtered and deconvolved data.

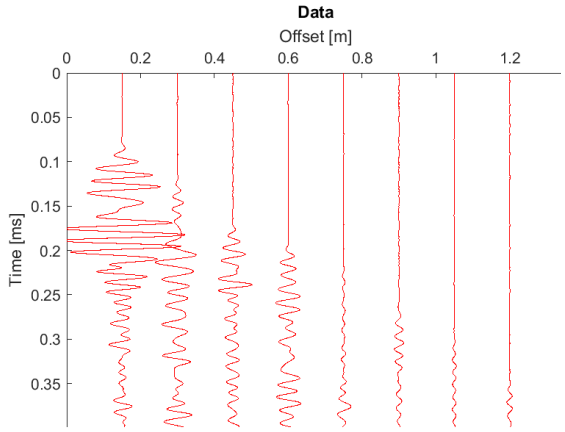

(a) Original Data

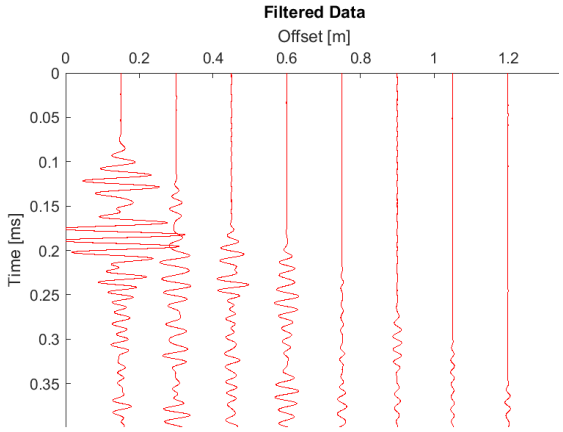

(b) Low-cut Filtered Data

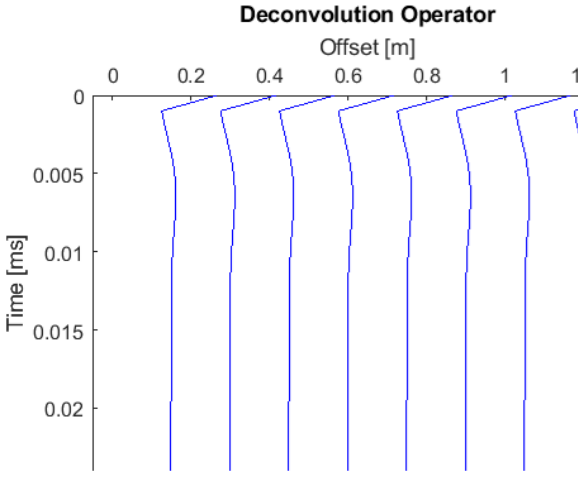

(c) Deconvolution operator

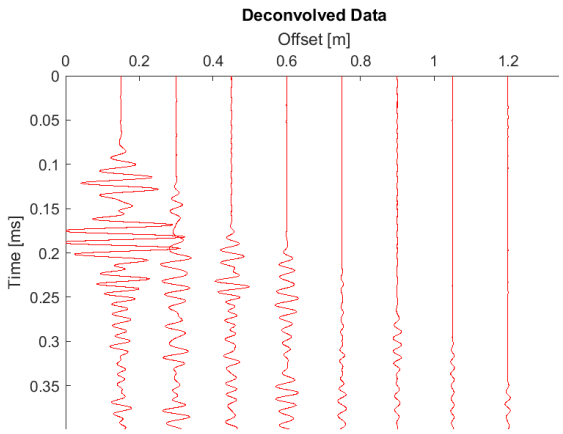

(d) Deconvolved Data

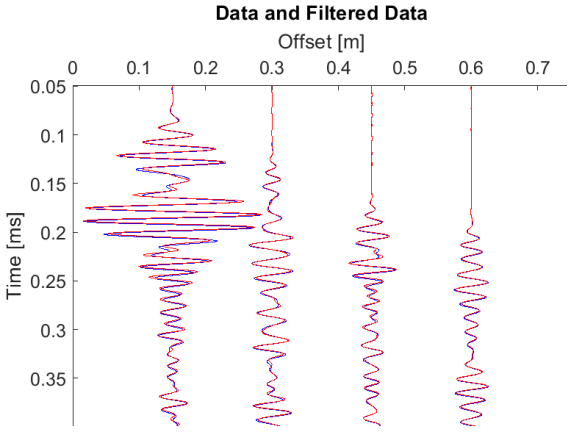

(e) Data in red and Filtered Data in blue

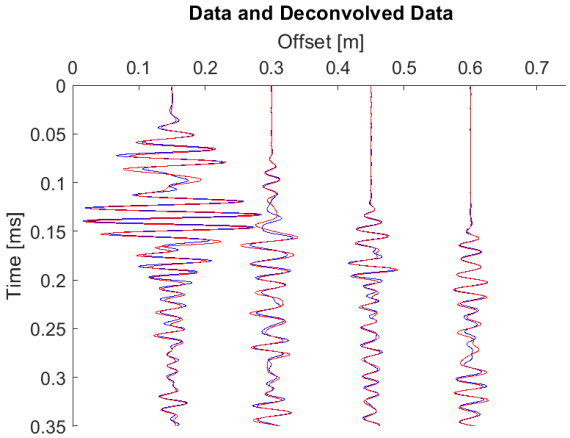

(f) Data in red and Deconvolved Data in blue

Figure C-13: Filtering and Deconvolution results of Pile 13 shot 1 at Deltares test site.

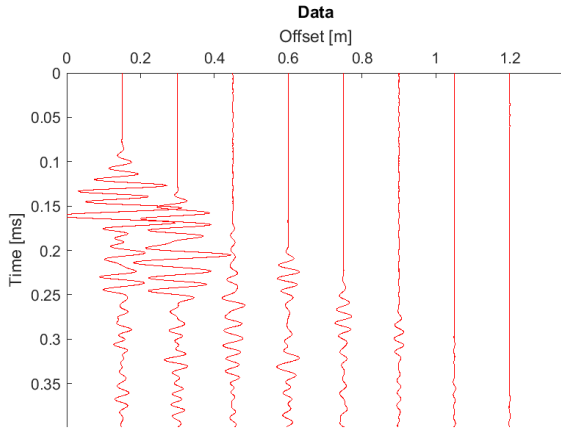

(a) Original Data

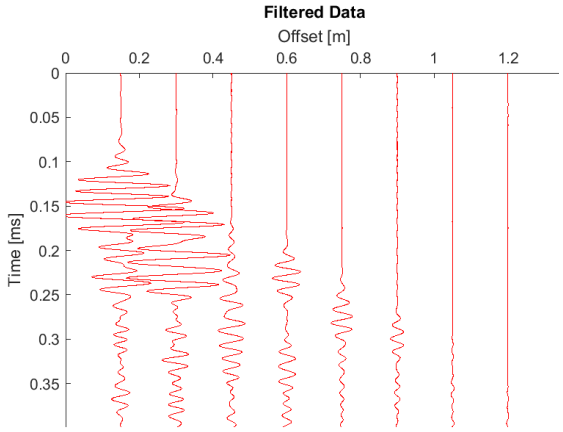

(b) Low-cut Filtered Data

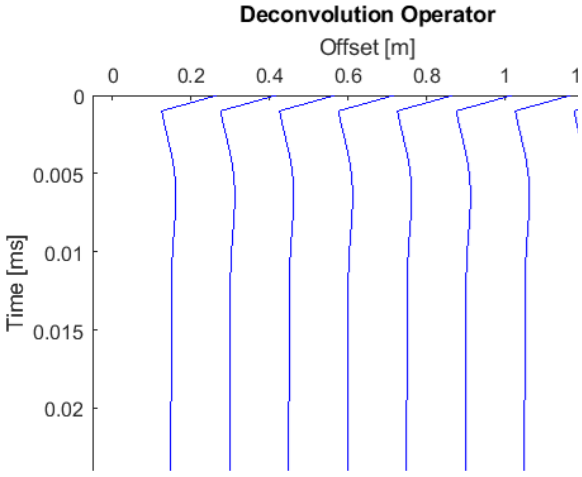

(c) Deconvolution operator

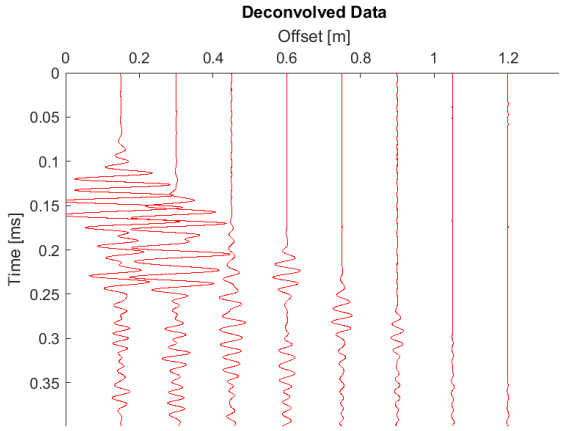

(d) Deconvolved Data

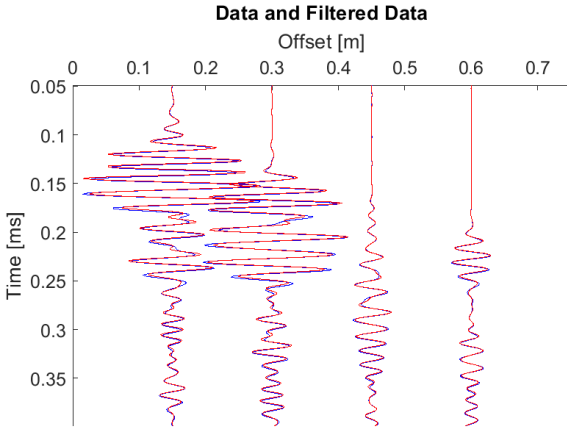

(e) Data in red and Filtered Data in blue

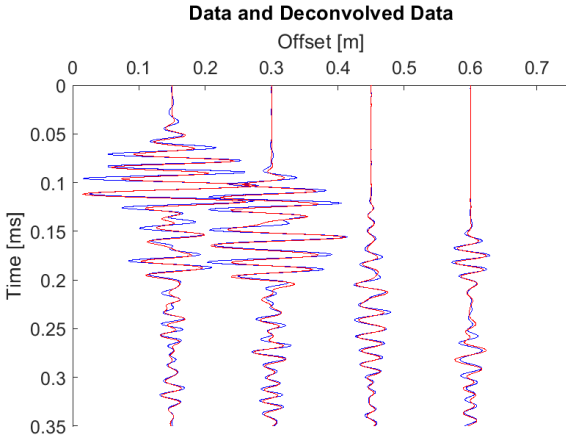

(f) Data in red and Deconvolved Data in blue

Figure C-14: Filtering and Deconvolution results of Pile 13 shot 2 at Deltares test site.

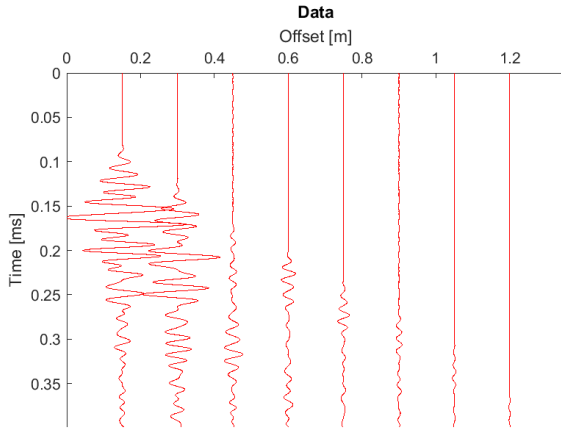

(a) Original Data

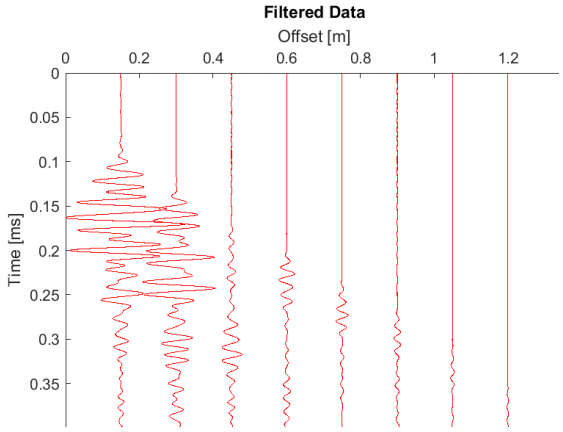

(b) Low-cut Filtered Data

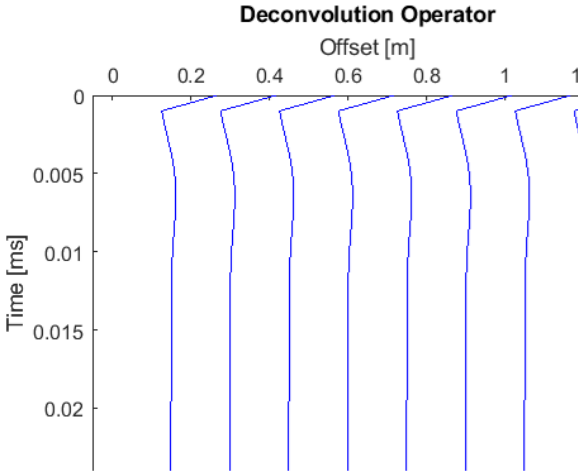

(c) Deconvolution operator

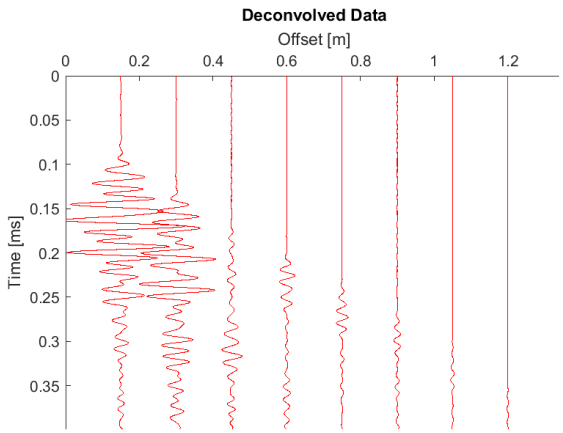

(d) Deconvolved Data

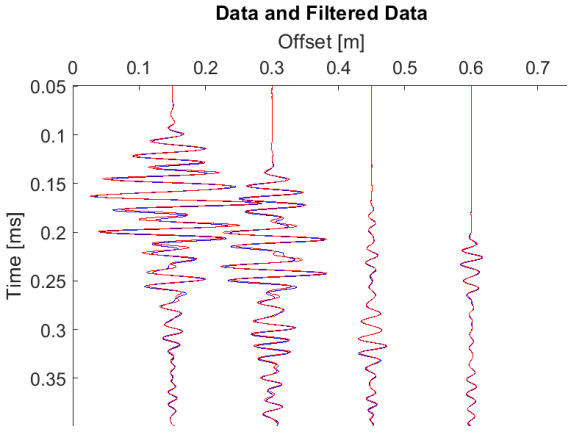

(e) Data in red and Filtered Data in blue

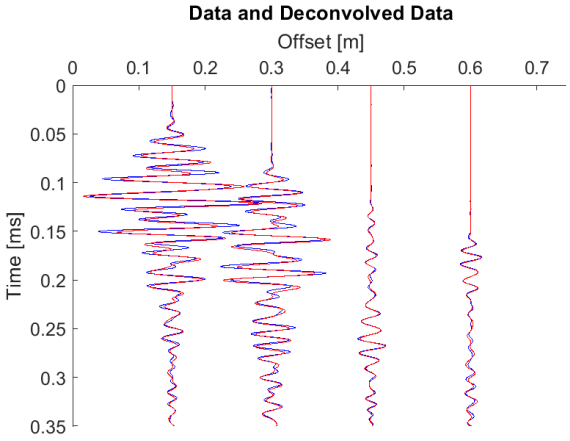

(f) Data in red and Deconvolved Data in blue

Figure C-15: Filtering and Deconvolution results of Pile 13 shot 3 at Deltares test site.

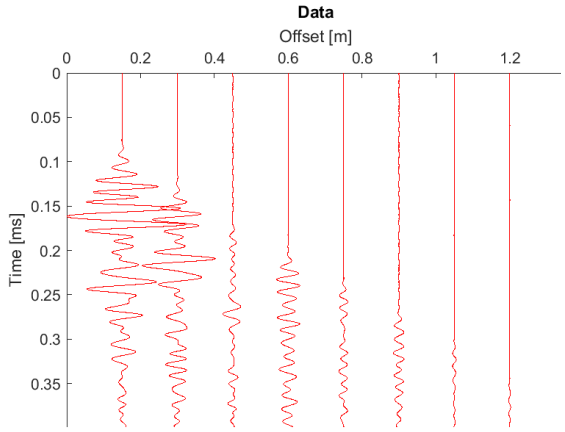

(a) Original Data

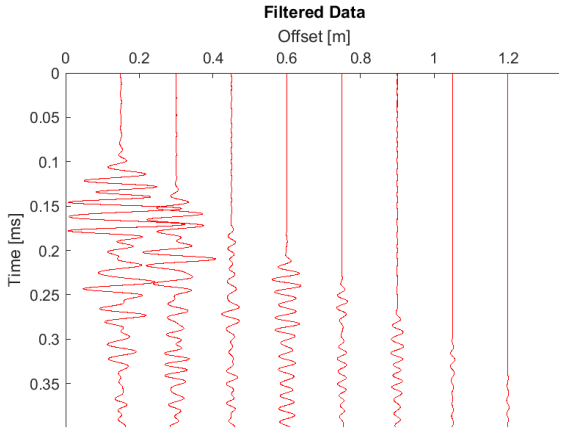

(b) Low-cut Filtered Data

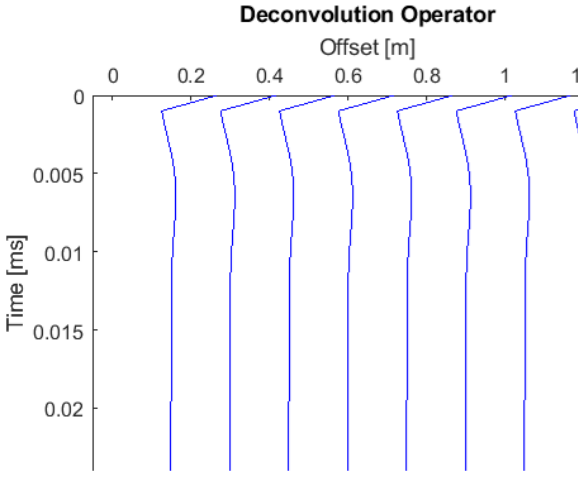

(c) Deconvolution operator

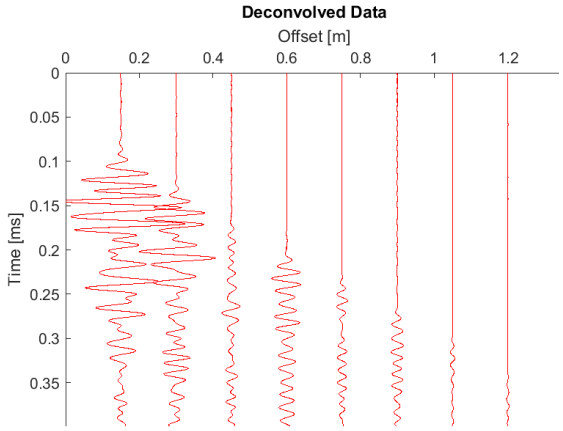

(d) Deconvolved Data

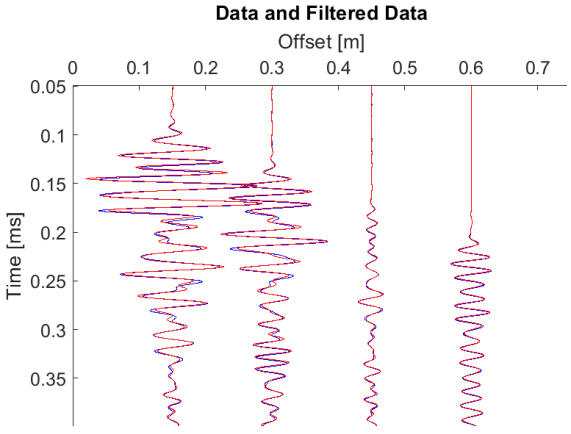

(e) Data in red and Filtered Data in blue

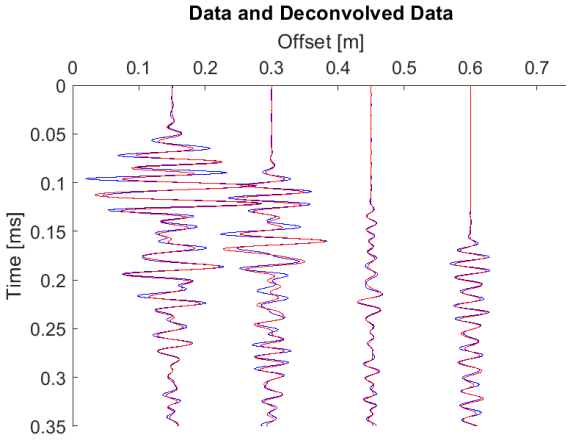

(f) Data in red and Deconvolved Data in blue

Figure C-16: Filtering and Deconvolution results of Pile 13 shot 4 at Deltares test site.

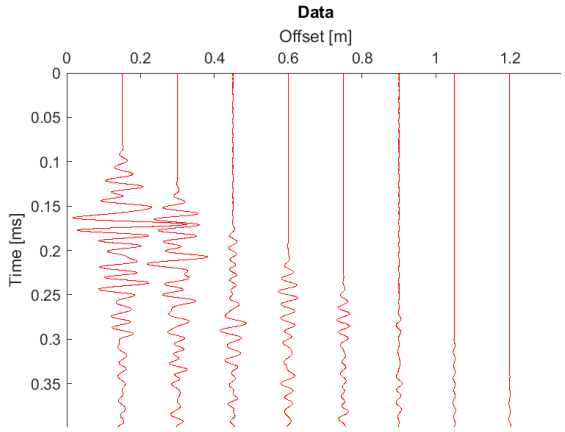

(a) Original Data

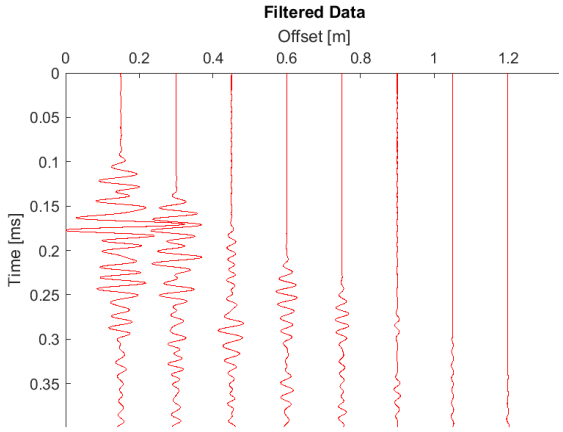

(b) Low-cut Filtered Data

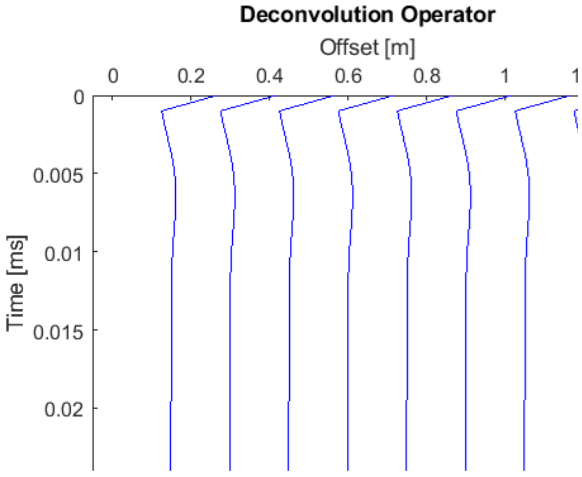

(c) Deconvolution operator

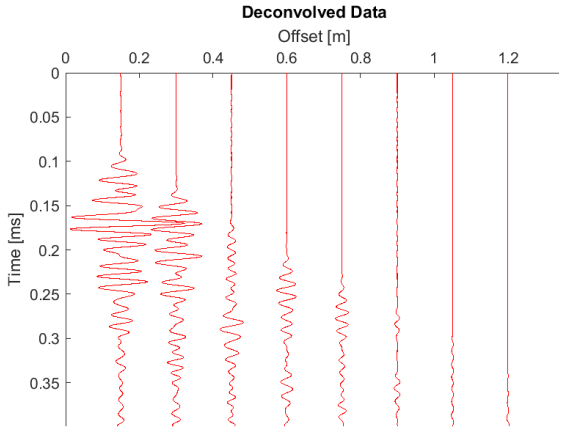

(d) Deconvolved Data

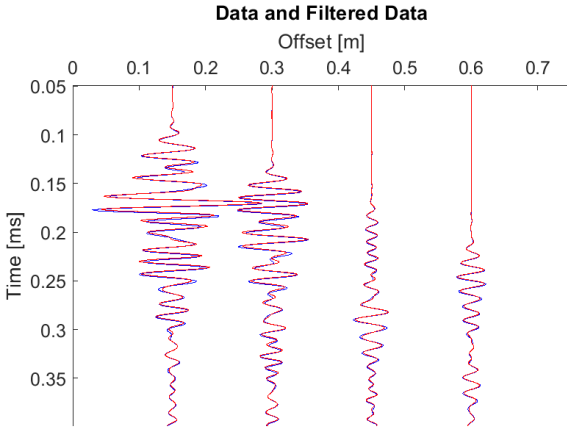

(e) Data in red and Filtered Data in blue

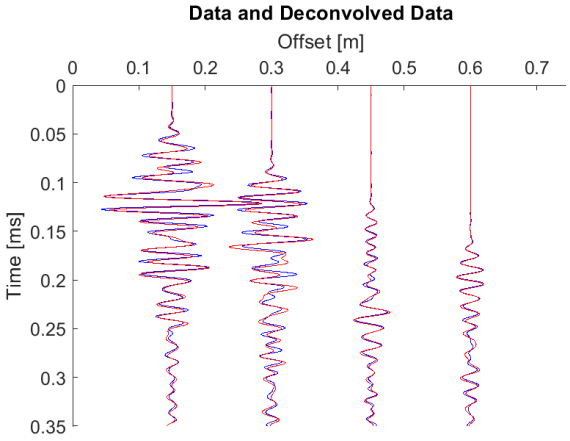

(f) Data in red and Deconvolved Data in blue

Figure C-17: Filtering and Deconvolution results of Pile 13 shot 5 at Deltares test site.

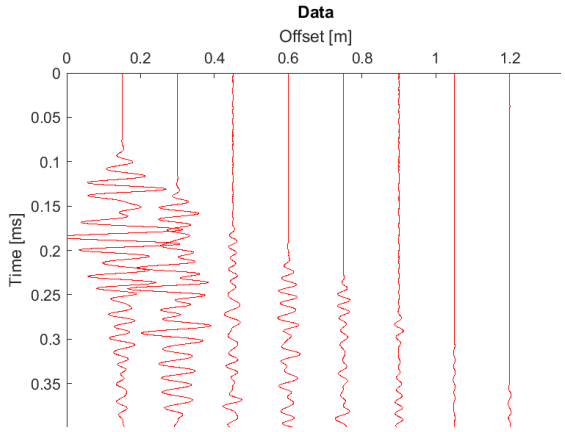

(a) Original Data

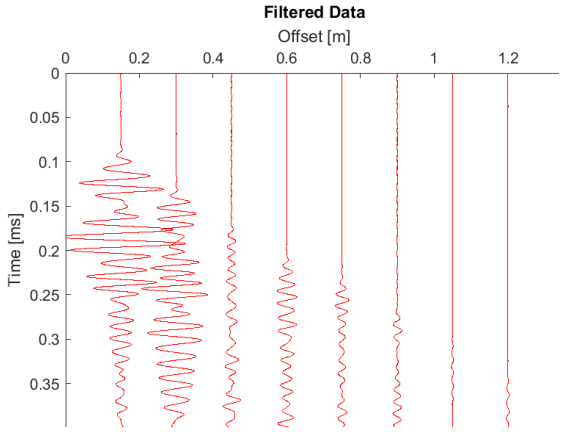

(b) Low-cut Filtered Data

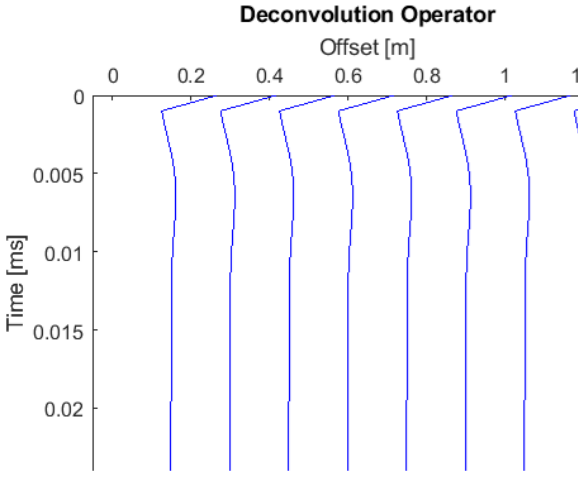

(c) Deconvolution operator

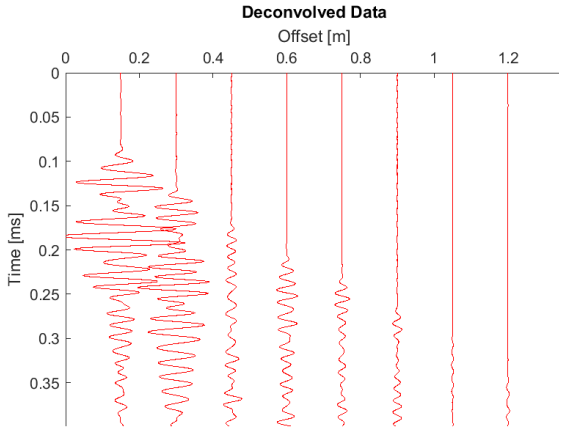

(d) Deconvolved Data

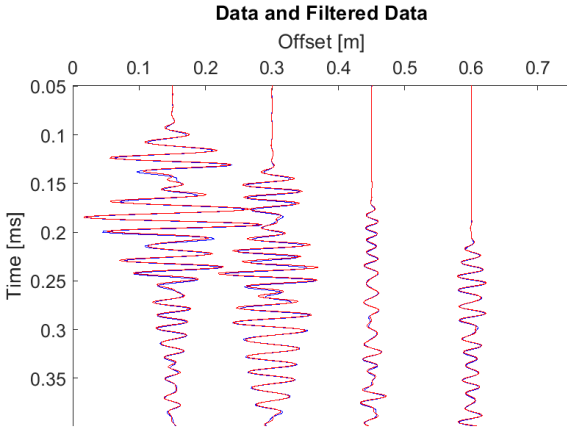

(e) Data in red and Filtered Data in blue

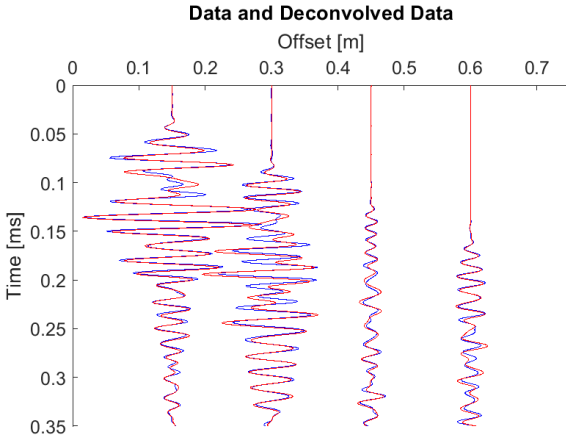

(f) Data in red and Deconvolved Data in blue

Figure C-18: Filtering and Deconvolution results of Pile 13 shot 6 at Deltares test site.

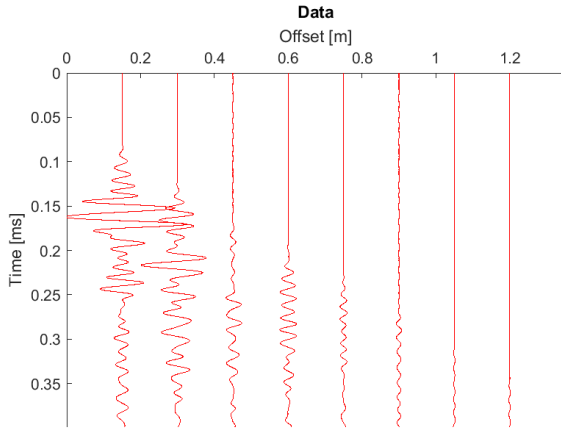

(a) Original Data

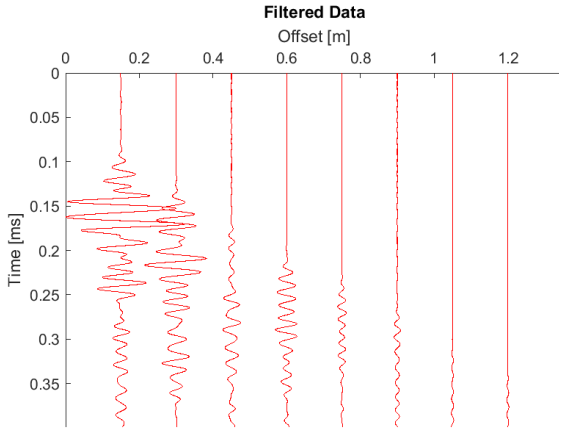

(b) Low-cut Filtered Data

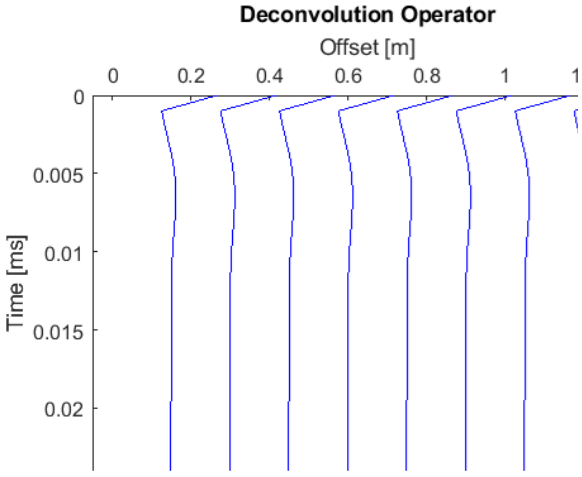

(c) Deconvolution operator

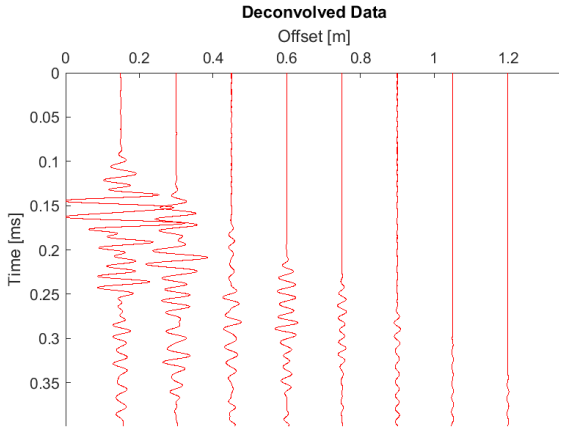

(d) Deconvolved Data

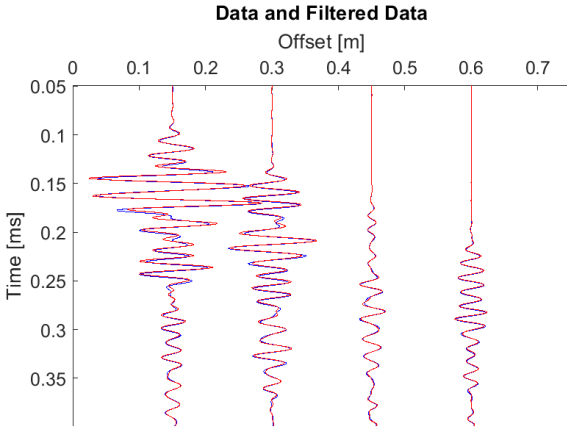

(e) Data in red and Filtered Data in blue

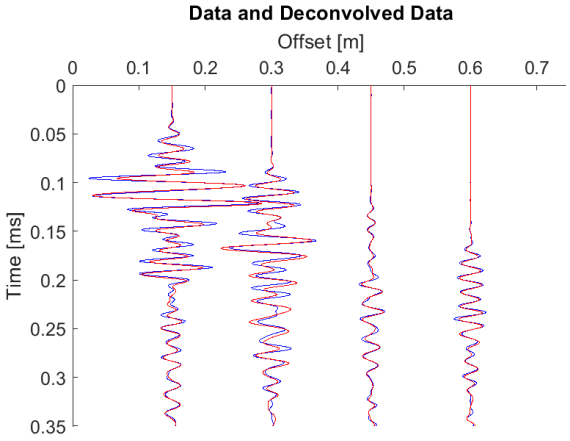

(f) Data in red and Deconvolved Data in blue

Figure C-19: Filtering and Deconvolution results of Pile 13 shot 7 at Deltares test site.

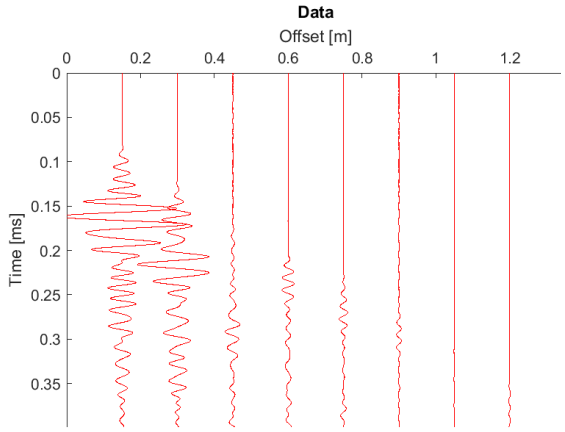

(a) Original Data

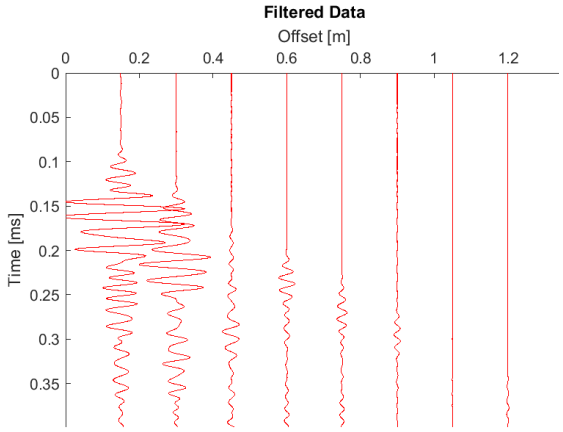

(b) Low-cut Filtered Data

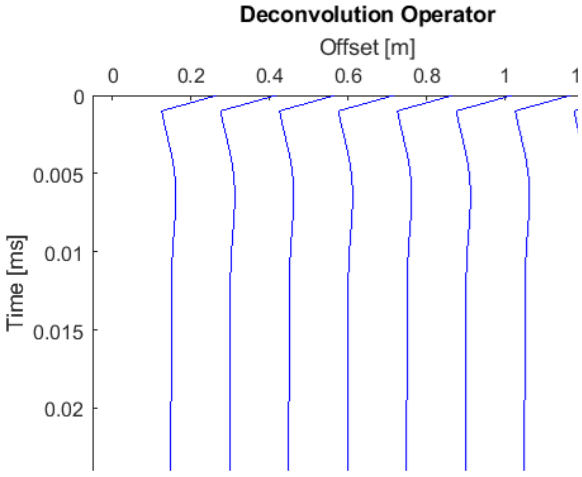

(c) Deconvolution operator

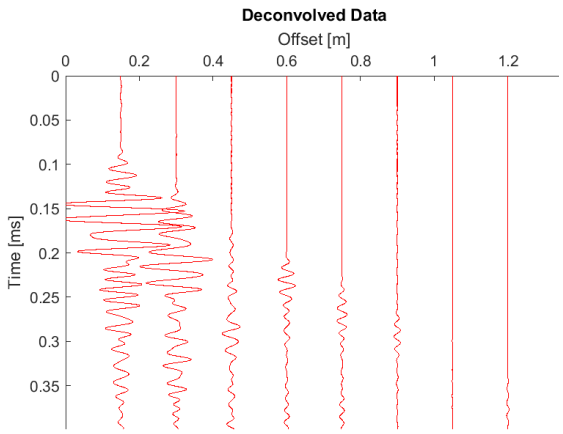

(d) Deconvolved Data

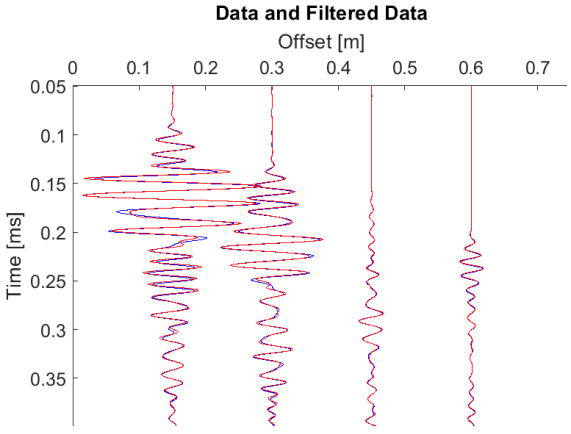

(e) Data in red and Filtered Data in blue

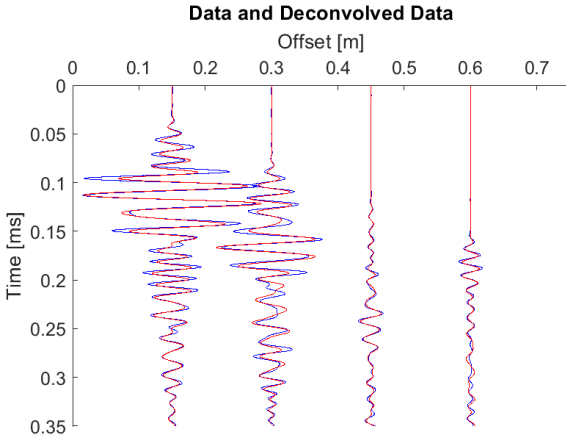

(f) Data in red and Deconvolved Data in blue

Figure C-20: Filtering and Deconvolution results of Pile 13 shot 8 at Deltares test site.

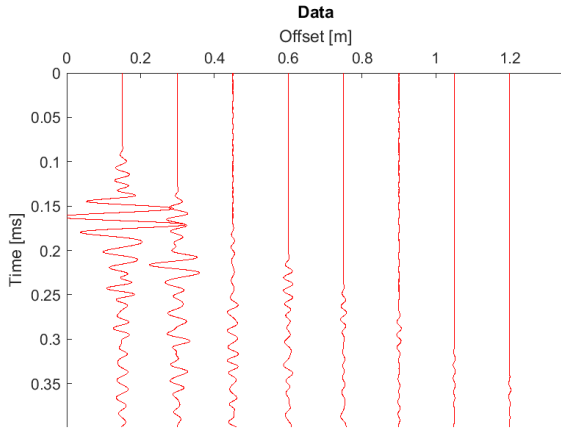

(a) Original Data

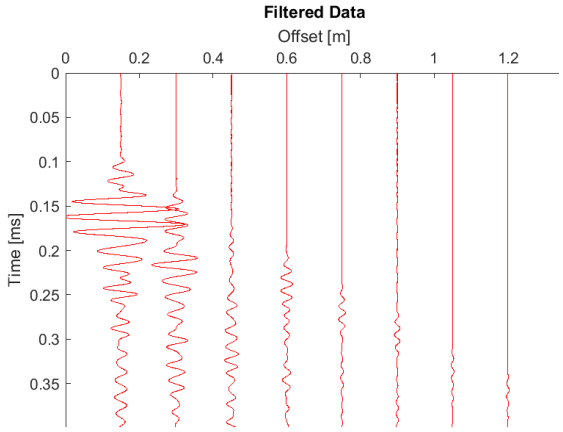

(b) Low-cut Filtered Data

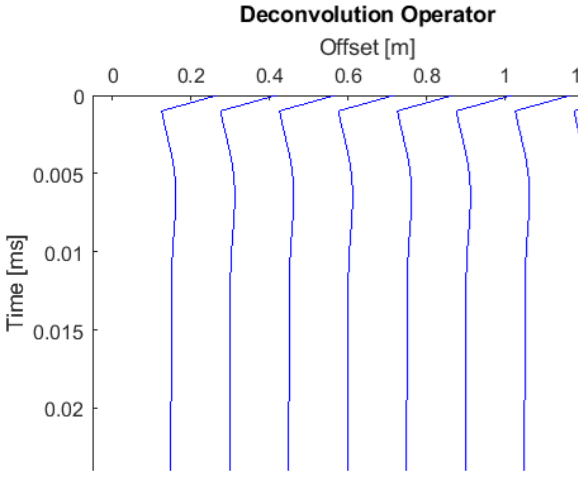

(c) Deconvolution operator

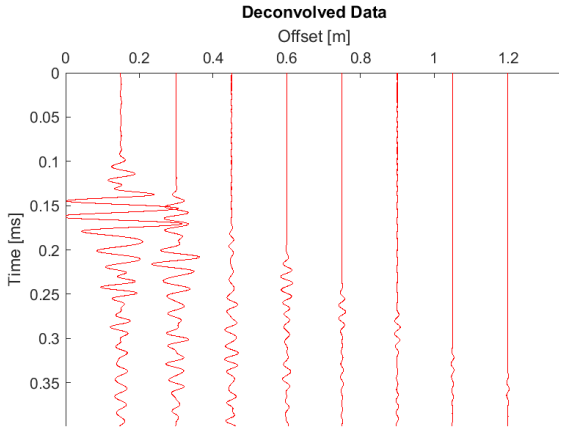

(d) Deconvolved Data

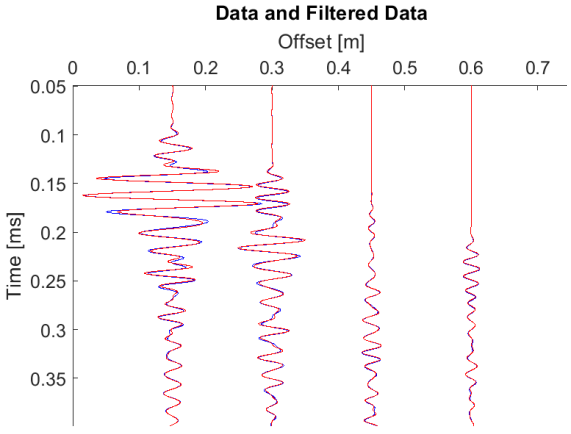

(e) Data in red and Filtered Data in blue

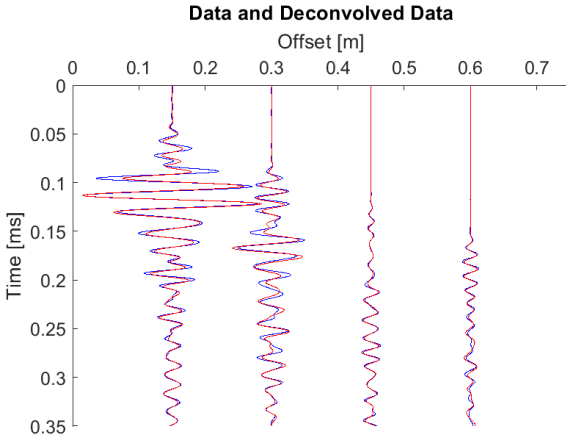

(f) Data in red and Deconvolved Data in blue

Figure C-21: Filtering and Deconvolution results of Pile 13 shot 9 at Deltares test site.

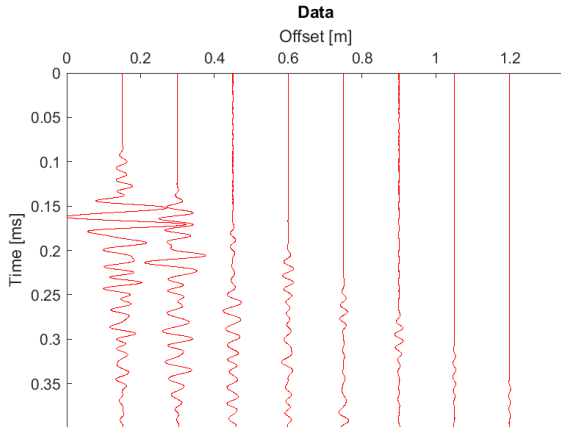

(a) Original Data

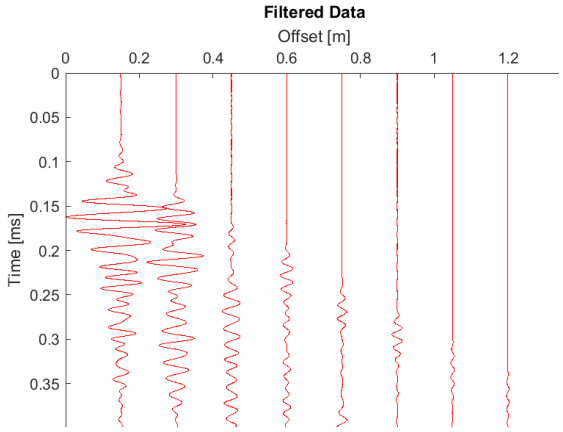

(b) Low-cut Filtered Data

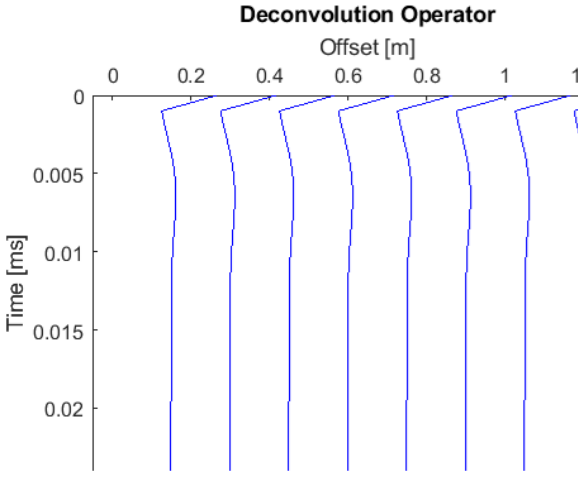

(c) Deconvolution operator

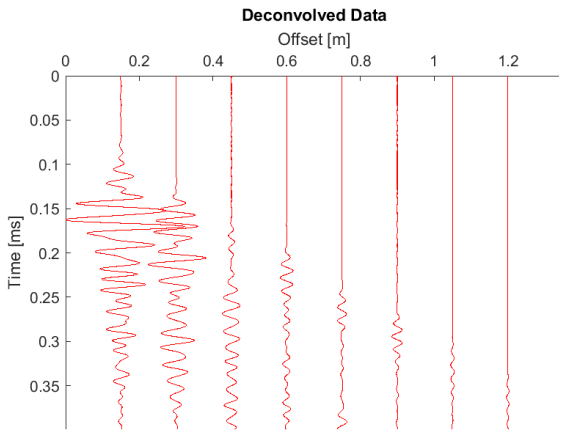

(d) Deconvolved Data

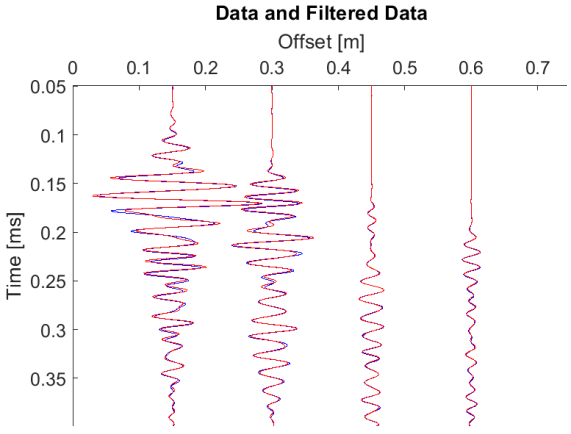

(e) Data in red and Filtered Data in blue

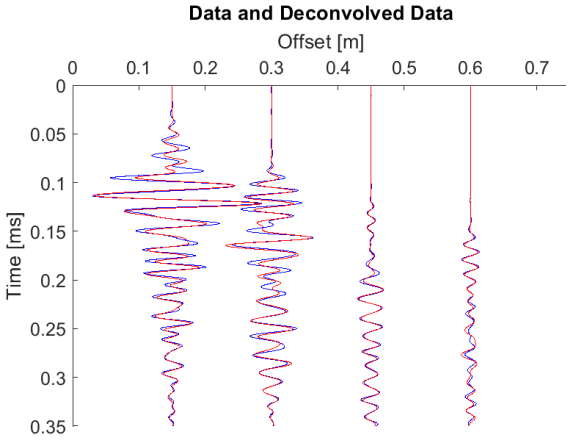

(f) Data in red and Deconvolved Data in blue

Figure C-22: Filtering and Deconvolution results of Pile 13 shot 10 at Deltares test site.

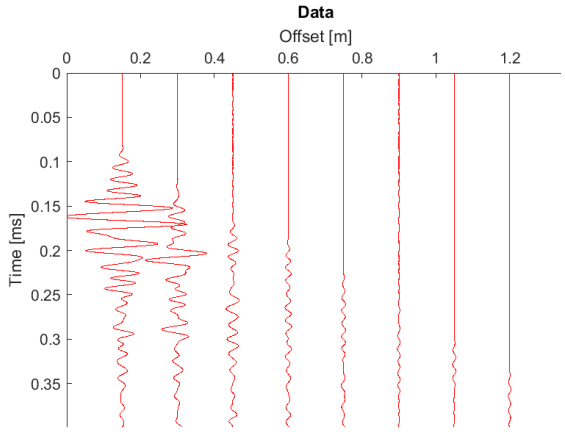

(a) Original Data

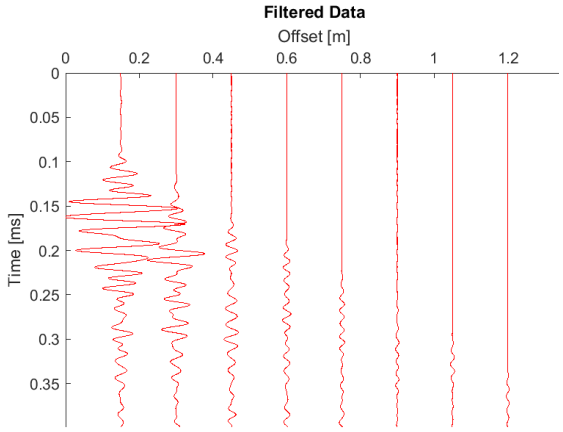

(b) Low-cut Filtered Data

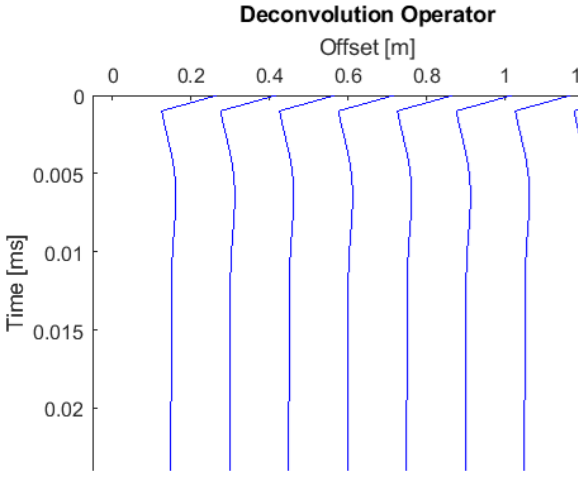

(c) Deconvolution operator

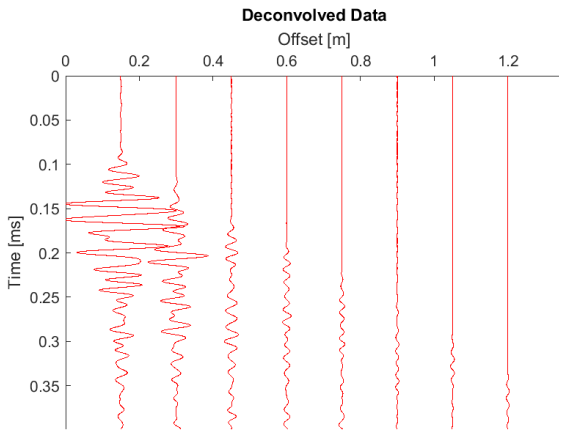

(d) Deconvolved Data

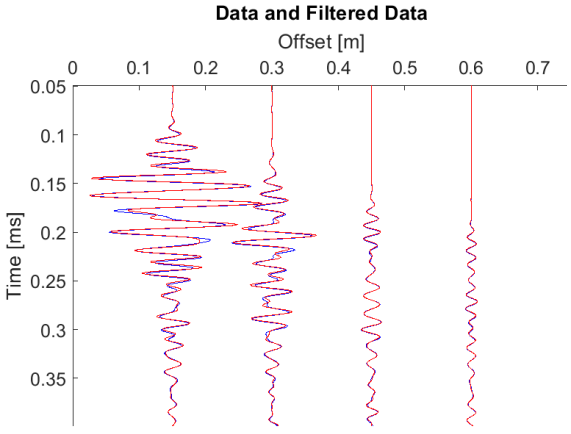

(e) Data in red and Filtered Data in blue

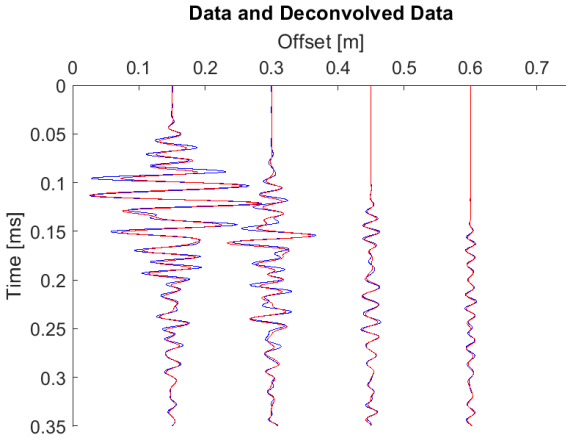

(f) Data in red and Deconvolved Data in blue

Figure C-23: Filtering and Deconvolution results of Pile 13 shot 11 at Deltares test site.

Appendix D

Results Beemster Data

This appendix shows the results of the seismograms of Beemster piles 1 to 3. In a table the found wave velocities are listed.

D-1 Frequency Spectrum

This appendix shows the frequency spectrum of all shots of pile 13 at the Deltares test site.

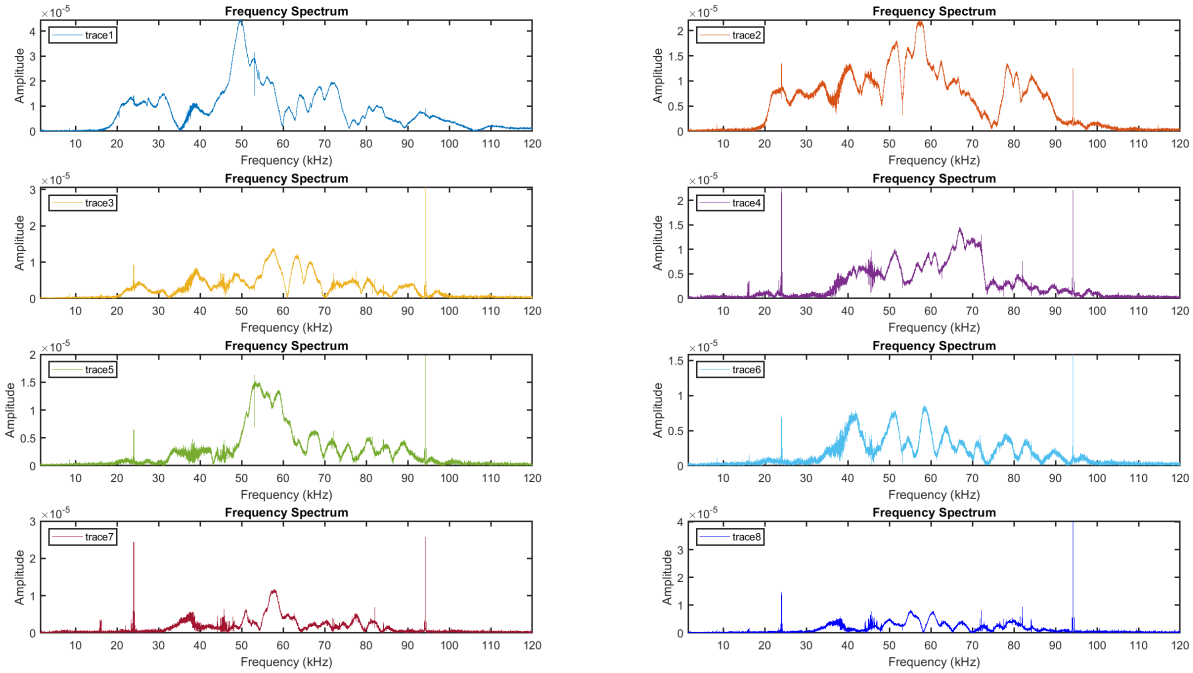

Figure D-1: Frequency spectrum of pile 1 shot 34 of Beemster test site.

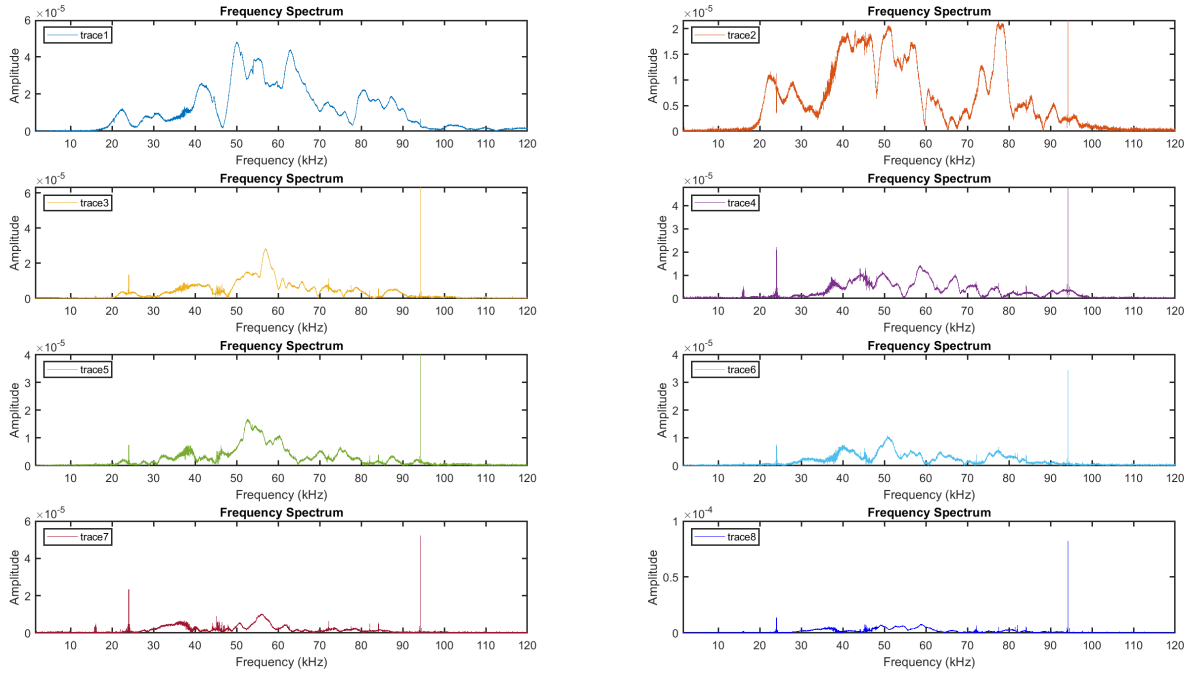

Figure D-2: Frequency spectrum of pile 2 shot 34 of Beemster test site.

D-2 Results Beemster processing

This appendix shows the frequency spectra of shot 34 of the piles at the Beemster test site. It also shows the results of filtering and deconvolution.

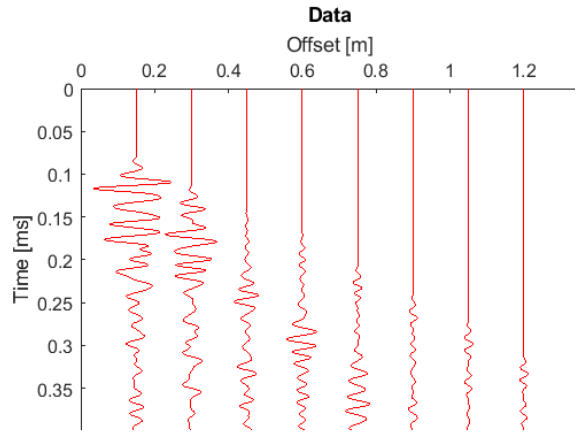

(a) Original Data

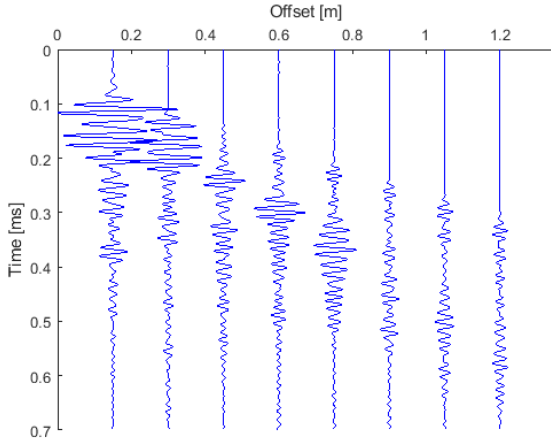

(b) Low-cut Filtered Data

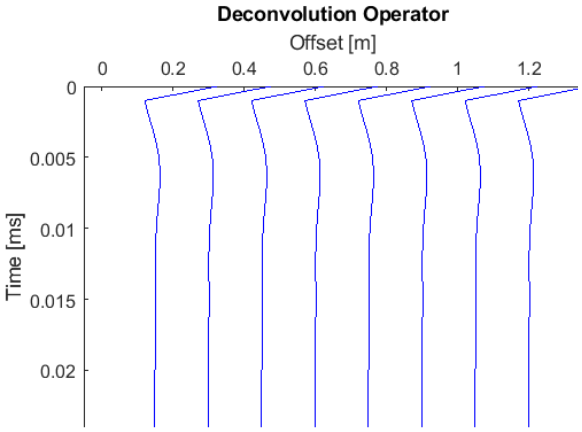

(c) Deconvolution operator

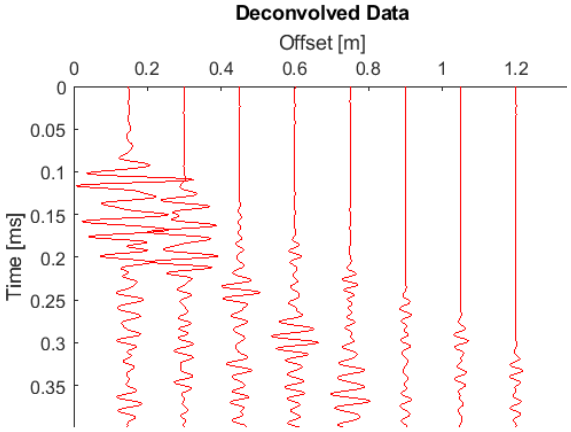

(d) Deconvolved Data

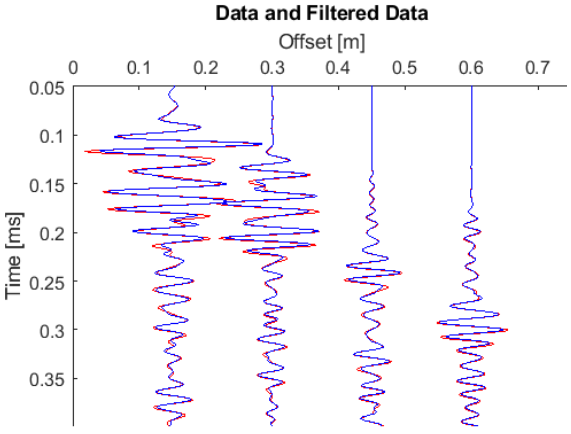

(e) Original Data in red and Filtered Data in blue

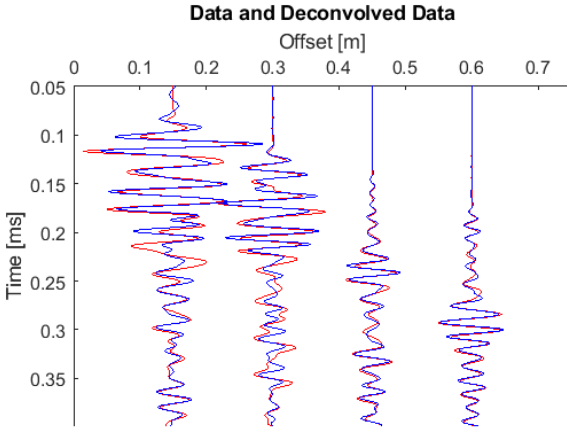

(f) Original Data in red and Deconvolved Data in blue

Figure D-3: Filtering and Deconvolution results of Pile 1 shot 34 extra measurements at Beemster test site.

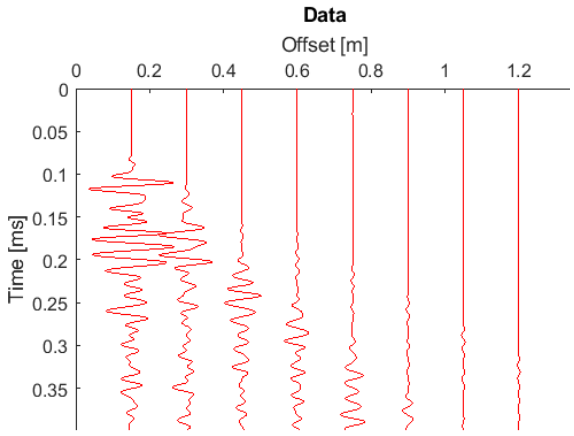

(a) Original Data

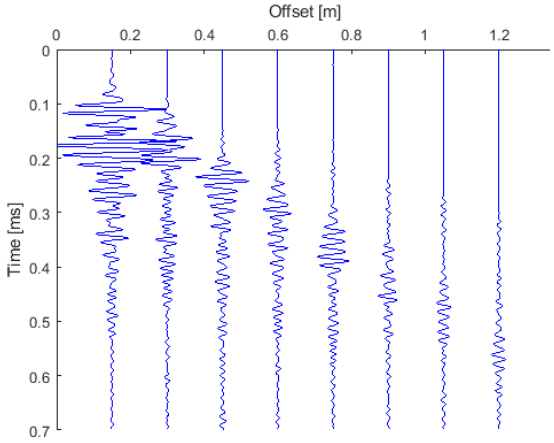

(b) Low-cut Filtered Data

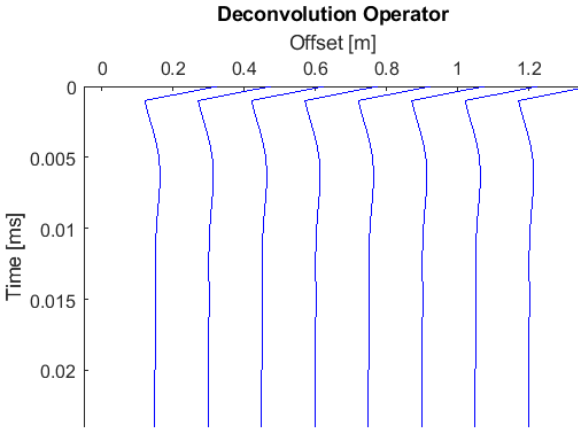

(c) Deconvolution operator

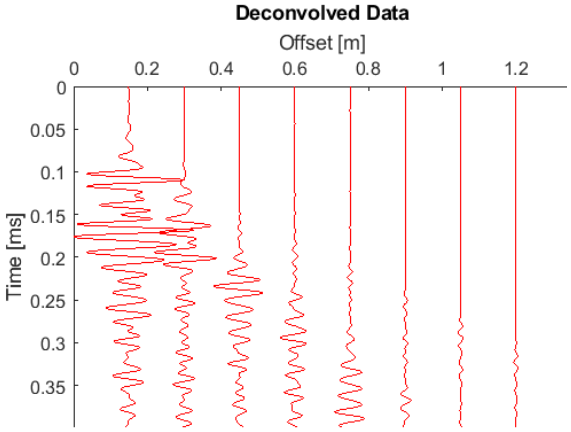

(d) Deconvolved Data

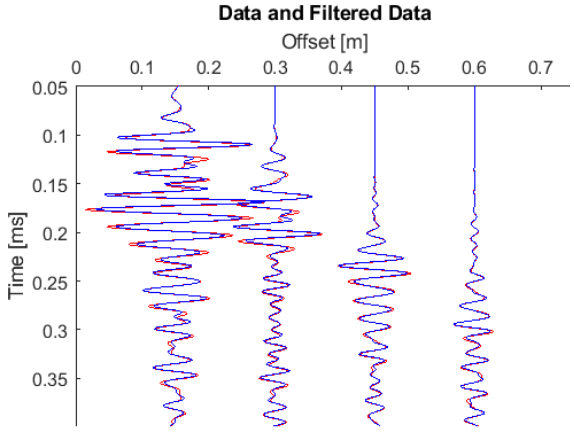

(e) Original Data in red and Filtered Data in blue

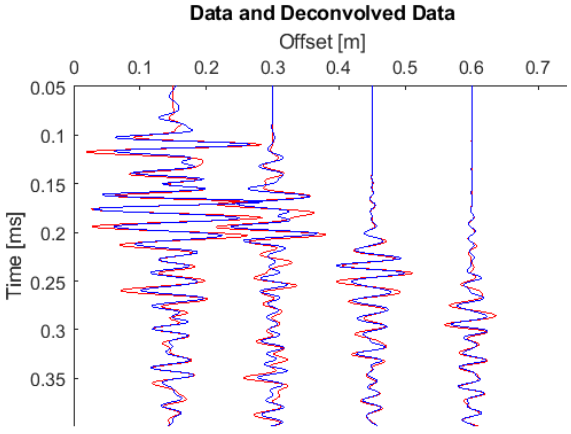

(f) Original Data in red and Deconvolved Data in blue

Figure D-4: Filtering and Deconvolution results of Pile 2 shot 34 extra measurements at Beemster test site.

D-3 Interpreted Beemster Data

This section show the two possible reflected wave interpretations for the data of pile 2.

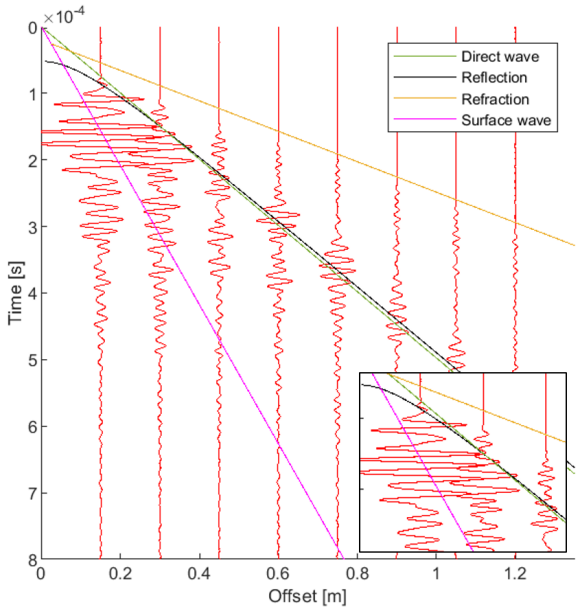

(a) Shot 34. Direct wave, refracted wave, surface (Tube) wave and reflected wave indicated.

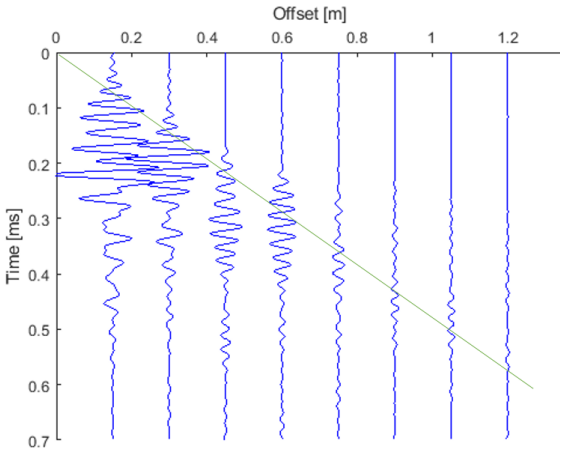

(b) Shot 34 after low-pass frequency filter is applied (low-pass corner frequencies: [1500 20000 40000 50000]). Direct wave indicated.

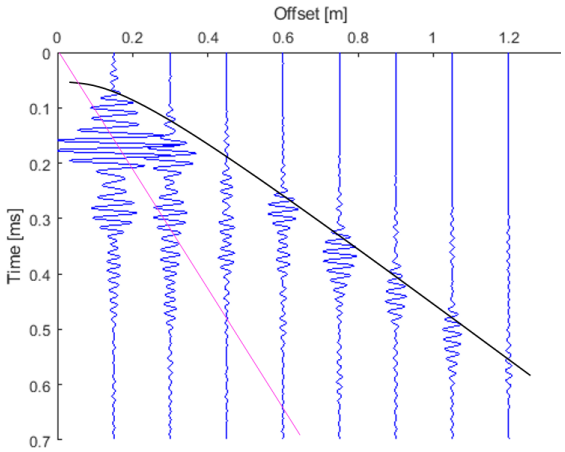

(c) Shot 34 after mid-pass frequency filter is applied (mid-bandpass corner frequencies: [40000 50000 65000 70000]). Surface (Tube) wave and reflected wave indicated in pink and black respectively.

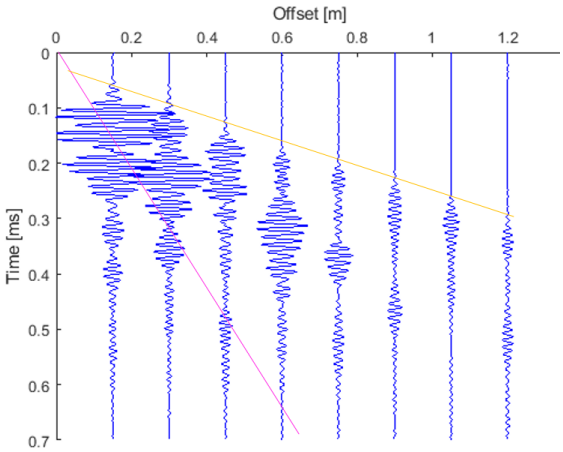

(d) Shot 34 after high-pass frequency filter is applied (high-pass corner frequencies: [63000 73000 100000 120000]). Surface (Tube) wave in pink and Refracted wave in yellow indicated.

Figure D-5: Seismograms showing the result after frequency filtering with interpreted waves indicated. Shot 34 of foundation pile nr 3 at the Beemster test site.

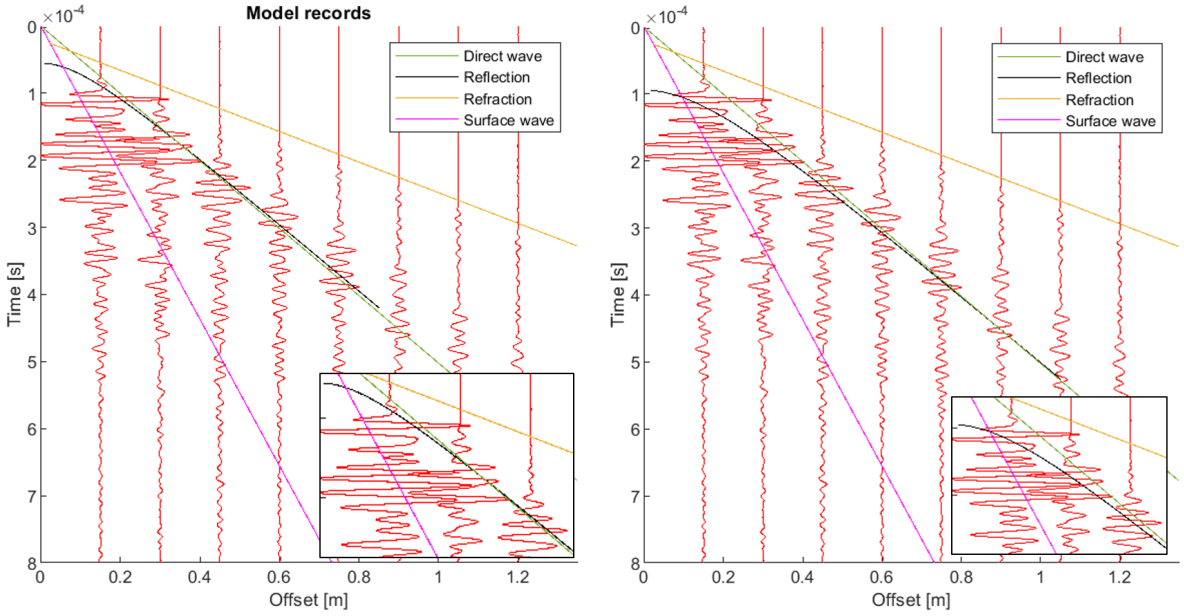

(a) The picked concrete thickness is 0.111 m corresponds to a diameter of 0.267 m.

(b) The picked concrete thickness is 0.201 m corresponds to a diameter of 0.447 m.

Figure D-6: Beemster data of shot 34 pile 2, including the picked arrivals of the surface, direct, refracted and reflected wave. In lower right corner enlargement of first three traces.

Appendix E

Surface Wave Inversion

This appendix shows the results of the surface wave inversion of shot 10 of pile 13 of the Deltares test site. The figure below shows the result of the six runs. Shown are the p-velocity, s-velocity and density profiles of the models with the lowest misfits of the total investigated models.

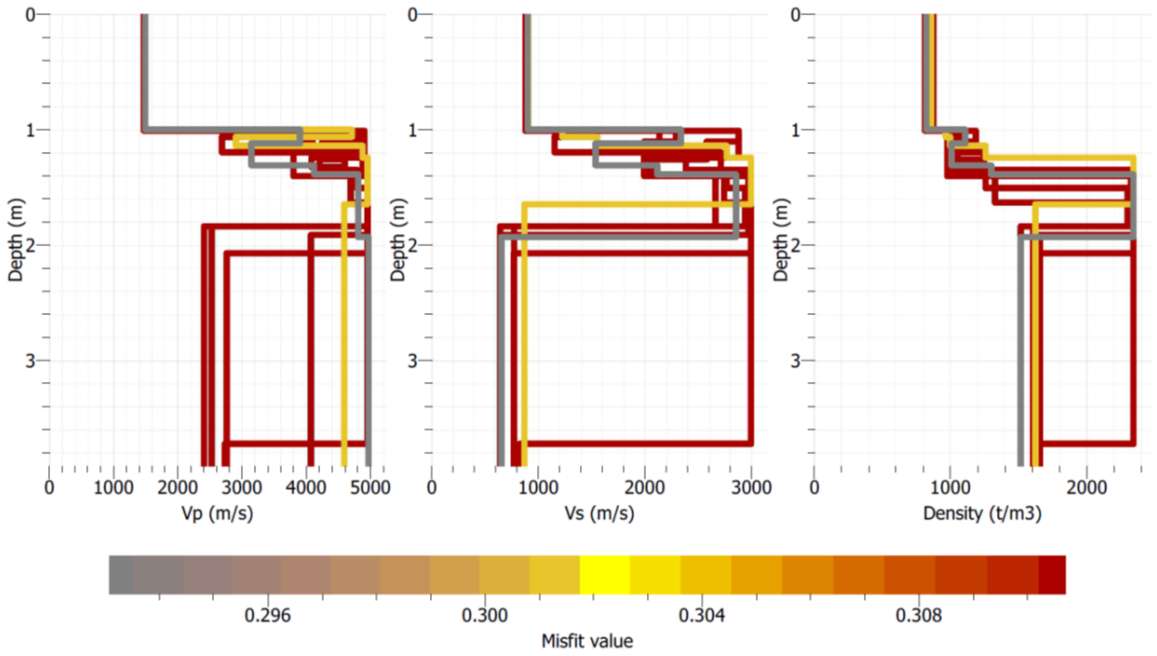

(a) Profiles surface wave inversion run 1

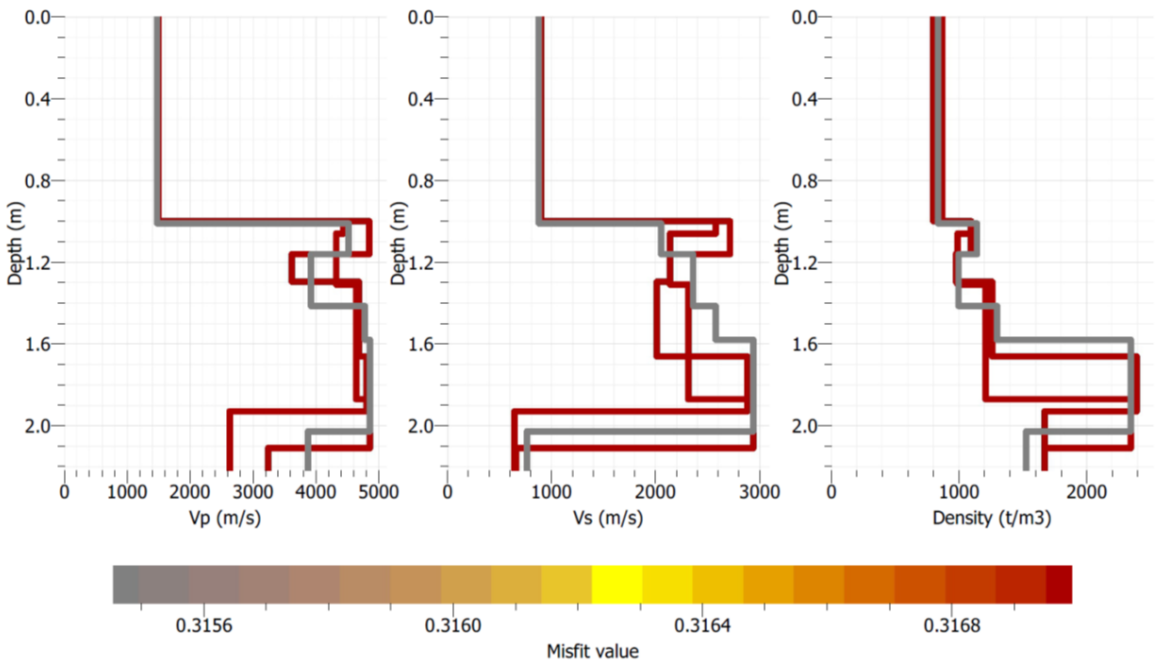

(b) Profiles surface wave inversion run 2

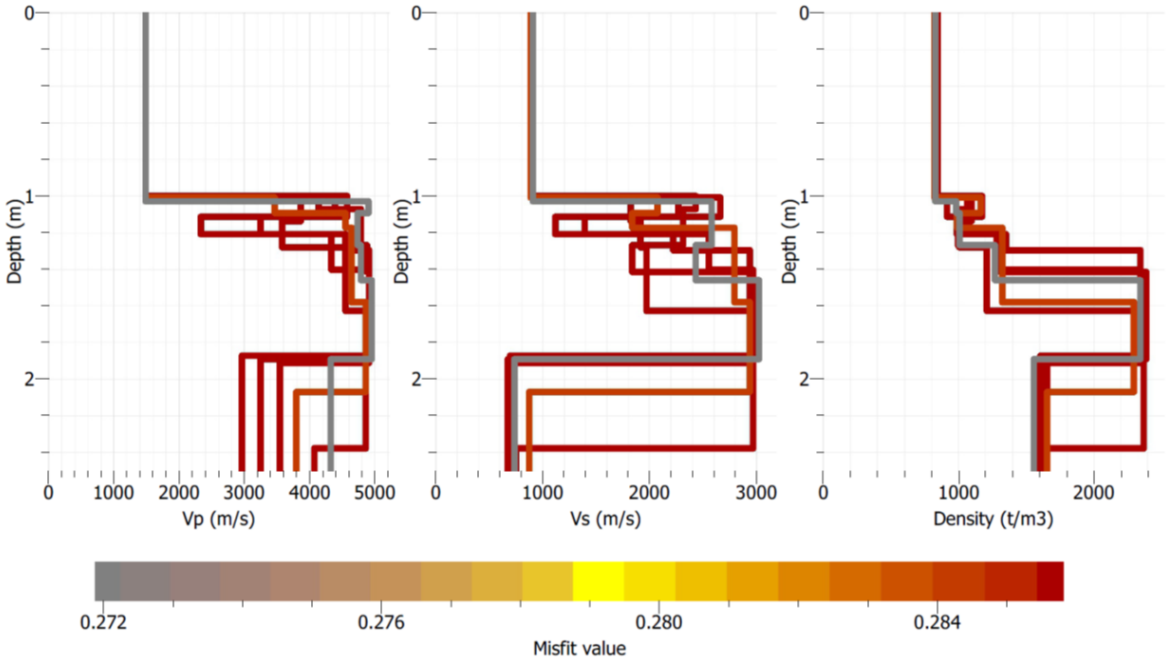

(c) Profiles surface wave inversion run 3

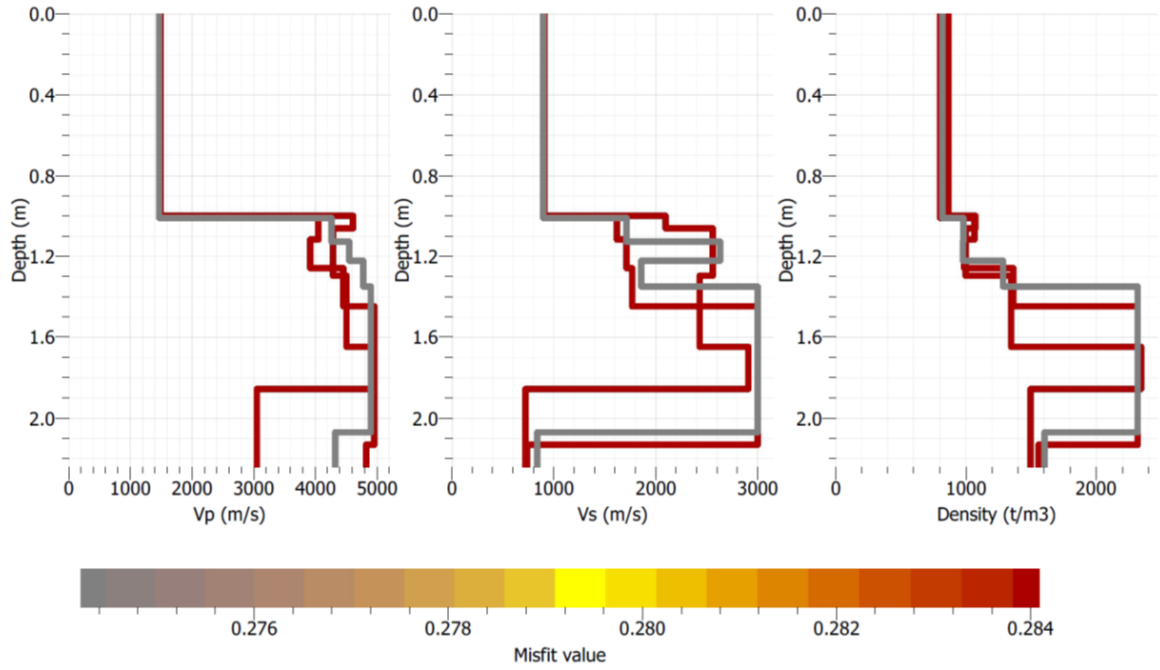

(d) Profiles surface wave inversion run 4

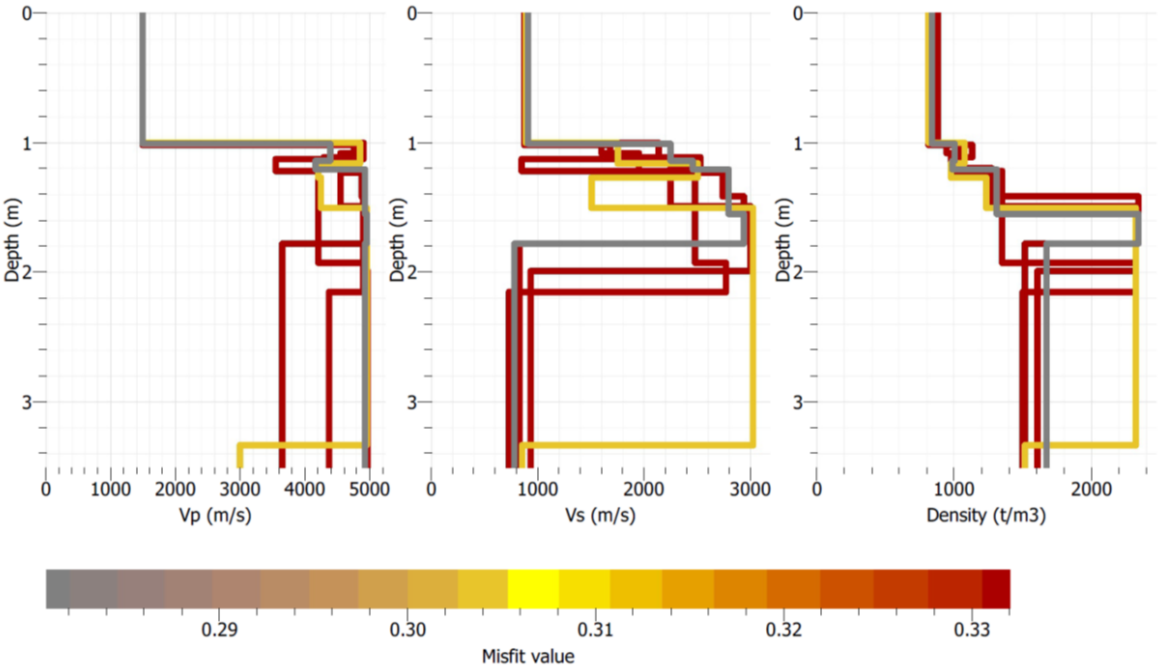

(e) Profiles surface wave inversion run 5

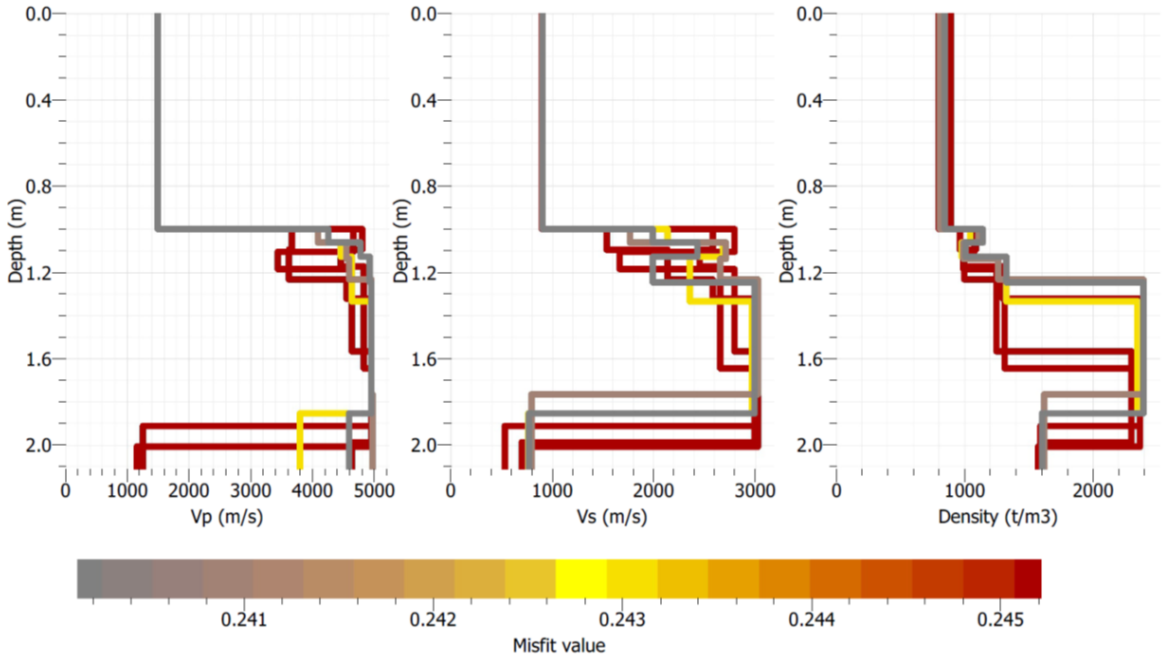

(f) Profiles surface wave inversion run 6

Figure E-1: Inversion results surface wave inversion runs 1 to 6. Shown are the p-velocity, s-velocity and density profiles of the models with the lowest misfits of the total investigated models

Appendix F

Profiles Foundation Piles

In this appendix the profiles of all the measured piles are listed. Profiles are determined for piles 1 to 20 at the Deltares test site. The profiles are shown in groups of 4 according to their placement in the field shown in figure F-1. The profiles of pile nr. 10, 12 and 15 are shown for the two different measurements. One profile determined before the extra measurements and one using the extra measurements. The profiles show the radius of the pile and nominal designed diameter with the defects, necking, bulging and fractures are indicated. In table F-2 the velocities found using the interpretation tool are listed. In the table below the distances to shift the depths to a common reference depth are listed for all 20 piles.

Shift in reference depth [m]									
Pile 1	**Pile 2**	**Pile 3**	**Pile 4**	**Pile 5**	**Pile 6**	**Pile 7**	**Pile 8**	**Pile 9**	**Pile 10**
0.95	0.51	1.02	0.84	1.41	1.11	0.62	0.85	0.77	0.77
Pile 11	**Pile 12**	**Pile 13**	**Pile 14**	**Pile 15**	**Pile 16**	**Pile 17**	**Pile 18**	**Pile 19**	**Pile 20**
1.09	0.59	0.67	1.05	0.72	0.80	0.96	0.89	1.03	1.07

Table F-1: Distance of top of reinforcement bar of each pile to flattened top concrete.

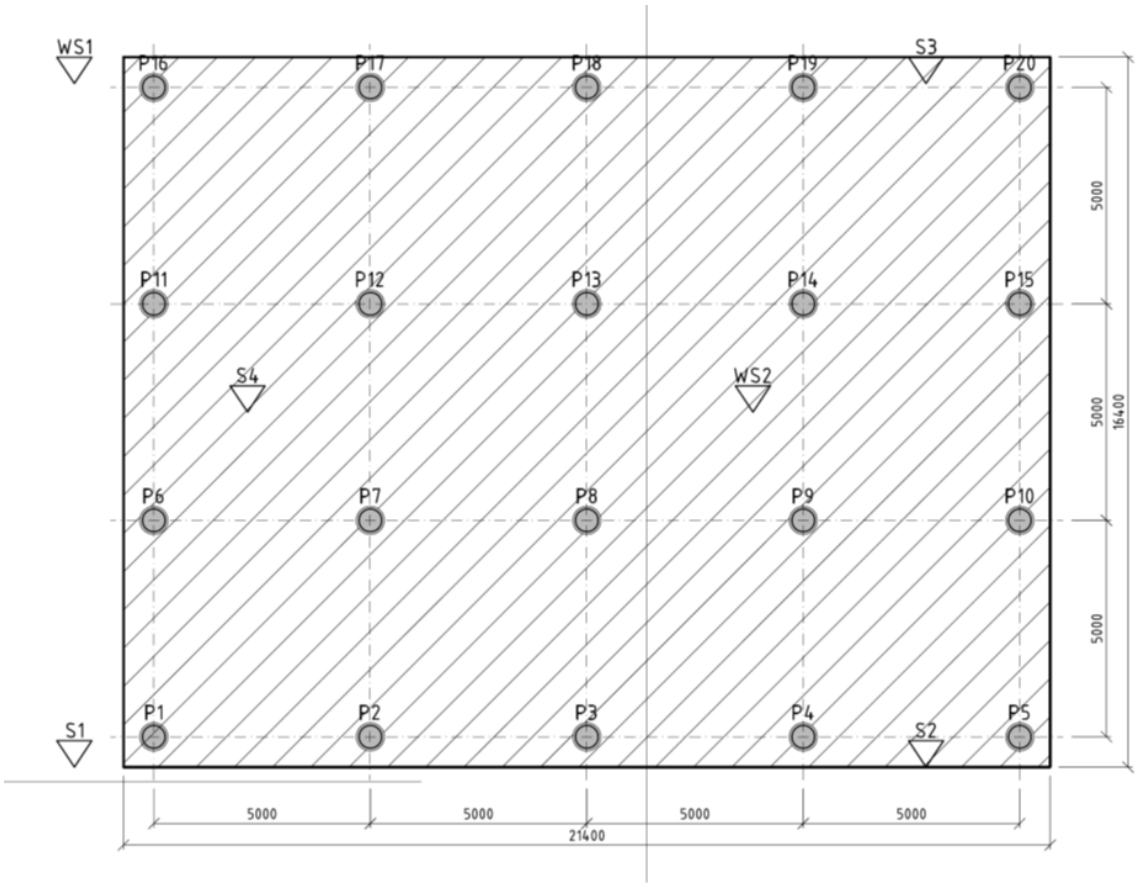

Figure F-1: Design test site showing the location of each pile.

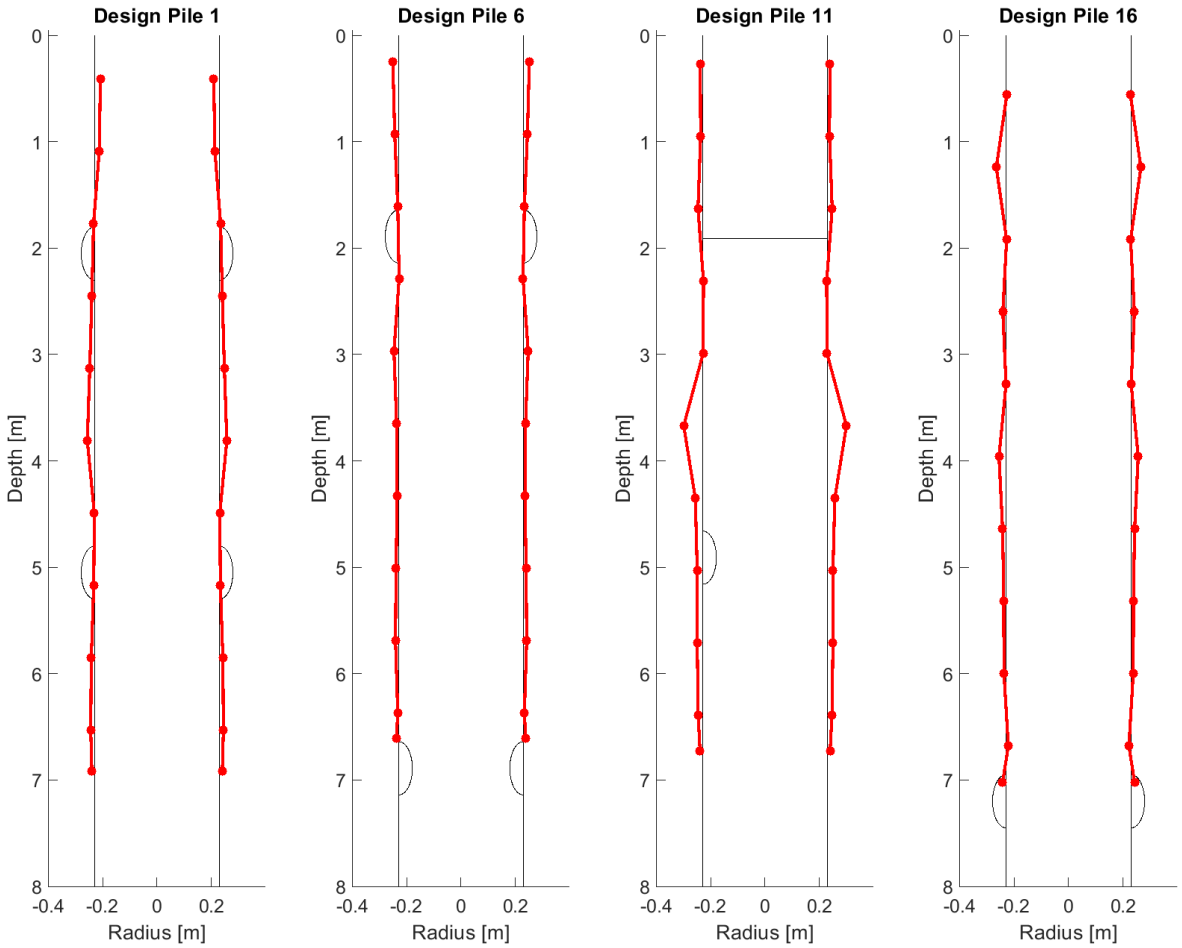

(a) Pile 1 **(b)** Pile 6 **(c)** Pile 11 **(d)** Pile 16

Figure F-2: Profile foundation piles left row. Determined thickness in red and designed shape in black. Designed defects not to scale. Source location of each measurement indicated with a dot.

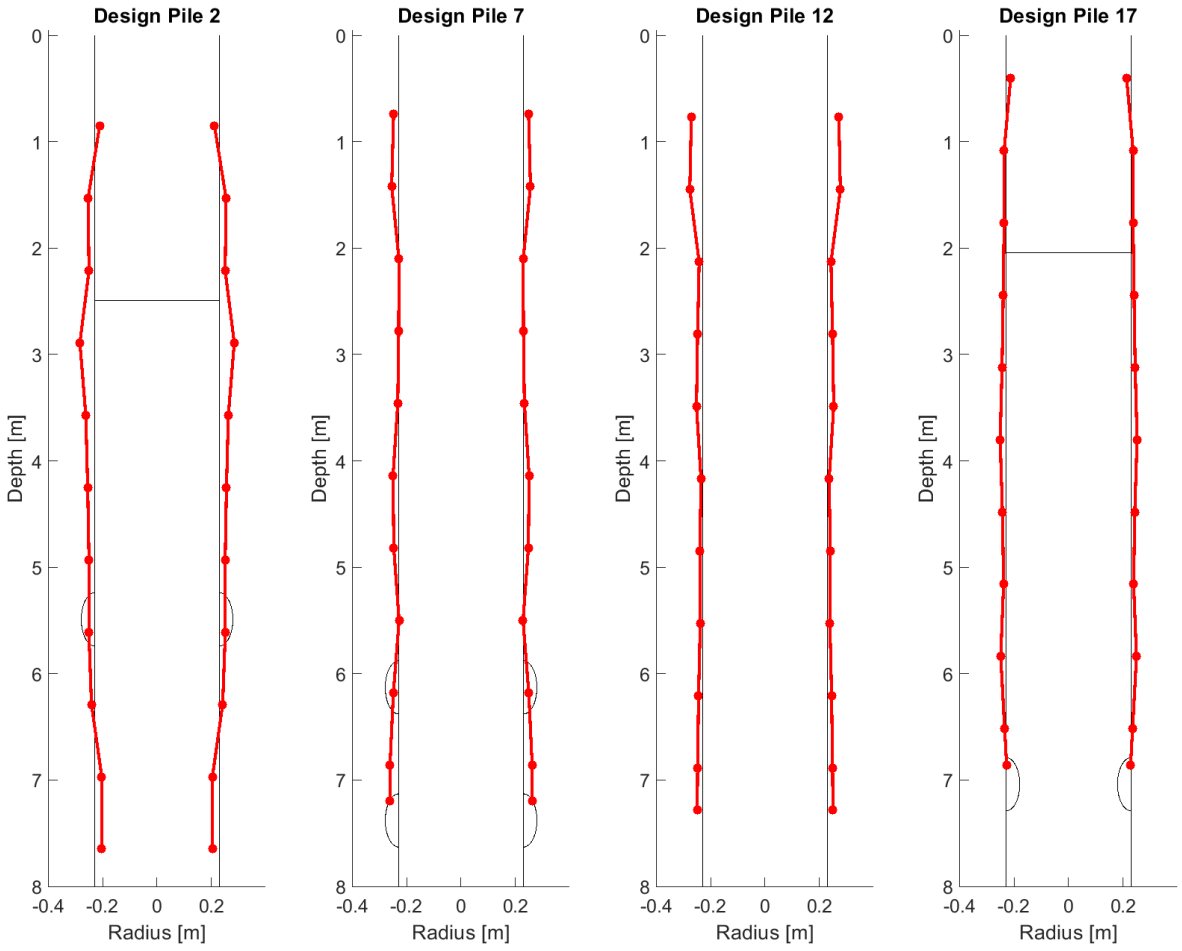

(e) Pile 2 **(f)** Pile 7 **(g)** Pile 12 **(h)** Pile 17

Figure F-2: Profile foundation piles second row from left. Determined thickness in red and designed shape in black. Designed defects not to scale. Source location of each measurement indicated with a dot.

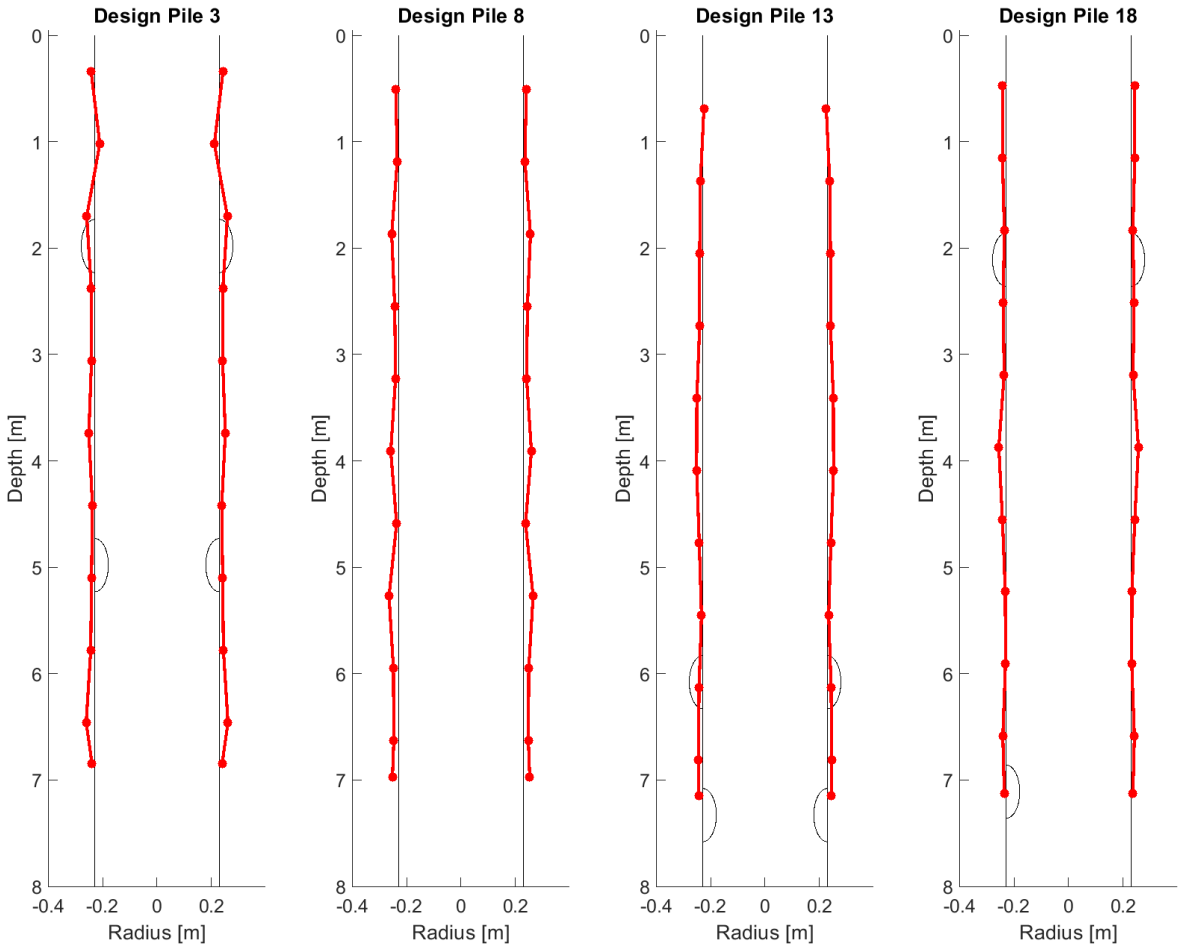

(i) Pile 3 **(j)** Pile 8 **(k)** Pile 13 **(l)** Pile 18

Figure F-2: Profile foundation piles third row from left. Determined thickness in red and designed shape in black. Designed defects not to scale. Source location of each measurement indicated with a dot.

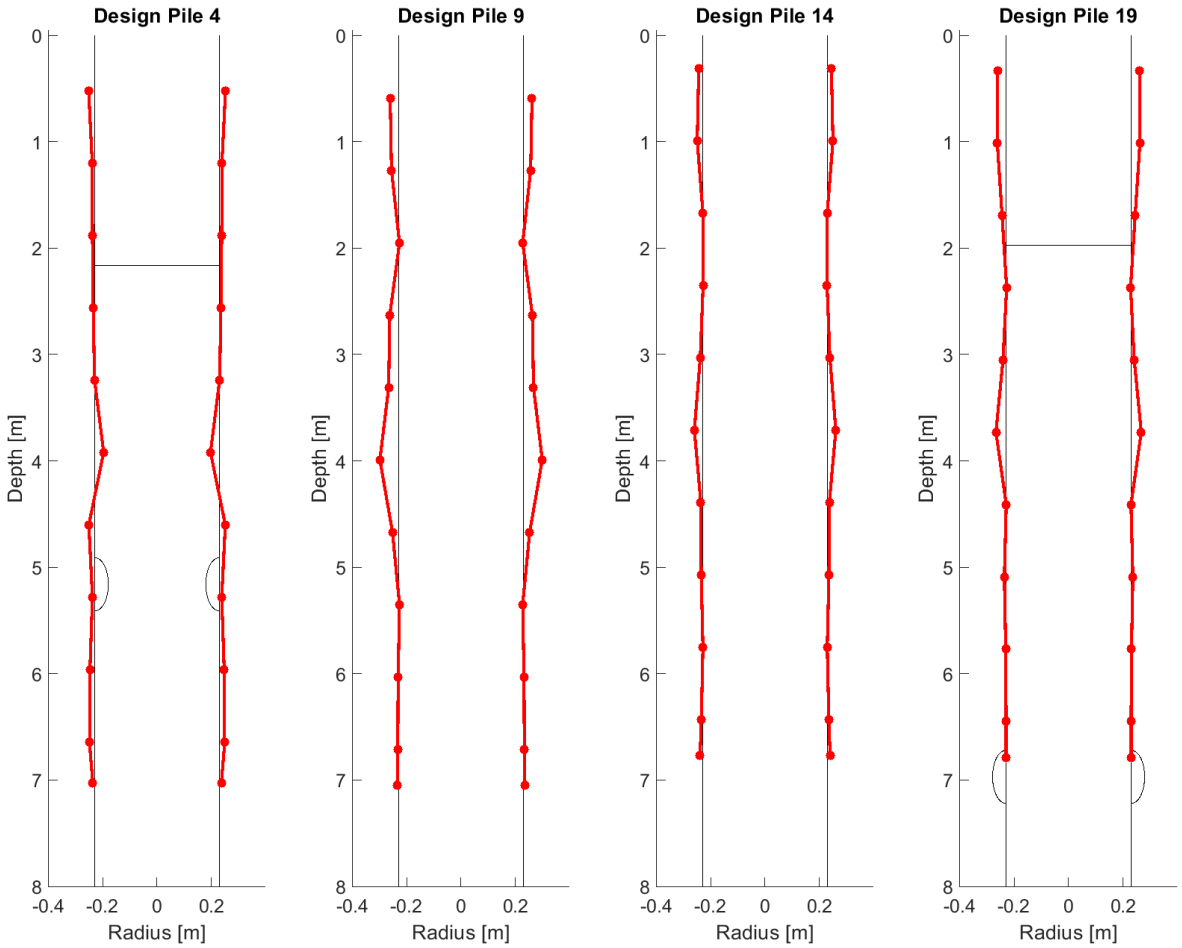

(m) Pile 4 **(n)** Pile 9 **(o)** Pile 14 **(p)** Pile 19

Figure F-2: Profile foundation piles second row from right. Determined thickness in red and designed shape in black. Designed defects not to scale. Source location of each measurement indicated with a dot.

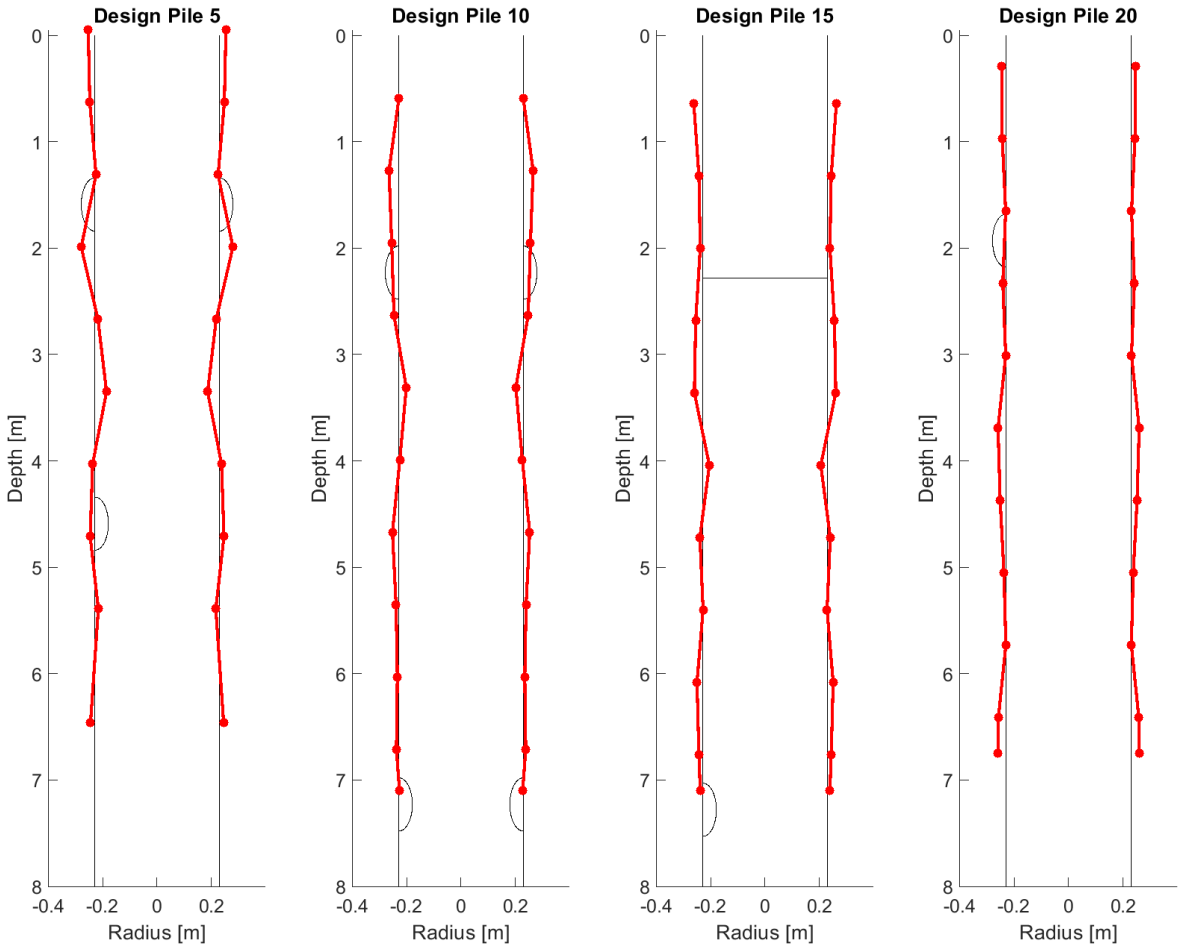

(q) Pile 5 **(r)** Pile 10 **(s)** Pile 15 **(t)** Pile 20

Figure F-2: Profile foundation piles first row from right. Determined thickness in red and designed shape in black. Designed defects not to scale. Source location of each measurement indicated with a dot.

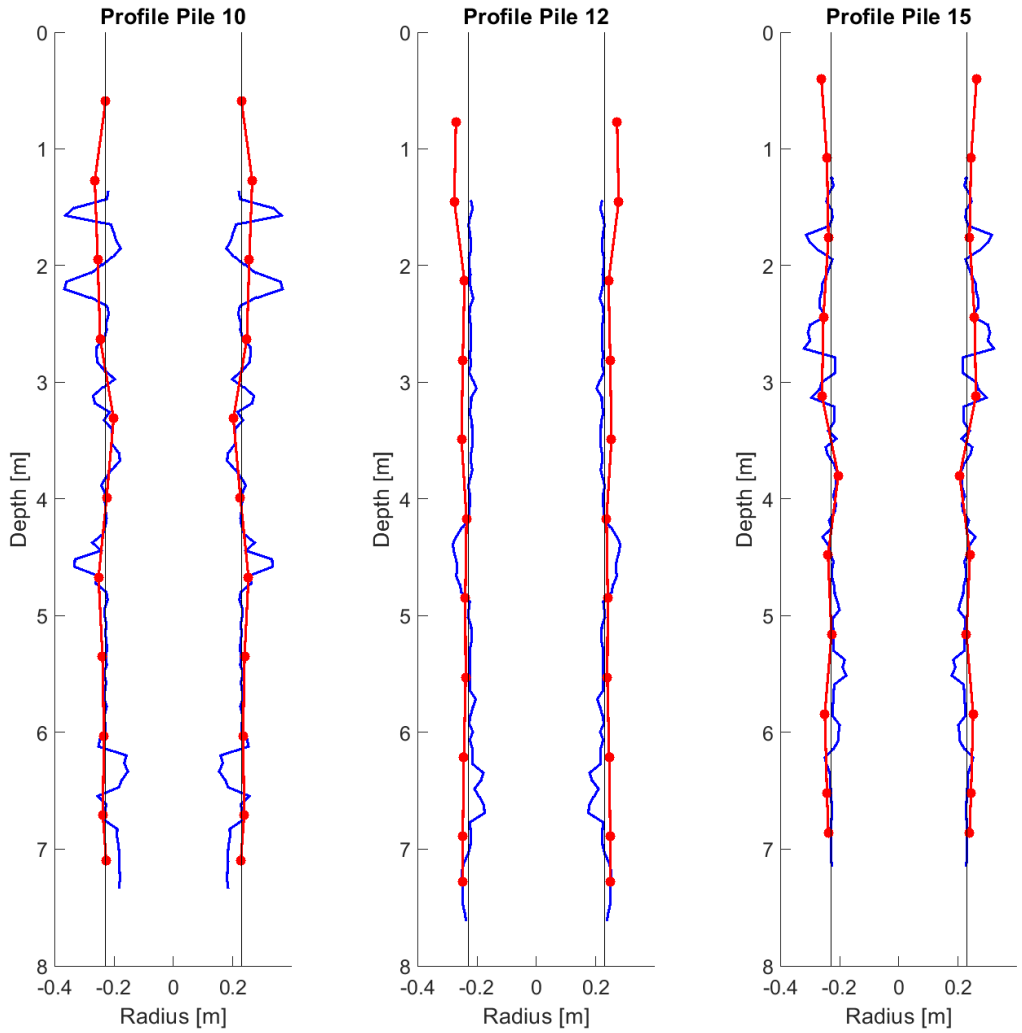

(a) Pile 10 **(b)** Pile 12 **(c)** Pile 17

Figure F-3: Profile foundation Pile 10, 12 and 15 from extra measurements. First measurements in red, second in blue and nominal diameter.. Source location of each measurement indicated with a dot.

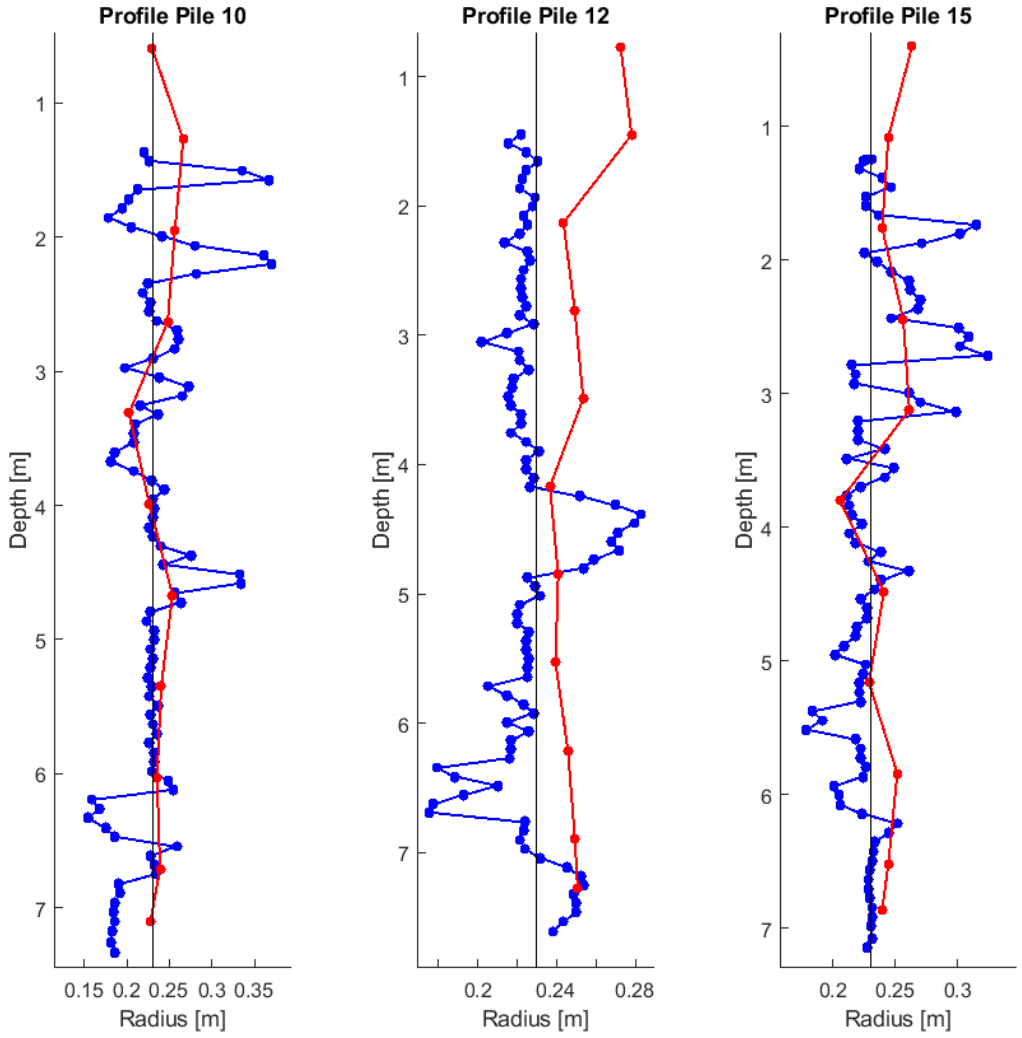

(a) Pile 10 **(b)** Pile 12 **(c)** Pile 17

Figure F-4: Close up of one side of the pile, showing the radius of the pile determine using the seismic tube in red and blue and the designed radius in black. Designed defects excluded. Location of each measurement indicated with a dot. Profile foundation Pile 10, 12 and 15 from extra measurements. First measurements in red second in blue. Source location of each measurement indicated with a dot.

F-1 Extracted Piles

Profiles of the extracted piles determined by interpretation of seismic tube data next to results of visual inspection are plotted below. These are piles number 1, 6, 7, 8, 13 and 17.

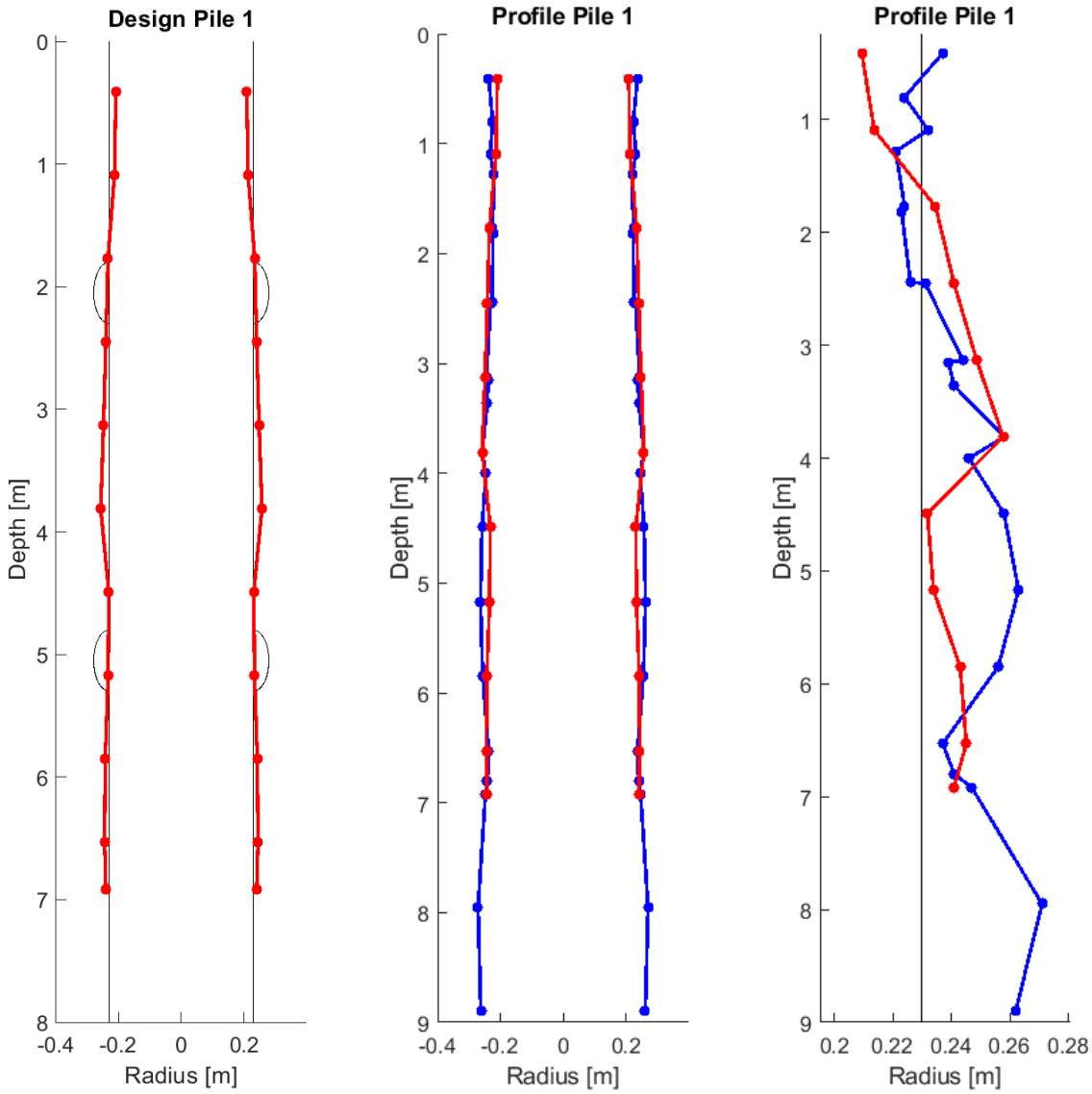

(a) Determined thickness in red and designed shape in black. Designed defects excluded. Source location of each measurement indicated with a dot.

(b) Determined thickness in red and measured shape in blue. Location of each measurement indicated with a dot.

(c) Close up of one side of the pile, showing the radius of the pile determine using the seismic tube in red, the measured shape in blue and the designed radius in black. Designed defects excluded. Location of each measurement indicated with a dot.

Figure F-5: Profiles foundation Pile 1.

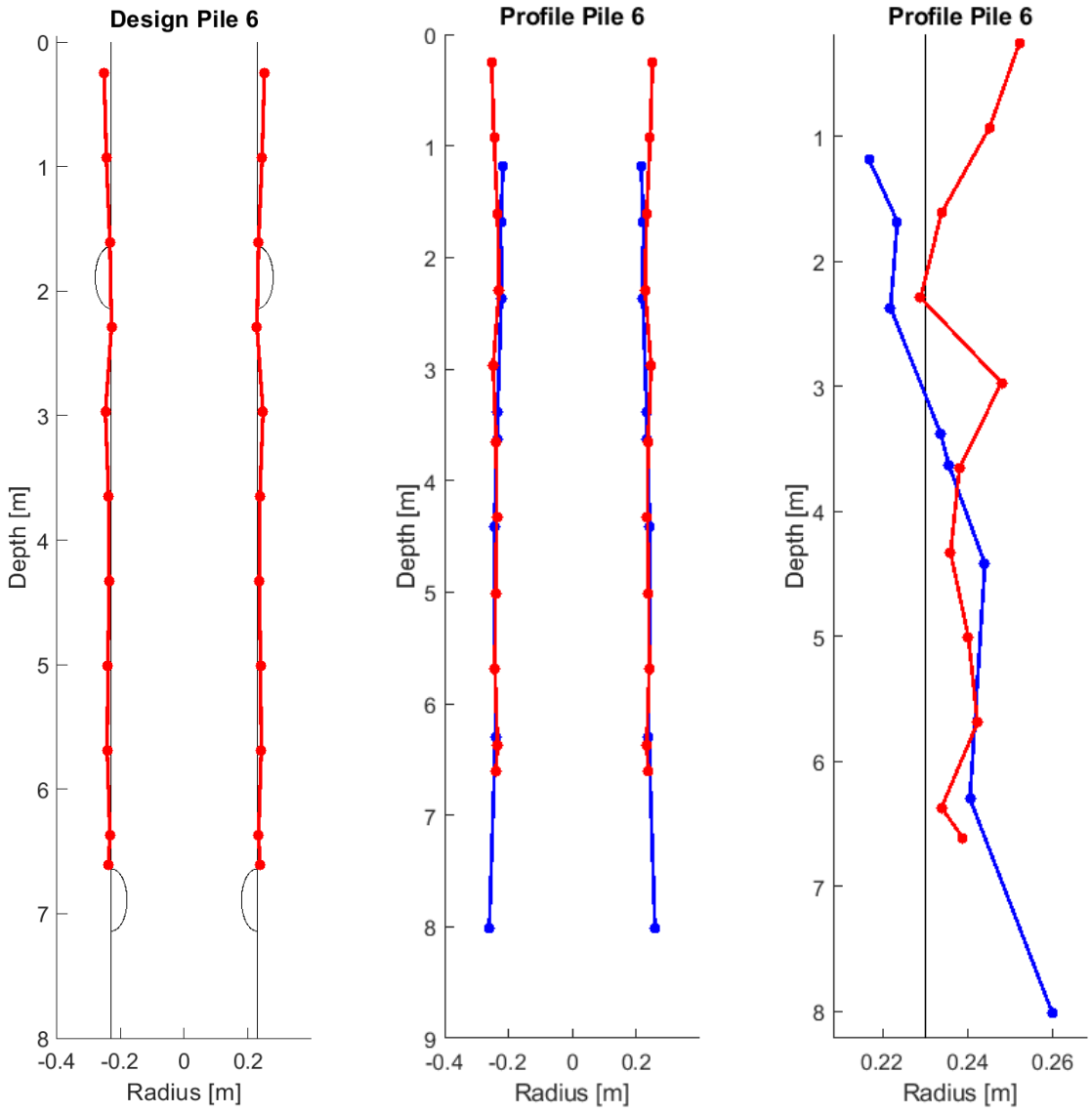

(a) Determined thickness in red and designed shape in black. Designed defects excluded. Source location of each measurement indicated with a dot.

(b) Determined thickness in red and measured shape in blue. Location of each measurement indicated with a dot.

(c) Close up of one side of the pile, showing the radius of the pile determine using the seismic tube in red, the measured shape in blue and the designed radius in black. Designed defects excluded. Location of each measurement indicated with a dot.

Figure F-6: Profiles foundation Pile 6.

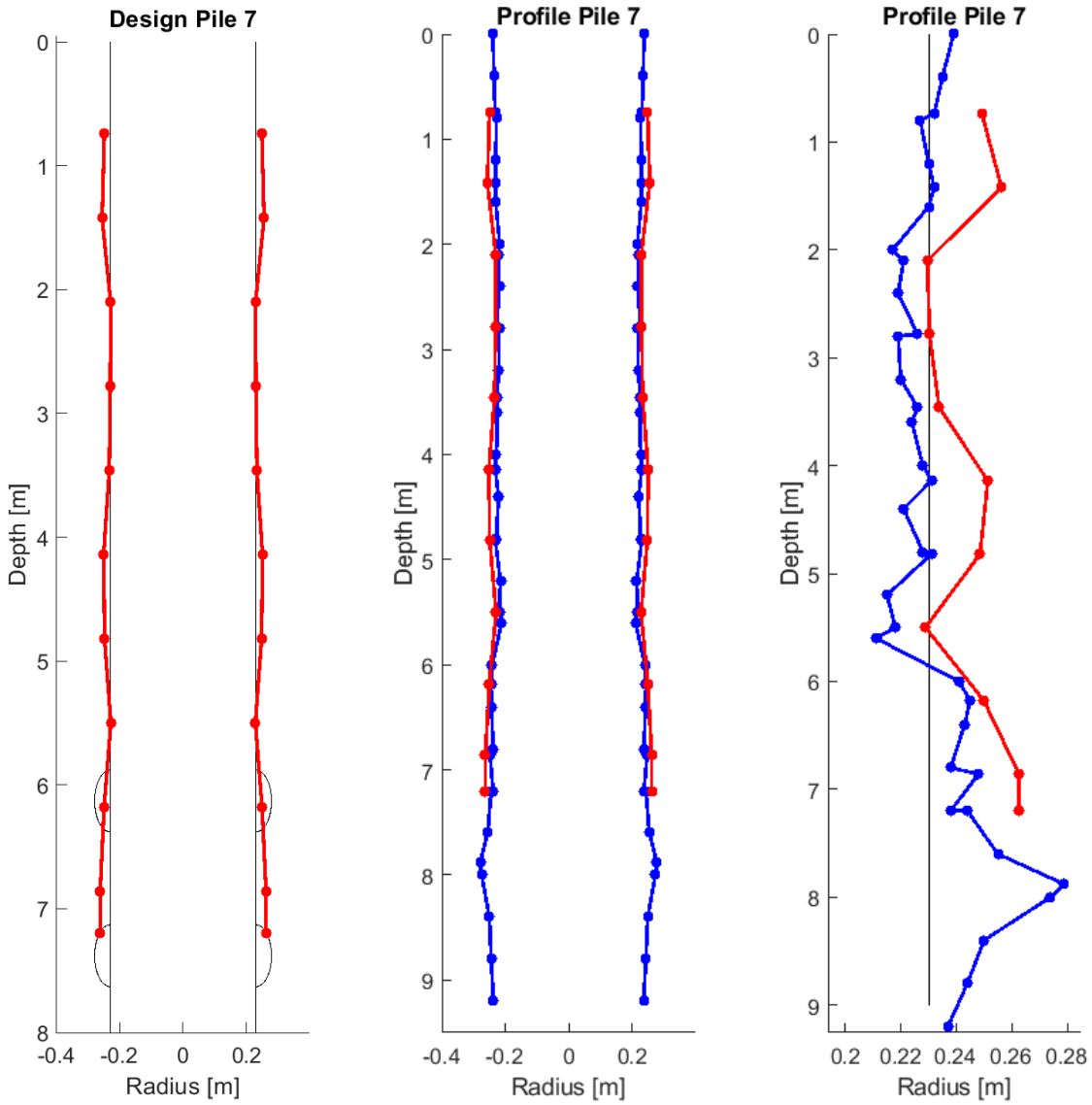

(a) Determined thickness in red and designed shape in black. Designed defects excluded. Source location of each measurement indicated with a dot.

(b) Determined thickness in red and measured shape in blue. Location of each measurement indicated with a dot.

(c) Close up of one side of the pile, showing the radius of the pile determine using the seismic tube in red, the measured shape in blue and the designed radius in black. Designed defects excluded. Location of each measurement indicated with a dot.

Figure F-7: Profiles foundation Pile 7.

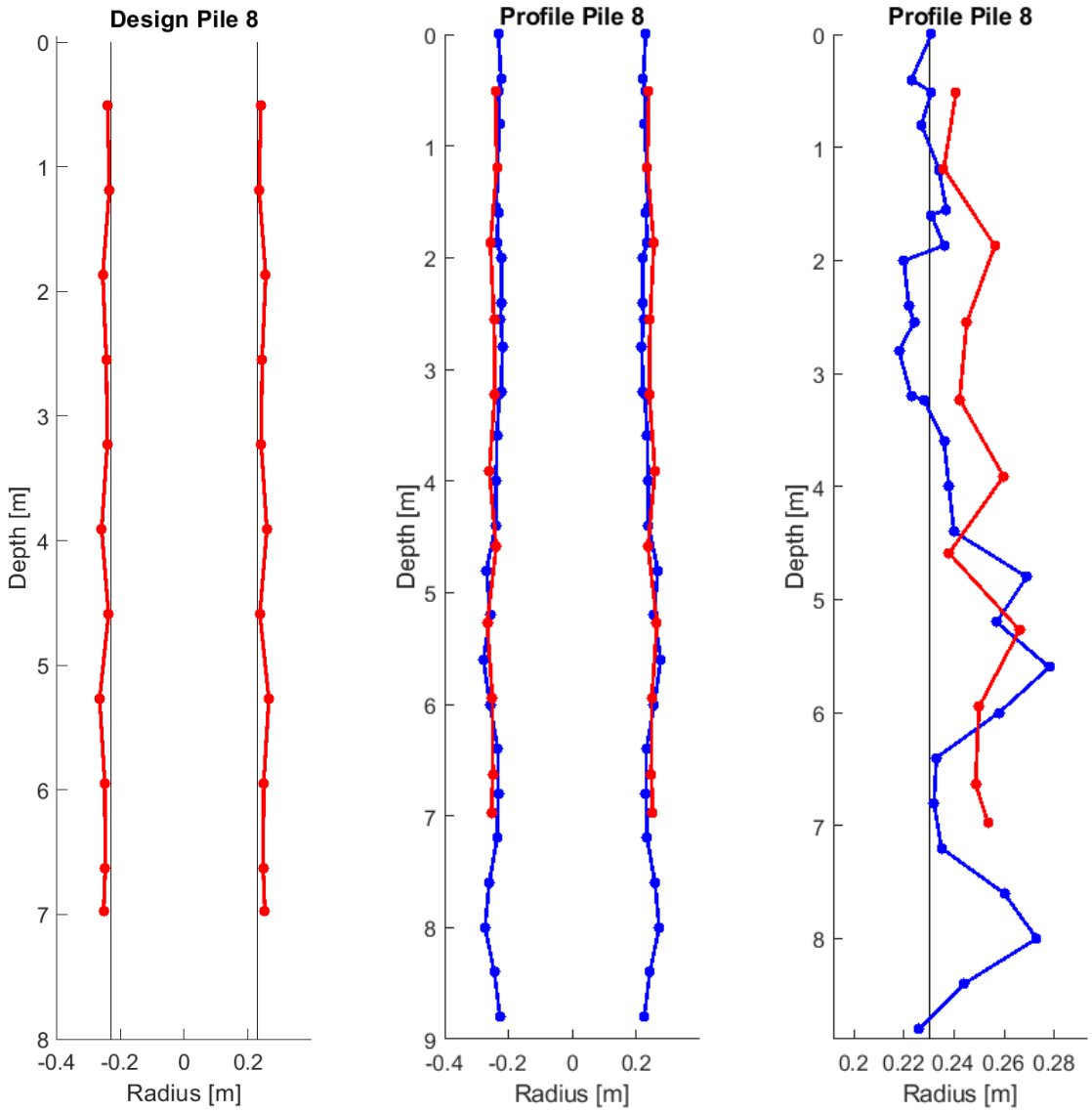

(a) Determined thickness in red and designed shape in black. Designed defects excluded. Source location of each measurement indicated with a dot.

(b) Determined thickness in red and measured shape in blue. Location of each measurement indicated with a dot.

(c) Close up of one side of the pile, showing the radius of the pile determine using the seismic tube in red, the measured shape in blue and the designed radius in black. Designed defects excluded. Location of each measurement indicated with a dot.

Figure F-8: Profiles foundation Pile 8.

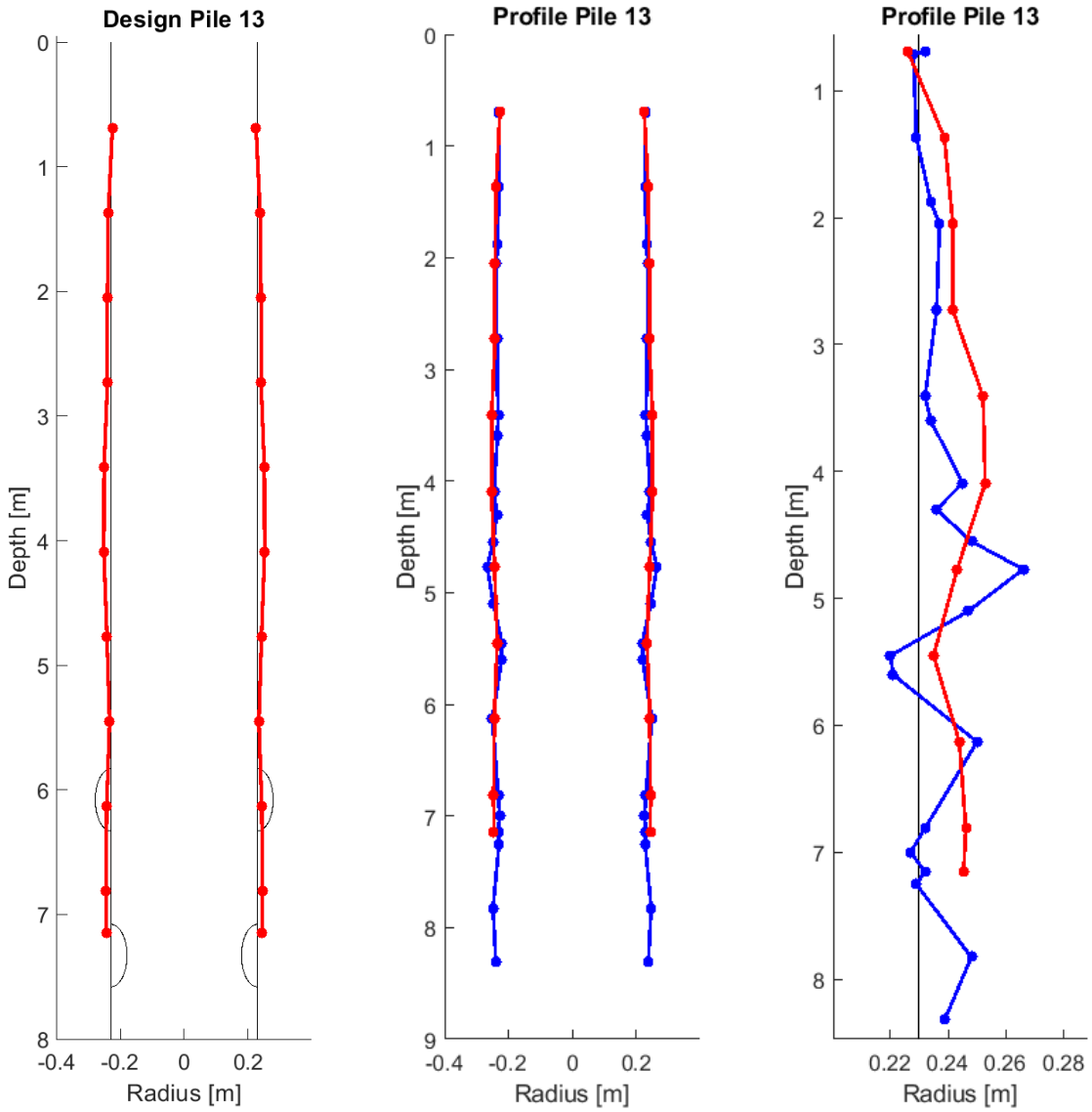

(a) Determined thickness in red and designed shape in black. Designed defects excluded. Source location of each measurement indicated with a dot.

(b) Determined thickness in red and measured shape in blue. Location of each measurement indicated with a dot.

(c) Close up of one side of the pile, showing the radius of the pile determine using the seismic tube in red, the measured shape in blue and the designed radius in black. Designed defects excluded. Location of each measurement indicated with a dot.

Figure F-9: Profiles foundation Pile 13.

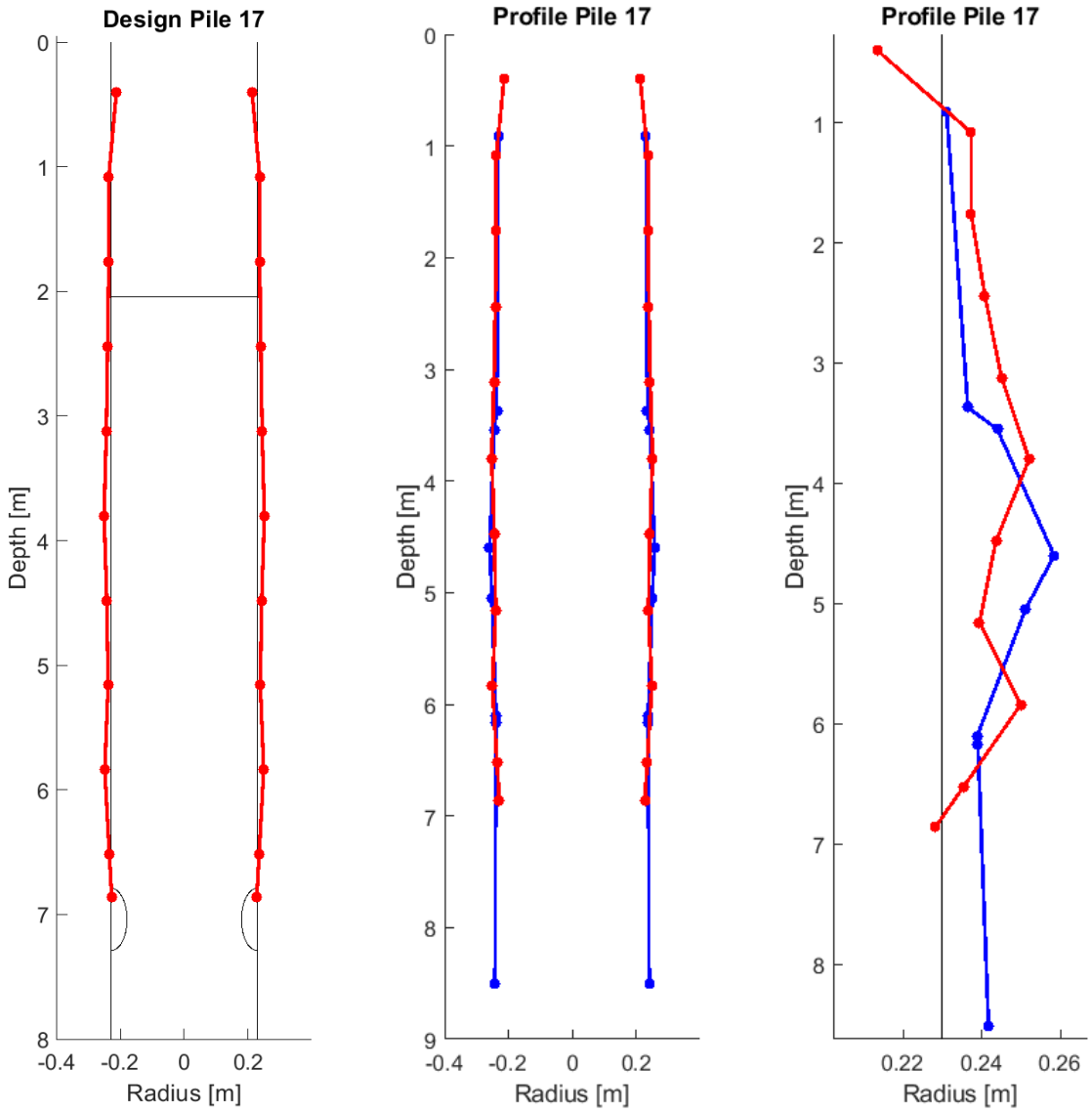

(a) Determined thickness in red and designed shape in black. Designed defects excluded. Source location of each measurement indicated with a dot.

(b) Determined thickness in red and measured shape in blue. Location of each measurement indicated with a dot.

(c) Close up of one side of the pile, showing the radius of the pile determine using the seismic tube in red, the measured shape in blue and the designed radius in black. Designed defects excluded. Location of each measurement indicated with a dot.

Figure F-10: Profiles foundation Pile 17.

F-2 Velocities

Velocities Test Piles Deltares test site			
Pile	**Velocity Pipe [m/s]**	**Surface wave velocity [m/s]**	**Concrete Velocity [m/s]**
nr. 1	1843	870	3957
nr. 2	1835	878	3942
nr. 3	1841	859	3974
nr. 4	1848	878	3890
nr. 5	1848	846	4045
nr. 6	1841	943	3884
nr. 7	1841	859	3955
nr. 8	1893	891	3968
nr. 9	1861	891	4019
nr. 10	1843	954	401
nr. 11	1874	898	4019
nr. 12	1843	860	401
nr. 13	1848	878	3945
nr. 14	1828	878	3942
nr. 15	1848	860	3961
nr. 16	1815	872	3988
nr. 17	1822	885	3961
nr. 18	1848	891	3871
nr. 19	1841	872	3968
nr. 20	1848	884	3993
Velocities Test Piles Additional measurements			
Pile	**Velocity Pipe [m/s]**	**Surface wave velocity [m/s]**	**Concrete Velocity [m/s]**
nr. 10	1843		4298
nr. 12	1809		4258
nr. 15	1796		4265

Table F-2: Velocities found in foundation piles at Deltares test site.

Appendix G

CPT data

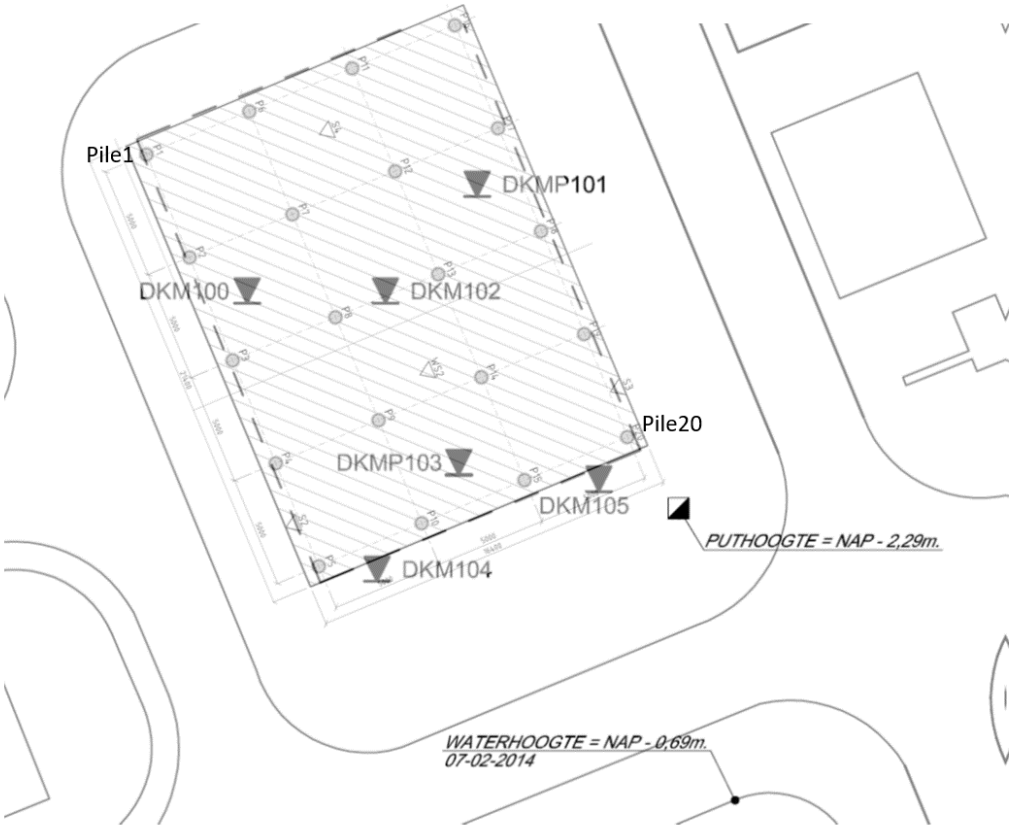

Figure G-1: Location CPT's performed at Deltares test site.

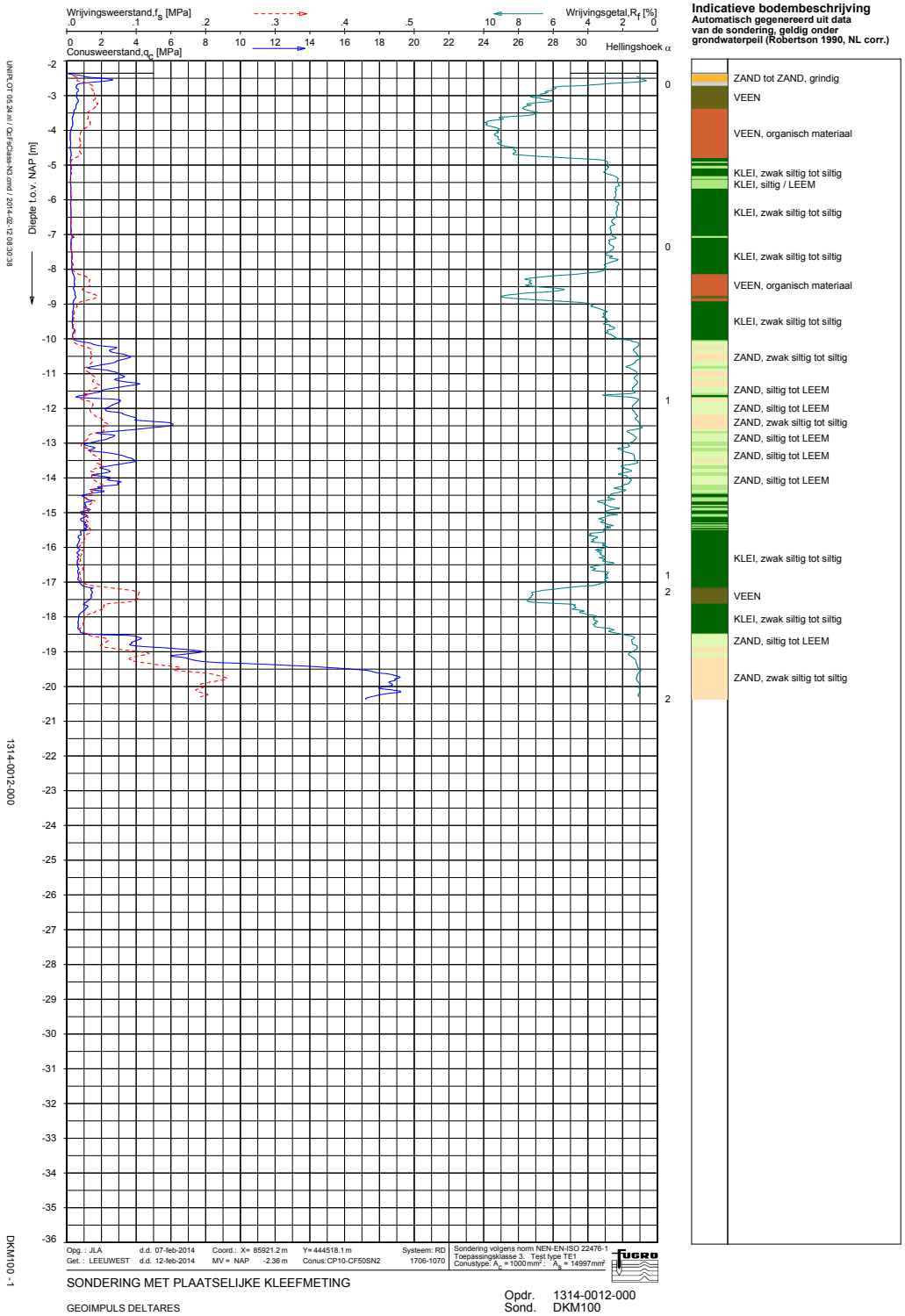

Figure G-2: CPT DKM100

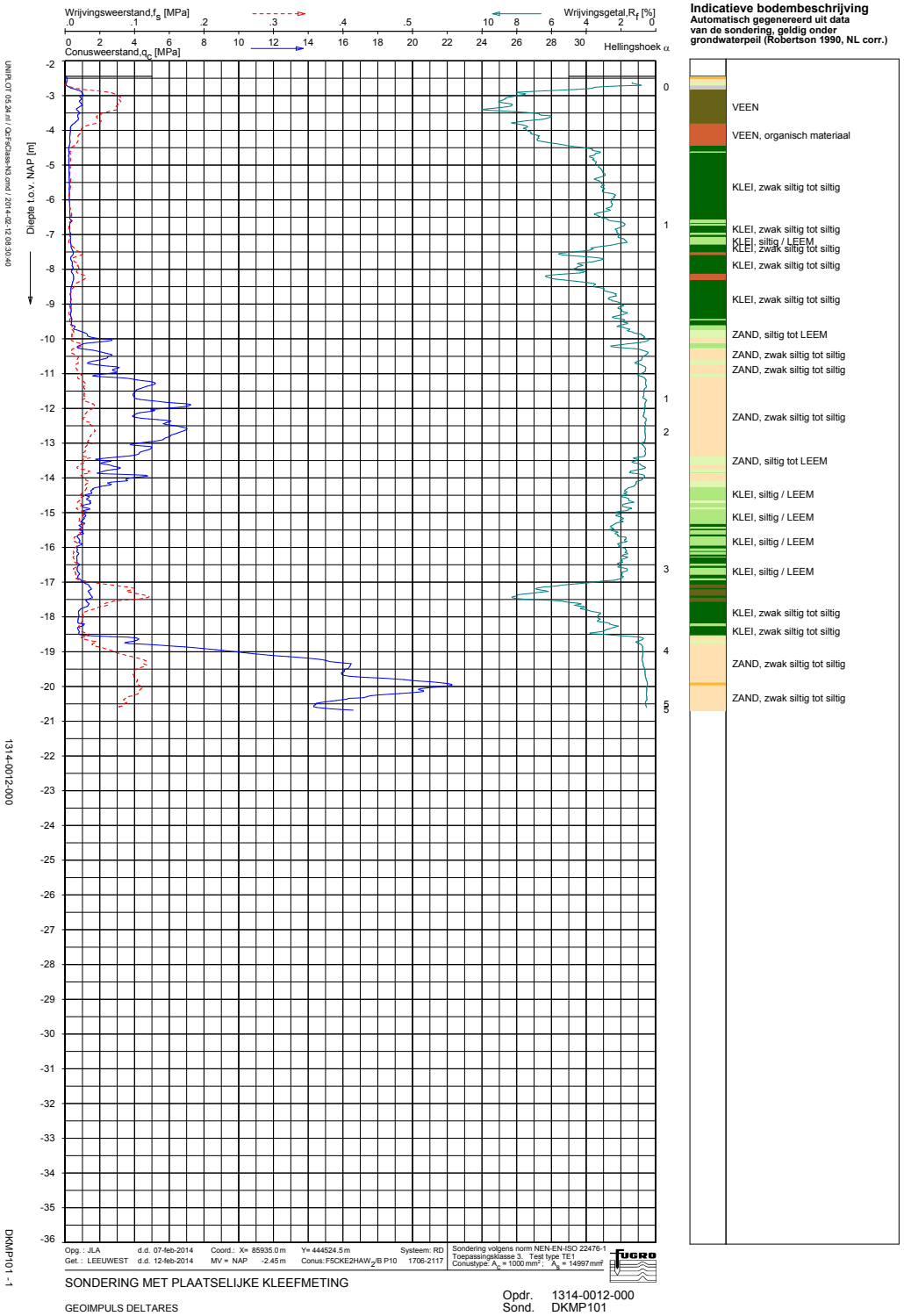

Figure G-3: CPT DKM101

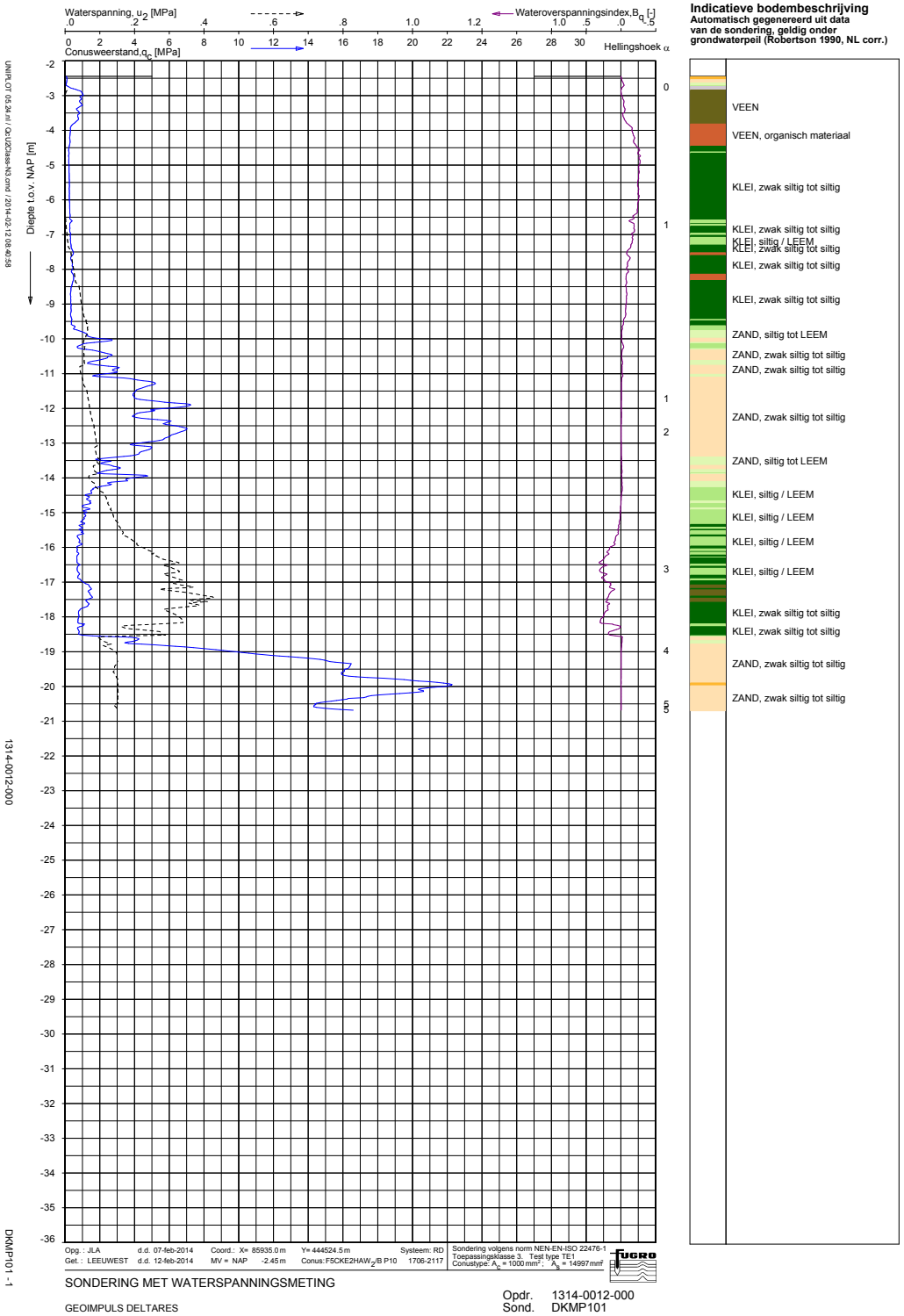

Figure G-4: CPT DKM101

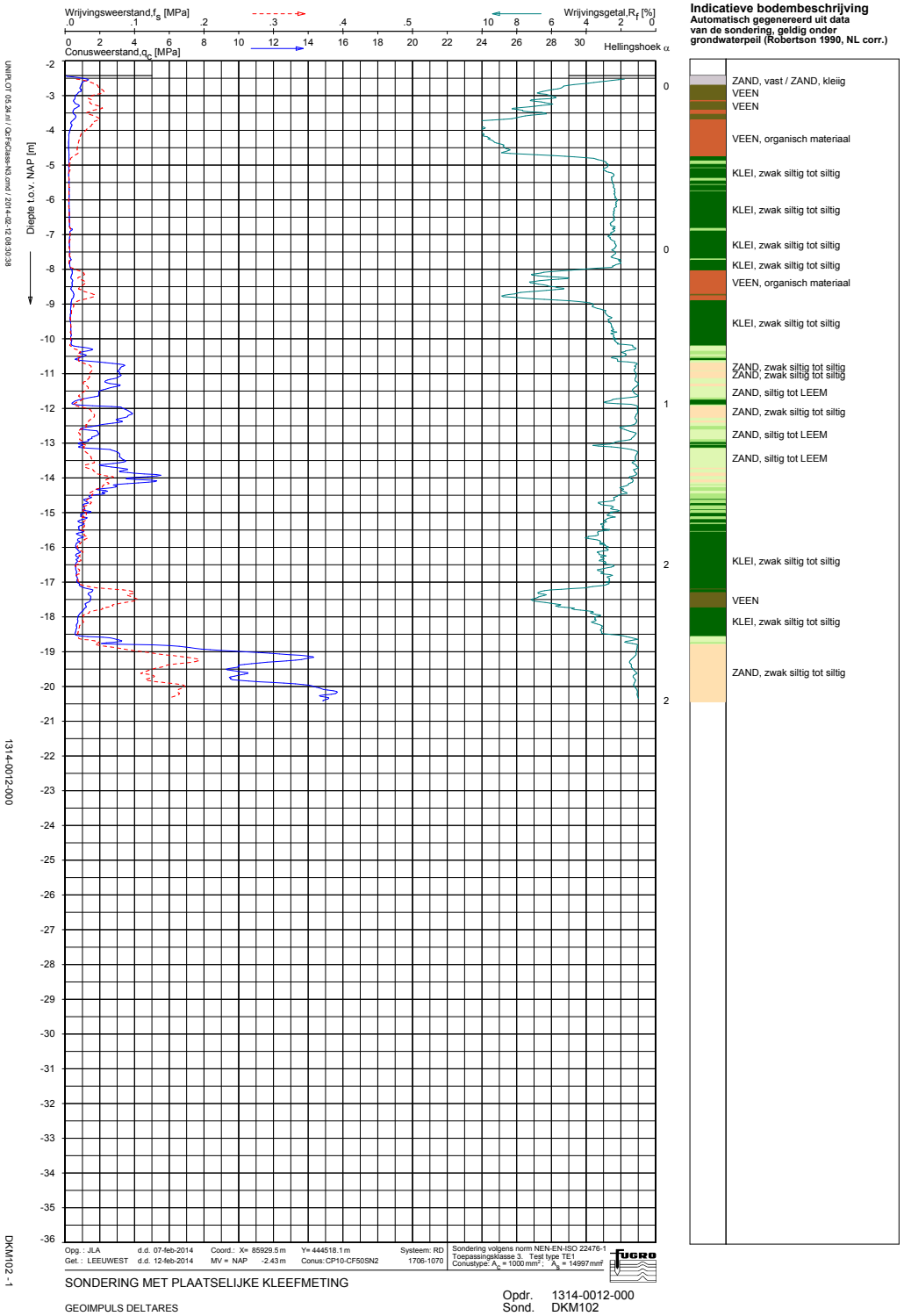

Figure G-5: CPT DKM102

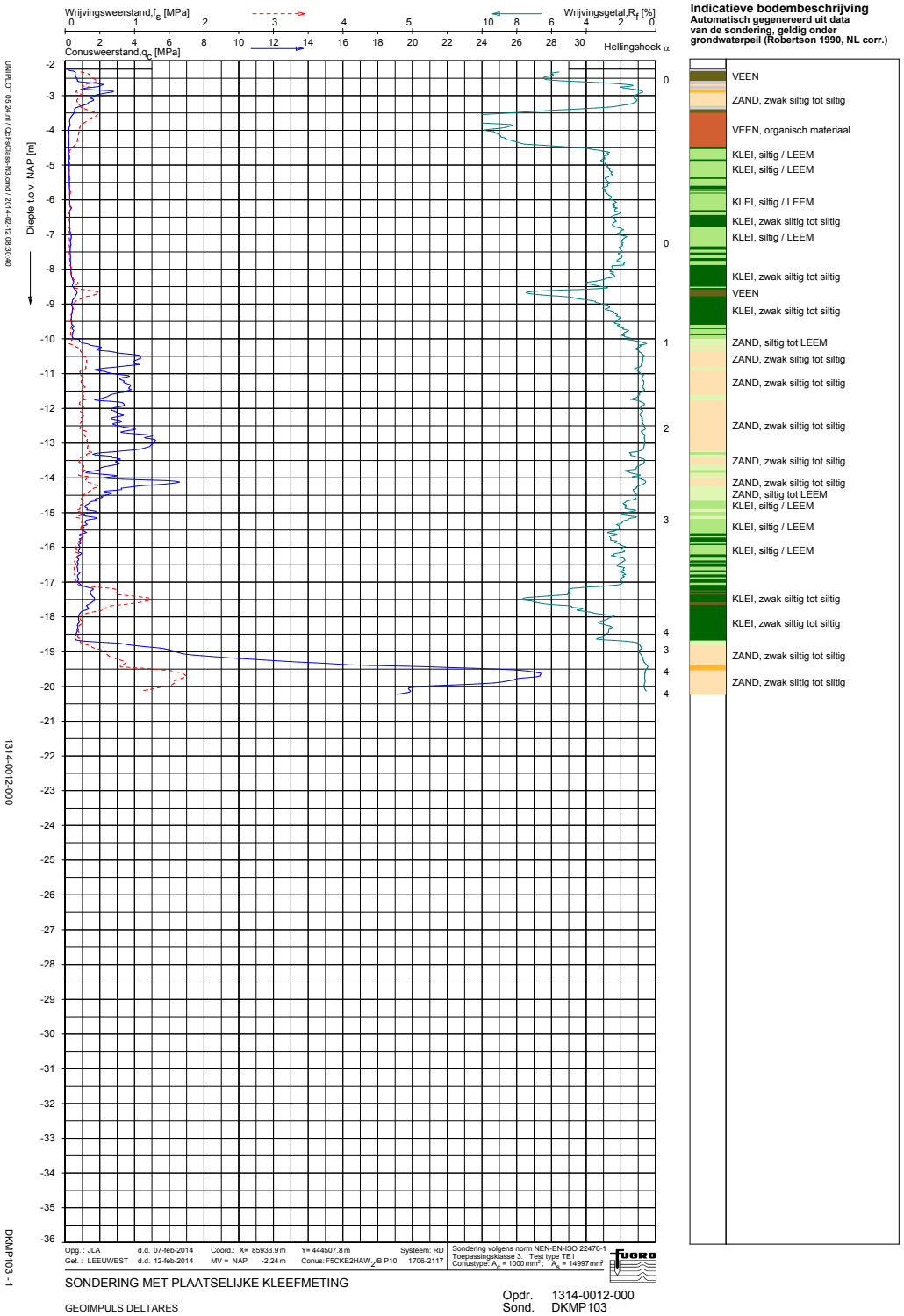

Figure G-6: CPT DKM103

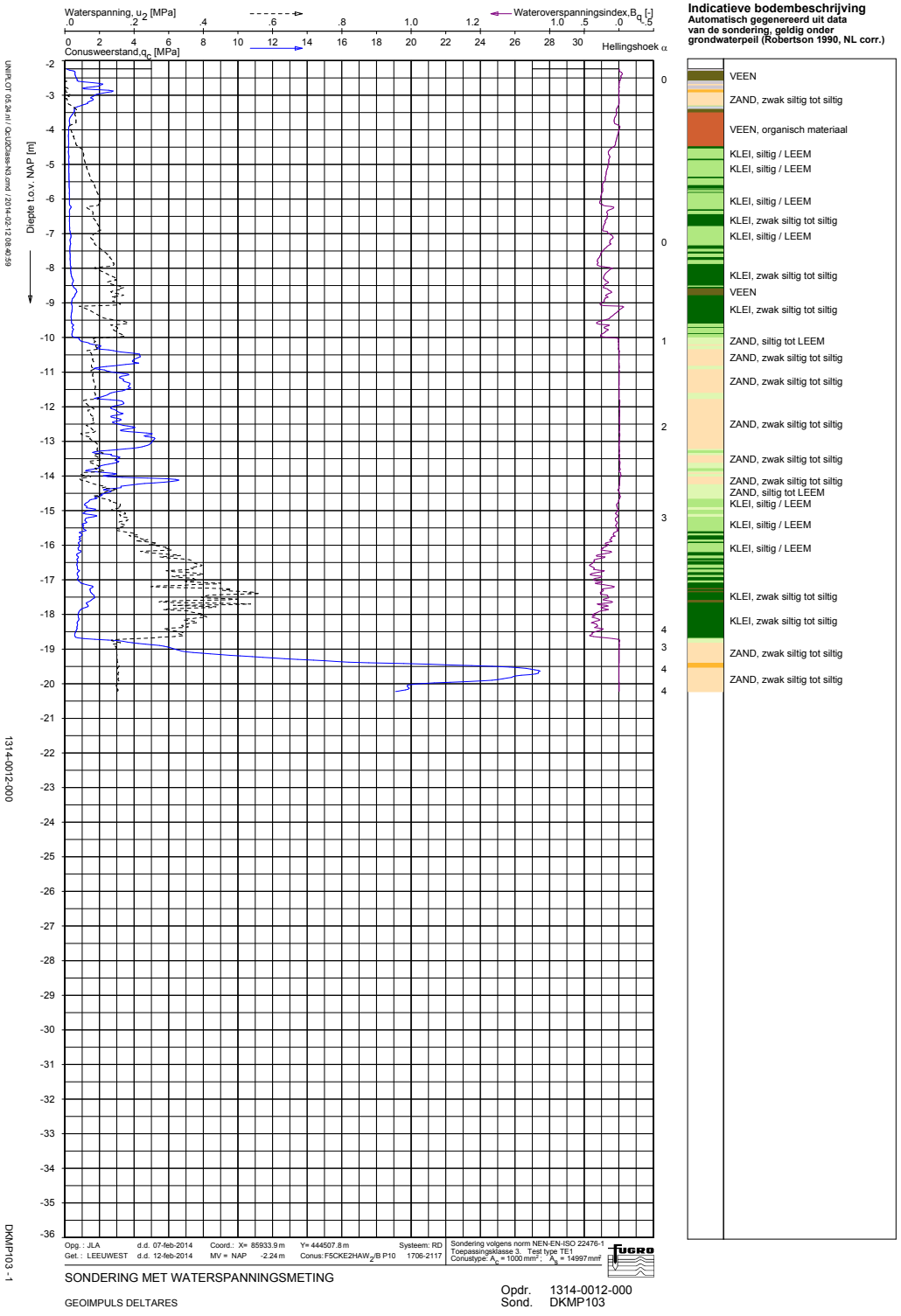

Figure G-7: CPT DKM103

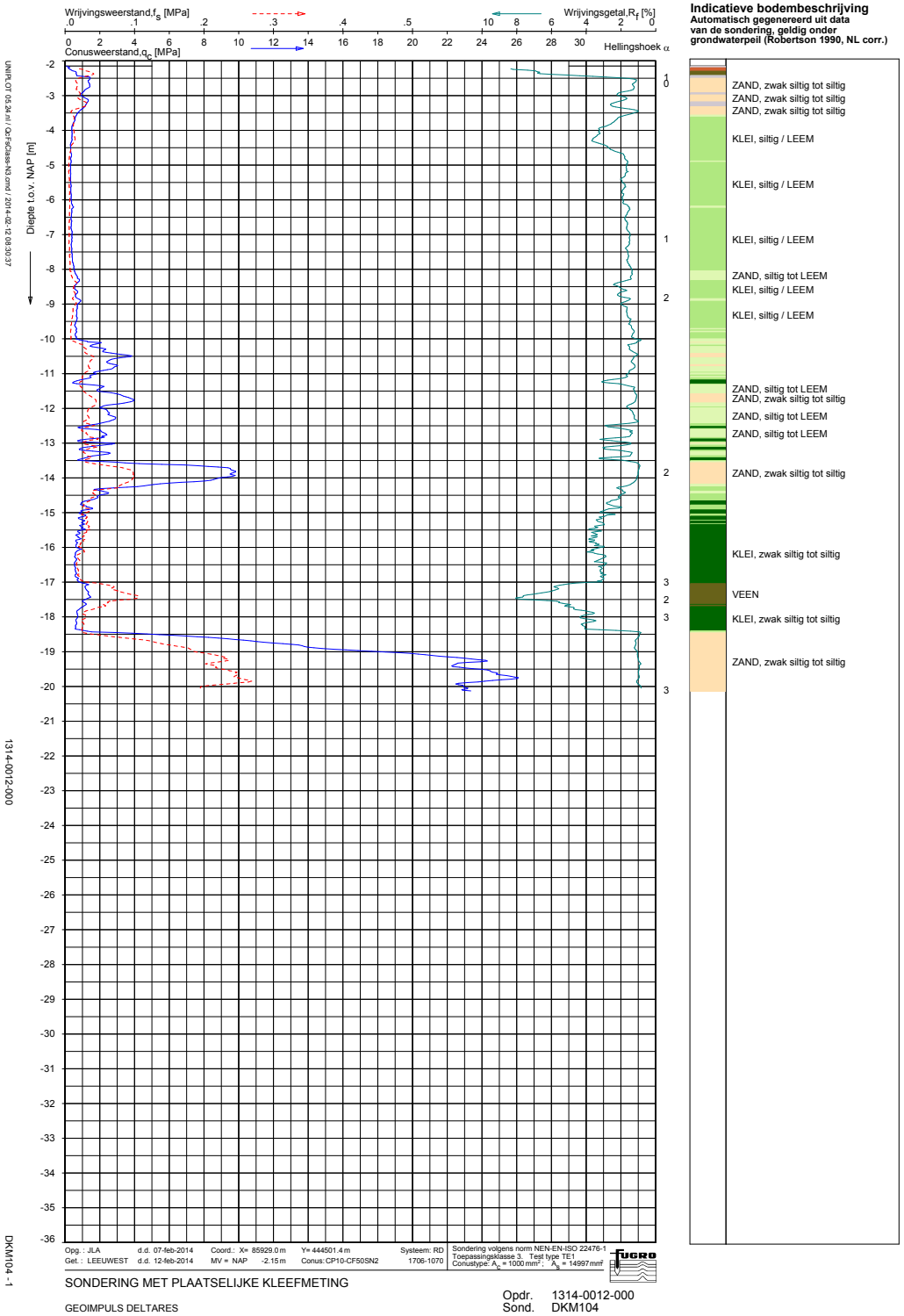

Figure G-8: CPT DKM104

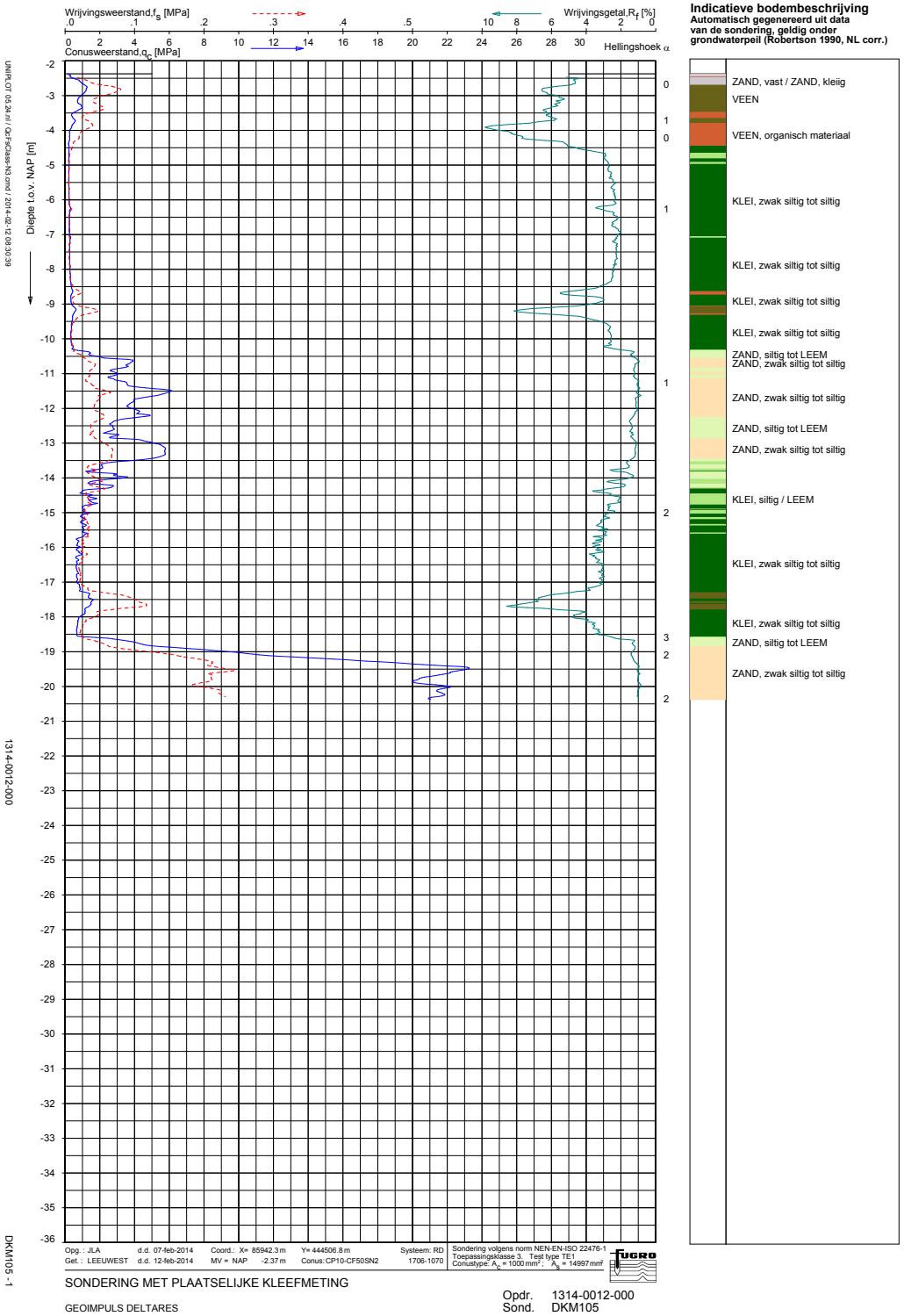

Figure G-9: CPT DKM105